DESIGN AND DEVELOPMENT OF BA-SR-CO DOPED HEXAFERRITE COMPOSITE BASED MICROWAVE ABSORBERS AT X-BAND

Thesis Submitted for the Award of the Degree of

DOCTOR OF PHILOSOPHY

in

Electronics and Communication Engineering

By

Aherrao Disha Sunil

Registration Number: 41900179

Supervised By

Dr. Charanjeet Singh (21882)

Electronics and Communication (Professor)

School of Electronics and Electrical Engineering, Lovely Professional University, Punjab

Co-Supervised by

Dr. A.K. Srivastava (11459)

Department of Physics (Professor)

School of Computer Science and Engineering, Lovely Professional University, Punjab

LOVELY PROFESSIONAL UNIVERSITY, PUNJAB

2025

DECLARATION

I, hereby declared that the presented work in the thesis entitled "**Design and Development of Ba-Sr-Co doped Hexaferrite Composite based Microwave Absorbers at X-band**" in fulfilment of degree of **Doctor of Philosophy (Ph. D.)** is outcome of research work carried out by me under the supervision of **Dr. Charanjeet Singh**, working as **Professor**, in the **Electronics and Communication Engineering, School of Electronics and Electrical Engineering** of **Lovely Professional University, Punjab, India**. In keeping with general practice of reporting scientific observations, due acknowledgements have been made whenever work described here has been based on findings of other investigator. This work has not been submitted in part or full to any other University or Institute for the award of any degree.

(Signature of Scholar)

Name of the scholar: Aherrao Disha Sunil

Registration No.: 41900179

Department/school: Electronics and Communication Engineering, School of Electronics and Electrical Engineering

Lovely Professional University,

Punjab, India

CERTIFICATE

This is to certify that the work reported in the Ph. D. thesis entitled "**Design and Development of Ba-Sr-Co doped Hexaferrite Composite-based Microwave Absorbers at X-band**" submitted in fulfillment of the requirement for the award of degree of **Doctor of Philosophy (Ph.D.)** in the **Electronics and Communication Engineering, School of Electronics and Electrical Engineering**, is a research work carried out by **Aherrao Disha Sunil, 41900179**, is bonafide record of her original work carried out under my supervision and that no part of thesis has been submitted for any other degree, diploma or equivalent course.

(Signature of Supervisor)

Name of supervisor: Dr. Charanjeet Singh

Designation: Professor

Department/school: Electronics and Communication Engineering,

University: Lovely Professional University, Punjab

(Signature of Co-Supervisor)

Name of Co-Supervisor: Dr. A. K. Srivastava

Designation: Professor

Department/school: Department of Physics

University: Lovely Professional University, Punjab

ABSTRACT

Without much understanding of the ramifications, electromagnetic pollution from growing human activity in the domain of electrical and electromagnetic energy use is gradually expanding. Although everyone is aware of the advantages of advanced electronic and electrical gadgets, only a few users are aware of gadgets and systems' real or unsuspected dangers. For routine operation, the majority of contemporary electronic gadgets send, receive, and process electromagnetic signals. Wireless communication relies on electromagnetic signals, with their strength primarily determined by the distance between the transmitting and receiving devices. These devices can be seen as sources of operational electromagnetic radiation. Additionally, many gadgets emit electromagnetic radiation, either intentionally or incidentally. Nearly all consumer electronics, including appliances like motorized laundry machines, mixers, grinders, laptops as well as televisions and other media devices, contribute to this. In the medical field, electronics have paved the way for a new generation of electromedical equipment, which can be used for diagnostic or therapeutic purposes. The advent of electronic display devices has also ushered in a new era of patient care. Whether operating as intended or as a byproduct of normal use, these devices all utilize electromagnetic waves, contributing to the growth of the electrical fields within hospital environments. These fields extend beyond the usual power frequency electromagnetic fields emitted by utility power lines in surrounding areas. Hazards like this have given the reason for this research, which is the design of microwave-absorbing materials that can absorb and reduce the impact of this electromagnetic pollution on nearby surroundings.

Better impedance matching, careful control of electromagnetic properties, affordability, a wide absorption bandwidth, lightweight design, and the creation of substantial dielectric/magnetic loss mechanisms are all necessary for an efficient microwave absorber. Consequently, we study M-type hexaferrites, a class of high saturation magnetization magnetic materials. However, these specifications for a microwave absorber cannot be entirely satisfied by pure M-type hexaferrite alone. As a result, we need to focus on M-type hexaferrite substitutes and their composites, which include low-coercivity and reasonably priced materials like polyaniline. In this study, we have synthesized $Ba_{0.2}Sr_{0.8}Co_xMg_xFe_{12-2x}O_{19}$, $Ba_{0.2}Sr_{0.8}Co_xCu_xFe_{12-2x}O_{19}$, $Ba_{0.2}Sr_{0.8}Co_xAl_xFe_{12-2x}O_{19}$ and $Ba_{1-x}Sr_xFe_{12}O_{19}$ with PANI as an effective matrix via sol-gel synthesis method. During the sintering process, the pre-heating was done at 550 °C and heating at 1100 °C. The Structural Analysis included XRD, FESEM, and EDAX. The X-ray diffraction patterns verified the synthesized samples' Bragg peaks appear to be well-defined, pointing to a good crystal structure, only with minor traces of hematite. FESEM validated that the doping is

increased, and the particle size, in some compositions particles, has changed their shape from oval to Rice-like. Also increased doping caused more fused grains. Due to the electrostatic and magnetic interactions between ferrite particles, doping results in grain clusters with an uneven size distribution. EDAX of each composition confirmed the presence of various elements in the given synthesized samples. Electrical Analysis included the investigation of Dielectric permittivity, electric modulus, complex impedance spectra, and ac conductivity. The relaxation processes vary the active performance of grains and grain boundaries in respective frequency regions. Valence electron hopping between Fe^{2+} and Fe^{3+} at Octahedral sites is the primary cause of the conduction mechanism in ferrites. Increased frequency leads to a rise in the hopping frequencies of charge carriers, which improves conductivity. This frequency-dependent conduction process may be explained by the polaron hopping model. The AC conductivity rises with rising frequency within the constrained range of polaron hopping. However, the conductivity tends to diminish for long-range polarisation hopping. AC conductivity study verified the sudden translational motion with the hopping of charge carriers in the synthesized samples. Magnetic analysis was confirmed with the help of the hysteresis loops and linear fits of each sample. The M-H loop showed that all prepared specimens showed a linear relationship, with a sharp rise in M_s at low-applied fields that decreases at high-applied fields. The persistent retention of magnetization following the removal of an applied field is determined by remanence magnetization, which is frequently large in M-type hexaferrite and suggests significant remanence. Additionally, the M_r/M_s ratio was used to assess the material's magnetic hardness and inter-grain group growth; its value had fallen between 0 and 1 as required. The agglomeration and voids shown in the micrographs confirmed the respective increase and decrease in H_c of the prepared samples.

Porosity, electron spin, grain size distribution, charge buildup at grain boundaries, and dipole polarization are some of the elements that affect the complex permittivity and permeability in the microwave range. Electron hopping in Fe^{2+}/Fe^{3+} is the cause of dielectric polarization in ferrites. The porosity prevents polarization and acts as a barrier to the field flow. The mechanism of complex permeability is controlled by ferromagnetic resonance and exchange resonance between Fe^{2+}/Fe^{3+} ions. The ε', ε'', μ', μ'' graphs in the microwave section verified that complex permittivity and permeability elements affected the microwave absorption. The RL graphs varied the quarter wavelength mechanism. The RL graphs, the impedance graphs (i.e., Z_{in}), and the 3D graphs for all compositions are displayed individually in Figures verifying the microwave absorption phenomenon.

ACKNOWLEDGMENT

I would like to begin by expressing my heartfelt gratitude to God for granting me the strength, determination, and courage to carry out my research.

I wish to express my sincere thanks to my supervisor, Dr. Charanjit Singh (Professor), for his valuable guidance, encouragement, and constant support throughout my research. I would also like to thank my co-supervisor for his support during this research journey.

I sincerely wish to thank Dr. R.B. Jotania (Department of Physics, Gujarat University, Ahmedabad, India), Dr. V. L. Mathe (Department of Physics, Savitri Phule Pune University), Dr. Sachin Godara (Department of Apparel and Textile Technology, Guru Nanak Dev University, Amritsar), Dr. Suwarna Datar (Department of Applied Physics, Defence Institute of Advanced Technology, Pune, India) for providing various supports in characterization.

I also want to thank my parents (Sunil and Vandana Aherrao), my mother-in-law (Pushpa Gawande, my father-in-law (Pralhad Gawande), my kids (Anaisha and Veer), and special thanks to my husband, Swapnil Gawande for his constant support and motivation throughout the journey.

Aherrao Disha Sunil
Registration no. 41900179
Date: 19/11/24

TABLE OF CONTENTS

Figure Content

Table Content

CHAPTER 1

INTRODUCTION

Potential uses for electromagnetic waves include industry, healthcare, and communication. Cellular phones, satellite communication, terrestrial communication systems, etc., are examples of applications in communication. Non-destructive testing of dielectric materials, microwave heating, microwave thawing, drying, food processing, etc., are industrial uses. Microwave hyperthermia and diathermy are two common medical procedures for treating malignant growths and tumors. Microwaves have a wide range of applications, and several studies have discussed their value for biological imaging by using the concept of the dielectric permittivity of biological materials.

Numerous researchers have recently questioned whether prolonged exposure to electromagnetic fields, particularly microwaves, might harm human health [1- 4]. According to studies, electromagnetic (EM) fields may contribute to the development or spread of cancer. Researchers have shown that exposure to microwaves in the home and workplace (cellular phones, Cell phone towers, WIFI, etc.) increases the chance of developing cancer. According to reports, different biological systems are impacted by EM fields in different ways. It could change a cell's shape or basic functioning. Until now, it has not been entirely known how EM fields interact with live cells. It has been suggested that contact can have a variety of consequences and change how cells signal, altering factors such as ionic transport and plasma membrane permeability [5-10].

Even if the uses for microwaves are expanding, reports also point to their danger. The dangers of microwaves and other areas of the electromagnetic spectrum have been the subject of several study articles. Hence, researchers have been studying microwave absorbers, and ferrite plays a prime role in these absorbers [9-10].

For more than 85 years after their development, ferrites have been extensively employed in several electric and electronic applications. The initial use was for radios. At that time, it was highly anticipated that radio equipment would become smaller. The size of radios decreased significantly when ferrite cores were used as inductors instead of air cores. A novel use of ferrites for electromagnetic noise suppression emerged in the 1980s with the proliferation of digital technology. Ferrites are used in a wide range of applications in the electric and electronic sectors today. A variety of modern mobile instruments and vehicles need high-frequency operations to perform their duties. More and more of these gadgets will employ ferrite. Currently, the world produces around 200,000 tonnes of soft ferrite every year. A significant portion of the output of ferrite is now used for power supply and noise reduction [2][7].

An insulator that can be magnetized is FERRITE. It is a metal oxide with magnetic ions organized in a way that results in spontaneous magnetization while preserving good dielectric characteristics, to be more precise. Ferrites have solidified their position as a significant class of magnetic materials over the past 20 years, finding use in a variety of linear, digital, and microwave applications, including magnetic memory cores, cylindrical-domain (bubble) memories, magnetic recording heads, and microwave applications.

1.1 Ferrites and its History

Ferrites are a kind of magnetic ceramic material made mostly of iron (III) oxide. Lodestone, a naturally magnetized mineral form of magnetite (Fe_3O_4), was the first of these minerals that humans were aware of. Thales of Miletus provided one of the earliest accounts of the special qualities of this mineral. The philosopher explained lodestone's attraction to iron and other lodestones around the sixth century BC." By the end of the Warring States era (fourth century BC), the Chinese were also aware of the attraction phenomena, according to references in the Guiguzi.

Chinese diviners are said to have utilized compass-like tools constructed of lodestone in their esoteric rites by the early centuries of the current period. William Gilbert's "De Magnete, Magneticisque Corporibus, et de Magno Magnete Tellure," written in 1600, is one of the earliest examples of contemporary science to describe the characteristics of lodestones. Gilbert argued in this dissertation that the planet's behavior was more like that of a massive magnet than that of a single pole. Terrella, which means "small Earth" in Latin, was a scale model of the planet that he used to research its characteristics. The expert said that the moon is held in orbit around Earth by magnetism. This was one of the earliest attempts to provide a rational scientific alternative to Aristotelian astronomy for the motion of celestial bodies, even if it was incorrect.

The use of ferrites in electrical appliances was pioneered by Takei and Kato's work. Scientists at the Tokyo Institute of Technology found that iron and divalent cation oxides exhibited unique magnetic characteristics in 1930. They presented their findings about these "ferrites" at the American Electrochemical Society's Annual Meeting in St. Louis [1]. They didn't know at first if these materials would have any practical use, but their work resulted in the establishment of the TDK Corporation in 1935. In 1937, ferrite cores were first created and used extensively, mostly in wireless communication equipment. The business had already created 5 million ferrite cores by the conclusion of World War II, mostly for the Japanese war effort.

Neel presented his theoretical explanation of ferrimagnetism in 1948. The magnetic characteristics of the zinc ferrites created by Takei and Kato were satisfactorily explained by

his study. The development of ferrites was significantly aided by research done in the 1940s and 1950s at Philips facilities in the Netherlands. Some of the well-known scientists from this period who contributed to the development of materials with high electrical resistivity and minimal relaxation losses are Snoeck and Verwey. A comparable substance with better characteristics was created by Philips ten years later: strontium hexaferrite. The global market for these materials is presently dominated by hexaferrite.

Since then, ferrites have spread throughout most electrical gadgets. Ferrites are used in a variety of applications in modern life, such as antennas, ferrite cores, and EMI suppressors. Nevertheless, since these materials were in their infancy, their range of applications has been expanding. Ferrites are being used for a variety of commercial reasons, from quantum computing to the medical industry. It is not surprising that the industry has shown interest in these materials, given their low cost and unique characteristics.

Ferromagnetic materials that are just as ceramic but majorly composed of ferric oxide, namely alpha-Fe_2O_3, are termed ferrites. Even though this has less saturation magnetization compared to ferromagnetic alloys, its benefits, such as normal behavior at higher frequencies, heat resistance, and corrosion-resistant behavior, make them fit for several applications at a cheaper expense [2][10].

It is said that magnetite (Fe_2O_3) was found as a natural mineral and was utilized by our ancestors as a mariners' compass due to its attribute of magnetism. Anyhow, nobody attempted the industrialization application of ferrites until the beginning of the last century. However, in the early ages, its magnetization properties were considered inferior to its ferromagnetic alloys, so the commercial utility of ferrites did not fetch global interest.

Later in the 1950s, a few applications, namely radio, television, radio circuits, telephony circuits, and microwave devices, brought about a sudden awareness in the minds of people for Ferrites and their outstanding qualities. Researcher in various fields, such as ceramics, chemicals, and metallurgy, initiated their works toward improving the existing properties of ferrites. Synthesis methods for the production of ferrite are mostly similar to general ceramics, but ferrite requires more steps in synthesis.

They believe that work on ferrites has been fully developed in all fields along with its applications. But as the year passes, the applications become wider as the study progresses in each field [3][10].

1.2 Spinel Ferrites

The ferrites that are easiest to identify are those made of spinel. Magnetite (Fe_3O_4), the most well-known member of this group, is not only the prototypical ferrite but also the first substance to be recognized as magnetic, giving rise to the name "magnetism" itself.

The formula MFe_2O_4 can be used to describe spinel ferrites, where M is often a combination of two-valent cations (Li^+ and Fe^{3+}) or a divalent cation, such as cobalt or zinc. The name of this group comes from the ability of these materials to exhibit a structural arrangement like that of spinel ($MgAl_2O_4$).

1.3 Hexaferrites

Hexaferrites, a noteworthy subclass of ferrites, are those that crystallize with hexagonal symmetry. Since their discovery in the 1950s, these materials have played a crucial role in business and technology across a wide range of applications, including data storage and magnetic recording, they are preferred over spirals since they have better dielectric as well as magnetic properties over later.

The magnetic mineral magnetoplumbite was originally identified in the 1920s. According to the empirical formula $PbFe_{7.5}Mn_{3.5}Al_{0.5}O_{19}$ [9], it was characterized as a hexagonal crystal. This mineral ($PbFe_{12}O_{19}$) and its analogs were replicated in multiple investigations by Philips Laboratories in the 1950s, which helped to advance the young area of hexaferrite research. Lead was used to replace the massive divalent cations strontium ($SrFe_{12}O_{19}$) and barium ($BaFe_{12}O_{19}$) in these synthetic ferrites. These compounds are now the most economically significant group of magnetic materials.

Hexaferrites contain oxygen, iron, and at least one additional metallic atom, just like their spinel counterparts. The two elements that are most frequently found in these materials are barium and strontium. Hexaferrites, in contrast to spinels, cannot be simply described by a single space group or even a condensed formula. Instead, this huge family of ferrites is classified into several groups with comparable crystal structures and chemical makeup.

Hexaferrites can be conceptualized chemically as mixtures of spinel ferrites with Y and M ferrites. Z ferrites ($Ba_3Me_2Fe_{24}O_{41}$), for instance, may be represented as a sum of the corresponding Y ($Ba_2Me_2Fe_{12}O_{22}$) and M ferrite ($BaFe_{12}O_{19}$). From a crystallographic perspective, spinel and hexagonal layers make up all hexaferrites. The unit cells of each hexaferrite subgroup would be produced by different stacking patterns of these fundamental elements. Pullar provided a thorough explanation of the many stacking options available in these systems [10][11-13].

The M ferrites, which were the first hexaferrite to be described, continue to be the most commercially significant. The most prevalent chemicals in this class are SrM and BaM. Ferrites

belonging to this group, as well as W and Z ferrites, crystallize in the P63/MMC space group. The final three families (Y, X, and U) are members of the R3C group. They often have significant magnetocrystalline anisotropies that are aligned with the c-axis due to their composition and hexagonal structure. Large anisotropies result in extremely high energy needs for the magnetization direction to shift. One of the most noticeable characteristics of hexaferrite is its high coercivity, which is the macroscopic result of this process. Additionally, because of their high Curie temperatures, these materials may be used at room temperature.

Ever since Neolithic man first used a piece to navigate, mankind has used magnetic materials of various kinds. These have become massively important materials commercially and technologically, with BaM hexaferrite alone accounting for 50% of the total magnetic materials manufactured globally, at over 300,000 tonnes per year, and they have a multitude of uses and applications [2][10].

1.4 Progress in Applications Of Ferrite

1.4.1 Cores

The constant efforts of several people in the chemical industry have contributed significantly to the steady advancement of soft ferrites since manufacturing began in 1936. The initial production of Cu-Zn ferrite as ferrite cores for antennas and intermediate frequency transformers (IFTs) in radios. However, the manufacture of it was stopped around 1970, and presently, Ni-Cu-Zn ferrite is made and used. Currently, Ni-Cu-Zn ferrite is used in a wide range of products, such as multilayer ferrite chip components, noise filters, and rotary transformers.

Wide-band as well as pulse transformers for high initial permeability materials, inductors, and telecommunication parts over low-loss materials, while power applications for high-saturation magnetization are the three general classifications of Mn-Zn ferrite used based on its properties. Flyback transformers, deflection yokes in television sets, and carrier telephony have been the three main traditional applications of Mn-Zn ferrites. The most significant uses lately, nevertheless, have been switching transformers [4][14-18].

Because of their excellent cost-effectiveness, Mn-Zn, Mn-Mg-Zn [19], or Mg-Zn ferrites [20] have lately been employed extensively for deflection yokes. The introduction of better resolution home wide-screen television calls for significant advancements in the saturation magnetization and power loss of the ferrite used in deflection yokes.

One of the quickest-growing and potentially useful ferrites, Mn-Mg ferrites with rectangular hysteresis loop properties, which were previously employed for memory and switching cores

in digital computers, vanished entirely in the 1980s. Additionally, magnetic bubble devices vanished about 1985.

1.4.2 Multilayer Chip Inductors

In the 1990s, electronic component sizes started to go downward. Concurrently, advances in surface-mount technology were developed, and efforts were made to integrate ferrite inductors at high densities into printed circuit boards. This has made it possible for several kinds of multilayer ferrite chip inductors with dimensions of 10 mm in length and 0.5 mm in width, to be utilized in a variety of devices, including television receivers, video equipment, headphone stereos, hard disc drive systems, personal computers, cordless phones, automotive components, etc.The chip inductor makes use of the ease of shrinking. Because the coil is protected by ferrites, the flux is completely leak-free. Automatic equipment makes high-density equipment conceivable. As a result, it is anticipated that demand for chip inductors will rise in the future.

1.4.3 Microwave Devices

Since the 1950s, when microwave ferrite devices were created in the United States, ferrite materials have been utilized in a variety of microwave devices, including filters, switches, limiters, isolators, and tunable electro-optic modulators. At the moment, the most popular microwave ferrites are hexagonal-type barium ferrites [21-22], spinel-type Ni-Zn, Mn-Mg-Zn, and lithium ferrites, both in bulk and film form. Global demand for highly low-loss and environmentally friendly microwave devices made of ferrite materials has been further highlighted by the recent exponential rise in microwave communication via mobile and satellite communications.

1.4.4 Microwave Wave Absorber

Due to the growing need for a countermeasure for electromagnetic compatibility (EMC), ferrite wave absorbers [23-28] have drawn significant interest on a global scale. This ferrite absorber is predicted to degrade electromagnetic wave leakage from various electric devices, television ghosting, faked echoes in ship radar signals, and more. An electromagnetic wave absorber's usual construction consists of a ferrite plate with a conductive metal plate backing.

1.4.5 Magnetic Recording Media

Camras' 1954 invention of acicular γ-Fe_2O_3 particles made it possible to successfully commercialize high-quality magnetic recording cassettes. The development of cobalt doping and coating technologies has made it possible for γ-Fe_2O_3 to be coerced, which affects recording performance [29]. As a result, the magnetic recording industry's future seemed bright. The optical recording technology, meanwhile, was created by Philips Corporation in 1974 [30] and has spread quickly throughout the industry. The production of longitudinal-type

magnetic recording cassettes and hard discs, which employ γ-Fe_2O_3 particles, is now trending downward globally. Over the past two decades, there has been documented advancement in the properties of magnetic recording mediums such as γ-Fe_2O_3 and CrO_2.

The demand for magnetic heads constructed of high-density Mn-Zn ferrite produced by the hot isostatic pressing method [27] or single-crystal Mn-Zn ferrite generated by the Bridgman method has steadily reduced due to the trend towards optical recording systems. Magnetic resistance (MR) heads, or giant magnetic resistance (GMR) heads [31-32], which are quickly entering the market, are replacing Mn-Zn ferrite heads. The study of magnetic medium and heads for perpendicular magnetic recording is a popular research topic [10][33].

1.4.6 Advanced Applications In The Biomedical Field

Magnetic nanoparticles (MNPs), a class of nanomaterials that may be readily regulated and activated at a specific location by an external magnetic field, have been identified as potential tools for biomedical applications [1]. As a result, they can be utilized as drug delivery mechanisms [3], tracers for magnetic resonance imaging [2], or agents for magnetic hyperthermia [4-5][33-35].

1.4.7 Targeted Drug Delivery

By using targeted drug delivery (TDD), it is possible to ensure that the therapeutic substance only affects the diseased area while sparing the other organs. The conventional method of administering medication included swallowing pills or injecting medications, which allowed the medication to be distributed throughout the body and reach the damaged organ for healing. Nevertheless, it has a significant drawback in that it can negatively impact the body's healthy portions. Therefore, nanotechnology has aided through focused drug delivery strategy in overcoming the difficulties of conventional drug administration practices whereby a medication had to be taken across a biological membrane.

The process of increasing medication concentration in the body's afflicted regions relative to other regions is the main goal of targeted drug delivery. Therefore, rather than treating the entire body, just the tissues that are important for healing are being focused on. It may be compared to a target-pointing game where the goal is to hit the center target to get a perfect 10 (in medicine, a perfect ten indicates that the damaged tissues have been fully treated).

The fundamental nanostructures used to transport drugs are called nanoparticles, and they include things like nanotubes, nanowires, quantum dots, mesostructured, polymers, dendrimers, liposomes, artificial DNA structures, and others with properties like nontoxicity, biodegradability, biocompatibility, and immunogenicity [1-2].

This is accomplished with the aid of a target molecule, whose function is to preserve the vehicle's normal circulation time to shield the nanocarriers from premature drug release upon contact with bodily fluids or blood cells. By developing abnormalities in the body's vasculature, nanocarriers can use the increased permeability and retention (EPR) effect to pinpoint the locations of damaged cells [3].

It is well known that many solid tumors have leaky capillary walls, allowing drug-loaded nanocarriers to discharge medications. Because they are bigger to be caught by the reticuloendothelial system (RES) and smaller to be eliminated by the kidneys, nano-sized medicines are adjusted to circulate for longer periods [4]. Due to limited lymphatic drainage, these nano-sized medicines prefer to enter tumor tissues through permeable vasculature and remain absorbed inside the tumor structure; this mechanism is known as the EPR effect [3-5]. Due to their improved capacity to penetrate tumor tissues, nanocarriers that are typically resistant to normal endothelium traversal have considerably lower toxicities in normal tissues than in afflicted ones [6-8][10][33-35].

The drug carrier particle must be tailored to a size (10 nm) that is favorable for absorption by tumor tissue. However, particles of this size are susceptible to RES removal [2]. Polyethylene glycol (PEG) surface modification, often known as "PEGlyzation," is frequently used to prevent this removal. Water molecules can establish hydrogen bonds with oxygen molecules thanks to hydrophilic tails that are created during PEGlyzation, which prevents opsonization from occurring [10]. Additionally, it has been discovered that PEGlyzation increases circulation times, helping to increase the likelihood of medication accumulation in tumor tissues. Functionalizing nanocarriers with specific molecules that can bind to targeted receptors in diseased tissues can further improve their performance for medication delivery [15-19] [33-35].

1.4.8 Hyperthermia

One of the most promising uses of magnetic nanoparticles in biomedicine today is magnetic hyperthermia. Its fundamentals are based on the influence of an external alternating magnetic field on the oscillation of a nanoparticle's magnetic moment. Through this mechanism, magnetic field energy is transformed into heat, which can kill tumor cells. It has been discovered that the hyperthermia temperature range (42-46 °C) stops the growth of tumor cells while having no appreciable impact on normal cells. It has been hypothesized that employing magnetic particles to induce hyperthermia enables localized, adjustable heating [6].

Several factors, including the structural and magnetic characteristics of MNPs, have an impact on heating efficiency [7]. Due to their relatively high specific absorption rate (SAR), chemical

stability, medium magnetic moment, and biocompatibility, ferrites (MFe_2O_4, M: Mn, Co, Fe....) MNPs make suitable candidates for hyperthermia [10][33-35]

In general, magnetic nanoparticles produce heat by four distinct processes, including eddy currents, hysteresis loss, Brownian motion, and Neél relaxation [9]. Since ferrites MNPs have poor electrical conductivity, eddy current is known to exist in conductive bulk materials but is often insignificant [9-10].

The particle size has a significant impact on the other mechanisms listed. Despite being linked to large MNPs [9], the hysteresis loss mechanism is still important for particle sizes greater than the superparamagnetic limit because of the irreversible magnetization process in an AC magnetic field [11]. Reorientation is simple with particles of this size, but domain wall displacement is what generates heat. The relaxation losses become more significant as the particle size decreases [12]. While in the Neél relaxation, the particle is fixed while the atomic dipole moments within the crystal rotate and rearrange themselves, dissipating thermal energy, in the Brownian relaxation mechanism, a shear stress is induced by the complete rotation of the particle in the surrounding fluid [9].

Both mechanisms function and contribute to warmth in actuality. It has been demonstrated that increasing superparamagnetic behavior and reducing particle size result in the dominance of relaxation loss mechanisms. As a result, both a decrease in coercivity (H_c) and an increase in magnetization (M_s) improve the inductive heating property. The size and form of ferrite MNPs are significantly influenced by the synthesis processes and factors. Additionally, they have a significant impact on crystal defects, lattice strain, and cation distribution within ferrite crystal structures [10] [13-16].

1.5 Synthesis methods

The development of hexagonal ferrites is not a simple process but an intensely complicated mechanism. These mechanisms which are involved in the formation of hexagonal ferrites are still not exactly inferred by the researchers. They have been working on the same for the last few decades. Following are certain methods that are appreciated for the synthesis of hexagonal ferrites.

1.5.1 Standard ceramic method

The oxide and barium carbonate powder are combined in the traditional ceramic way and heated to produce the appropriate phase formation. To obtain grains with an average size of 1-10 µm for some ferrites and 50 µm for some hexagonal ferrites, the phase formation often necessitates higher temperatures and longer heating durations, but the resulting particles are not small enough. There are many other synthesis methods for the preparation of hexaferrite,

but most of them involve precursor formation at a certain point while achievement of hexaferrite is obtained in differing degrees of accomplishment. However, there is a higher temperature requirement for phase formation, and also another disadvantage is that it's not used for the formation of nanomaterial, along with an emphasis on better grinding[10] [37-39].

1.5.2 Co-precipitation method

Since the early 1960s, this technique has been utilized to produce desirable ferrites that include the chemical co-precipitation of salts and bases. A wet chemical technique was developed to improve uniformity. In that procedure, an aqueous solution of metal salts was precipitated using a powerful base, and the hydroxide that resulted was subsequently oxidized by bubbling air through the suspended product to produce a fine ferrite product. More recently, a solution with non-stoichiometric amounts of iron and barium salts was co-precipitated with sodium hydroxide while maintaining a pH of 14. To keep the pH at 7, the resulting hydroxides are subsequently oxidized with hydrogen peroxide. The final product in the form of dried hydroxide is then heated at around 600 °C to get pure BaM (M-type hexaferrite). The advantage of the co-precipitation method is that it is a cost-effective and simple method. In this method, particle size can be controlled effectively [40], and there is a requirement for lower temperatures and homogenous particle sizes obtained[10] [41-44].

1.5.3 Hydrothermal method

This approach involves placing an aqueous medium in a stainless steel autoclave and applying autogenous pressure while keeping a consistent temperature. The process of oxidation, hydrolysis, or neutralization of mixed metal hydroxides is used to create ferrite. The temperature of the reaction, the reaction duration, the ratio of solvent and precursors, and the reactant concentration can all be altered to regulate the particle size in this situation. The simplicity of creating such crystalline phases, which are proven to be unstable at higher temperatures, is a benefit of this technology. Materials with high vapor pressure can be grown, and this method also helps in producing large-size as well as better-quality crystals [10][45].

1.5.4 Sol-gel method

The needed amount of citric acid is added to nitrate solutions using this approach (Figure 3.1), and a pH of 7 is subsequently maintained by adding ammonia solution to the mixture. This solution is now heated until it transforms into a gel, auto-combustion occurs, and a dry ash product is formed. The final ferrite product is produced by heating the ash product to temperatures between 1000 and 2000 °C after a preheating step of about 500 °C.

The procedure of using sol-gel is straightforward, economical, and energy-efficient. Additionally, the finished product is homogeneous. The creation of nanoparticles can be done

without the need for significantly greater temperatures. The main drawback to this approach is that the raw materials needed occasionally could be more expensive [10][46-49].

1.5.5. Ball milling

A ball mill is a primary piece for crushing/milling. It's extensively utilized for products like cement, silicate, ceramics, etc. Wet or dry processes can be used in the ball milling process, depending on the requirement. The surface area of the solid material can be increased appreciatively using ball milling, even the desired size of grain can be obtained using this method [10][50].

Alternative materials to ferrites for microwave absorption include carbon-based composites, conducting polymers, and dielectric ceramics. Materials like carbon nanotubes, graphene, and carbon black offer lightweight, flexible designs with tunable electrical properties and broad frequency coverage. Conducting polymers such as polyaniline are also low-density and easy to process. While dielectric ceramics have limited magnetic loss, they can enhance hybrid absorber performance. These alternatives are better suited for high-frequency, compact, and flexible applications, making them ideal for modern EMI shielding and stealth technologies. So we are opting for PANI here along with ferrite materials [1][12][17][24-25].

Table 1.1 Performance comparisons of different materials

Sr. no.	Material	Application	RL_{max} (dB)	Frequency (GHz)	Refrence
1.	Conductive polymeric blends of polystyrene and polyaniline	Microwave absorption	-45	9 to 18	[16]
2.	Nickel polyetherketone (PEK)	Shielding	-25	8.2-12.4	[18]
3.	Multishell TiO_2@Fe_3O_4@Polypyrrole	Shielding	-61.8	8.2-18	[29]
4.	Cu/C Nanowires	Microwave absorption	-39.43	-	[30]
5.	Ferrite nanoparticle	Hyperthermia	-	-	[36]
6.	Ni–Zn ferrites with different neodymium content	Microwave absorption	-20.8	2-8	[49]
7.	Nickel ferrite ($NiFe_2O_4$) by dextrin from corn-mediated combustion	Microwave absorption	-45.56	8.2-12.4	[41]

1.6 Polyaniline

Depending on its degree of oxidation, polyaniline (PANI), formerly known as black aniline, can take on several forms. Moreover, PANI is well-known for its environmental stability, doping potential, and simplicity [51]. By linking the 1, and 4-coupling of the aniline monomer components, PANI can be formed. PANI may exist in several stages of oxidation. One of the key factors that contributed to PANI's enormous research revolution was its unique properties, which attracted the attention of scientists from a range of academic fields, as well as its easy and affordable preparation methods that yield a product with extremely high purity.

Due to its intrinsic conduction loss, polyaniline (PANI), a low-cost polymer, can boost microwave absorption. It also has strong conducting behavior and stable chemical and thermal properties [10][52].

Ferrite-based microwave absorbers exhibit significant magnetic loss and wideband absorption capabilities. However, their practical application is often limited by inherent drawbacks such as high density, brittleness, and machineability which render them unsuitable for weight-sensitive or flexible systems. To overcome these limitations, ferrites are frequently incorporated into various matrix materials to enhance performance and address physical constraints. Despite these drawbacks, ferrite absorbers remain effective in electromagnetic interference control, but designers have to balance performance with trade-offs in weight and cost [9-11][14][22-27].

Summary:

Microwave absorbers are materials designed to absorb electromagnetic waves in the microwave frequency range, effectively converting the energy into heat. These materials play a crucial role in minimizing signal reflection, reducing electromagnetic interference (EMI), and enhancing device performance. Ferrites, particularly spinel ferrites and hexaferrites, are widely used as microwave absorbers due to their exceptional magnetic properties. Ferrites have a long history of use in electromagnetic applications, particularly in cores, multilayer chip inductors, and microwave devices. These materials are also employed in magnetic recording media and in advanced biomedical applications such as targeted drug delivery and hyperthermia treatment, where their magnetic properties can be exploited for therapeutic benefits. The development of microwave absorbers has progressed significantly, driven by the need for improved EMI shielding and better performance of electronic devices. Advances in the synthesis methods, including standard ceramic, co-precipitation, hydrothermal, sol-gel, and ball-milling techniques, have contributed to the enhanced properties of microwave absorbers, allowing for better control over the material's performance.

CHAPTER 2

REVIEW OF LITERATURE, RESEARCH GAP AND OBJECTIVES

We have discussed the study on ferrites conducted by several researchers in this chapter.

Ljaz M. et al. [2024] examined how cobalt affected the composition's magnetic and microstructural properties of sol-gel routed barium-strontium hexaferrite. For $Ba_{0.6}Sr_{0.3}Er_{0.1}Fe_{11.5-x}Al_{0.5}Co_xO_{19}$. All samples showed uniform particle dispersion, according to XRD analysis, and a hexagonal phase formed, according to SEM analysis. The magnetic characteristics were ascertained using the hysteresis loop approach. According to the authors, doping greatly improved the magnetic characteristics; at x = 1.5 compositions, H_a (anisotropy field) = 1.303 kOe, and H_c (coercivity) = 4.172 kOe, saturation magnetization rose from 37.76 emu/g (x = 0.0) to 57.12 emu/g (x = 1.5). Researchers concluded that synthetic samples might be used in magnetic applications [52].

Jin et al. [2024] synthesized chromium-doped M-type hexaferrites with the chemical formula $BaCe_xFe_{12-2x}O_{19}$ employing the sol-gel technique. Microstructural, morphological, and absorption properties have all been investigated. The crystal structure was unaffected by the Ce doping amount; nonetheless, the doping enhanced the absorption and electromagnetic characteristics. With a reflection loss of -58 dB, composition x = 0.2 had the best absorption performance. Bandwidth with 9.44 GHz band was achieved with 2.3 mm of thickness [53].

Jing et al. [2024] created strontium ferrites doped with praseodymium (Pr) and dysprosium (Dy) using the sol-gel technique. Several calcination temperatures and doping concentrations were used to examine the structural, magnetic, and absorption properties. According to XRD, the doping of Pr and Dy in the ferrites resulted in both an M-type phase and a heterophase. Micrographs showed that when the doping amount increased, the grain size decreased. It was shown that when the degree of Pr-Dy doping increased, coercivity rose, but saturation magnetization decreased. They said that the effective absorption bandwidth was 4.81 GHz, and the RL was -52.51 dB [54].

Siddique et al. [2024] synthesized Co-Cd ferrites and examined how the addition of Zn affected the compositions' structural, electrical, and absorbance properties. Here, the $Cd_{0.5-x}Zn_xCo_{0.5}Fe_2O_4$ chemical composition was utilized for the same. The scientists obtained crystalline diameters ranging from 43 to 50 nm after developing ferrites using the sol-gel approach. Coercivity decreased from 246.47 to 192.10 Oe when Zn^{2+} was substituted. However, saturation magnetization increased from 58.92 to 106.41 emu/g. At 3.9 GHz, the authors' greatest RL of -26.85 dB was obtained for composition x = 0.3 [55].

Suman Kumari et al. [2024] used an in situ chemical polymerization approach to create graphene composites with conducting polymers (PEDOT and polyaniline). Additionally, the potential of these composite materials to mitigate the problem of electromagnetic radiation pollution in the microwave frequency range of 12.4 GHz to 18 GHz was assessed. With a green index (gs) of 1.17, the PEDOT/graphene composites demonstrated notable shielding efficacy of up to 46.53 dB. Since the samples at 18 GHz had high dielectric losses ($\varepsilon''/\varepsilon' \approx 1.9$-3.1) and microwave conductivity (σ_s = 19.9-73.6) absorption was also found to be the predominant shielding mechanism in all of the samples. Strong interactions involving polarisation and charge propagation led to both dielectric loss and conduction loss [56].

W. M. Abd El-Gawad et al. [2024] synthesized nano-$CuFe_2O_4$ and nano-$CaFe_2O_4$ coatings, sol-gel method was used to create nano-$CuFe_2O_4$ and nano-$CaFe_2O_4$. The potential use of these materials in high-frequency applications (such as microwave absorbency coatings) was then determined by examining their structural, electrical, dielectric, and magnetic characteristics. To create modified epoxy resin as microwave coatings, two dosages (2.5 weight percent and five weight percent) of nano-$CuFe_2O_4$ and nano-$CaFe_2O_4$ were then added to the epoxy resin. The produced samples' strong AC conductivity at high frequencies was demonstrated by the dielectric studies. Furthermore, a low coercivity value was revealed by the magnetic characteristics, which qualified these samples for high-frequency devices. The two films showed two absorption bands with RL < -10 dB that span 10.61 to 10.97 GHz and 10.25 to 11.2 GHz, respectively. In both cases, a minimum return loss of -13 and -16 dB was attained [57].

Kaur et al. [2024] synthesized Zinc-cobalt ferrites with Ni-Zr substitutions for use as a Ka-band microwave absorber. They studied structural, optical, magnetic, and microwave absorption properties while developing ferrite compositions using the sol-gel process. It is discovered that adding Ni-Zr lowers the saturation magnetization levels. With a thickness of 1.3 mm, the composition x = 0.1 yielded the RL of - 50.34 dB at 29.2 GHz [58].

S. Caliskan et al. [2023] prepared Co-V co-substituted nano Sr-hexaferrite, namely $Sr_{0.5}Co_{0.5}V_xFe_{12-x}O_{19}$ (NHFs), with x values ranging from 0.00 to 0.08, was thoroughly examined by the average crystallite size of the products produced by citrate combustion ranged from 37 to 83 nm. Mössbauer spectra showed that the electron density surrounding Fe^{3+} ions at all sites was affected by the presence of V^{3+}. All samples showed magnetic hardness at both high and low temperatures, according to VSM data. The dopant concentration affected the values of M_s, M_r ; the maximum value was found at x = 0.04. At all temperatures, the samples showed a squareness ratio (SQR) of roughly 0.5 [59].

T. D. Thanh et al. [2023] prepared Cobalt-doped $SrFe_{12}O_{19}$ (Co-SrM) samples using the ball milling method, along with microwave absorption, saturation magnetization (M_s) and coercivity (H_c) were also studied. Additionally, the doping caused EM characteristics to fluctuate and change, which had an impact on the materials' microwave absorption capabilities. The samples exhibited satisfactory microwave absorption capabilities within the frequency and thickness ranges of 4-6 mm and 12-18 GHz (Ku band), respectively. With a reflection loss (RL) of -30.7 dB, about 99.9% of the incoming wave was absorbed, which is the best result. Dielectric relaxation loss, eddy current effects, impedance matching, and natural resonance may all have contributed to good microwave absorption performance. Furthermore, the samples also improved the performance of microwave absorption in the C and X bands (4-12 GHz). These findings demonstrated the potential of Co-SrM epoxied samples as viable MAMs for real-world uses [60].

K. Khan et al. [2023] prepared Mg/Ba hexaferrite using the auto-combustion sol-gel method. The synthesis of the intended samples without any impurities was verified by the FTIR and Raman spectra. The complex impedance analysis (Nyquist/Cole-Cole plots) shows that grains and grain boundaries play a significant role in the overall conduction mechanism of nanocomposite (NC) materials. The results showed that these NCs are good candidates for a variety of technical applications, including as high band-pass filters and electromagnetic shielding, due to their higher impedance values [61].

Rana K et al. (2023) created strontium hexaferrite by sintering it at 800 ℃ and 910 ℃ using a modified version of the traditional citrate precursor technique. At both temperatures, XRD confirmed the production of magnetoplumbite structure, while FTIR and Raman spectroscopy corroborated the observations. The M_s and H_c increased from 81 to 92 emu/g and from 107 to 262 Oe, respectively, as the sintering temperature rose. Additionally, the impurity content dropped as the sintering temperature increased, and the hard character of SrM hexaferrite changed to a soft one [62].

A. Yu. Mironovich et al. [2023] prepared $BaFe_{12-x}Ni_xO_{19}$ (x = 0, 0.1, 0.3, 0.5) powders by the hydrothermal method. Ni ions entry into the hexaferrite lattice is confirmed by structural and elemental investigations. At the same time, according to XRD data, the lattice volume unexpectedly decreased. Ni^{2+} takes the role of $Fe^{3+.}$ Hence, a charge adjustment mechanism is required. The preference of the Ni^{2+} ions to occupy the 12k location causes the saturation magnetization to drop. The saturation magnetization, coercivity, and remanence of all magnetic parameters have a negative correlation with the concentration of Ni [63].

V. Bilovol et al. [2023] synthesized composites (100-x) $SrFe_{12}O_{19}$/(x)$CoFe_2O_4$ by ball milling, a variety of precursor fractions of hexagonal and cubic ferrite powder were prepared, where x = 10, 20, 30, 40 wt%. The prepared composites were annealed at 900 °C for three hours following grinding in a ball mill. It was observed that the component weight ratios had a significant impact on magnetic interactions. Exchange coupling and dipolar interactions were seen to compete. A correlation has been found between the magnetic characteristics of the composites and their structural parameters, which are contingent on the ratios of fractions with varying crystallite sizes. The greatest energy product $(BH)_{max}$ = 10.9 kJ/m^3 was found in the composite sample, including 10 weight percent $CoFe_2O_4$, which is almost 20% higher than that of pristine $SrFe_{12}O_{19}$. The synthesized composites were found to have better magnetic characteristics [64].

Nishkala, K. R. et al. [2023] using ball milling and heat treatment manufactured La substituted Barium hexaferrite, $Ba_{(1-x)}La_{(x)}Fe_{12}O_{19}$, (x = 0, 0.1, 0.15, and 0.20). For all samples, a single-phase magnetoplumbite structure with hexagonal plate-like grains corresponding to P63/mmc was generated. The replacement of La^{3+} did not result in the formation of Fe^{2+}. On the other hand, electron delocalization might have occurred. Dielectric loss and dielectric permittivity appeared to vary with frequency, which was attributed to the interfacial polarization of the M-W type. With La_{3+} concentration, leaky ferroelectric material to leaky resistor-type behavior was discovered, and maximum Pr is shown at x = 0.10. The dielectric spectroscopy also revealed that the La content, x = 0.20, had the lowest loss and the maximum dielectric permittivity [65].

Kush Rana et al. [2023], with the help of a modified version of the standard citrate precursor technique, generated a pure M-type strontium hexaferrite with the nominal composition $SrFe_{12}O_{19}$. The goal of the overall project was to raise the standard of hexagonal ferrite without using high-temperature thermal processing. The M-phase and some Fe_2O_3 impurities were proven to have formed with the help of the XRD. As the sintering temperature rises from 800°C to 910°C, the saturation magnetization M_s of SrM hexaferrites increases to 92 emu/g, according to their magnetic characteristics. The important results of this study were the H_c values of 107 Oe and 262 Oe, respectively, in addition to the higher Ms for SrM hexaferrite. The emergence of soft character in hard SrM hexaferrites is indicated by the uncommon nature of SrM hexaferrite. Furthermore, the rapid shift from multidomains to single domains is shown by the squareness ratio (SQR) increased from 0.26 to 0.54 [66].

A. Gupta et al. [2023] synthesised $SrFe_{8-x}Al_4Zn_xO_{19}$ ($0 \leq x \leq 1$) hexaferrites with the goal of enhancing the magnetic characteristics of strontium hexaferrite magnets. Sol-gel auto-combustion method was used for preparation. The impact of Zn substitution on the structural, magnetic, dielectric, and electrical characteristics of $SrFe_8Al_4O_{19}$ hexaferrite was investigated. With an effective improvement to 19.15 MGOe (Mega Gauss Oersteds) for energy density $(BH)_{max}$, the inexpensive magnet became advantageous for many permanent magnet applications. The usual behaviour of hexaferrites was indicated by the dielectric characteristics. It is anticipated that the effort would provide a practical and affordable substitute for permanent magnets based on rare earth elements [67].

Md. Z. Khan et al. [2023] produced Ba-Sr hexaferrite nanoparticles using Sol-Gel auto combustion. Their composites with MWCNTs (Multi-walled Carbon Nanotubes) and conductive polymers were created using in-situ polymerization. Increased dielectric losses were found by the low-frequency dielectric assessments. The weakening of exchange coupling was the cause of the decreasing magnetism. As a result of increased charge carrier conduction, increasing DC conductivity contributed to the nominal increase in shielding effectiveness (Reflection) values. At 8.1 GHz and 16.2 GHz, respectively, the greatest apparent total shielding efficiency for the $Ba_{0.5}Sr_{0.5}Fe_{12}O_{19}$/MWCNTs/Polythiophene composition was -34 dB and -33 dB. They investigated the microwave absorption of the samples as a function of thickness and frequency and found that it was dependent on the quarter wavelength phenomena [68].

Xiayu Liu et al. [2023] prepared BaM nanopowders and the BaM/PANI composites exploring a facile technique involving doping of rare earth elements. It was found that the limitations of the electric polarization in PANI at the surfaces of the BaM particles were lessened by the introduction of rare earth elements, such as La, Nd, and Ce, in the BaM particles. This offered a flexible means of lowering the thickness, increasing the absorption effectiveness, and extending the absorption frequency range. At 7.76 GHz, the La-BaM/PANI composite showed an optimal thickness of 3.28 mm and a maximum reflection loss of around - 63.6 dB [69].

Md. Dilshad et al. [2022] prepared aluminium-substituted M-type hexagonal ferrites. Sol-gel auto combustion was used to successfully manufacture aluminium-substituted M-type hexaferrite with nominal composition $SrAl_{2x}Fe_{12-2x}O_{19}$ with x = (0.0, 0.2, 0.4, 0.6, 0.8, 1.0). The XRD investigation confirmed the presence of M-type hexagonal ferrites with high purity phase. The lattice parameters *a* and *c*, as well as the c/a ratio and cell volume, have all been computed. The lattice parameter 'a' ranges from (5.86-5.88) Å, whereas the '*c*' ranges from (22.87 to 23.08) Å, Cell volume is in the (687.10-688.90) $Å^3$ range with crystallite sizes ranging

from 39 to 61 nm. The optical bandgap was used to determine the optical properties of materials. With increasing Aluminium substitution, the bandgap decreases linearly and approaches its maximum within the energy range of 1.74 to 2.80 eV. Permittivity, permit loss, tan loss, ac conductivity, and the real and imaginary portions of the electric modulus were also covered. At 2.5 GHz, the maximum dielectric permittivity (15.5) was achieved for $SrAl_{2x}Fe_{12-2x}O_{19}$ at x = 1.0 composition. Similarly, the maximum Q-value for this mixture was achieved. The observed shift in dielectric properties has been explained using space charge polarisation and electron hopping between Fe^{3+} and Fe^{2+} [70].

Tim fricke et al. [2022] prepared, from a Na_2CO_3 flux, single crystals of $Ba_{1-x}Sr_xFe_{12}O_{19}$ with x = 0, 0.25, 0.5, 0.75, and 1. The resulting crystals were hexagon-shaped plates with several millimeters in thickness and edge lengths up to one centimeter. By using X-ray powder diffraction on crushed samples, phase purity was verified. A strong (thermo) mechanical anisotropy is revealed by combining thermal expansion data with the development of cell parameters *a* and *c* as a function of x. As is common for M-type hexaferrites, magnetic measurements reveal an extra high magnetic anisotropy with the c-axis being the easy-axis. The mild magnetization of the crystals is shown by the lack of any discernible coercivity or remanence [71].

D. Baba Basha et al. [2022] synthesized $Sr_{1-x}La_xFe_{12}O_{19}$ (x = 0.2-0.8) (SLFO) nanoparticles. Focused on the synthesis, structural, electrical, and magnetic characterization of (SLFO) nanoparticles by hydrothermal method is the major focus of the current work. The analysis of X-ray diffraction was used to determine the hexagonal peaks. The acquired data showed that when 'x' increased, the lattice constants increased as well, going from 0.58801 to 0.58825 nm (*a* = *b*) and 2.30309 to 2.30341 nm *(c*). The morphological investigations confirmed that the SLFO grains and nanoparticles took on a nearly spherical form. The FTIR and UV-visible spectra were used to study the optical characteristics. It was discovered that when the dopant concentration increased, the optical bandgap (Eg) of SLFO increased from 1.866 to 2.118 eV [72].

Avesh Garg et al. [2021] successfully synthesized $Sr_{1-x}Nd_xFe_{12}O_{19}$ (x = 0.1, 0.2, and 0.3) a strontium hexaferrite utilizing the auto-combustion approach. With increasing doping concentration, the average particle size decreased from 638.02 to 478.19 nm in the produced ferrites, displaying platelet-like particles. With an increase in doping concentration, the saturation magnetization fell from 41.185 emu/g to 37.145 emu/g as a result of a lower magnetic moment brought on by the partial conversion of Fe^{3+} ions to Fe^{2+} ions. Due to the weakened uniaxial magnetocrystalline anisotropy of strontium hexaferrite, the coercivity of the

doped strontium hexaferrite similarly reduced from 387.97 G to 278.37 G with an increase in Nd doping concentration. Due to the weakened uniaxial magnetocrystalline anisotropy of strontium hexaferrite, the coercivity of the doped strontium hexaferrite similarly reduced from 387.97 G to 278.37 G with an increase in Nd doping concentration. With a normalized impedance of 1.002, ferrite Nd3 provides the best impedance matching. The improvement in the neodymium doping concentration has improved the attenuation constant and reflection loss. The ferrite $Sr_{0.7}Nd_{0.3}Fe_{12}O_{19}$ (Nd3) has been found to have a maximum reflection loss value of 40.595 dB at 9.62 GHz and a 10 dB bandwidth of 3.13 GHz (about 75% of the X-band) [73].

Md. Rostam et al. [2021] prepared nanoparticles with the chemical formula $BaCo_xAl_xTi_xFe_{12-3x}O_{19}$ (x = 0.2, 0.3, and 0.4) are synthesized by the sol-gel auto combustion method. In the frequency band ranging from 1-18 GHz, the microwave absorption characteristics of Co-Al-Ti substituted barium hexaferrite-multiwalled carbon nanotubes (MWCNTs)-epoxy resin nanocomposites were fully examined. Each one of the nanocomposites had a thickness of less than 1.75 mm and suitable microwave absorption characteristics. In addition, the minimum reflection loss is less than -20 dB, meaning that over 99.9% of the electromagnetic wave energy was absorbed. By varying the sample thickness, the nanocomposites' bandwidth essentially spanned the whole frequency range of 1-18 GHz. With a bandwidth of 4.59 GHz and a matched thickness of just 1.5 mm, the nanocomposite with x = 0.2 exhibits the highest microwave absorption performance, with the reflection loss minimum (RL_{min}) for the sample with x = 0.3 reaching -47.40 dB. As a result, these nanocomposites had the potential to be very effective microwave absorbers [74].

Avesh Garg et al. [2021] created microwave-absorbing materials, $Sr_{1-x}Nd_xFe_{12}O_{19}$ (x = 0.1, 0.2, and 0.3), that consist of strontium hexaferrites doped with neodymium (Nd). Nd had an inhibitory effect on the formation of hexaferrite particles. The hysteresis loop demonstrated the elevated saturation magnetization of the undoped ferrite, which was shown to diminish as the neodymium doping concentration increased. The doped strontium hexaferrites' coercivity exhibited a similar trend. As the neodymium doping concentration increased, so did the impedance matching and reflection loss. With a -10 dB bandwidth of 3.13 GHz, the greatest reflection loss value of - 40.595 dB at 9.62 GHz was achieved [75].

Haifeng Li et al. [2021] synthesized $BaFe_{12-2x}(Mn_{0.5}Co_{0.5}Ti)_xO_{19}$ (x = 0, 0.5, 1.0, 2.0) by the use of the solid-state reaction (SSR) method and investigated its microwave absorption range. The findings of the scanning electron microscopy (SEM) and X-ray diffraction (XRD) patterns demonstrated that the processed samples were all made up of single-phase flake-shaped grains. Hard magnetic samples turned soft magnetic when the substitution of x

increased. This was due to changes in saturation magnetization (M_s) and coercivity (H_c). The substituted samples' dielectric and magnetic spectra indicated resonance at nearly the same location. As the doping amount x increased, multiple magnetic spectra resonances were seen, which improved the MW absorption and expanded the effective absorption bandwidth (EAB). The minimal reflection loss (RLmin) for the x = 0.5 sample was -40.2 dB, and the EABs of RL < -10 dB and RL < -20 dB expanded to 7.0 GHz and 4.2 GHz, respectively [76].

S. Goel et al. [2021] examined how adding activated carbon (AC) produced from biowaste affected the magnetic and dielectric characteristics of barium hexaferrite ($BaFe_{12}O_{19}$). While the auto-combustion method was employed to create low-density barium hexaferrite, activated carbon was made from banana peels. The low-cost ball-milling approach was implemented to make the composites made of magnetic barium hexaferrite and highly conductive activated carbon. Interfacial polarisation caused by the addition of activated carbon to the ferrite matrix led to a rise in reflection loss. To quantify the microwave absorption of composites, reflection loss, attenuation constant, and impedance matching were computed. At a coating thickness of 1.3 mm, the composite consisting of 40% $BaFe_{12}O_{19}$ and 60% AC had a maximum reflection loss of -35.5 dB in the X-band. In the frequency range of 9.8 to 11.8 GHz, the composite reached 90% microwave absorption [77].

Golfrid Gultom et al. [2021] synthesized chemical composition of $BaFe_{12-2x}Mg_xAl_xO_{19}$ using by co-precipitation method The effective replacement of Mg and Al cations in the barium hexaferrite lattice was validated by the XRD analyses. The VSM study demonstrated that coercivity dropped while saturation magnetization and remanence increased with increasing Mg and Al substitutes. With saturation magnetization of 28.34 emu/g, remanence of 15.23 emu/g, and coercivity of 1144 Oe, the ideal circumstances were found for x = 0.1 mol%. Furthermore, at 10.83 GHz, the greatest reflection loss of around 53.23 dB was recorded [78].

Zhanjun Zhang et al. **[2020]** prepared Ce-Cu-co-substituted M-type strontium hexaferrite $Sr_{0.7}Ce_{0.3}Fe_{12-x}Cu_xO_{19}$ compounds, using the solid-state approach, all of the produced samples appeared to have formed the M-type hexagonal phase, according to XRD patterns, which have also been supported by the FTIR spectrum. Furthermore, Ce-Cu substitution in SrM hexaferrites resulted in a clear enhancement of M_s and H_c. After substitution, M_s maximum values reached 70.305 emu/g and H_c almost reached 3800 Oe [79].

Didin S. Winatapura et al. [2020] used a chemical co-precipitation method to create M-type barium ferrite nanoparticle materials with varying levels of Mn^{3+}, Zn^{2+}, and La^{3+} ions doping. BLFMZ-02 and BLFMZ-05 samples identified the secondary phase, which was associated with the Fe_2O_3 phase, whereas the XRD peaks belonging to BFO and BLF samples showed single

phases. The saturation magnetization and coercivity (H_c) are both raised when Ba^{2+} is replaced with La^{3+}. The magnetic characteristics were shown to be impacted by the replacement of Mn^{3+}, Zn^{2+}, for F^{3+} ions. With Mn^{3+} and Zn^{2+}, substitution, magnetization (M_s) rose but coercivity (H_c) sharply decreased. The samples' average particle size was determined by TEM visual inspection to be between 70 and 150 nm. For the BLFMZ-02 sample, the RL maximum of -21 dB was measured at a frequency of 11.20 GHz [80].

Haq, et al. [**2020]** used a simpler sol-gel approach to create $SrFe_{12-2x}Zn_xCr_xO19$ (x = 0.0 to 0.5). Nitrates were utilized as the only precursors. Ethylene glycol was the solvent utilized. Less sintering time and dopants with varied physical characteristics have an impact on in-phase growth. Nearly 70% phase purity was revealed by XRD. Dimensional differences have an impact on the provided characteristics, as demonstrated by XRD and SEM. Fe crystallographic location in the Sr-hexagonal structure, together with factors like Cr and Zn's preferred occupied states. It changed the compositions' electrical behavior. A variety of distinct AC and DC properties, such as the resistivity, dielectric losses, and dielectric permittivity of the synthesized material, may be suitable for use with contemporary IT devices, intelligent microwave applications, and eddy current losses [81].

Atendra Kumar et al. [2020] prepared $BaFe_{12x-1}Co_xO_{19}$ (BHFC) hexaferrite with the chemical formula (x = 0.0, 0.05, 0.1, and 0.2) utilizing economical metal nitrates and a 12-hour sintering process at 1150 °C. X-ray diffraction (XRD) examination was used to look into the single-phase validation of the synthesized materials. The hexagonal form of the grains was verified by TEM examination with particle sizes of 213, 185, and 52 nm, respectively, about Co^{+2} concentrations, and by SEM results for diameters of 0.50, 0.84, and 1.0 micrometer for the compositions x = 0.0, 0.05, and 0.1, respectively. For the BHFC ceramic, the values of e and tan d measured at 100 Hz are 2.3 9 103 and 0.32, respectively. The synthesized BHFC ceramic's value of squareness (M_r/M_s) ratio is discovered to be 0.7, indicating the hard magnetic materials' single magnetic domain crystal structure, which makes them ideal for use in a variety of fields, including ferrite cores, detectors, permanent magnets for electricity production, etc [82].

Yaseen K.R. et al. [2020] analyzed the phases that formed during the initial annealing of the Ba-Sr-hexaferrite ($Ba_{1-x}Sr_xFe_{12}O_{19}$; x = 0, 0.25, 0.5, 0.75 and 1, BSFO) ceramic powders, along with their structure and morphological studies, they reported the mechanism involved in sol-gel auto combustion synthesis of this material. The barium/strontium mono ferrite ($(Ba/Sr)Fe_2O_4$)) and maghemite (γ-Fe_2O_3) phases, as well as a trace quantity of hematite (α-Fe_2O_3) phase, were formed, according to the XRD patterns of the samples as they were

synthesized. These samples' annealing speeds up the solid-state reaction between the $BaFe_2O_4$ and γ- Fe_2O_3 phases, which resulted in the development of the BSFO phase. Interestingly, they found that pure Ba-Sr hexaferrite structure occurs after annealing the samples with x = 0, 0.5, and 1 at 1000 °C for 2 h, but for samples with x = 0.25 and 0.75, a significant quantity of hematite (α-Fe_2O_3) phase is found, particularly for x = 0.75. The development of a single-phase Ba-Sr hexaferrite is also prohibited by this difference in ionic radii, according to their work on annealing-dependent phase evolution. For all of the samples, the development of transparent, plate-like particles with varying particle sizes was seen [83].

A. Garg et al. **[2020]** used the auto-combustion process to produce yttrium-doped strontium hexaferrite particles, $Sr_{1-x}Y_xFe_{12}O_{19}$ (x = 0.1, 0.2, and 0.3). Strontium hexaferrite's partial replacement of Fe^{3+} ions with Fe^{2+} ions as a result of doping has been discovered to be a useful tool for adjusting the material's microwave absorption capabilities. The development of ferrite without the presence of a secondary phase was confirmed by the XRD spectrum. All of the generated samples had platelet-like morphology, with the undoped sample's average particle size being 590 nm. With an increase in Y doping, the average particle size shrank. The hysteresis loop showed that when the yttrium doping concentration in strontium hexaferrite increased, so did the saturation magnetization. Coercivity, on the other hand, dropped from 296 to 209 G as a result of a decrease in the magnetic anisotropy of the ferrite. The reflection loss is examined for a frequency range of 8.2 GHz to 12.4 GHz (X-band), and results showed that for x = 0.3 and a coating thickness of 2.6 mm, the highest reflection loss was -18.91 dB with a -10 dB bandwidth of 2.18 GHz [84].

W. Widanarto et al. [2020], prepared a bio-silica integrated barium-ferrite-composite. The modified solid-state reaction technique was used to produce the composite at x = 0, 1, 2, and 3 wt%. The effect of various bio-silica (extracted from sintered rice husk) contents on the surface morphologies, structures, and magnetic properties of these composites was investigated. In the frequency range of 8-13 GHz, the Nicholson-Ross-Weir approach was used to determine the relatively complicated permittivity and permeability. Meanwhile, the transmission/reflection line theory was used to predict the reflection loss to evaluate the composite's MW absorption qualities. The incorporation of bio-silica into barium ferrite composites resulted in the formation of a novel hexagonal phase ($Ba_3Fe_{32}O_{51}$) and a tetragonal phase ($BaFeSi_4O_{10}$), resulting in a drop in saturation magnetization and a considerable shift in the MW frequency absorption peak locations [85].

H. Nikmanesh et al. [2020] synthesized Strontium hexaferrite particles substituted with erbium and chromium, nominal composition $SrEr_xCr_xFe_{12-2x}O_{19}$ utilizing the auto-combustion

process of sol-gel. When the chromium and erbium replacements were increased, H_c and M_r. consistently seemed to decrease, while M_S grew until x = 0.2 and then started to decrease as the substitution quantity increased. Through simultaneous substitution, they also look at the reason for the variations in the magnetic and microwave absorption characteristics. The $SrEr_{0.5}Cr_{0.5}Fe_{11}O_{19}$ sample showed the greatest reflection loss of -34.71 dB for the whole tested microwave frequency range of 12-18 GHz (Ku band) [86].

Li Peibo et al. [2020] prepared the blend of MWCNTs (Multi-walled Carbon nanotubes), Ba-hexaferrite, and Co/C particles. This blend was utilized to create the microwave absorber composites using the solvothermal method. The study investigated the permeability and permittivity values of composite material throughout the X band frequency range of 8.2-12.4 GHz. Permeability and permittivity measurements were used to evaluate the ability of the composite to absorb electromagnetic (EM) waves. It was shown that adding MWCNTs improved the composites' EM absorption ability. Because of the enhanced polarisation and surface area, the combination of MWCNT with Ba-M and Co/C resulted in higher magnetic and dielectric losses. For matching thicknesses of 3.1 mm, the minimum reflection loss (RL) was -34 dB with an effective bandwidth (< -10 dB) in the X band frequency range [87].

Ghulam A. A. et al. [2019] synthesized the Nd substituted Sn Mg-based hexaferrite $BaFe11(Sn_{0.5}Mg_{0.5})1_xNd_xO_{19}$ (x = 0, 0.5, 1), using the chemical co-precipitation method, Thermal investigation demonstrated that the hexagonal phase of the magnetic powder was reached at around 900 °C. The growth of single-phase M-type hexagonal structures was seen in the XRD patterns. Increasing the content of x raised the lattice values. The crystallite size was found to be between 28 and 39 nm. Two distinct bands, at 439-442 cm-1 and 590-594 cm-1, were detected by FTIR analysis without the presence of any additional bands. The morphological study (SEM) amply showed that substitution and grain size (138-103 nm) had an impact on the platelet-like hexagonal microstructures of the magnetic powder. When Nd is present, Ms has values between 38.256 and 56.293 emu/g, and H_c has values between 626 and 5423 Oe, exhibiting a linearly increasing behavior [88].

M. A. Almessiere et al. [**2019]** made a comparative study of Sr-hexaferrite (HFs) with Ni-Zr and Co-Zr substitution. Sonochemical methods were used to create $SrCo_xZr_xFe_{12-2x}O_{19}$ HFs (also known as SrCoZr HFs) and $SrNi_xZr_xFe_{12-2x}O_{19}$ HFs (also known as SrNiZr HFs). The formation of M-type hexaferrite was discovered by investigations using X-ray diffraction (XRD), Fourier transform-infrared spectroscopy (FT-IR), and high-resolution transmission electron microscopy (HR-TEM). Scanning electron microscopy (SEM) is used to study the hexagonal platelet form. At (RT; T = 300 K) and (T = 10 K), several synthesized SrCoZr and

SrNiZr HFs were tested for their magnetic characteristics. SQR = M_r/M_s (squareness ratio), H_c (coercivity), M_s (saturation magnetization), M_r (remanence), and nB (magnetic moment) were calculated. Different goods' M-H hysteresis loops demonstrated their hard ferrimagnetic (FM) characteristics [89].

K. Zhang et al. [2019] successfully synthesized a new composite made of RGO, PANI, and $BaNd_{0.2}Sm_{0.2}Fe_{11.6}O_{19}$ (BNSF) to provide high efficiency and lightweight microwave (MW) absorption material. In-situ polymerization was used to create the RGO/PANI composite, chemical co-precipitation was used to create the BNSF, and a high-energy ball mill was used to create the RGO/PANI/BNSF ternary nanocomposite. We looked at and spoke about the phase composition, microstructure, and MW absorption capability of the samples. In addition to a superb composite structure, the results showed exceptional MW absorption capability. With 30 weight percent of BNSF, the RGO/PANI/BNSF nanocomposites demonstrated exceptional MW absorption properties. At 13.68 GHz, the lowest reflection loss (RL) could approach 50.5 dB with a 2.90 mm thickness [90].

M. Shezad et al. [2019], Using a traditional ceramic process, have created Ce-Co co-doped SrM based nano hexaferrite crystallites with success. Numerous characterizations were used in an analytical study of the magneto-structural characteristics. As a result, the phase singularity was confirmed by Rietveld refinement of X-ray diffraction (XRD), with space group P63/mmc hexagonal. Grain aggregation into regular hexagonal platelets, approximately 1-2 μm in size, was seen using a Field Emission Scanning Electron Microscope (FESEM). Stoner Wolhfarth (S-W) model confirmed the MS values, the domain singularity with squareness ratio (SQR) of ~ 0.51, and the high uniaxial magneto-crystalline anisotropy (MCA) of the prepared hexaferrites. Different magnetic parameters were analyzed using coupled intrinsic and normal demagnetization curves, resulting in B_r > 1 kG & H_c > 1 kOe, validating the usage of the sample in the permanent magnetic industry [91].

I. Araz et al. [2019] prepared barium hexaferrite that contains the chemical formula $Ba_{0.5}Ce_{0.5}Fe_{11}CoO_{19}$. Using an X-ray diffractometer, the structural characteristics of Ce-Co substituted barium hexaferrite were examined. The sample's surface morphology was identified using field emission scanning electron microscopy. The complex permeability and complex permittivity, reflection loss (RL) characteristics, absorption loss, and shielding efficacy of the produced composition were all measured using the transmission/reflection coaxial line technique in the 2-18 GHz frequency range. With a sample of 3 mm thickness, the highest RL value of 31.4 dB at 11.4 GHz was attained, while the maximum shielding efficacy value was noted at 59.2 dB [92].

G. Venkatesh et al. [2019] used the precursors (Sr (NO3)2, Ba(NO3)2, Ca(NO3)2, Fe(NO3)3, Al(NO3)3, Ce(NO3)3) and fuels (C6H8O7, C12H22O11) and fuels (C6H8O7, C12H22O11) to synthesize Al and Ce doped hexa-ferrites ($AB_{12}O_{19}$). The produced powder was calcined for 12 hours at three different temperatures (800 C, 900 C, and 1100 C). The phases were identified using the X-ray diffraction (XRD) method, and the morphological behavior was investigated using Scanning Electron Microscopy (SEM). Energy Dispersive Spectroscopy was used to analyze the elements. The intrinsic magnetic characteristics of hexaferrites were investigated using a vibrating sample magnetometer, where it was discovered that partial substitution of Sr and Fe sites by rare earth elements (RE^{3+}) and non-magnetic trivalent Al^{3+} ions, respectively, affects the hexaferrites, as does $BaFe_{12}O_{19}$ and $CaFe_{12}O_{19}$. The incorporation of Ce^{3+} and Al^{3+} into the hexagonal lattice increases coercivity via magneto-crystalline anisotropy or grain refining [93].

H. Sozeri et al. [2018], prepared using a sol-gel auto-combustion method, Ba nano hexaferrite (NHFs) replaced with Cr^{3+}. Using X-ray diffractometry, transmission electron microscopy, vibrating sample magnetometry, and reflection/transmission measurements in a vector network analyzer, the structural, magnetic, and microwave characteristics of the samples were examined. The X-ray diffraction patterns confirmed the existence of a single barium hexaferrite phase. Scanning electron microscopy revealed hexagonal crystal forms with an average particle size of 2 mm. Additionally, M-H hysteresis curves at room temperature showed hard ferromagnetic ordering. The saturation magnetization and coercivity of the nanoparticles declined with an increase in Cr^{3+} ions concentration, according to magnetic measurements. The matching frequency at which microwave absorption takes place was moved from 14 to 12 GHz by the substitution of Cr^{3+} ions in the Ba NHFs [94].

N. Tran et al. [2018] synthesized $BaFe_{11}CoO_{19}$ hexaferrites by heat treatment and co-precipitation. They discovered a noticeable variation in the magnetic and crystalline structure characteristics by adjusting the ion molar ratio. Saturation magnetization and coercivity results indicate that the magnetic characteristics peaked at x = 11-13. An evaluation was conducted on the morphological, structural, and magnetic characteristics in relation to heat treatment. Based on the findings of thermal gravimetric studies, X-ray diffraction patterns, and magnetic-field-dependent magnetization, they discovered that the formation of M-type hexaferrite nanocrystals begins at 650 °C, a significant temperature lower than previously reported [95].

Md. Ayub et al. [2018], using the chemical co-precipitation approach, M-type Ba-ferrite nanoparticles of various compositions were created in the current study effort. X-ray diffractions (XRD), scanning electron microscopy (SEM), and Fourier transmission infrared

spectroscopy (FTIR) were used to investigate the structural characteristics. M-type hexagonal phase development is confirmed by the XRD-indexed pattern. Synthesized samples have crystallite sizes that vary from 13 to 34±2 nm. The presence of the targeted product's metal-oxygen bond was further verified by FTIR peaks. The dielectric characteristics of every combination were often measured. With increasing frequency, the Dielectric permittivity, loss, and tangent loss drop from 26 to 9, 25 to 2, and 0.94 to 0.14, respectively. When the concentration of dopant is raised from 2.15 ×104 to 1.92 ×105 Ω·cm, DC electrical resistivity increases [96].

S. Mortazavinik et al. [2017] prepared M-type strontium hexaferrite with Zr^{4+}, Zn^{2+}, and Co^{2+} substitutions, using a sol-gel auto-combustion technique. XRD, FTIR, TGA-DSC, UV-Vis spectroscopy, and FESEM methods were used to analyze the structure, morphology, and composition of substituted hexaferrite and polyaniline. The outcomes demonstrated that M-type hexaferrite nanoparticles were generated and that polyaniline chains efficiently covered the nanoparticles. The vibrating sample magnetometer (VSM) was used to measure the magnetic characteristics of the samples. In comparison to pure hexaferrite, composite has lower saturation magnetization (M_s), magnetic remanence (M_r), and coercivity (H_c). Using a vector network analyzer (VNA), samples' characteristics for microwave absorption were evaluated. In comparison to pure hexaferrite, the saturation magnetization (M_s), magnetic remanence (M_r), and coercivity (H_c) of the composite are lower. The vector network analyzer (VNA) was used to examine the characteristics of the samples' microwave absorption. The findings showed that the composite's lowest reflection loss (RL) is -20 dB at 10.1 GHz and that its bandwidth has more than 90% absorption up to 3.5 GHz, covering the entire X-band [97].

Gholamreza Ramezanzaeh et al. [2017] synthesize ferrimagnetic nanoparticles of $SrFe_{12-x}(Mn_{0.5}Sn_{0.5})_xO_{19}$, by adjusting the efficient processing parameters of sol-gel methods. By using vector network analysis, vibrating sample magnetometry, EDS, and XRD, the microwave, magnetic, and structural characteristics of nanosize, high purity $SrFe_{12-x}(Mn_{0.5}Sn_{0.5})_xO_{19}$, ferrimagnetic nanoparticles were studied. To determine the occupancy locations of integrated cations, 57Fe Mössbauer spectroscopy was used. Reduced coercivity and magnetization saturation were brought on by the placement of manganese and tin in the 12k sites. Coercivity and magnetization saturation results demonstrate that superparamagnetism was not present in the synthesized products. According to the results, adding tin and manganese to hexagonal ferrite increases bandwidth and reflection loss. Such a mixture may be suggested as a good microwave electromagnetic wave absorber [98].

M. Ramzan et al. [2017] synthesized a series of $Ba_{0.8}Ni_{0.2}Fe_{(12-x)}Pr_xO_{19}$ ($0 \leq x \leq 0.4$) ferrites by co-precipitation route. The powder X-ray diffraction studies confirmed the formation of an M-type hexaferrite structure. XRD results were used to determine the crystallite size and lattice constants of the prepared powders. The average crystallite size was found in the range of 19.88–29.19 nm and increased with an increase in Pr^{3+} content. The FT-IR and Raman spectroscopy further confirmed the formation of an M-type hexagonal structure. The optical bandgap was determined by UV-vis spectroscopy and it was found in the range of 2.80–3.44 eV. It was also observed that the optical bandgap decreased when Pr^{3+} content increased until x = 0.3. With a further increase in Pr^{3+} content, the optical bandgap started to increase. This study demonstrates the potential of Pr-substituted Ba-Ni M-type hexagonal nano ferrites to be used in magneto-optical devices [99].

S. K. Godara et al. [2016] created a series of $BaZn_xZr_xFe_{(12-2x)}O_{19}$ ferrites (x = 0, 0.1, 0.3, 0.5, 0.7, and 0.9) during the current study. The primary goal of the experiment was to better understand how Zn/Zr dopant influences the structure and characteristics of M-type-barium hexagonal ferrites. The precursor was calcined at 900°C for 6 hours. FTIR, XRD, VSM, and TEM were used to characterize these compounds. Barium hexaferrite (BAM) material's XRD results show that it is a pure phase with no signs of intermediary phases such -as Fe_2O_3 and BaCO3. BaM series crystal sizes ranged from 38.9 to 66.9 nm, with a 49.7 nm average particle size. According to magnetic measurements, coercivity values ranged from H_c 4875Oe (x = 0) to 835Oe (x = 0.9). Values for saturation magnetization (M_s) fall between 58.2 and 33.4 emu/g [100].

C. Lei et al. **[2016]** created M-type hexagonal $Sr_{1-x}La_xFe_{12}O_{19}$ ferrites in a molten salt matrix, to prevent particle agglomeration and manage grain development. The impact of rare earth La^{3+} ion replacements on the lattice structure, morphology, and magnetic characteristics has been examined by removing the impurity phase. The findings demonstrate that La^{3+} substitutions have a significant impact on both the magnetic orientation and grain development. All replaced powders positioned with a 5 kOe magnetic field significantly improved the easy magnetization direction. The best coercivity of 6.25 kOe, saturation magnetization of 69.5 emu/g, and remanence ratio of 0.71 was noted [101].

Z. Mosleh et al. **[2016]** used Sol-gel synthesis process to produce $Ba_{1-x}Ce_xFe_{12}O_{19}$ (x = 0.0, 0.05, 0.1, 0.15, and 0.2) polycrystalline samples, which were then examined using techniques such as thermogravimetric analysis (TG), X-ray diffraction (XRD), Fourier transform infrared spectroscopy (FTIR), Field emission scanning electron microscopy (FESEM), vibrating

sample magnetometer (VSM), and vector network analyzer. The average particle size of the undoped sample was around 500 nm, and this value decreased with the amount of Ce doping present in all of the synthesized samples. On the other hand, coercivity showed no predictable behavior with Ce content whereas the magnetization first increased and subsequently dropped with the rise in Ce. For x = 0.1, the highest levels of magnetism (53 emu/g) and coercivity (5088 Oe) were achieved. Maximum reflection losses for x = 0.15 and x = 0.2 samples of microwave absorption within the 2-18 microwave frequency range were -16.74 dB at 10.3 GHz and -20.47 dB at 16.22 GHz, respectively [102].

Md. A. Rafiq et al. [2016] prepared polycrystalline barium hexaferrite $BaFe_{12-x}Ni_xO_{19}$ (x = 0, 0.3, and 0.5) ceramics by using the traditional solid-state method. Studies using Fourier transform infrared spectroscopy and X-ray diffraction demonstrated that Ni was successfully substituted for $BaFe_{12}O_{19}$ without the creation of any new phases. Images taken using scanning electron microscopy revealed that the Ni content rise resulted in an increase in the average grain size and a platelet-like shape of the particles. The remnant magnetization Mr and coercivity H_c both significantly increased with the increase in Ni from x = 0 to x = 0.5, according to a vibrating sample magnetometer, going from 20.24 to 25.51 emu/g and from 1027.20 to 1971.60 Oe, respectively. Saturation magnetization M_s, however, only slightly changed [103].

Isa Araz et al. [2016] made Co-doped $BaFe_{11}CoO_{19}$ barium hexaferrite using the typical sintering method often employed for microwave absorber materials. Here, the magnetic hysteresis loop of the synthesized sample was obtained using a vibrating sample magnetometer, and its surface shape was investigated using scanning electron microscopy. The Nicolson-Ross-Weir (NRW) method was used to assess the complex permeability and complex permittivity utilizing an automated commercial measuring setup in the frequency range of 18-26.5 Hz. The greatest reflection loss value in the domain wall resonance zone was found to be 18.3 dB, while the minimum reflection loss value was determined to be 14.5 dB. A domain wall resonance was observed at roughly 19 GHz. Barium hexaferrites co-doped with $BaFe_{11}CoO_{19}$ seem to be an excellent candidate as a microwave absorber [104].

Z. Vakil et al. [2015] prepared Ce^{3+} substituted barium ferrite with the chemical formula $BaCe_xFe_{12-x}O_{19}$, and Sol-gel auto-combustion was used. The X-ray diffractometer (XRD) patterns demonstrate that as the Ce^{3+} concentration grew, so did the lattice constants (a and c). SEM pictures reveal a hexagonal platelet-like structure forming. Magnetic measurements demonstrate that magnetic saturation (M_s) and remanent magnetization (M_r) had both increased to 56.65 emu/g and 29.66 emu/g, respectively. With increasing compositions, the coercivity

(H_c) dropped to 3357.260e. The dielectric behavior of synthesized barium ferrite powders was studied using a vector network analyzer (VNA) in the X-band frequency range (8.2 - 12.4 GHz) [105].

H. M. Khan et al. [2014] prepared and examined how the replacement of Pr-Ni affected the structural and magnetic characteristics of $Ca_{0.5}Ba_{0.5-x}Pr_xNi_yFe_{12-y}O_{19}$, which was made using the sol-gel auto-combustion technique. The single-phase M-type hexaferrite structure was verified by XRD analysis. The ionic size of the involved cations is thought to be the reason for the observed rise in lattice parameters with increasing Pr-Ni concentration. In the lattice, the Pr-Ni appears to be entirely soluble. According to transmission electron microscopy, the amount of Pr-Ni substitution causes the grain size to decrease. The ranges of the coercivity and remanent magnetization are respectively 1511-1925 (Oe) and 21.4-26.5 (emu/g). All of the samples' coercivity values are within the range of M-type hexa-ferrites [106].

A. Sharbati et al. [2013], by using the citrate sol-gel process, hexaferrite nanocrystallites with typical diameters in the range of 46 to 60 nm are produced. Using an X-ray diffractometer, a field emission scanning electron microscope, a vibrating sample magnetometer, and a vector network analyzer, powders' crystalline structure, morphology, magnetic characteristics, and microwave absorption properties were examined, respectively. Hysteresis loops were used to calculate the magnetic parameters such as saturation magnetization (M_s) and coercivity (H_c). The M-type strontium hexaferrite is the pure phase, according to the XRD patterns. Hexaferrite (70 wt%) and acrylic resin (30 wt%) composites' microwave absorption capabilities were assessed using the standing-wave-ratio (SWR) technique in the frequency range of 12 to 20 GHz. Results demonstrated that the compound's resonance frequency increased when Ho ions were substituted for Sr ions. A minimal reflection loss of -42 dB was attained for samples with x = 0.03 at 16.6 GHz for a layer that was 1.7 mm thick. The produced composites were shown to have the potential for electromagnetic compatibility and other high-frequency practical applications [107].

Ghasemi et al. [2006] made Hexaferrites of $BaFe_{12-x}(Mn_{0.5}Co_{0.5}Ti)_{x/2}O_{19}$ using the citrate sol-gel method with ferric citrate, barium carbonate, and metal nitrates as precursors. The findings demonstrate that doped BaM ferrite may be prepared at a temperature of around 1100 °C. Ba ferrites' magnetic characteristics and microstructure were significantly altered by Mn, Co, and Ti replacements. At a modest amount of substitution (x = 1), an Mn-Co-Ti combination reduced Hc quite well. Doped ferrite exhibits almost axial anisotropy at low substitution rates (x = 1), but when substitution rates increase (x = 2), the axial anisotropy is visibly diminished. The

magnetic susceptibility and coercive force are greater in the samples with x = 2 and 3 respectively [108].

2.1 Problem Formulation

A literature survey on several ferrite composites as electromagnetic absorbers has been done. From the literature survey and to the author's best knowledge, it has been found that only few microwave absorption studies have been conducted on Ba- Sr-Co (Barium-Strontium-Cobalt) doped ferrite composites. There is a need to work on the bandwidth-to-thickness ratio in hexaferrite composites for lightweight microwave absorption applications. The effect of doping on narrow-band as well as wide-band bandwidth needs to be explored. How the thickness can be reduced effectively by using the Ba-Sr-Co doped ferrite composites also needs an investigation.

It is therefore determined to synthesize and study the following series of M-type hexagonal ferrites to address these problems.

(i) $Ba_{0.2}Sr_{0.8}Co_xMg_xFe_{12-2x}O_{19}$ (x = 0.0, 0.2, 0.4, 0.6, 0.8,1.0)

(ii) $Ba_{0.2}Sr_{0.8}Co_xCu_xFe_{12-2x}O_{19}$ (x = 0.0, 0.2, 0.4, 0.6, 0.8,1.0)

(iii) $Ba_{0.2}Sr_{0.8}Co_xAl_xFe_{12-2x}O_{19}$ (x = 0.0, 0.4, 0.8, 1.2, 1.6, 2.0)

(iv) $Ba_{1-x}Sr_xFe_{12}O_{19}$ (x = 0.0, 0.2, 0.4, 0.6, 0.8,1.0)

2.2 Effect of Substitution

To get the desired ferrite characteristics for a given application, several replacements of other cations into BaSrM ferrites are done. Hysteresis and electromagnetic characteristics are altered as a result of the replacement, and these changes are beneficial for a variety of microwave absorption benefits.

2.3 Objectives

1. To prepare hexaferrite composites and study their electrical properties.
2. To measure microwave absorption by electromagnetic parameters of composites and analyze the tunable frequency and bandwidth to thickness ratio.
3. To optimize microwave absorption in hexaferrite composites.

Summary:

A literature survey reveals limited studies on Ba-Sr-Co doped ferrite composites for microwave absorption. Research needs to focus on improving the bandwidth-to-thickness ratio and exploring the effects of doping on narrow and wide-band absorption. The study aims to optimize microwave absorption in hexaferrite composites by adjusting electrical properties and analyzing frequency performance.

CHAPTER 3

RESEARCH METHODOLOGY AND CHARACTERIZATION

3.1 Research Methodology

3.1.1 Synthesis using Sol-Gel Method:

The sol-gel technique is a versatile and widely used method for the fabrication of materials, particularly ceramics and glasses. It involves the conversion of a solution (sol) into a gel and subsequently into a solid material. This process is used for the synthesis of various materials, including thin films, coatings, and bulk materials with tailored properties. Here's a detailed explanation of the sol-gel technique:

Steps in the Sol-Gel Process:

1. Sol Formation:

- The process begins with the preparation of a colloidal solution called a sol. The sol typically consists of metal-containing precursors, such as metal alkoxides (e.g., tetraethyl orthosilicate, Ti(OR)_4), metallic salts, or metal chlorides dissolved in a solvent.
- The solution is often stirred or sonicated to ensure uniform distribution of the components.

2. Gelation:

- Gelation is the transformation of the sol into a three-dimensional network, forming a gel. This step is crucial as it defines the structure and properties of the final material.
- Gelation can be achieved through various methods, including chemical reactions, pH adjustments, or temperature changes. For example, the addition of a catalyst or altering the pH can induce gelation.

3. Aging:

- After gelation, the material is allowed to age. Aging is a process where the gel undergoes slow structural changes, leading to increased strength and stability.
- Aging time and conditions depend on the specific materials being used and the desired properties of the final product.

4. Drying:

- The gel is then dried to remove the solvent, resulting in a porous structure.
- Different drying methods, such as air drying, freeze drying, or supercritical fluid drying, can be employed based on the specific requirements of the material.

5. Sintering or Calcination:

- The dried gel is often subjected to high temperatures in a process called sintering or calcination. This step removes any remaining organic components and promotes the densification of the material.

- The temperature and duration of this step depend on the composition of the gel and the desired properties of the final product.

Advantages of Sol-Gel Technique:

1. Control over Composition:
- The sol-gel process allows precise control over the composition of the final material by adjusting the precursor concentrations.
2. Homogeneity:
- It provides excellent homogeneity and uniform distribution of components at the molecular level, leading to improved material properties.
3. Versatility:
- Sol-gel can be applied to various materials, including oxides, nitrides, and hybrid organic-inorganic materials.
4. Tailored Properties:
- The properties of the final material, such as porosity, surface area, and crystallinity, can be tailored by adjusting the synthesis parameters.
5. Low-Temperature Processing:
- The sol-gel technique is often performed at relatively low temperatures compared to other synthesis methods, making it suitable for temperature-sensitive materials.

The sol-gel technique has applications in various fields, including optics, electronics, catalysis, sensors, and biomaterials, among others. Its versatility and controllability make it a powerful tool for the design and fabrication of advanced materials with specific properties for diverse applications.

Here, the intended M-type hexagonal ferrite, with the chemical formula $Ba_{0.2}Sr_{0.8}Co_xMg_xFe_{12-2x}O_{19}$ (x = 0.0, 0.2, 0.4, 0.6, 0.8,1.0), $Ba_{0.2}Sr_{0.8}Co_xCu_xFe_{12-2x}O_{19}$ (x = 0.0, 0.2, 0.4, 0.6, 0.8,1.0), $Ba_{0.2}Sr_{0.8}Co_xAl_xFe_{12-2x}O_{19}$ (x = 0.0, 0.4, 0.8, 1.2, 1.6, 2.0), $Ba_{1-x}Sr_xFe_{12}O_{19}$ (x = 0.0, 0.2, 0.4, 0.6, 0.8,1.0) was synthesized using the Sol-Gel method. The AR-grade nitrates were added to 100 ml of distilled water in stoichiometric proportions and swirled one at a time. Another 100 ml of distilled water was added to the same amount of citric acid. After mixing the two solutions, the pH was set at 7. The resulting solution was continually heated at 82 °C for 3 hours till it turned into gel. Auto combustion resulted from further heating. To create the finished product, the final ash was pre-heated for two hours at 550 °C and sintered for five hours at 1100 °C [10][46-49].

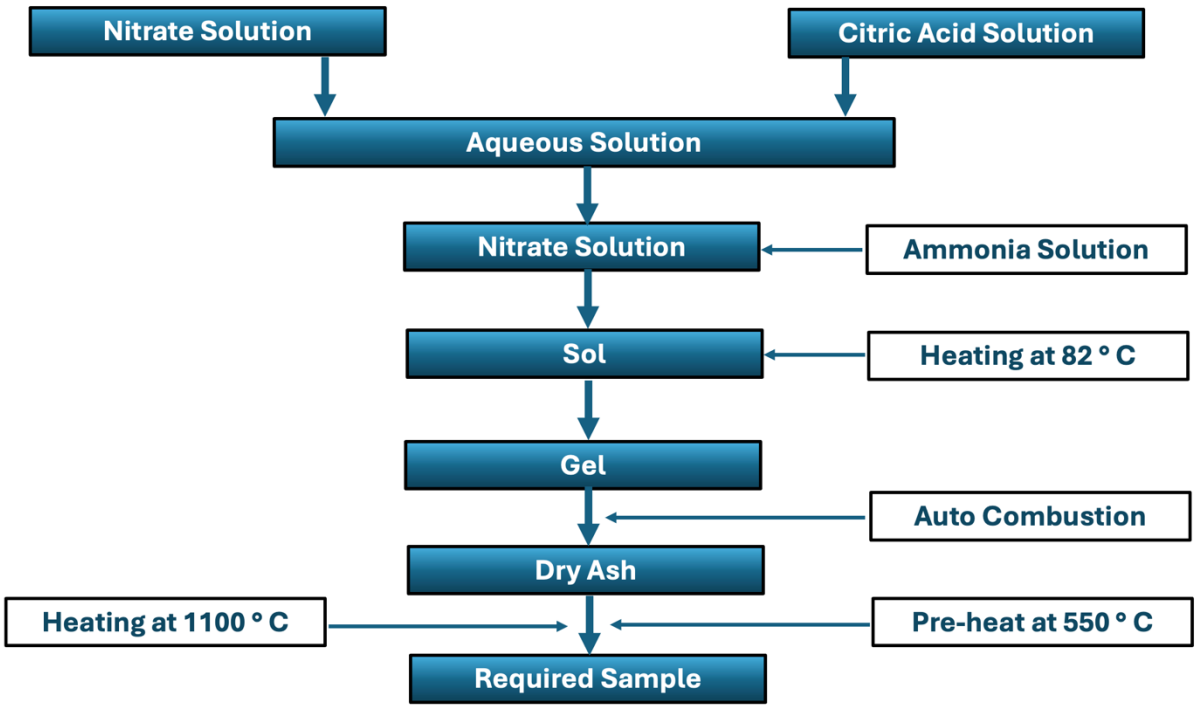

Figure 3.1: Sol-gel Technique for Synthesis

3.2 Microstructural Characterization

3.2.1 X-ray diffraction (XRD)

Using X-ray diffraction, the crystalline structure of ferrite was determined. For about 95 percent of all solid materials, the X-ray diffraction technique is a well-established method for determining structural information concerning the kind of unit cell, lattice parameter, crystallite size, percentage crystallinity, phase purity, and crystallographic structure. Figure 3.2 shows the X-ray diffractometer; the phase purity of all prepared samples was explored using this X-ray diffractometer. The X-ray diffraction (Rigaku Miniflex-II X-ray) technique using Cu Kα radiation (λ = 1.5405 Å) in the range of 2θ = 25°- 80°. Here, X-rays having wavelengths comparable with inter-atomic distances of powder material interact with X-rays with wavelengths similar to the interatomic distances of powdered materials, and the diffraction pattern reveals crystallographic structural information. Therefore, the X-ray diffraction method is ideal for identifying and characterizing the numerous phases found in polycrystalline materials.

To determine Miller indices of the obtained peaks, Powder-X software has been used. The lattice parameters, namely $a = b$, c and unit cell volume (V) of the prepared samples, were determined by the following equations:

Figure 3.2: Rigaku Miniflex-II X-ray Diffractometer

For hexagonal structure $a = b \neq c$ and $\alpha = \beta = 90°$ and $\gamma = 120°$

$$\frac{1}{d_{hkl}^2} = \frac{4}{3}\left(\frac{h^2}{a^2} + \frac{hk}{a^2} + \frac{k^2}{a^2}\right) + \frac{l^2}{c^2} \tag{3.1}$$

$$\text{Unit cell volume } V = \frac{\sqrt{3}}{2} a^2 c \tag{3.2}$$

Where d_{hkl} is termed as d-spacing in the X-ray diffraction pattern, and h, k, and l are Miller indices.

The average crystalline size of the prepared samples, i.e., $D_{xrd,}$ was determined by Scherrer equation:

$$D_{xrd} = 0.94 \frac{\lambda}{\beta 1/2 \cos\theta} \tag{3.3}$$

Here, D_{xrd} is the average crystalline size and λ is X-ray wavelength (1.5406 Å), β known as line broadening in radians, and $\beta_{1/2}$ full width at half maximum with θ stands for Braggs angle in degree.

3.2.2 EDAX

EDAX refers to Energy Dispersive X-ray Analysis, which is a technique used for the elemental analysis of materials. It is commonly employed in conjunction with scanning electron microscopy (SEM). SEM-EDAX allows scientists and researchers to determine the elemental composition of a sample by analyzing the characteristic X-rays emitted when the sample is bombarded with electrons in the SEM.

The basic principle involves directing a focused electron beam onto the sample surface. When the electrons interact with the atoms in the sample, inner-shell electrons are ejected, and outer-shell electrons fall into the inner shells to fill the vacancies. This process results in the emission

of characteristic X-rays. By measuring the energy and intensity of these X-rays, it is possible to identify the elements present in the sample and determine their relative concentrations.

The EDX analysis particularly provides an estimation of an elemental presence as per specifications of mixed chemicals at the time of preparation.

3.2.3 Field Emission Scanning Electron Microscopy

Field Emission Scanning Electron Microscopy (FE-SEM) is an advanced microscopy technique that utilizes a high-powered electron beam for imaging the surface of specimens at extremely high magnifications. It is an improvement upon conventional scanning electron microscopy (SEM) and is particularly useful for imaging nanoscale structures and obtaining high-resolution images.

Figure 3.3: FESEM by JEOL (Japan)

The key feature of FE-SEM is the use of a field emission electron source, which produces a highly focused and coherent electron beam. In contrast to the thermionic electron sources used in conventional SEM, field emission sources provide a much smaller electron source size, resulting in improved spatial resolution. This allows FE-SEM to achieve sub-nanometer resolution, making it an essential tool for studying materials and biological specimens at the nanoscale.

FE-SEM is widely used in various scientific and industrial fields, including materials science, nanotechnology, biology, and semiconductor research. The high-resolution imaging capabilities make it a valuable tool for characterizing and understanding the morphology and composition of materials at the nanoscale. Powder sample microstructure has been investigated utilizing FESEM by JEOL (Japan) shown in Figure 3.3.

3.2.4 Vibrating Sample Magnetometer

A Vibrating Sample Magnetometer (VSM) is an instrument used to measure the magnetic properties of materials. It operates by vibrating a sample in a magnetic field, which induces a

voltage in nearby coils. This voltage is proportional to the magnetic moment of the sample, allowing researchers to analyze its magnetic behavior.

Key Features:

- Sample Vibration: The sample is typically oscillated at a known frequency, which helps to improve the sensitivity and accuracy of the measurements.
- Magnetic Field Control: The VSM can apply a uniform magnetic field, allowing for measurements at different field strengths.
- Data Acquisition: The induced voltage is detected and processed, providing information on the magnetic moment, susceptibility, and hysteresis behavior of the sample.

Applications:

- Material Science: Investigating ferromagnetic, paramagnetic, and diamagnetic materials.
- Nanotechnology: Studying the magnetic properties of nanoparticles and thin films.
- Geophysics: Analysing magnetic minerals in rocks and soils.

Figure 3.4 VSM (Microsense EV-90, USA)

A VSM (Microsense EV-90, USA) was used to capture B (magnetic flux) vs. H (magnetizing force) graphs in the present investigation. The applied field ranged from -15 to +15 kOe at room temperature. Figure 3.4 displays the VSM image. Coercivity (H_c), remanence (M_r), and magnetic saturation (M_s) are the different magnetic properties that are derived from VSM. The magnetic measurements have typically been performed at room temperature.

3.3. Electrical Characterization

3.3.1 Dielectric permittivity

The calculation for the real part of the dielectric permittivity (ε') is done using the below formula:

$$\varepsilon' = \frac{L}{\omega A \varepsilon_o} \cdot \frac{Z''}{Z'^2 + Z''^2} \tag{3.4}$$

Where Z' stands for the real part of the impedance and Z'' for the imaginary part of the impedance,

L is the thickness of the pellet and A is the cross-sectional area of the disc-shaped pellet, $\varepsilon_o = 8.854\times10^{-12}\ F/m$ is the free space permittivity.

The calculations of the imaginary part of the dielectric loss (ε'') and dielectric loss tangent ($tan\delta$) have been performed from the following formulae: [109-110]

$$\varepsilon'' = \frac{L}{\omega A \varepsilon_o} \cdot \frac{Z'}{Z'^2 + Z''^2} \tag{3.5}$$

$$tan\delta = \frac{\varepsilon''}{\varepsilon'} \tag{3.6}$$

3.3.2 Electric Modulus Analysis

The exercise on complex electric modulus helps us analyze the electrical behavior of the material. This approach helps us to knowledge about the nature of polycrystalline material and also evaluates the electrical relaxation in ionic solids.

Dielectric modulus M^* is given by

$$M^* = (\varepsilon^*)^{-1} = (\varepsilon' - i\varepsilon'')^{-1} \tag{3.7}$$

$$M' = \frac{\varepsilon'}{\varepsilon'^2 + \varepsilon''^2} \tag{3.8}$$

$$M'' = \frac{\varepsilon''}{\varepsilon'^2 + \varepsilon''^2} \tag{3.9}$$

Here M' and M'' stand for the real and imaginary parts of complex electric modulus respectively [111-113].

3.3.3 Complex Impedance Spectra

The analysis of impedance provides us with information on resistance (Z') and reactance (Z'') in the material. The impedance behavior of polycrystalline materials is primarily due to bulk grains and grain boundaries. The impedance of bulk grains can be treated differently from the impedance of grain boundaries since both have different relaxation times.

In the Cole-Cole plot, Z'' (imaginary part of impedance) is plotted concerning Z' (real part of impedance) where the complex impedance is given by

$$Z^* = Z' + iZ'' \tag{3.10}$$

The complex impedance spectra are an important means to inspect the electrical properties of the samples. This inspection relates to data of resistive (real) and reactive (imaginary) parts of impedance that are devoted to the process of conduction in the applied ac field.

$$Z' = \frac{R_P}{1 + (\omega C_P R_P)^2} \tag{3.11}$$

$$Z'' = \frac{\omega C_P R_P^2}{1 + (\omega C_P R_P)^2} \tag{3.12}$$

where, ω - angular frequency = $2\pi f_{max}$, R_p, and C_p are resistive and capacitive components of parallel circuits respectively [114-122].

3.3.4 AC Conductivity

The conduction in ferrites is primarily reported due to the hopping of its valence electrons between Fe^{2+} and Fe^{3+} at Octahedral sites [123]. The increase in frequency boosts the hopping frequency of charge carriers and causes an increase in conductivity. This frequency-reliant conduction mechanism is explained based on the polaron hopping model reported in [124]. Based on that model, AC conductivity increases with an increase in frequency for the limited range of polaron hopping, however, it shows a decreasing trend for long-range polarization hopping. In the case of band conduction, the conductivity phenomenon is frequency-independent [125].

The frequency-dependent AC conductivity is given by the following expression of the Jonscher power law [126]

$$\sigma_{ac}(f) = \sigma_{dc} + A\omega^n \tag{3.13}$$

Where σ_{dc} is dc conductivity independent of frequency, A, as well as n, are constants that depend on the temperature and composition of the sample. Here n is dimensionless but A has units of conductivity. The dispersion in AC conductivity plots is quantified by the second term $A\omega^n$.

According to Funke [127], the value of n has a physical meaning: $n < 1$ means that the electron hopping involves a translational motion with sudden hopping, whereas $n > 1$ means that the motion involves localized hopping between neighboring sites [128-130].

3.4 Hysteresis

Hysteresis in ferromagnetic materials refers to the phenomenon where the magnetization of a material lags behind the applied magnetic field. When an external magnetic field is applied to a ferromagnetic material, the magnetic domains within the material align themselves with the external field. However, when the external magnetic field is removed or reversed, the magnetic domains do not immediately return to their original random orientations.

The relationship between the magnetic induction (B) and the magnetizing force (H) in a ferromagnetic material is typically represented by a hysteresis loop on a B-H curve. The hysteresis loop illustrates the lag or delay in the material's response to changes in the magnetic field.

A ferromagnetic sample being magnetized for the first time will follow the line with the arrowhead as the field intensity increases, as shown in Figure 3.5. Due to an increasing number of domains aligning in one direction, the magnetic flux density increases when a magnetic field

is applied. Nearly all of the domains have aligned at point A, so as the magnetic field increases, the magnetic flux density does not further rise. Saturation magnetization is represented by this point. The material follows the curve from point A to point B as the magnetic field is lowered to zero, indicating that some magnetic flux is still present in the material even after the field strength is lowered to zero. This point, which graphically depicts remanence or the amount of residual magnetism in the substance, is called retentivity. This occurs as a result of some magnetic domains losing alignment while others maintain it. To remove the magnetic flux in the material, the magnetic field must be directed in the opposite direction.

When this reverse magnetic field is applied, the graph reaches point C, which indicates the material's coercivity and represents the amount of reverse magnetizing force needed to eliminate any remaining magnetism. All of the domains are disoriented by this magnetic field acting in the opposite direction, resulting in zero net magnetic flux within the material. Saturation magnetization (M_s) is reached as the reverse magnetic field's strength increases once more, but in the opposite direction, denoted by point D on the graph. The material (point E) retains the same quantum of residual magnetic flux when the magnetic field is decreased to zero once more as it was in the opposite direction. Furthermore, the curve does not pass through the origin; instead, it travels to saturation point A and completes the loop since a certain amount of magnetizing force is still needed to make magnetic flux zero (point F).

The M_s and H_a values of the synthesized compositions are obtained by using the law of saturation:

$$M = M_s\,(1 - A/H - B/H^2) + \chi_p H \tag{3.14}$$

In the above formula, B is an anisotropy parameter, A is an inhomogeneity parameter, χp specifies susceptibility (at high field).

The following formula makes it simple to determine the value of B based on the crystal's hexagonal symmetry:

$$B = H_a^2/15 = 4K_1^2/15M_s^2 \tag{3.15}$$

Here, the anisotropy field is represented by H_a, i.e., the tendency of the material to magnetize in one direction, and the anisotropy constant is K_1.

Now, A/H and χ_p components from equation (3.14) may be removed, and the B term can be found using the slope of the linear relationship ($M = M_S\,(1 - B/H^2)$ versus $1/H^2$), Equation (3.15) may then calculate H_a by supplying the computed B value.

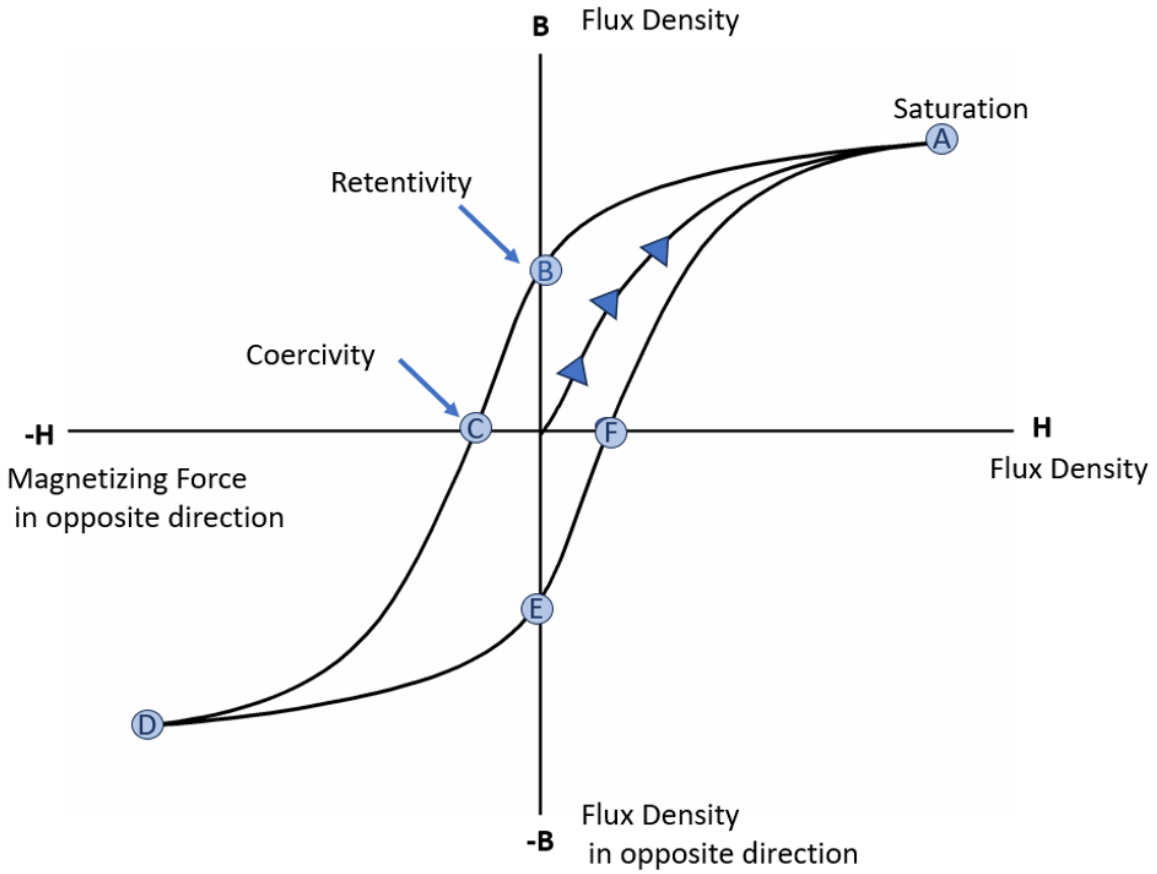

Figure 3.5: Hysteresis loop (Variation of Magnetic field with Flux Density)

The hysteresis parameters, i.e., coercivity, saturation magnetization, and Remanent magnetization of samples were measured by vibrating sample magnetometer (Microsense EV-90, USA) discussed in the above section [131-144].

3.5 Microwave Absorption Measurement

The measurement of microwave absorption for prepared ferrite samples is done using the Vector Network Analyzer (VNA), Figure 3.6 depicts the block diagram of VNA. The signal traveling through the ferrite sample is measured in terms of its scattering properties, or S-parameters. Figure 3.7 displays the S-parameter signal flow graph for a two-port device. When the input is provided at port 1 and the output response is taken at port 2, the response S_{21}. This also represents the frequency domain response characteristics from the device under test (b_1, b_2). From observed s-parameters, the complex permittivity and permeability were calculated using the Nicholson and G.F. Ross technique [145]. Over the 8.2 GHz to 12.4 GHz frequency range, the complex permittivity and permeability were measured using the Agilent model N5225A vector network analyzer. The permeability and permittivity of air were measured to calibrate the vector network analyzer. The reflection loss (RL) of -10 dB or -20 dB is represented by the 90% or 99% absorbed power, respectively [146].

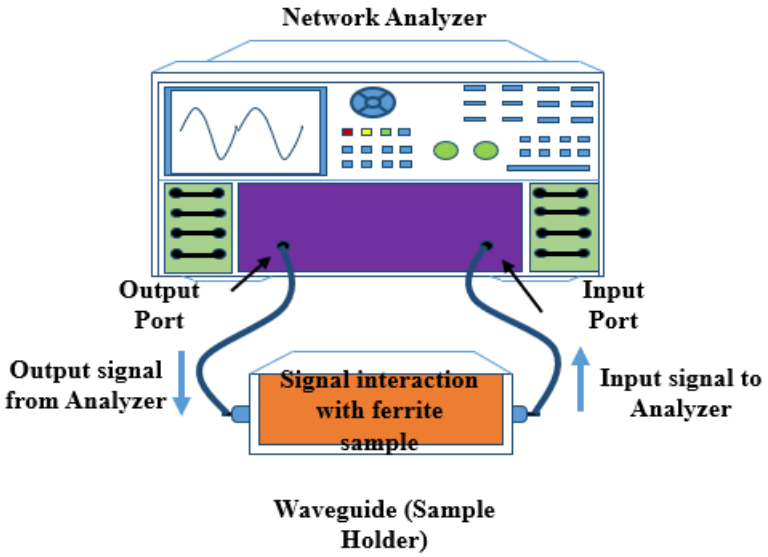

Figure 3.6: Block Diagram for Vector Network Analyser

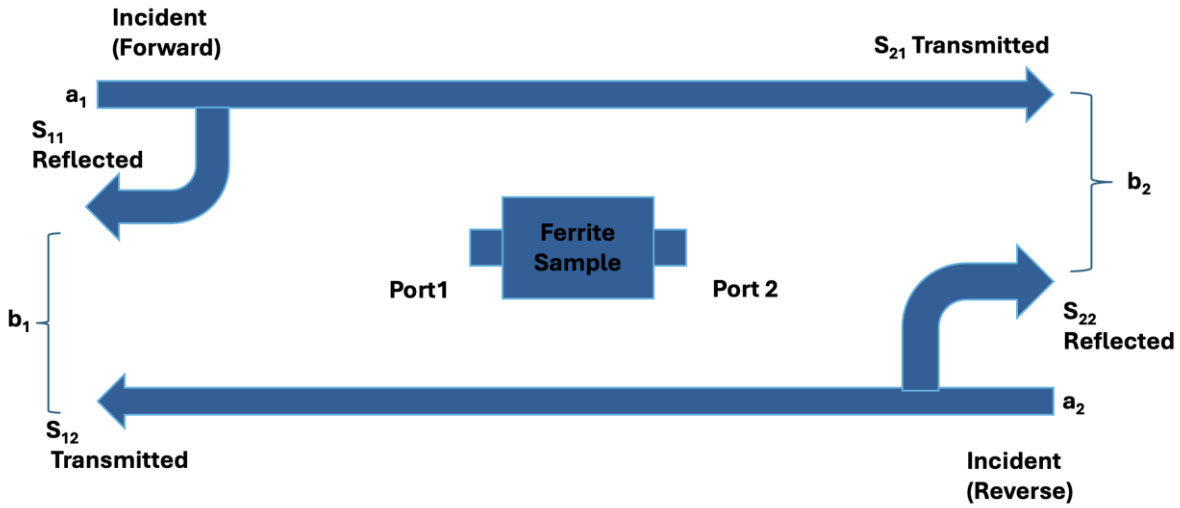

Figure 3.7: S-Parameter representation for 2-port network

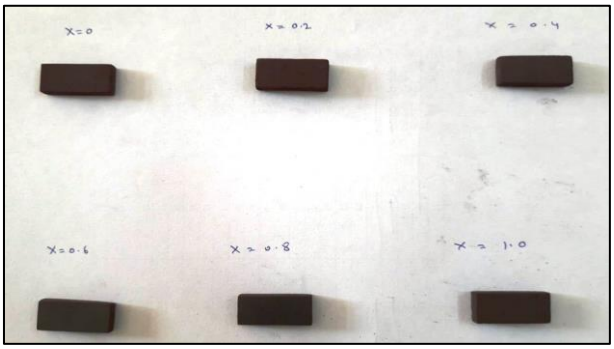

Figure 3.8: Samples used for microwave properties

3.5.1 Complex Permeability and Permittivity

When an external electric field passes through a material, permittivity creates an electric field inside it. While permeability is a material's property to allows the formation of a magnetic field

with the application of an external magnetic field. Complex permittivity is given by $\varepsilon_r = \varepsilon' - j\varepsilon''$, where ε' is the real part which gives us the dielectric permittivity accompanying the energy storage ability in the form of an electric field, and ε'' is the imaginary part which provides the dielectric loss associated with energy dissipation. Similarly, complex permeability is given by $\mu_r = \mu' - j\mu''$, wherein μ' is the real part that gives us the permeability value indicating energy storage ability in the form of a magnetic field and μ'' is the imaginary part that tells us the magnetic loss for energy dissipation.

Impedance matching takes place when the value of complex permittivity is equal to the value of complex permeability, i.e., $\varepsilon_r = \mu_r$. Theoretically, this condition curtails the value of the reflection of microwaves to zero. But practically, this impedance matching is very poor because of low values of complex permeability in the microwave region.

3.6 Reflection loss

The dependence of microwave absorption in the frequency (f) spectra is analyzed with the RL parameter in the conventional transmission line theory. The following relation is used to calculate RL

$$\text{RL} = 20 \log \left| \frac{(Z_{in} - Z_o)}{Z_{in} + Z_o} \right| \tag{3.16}$$

To calculate the value of microwave absorption, reflection loss has to be calculated from the above-given equation, where in Z_o is characteristic impedance if free space, 377 Ω and Z_{in} is the input impedance of the absorbing material given by

$$Z_{in} = Z_o \sqrt{\frac{\mu_r}{\varepsilon_r}} \tanh \left[j \left(\frac{2\pi f t}{c} \right) \sqrt{(\mu_r \varepsilon_r)} \right] \tag{3.17}$$

Where Z_o = 377 Ω is the characteristic value of the impedance of free space and ε_r, μ_r, t, f, c represents complex permittivity, complex permeability, thickness, frequency, and velocity of light respectively.

But for RL calculation, Z_{in} value can be calculated from equation (3.17), once the values of complex permittivity and permeability of the composition are known. Thus substituting the values of ε_r and μ_r, the above equation will give Z_{in} and the corresponding value of RL. This RL is calculated in decibels, when RL ≤ -10 dB the absorption is concluded to be 90% and when RL ≤ -20 dB, it is concluded to be 99% [147-151].

3.7 Mechanism of Microwave Absorption

The absorption of microwaves in compositions containing ferrite has been assessed through the utilization of the quarter-wavelength criterion and the impedance-matching mechanism.

3.7.1 Quarter Wavelength Mechanism

According to the quarter wavelength mechanism [152-153], if the absorber's thickness is equal to the microwave signal's quarter wavelength, the signal will be absorbed or diminished as it passes through the ferrite material. The propagating microwave signal in a ferrite sample backed by a metal plate will be partially reflected by its front surface, with the remaining portion passing through it and being reflected off the metal plate. After passing through ferrite, this reflected signal from the metal plate arrives at the ferrite sample's front face. Both signals will cancel each other out if the reflected microwave signals from the metal and the ferrite's front surface are 180 degrees out of phase but have the same magnitude.

The quarter-wavelength mechanism establishes a connection between the thickness of the microwave-absorbing material layer, the wavelength of the incident radiation, and the electromagnetic properties of the composition. This relationship is expressed by the following equation:

$$t_m = \frac{n\lambda}{4} = \frac{n.c}{4f\sqrt{|\varepsilon_r.\mu_r|}} \quad (3.18)$$

Here, n = 1,3,5..... t_m = matching thickness, c = velocity of light, f = matching frequency.

The calculated thickness from Equation 1 can be put in Equation 18 to calculate the reflection loss from Equation 3.16 [154-155].

3.7.2. Impedance Matching Mechanism

The impedance matching mechanism states that if the impedance of the composition is nearly equal to the input impedance of the free space i.e. 377 ohms, then we can get good results for Microwave absorption.

Transmission line theory can be used theoretically to calculate the input impedance (Z_{in}) of a single-layer absorber as given in Equation 3.17.

As given in section 3.6. In the case of Z_{in} equal to Zo, the condition leads towards the infinite absorption of the signal by the composition. However, in some cases despite $|Z_{in}| \sim Z_o$ (377 Ω), a large RL or RL peak is not found.

This peculiar situation is related to $|Z_{in}|$ in a complex transcendental equation: Z_{in} is a complex variable, rather than real variable. Z_{in} = a + jb, shows that input impedance is of complex nature, where "a" denotes the real part and "b" represents the imaginary part. The entire signal passing through the material will be absorbed if $|Z| = Z_o = 377$ Ω i.e. $Z_{real} = 377$ Ω and $Z_{img} = 0$. This corresponds to an ideal situation. However, practically $|Z| \neq Z_o = 377$ Ω or $Z_{real} \neq 377$ Ω and/or $Z_{img} \neq 0$, which leads to a decrease in absorption. This absorption further decreases when Z_{real} moves away from 377 Ω and/or Z_{img} is non-zero (positive or negative values) [152-155].

3.8 Bandwidth to thickness Ratio/Percentage Bandwidth

Besides the criterion of RL ≥ -10, an important factor in designing and assessing absorber performance is achieving a high bandwidth at low thickness for a typical RL or absorption dip. Once this RL threshold is met, the emphasis should shift to creating a thin layer rather than merely increasing the RL. To achieve this, the following formulas are utilized to calculate the bandwidth-to-thickness ratio (BWT) and percentage bandwidth (PBW) in ferrite samples.

$$BWT = \frac{\lambda_2 - \lambda_1}{t} \quad (3.19)$$

Where $\lambda_2 = c/f_2$, $\lambda_1 = c/f_1$ in which λ_1 and λ_2 are wavelengths at frequencies f_1 and f_2 respectively, for an *RL* peak.

$$PBW = \frac{f_2 - f_1}{f_0} \quad (3.20)$$

f_2 is the upper frequency, f_1 is the upper frequency, f_0 is the center frequency, and t is the thickness at the *RL* dip of interest [156-159].

Summary:

The research methodology for this study encompasses a detailed approach to synthesizing and characterizing ferrite composites for microwave absorption applications. The synthesis is carried out using the sol-gel method, a widely used technique known for producing homogeneous materials with controlled properties. Following synthesis, the microstructural characterization is performed using several advanced techniques, including X-ray diffraction (XRD) for phase identification, EDAX (Energy Dispersive X-ray Analysis) for elemental composition, and Field Emission Scanning Electron Microscopy (FESEM) for examining the surface morphology and grain structure. The magnetic properties of the composites are evaluated using a Vibrating Sample Magnetometer (VSM).

Electrical characterization is a critical component, involving the measurement of Dielectric permittivity, electric modulus, complex impedance, and AC conductivity to understand the electrical behavior of the composites. For microwave absorption performance, complex permeability and permittivity are measured, along with reflection loss to determine the effectiveness of the material in absorbing microwave radiation. The study also explores the mechanisms of microwave absorption, particularly the quarter wavelength and impedance matching mechanisms, which contribute to the material's ability to absorb electromagnetic waves. Finally, the bandwidth-to-thickness ratio and percentage bandwidth are calculated to optimize the composites for lightweight and efficient microwave absorption applications, further enhancing their performance in real-world conditions.

CHAPTER 4

RESULTS AND DISCUSSIONS

4.1 Co^{2+}-Mg^{2+} substituted $Ba_{0.2}Sr_{0.8}Co_xMg_xFe_{12-2x}O_{19}$ hexaferrite

In this section, we have synthesized a hexaferrite with Co and Mg substitutions via the sol-gel technique. This composition hexaferrite will be given as $Ba_{0.2}Sr_{0.8}Co_xMg_xFe_{12-2x}O_{19}$.The sample names with the codes for each level of substitution in $Ba_{0.2}Sr_{0.8}Co_xMg_xFe_{12-2x}O_{19}$ are given in Table 4.1.

Table 4.1: The Assignment of Sample Names Corresponding to Various Substitution Levels in $Ba_{0.2}Sr_{0.8}Co_xMg_xFe_{12-2x}O_{19}$ Hexaferrite

Sample Composition $Ba_{0.2}Sr_{0.8}Co_xMg_xFe_{12-2x}O_{19}$	Sample Code Name	Sample Code (M-Series)
x = 0.0	$Ba_{0.2}Sr_{0.8}Fe_{12-2x}O_{19}$	M1
x = 0.2	$Ba_{0.2}Sr_{0.8}Co_{0.2}Mg_{0.2}Fe_{11.6}O_{19}$	M2
x = 0.4	$Ba_{0.2}Sr_{0.8}Co_{0.4}Mg_{0.4}Fe_{11.2}O_{19}$	M3
x = 0.6	$Ba_{0.2}Sr_{0.8}Co_{0.6}Mg_{0.6}Fe_{10.8}O_{19}$	M4
x = 0.8	$Ba_{0.2}Sr_{0.8}Co_{0.8}Mg_{0.8}Fe_{10.4}O_{19}$	M5
x = 1.0	$Ba_{0.2}Sr_{0.8}Co_{1.0}Mg_{1.0}Fe_{10}O_{19}$	M6

4.1.1 Structural Analysis

4.1.1.1 X-ray Analysis

Figure 1 shows the X-ray diffraction patterns of $Ba_{0.2}Sr_{0.8}Co_xMg_xFe_{12-2x}O_{19}$ (*M1, M2, M3, M4, M5,* and *M6*). All of the aforementioned samples' Bragg peaks appear to be well-defined, pointing to a good crystal structure, only with minor traces of hematite. The Miller indices were located using the Powder X software. The sample's captured peaks were compared to the standard JCPDS #51-1879 (secondary peaks were matched with JCPDS-#86-0550), and the results are shown in the table below. The lattice parameters ($a = b$ and c), the volume of the unit cell, and the crystallite size for the synthesized samples are calculated using equations 3.1, 3.2, and 3.3 from section 3.2.1 and specified in Table 4.2. As seen from the table it is verified that lattice parameter a varies more than c.

The lattice parameters are calculated from the Powder X software. It can be seen from the given table numbers that with doping, the crystallite size does not vary much and stays within the 15.3907-15.9587 nm range.

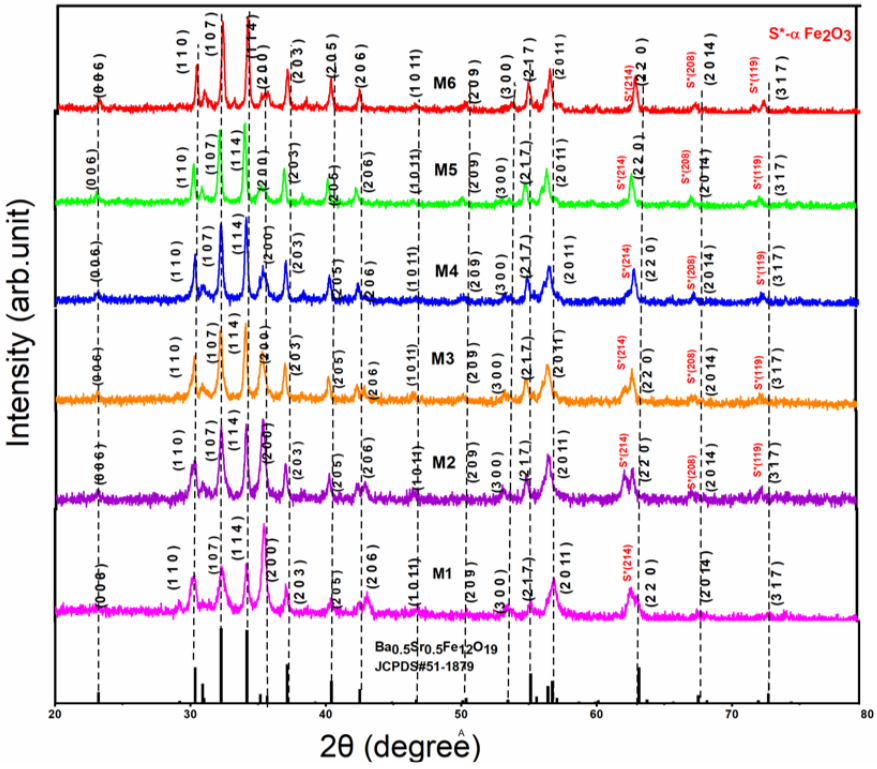

Figure 4.1: X-ray Diffractions of M-type $Ba_{0.2}Sr_{0.8}Co_xMg_xFe_{12-2x}O_{19}$ (*M1, M2, M3, M4, M5* and *M6*) Hexaferrite

Table 4.2: Co-Mg Content, Lattice Constants, Ratio c/a and Unit Cell Volume Ferrite Sample $Ba_{0.2}Sr_{0.8}Co_xMg_xFe_{12-2x}O_{19}$ (*M1, M2, M3, M4, M5 and M6*)

Co-Mg	**Lattice parameters**		**Ratio**	**Unit cell vol.**	**Crystallite Size**
Content (x)	a=b (Å)	c (Å)	c/a	V (Å) ^{3}	D_{xrd} (nm)
M1	5.8912	23.1831	3.9352	696.8021	15.4112
M2	5.8923	23.1822	3.9343	697.0353	15.3907
M3	5.8832	23.1821	3.9337	697.2453	15.8925
M4	5.8912	23.1821	3.935	696.7721	15.9426
M5	5.8922	23.1832	3.9346	697.0417	15.9587
M6	5.8922	23.1832	3.9346	697.0417	15.8923

4.1.1.2 Field Emission Scanning Electron Microscopy

Figure 4.2 (a-f) displays the grain morphology of the samples $Ba_{0.2}Sr_{0.8}Co_xMg_xFe_{12-2x}O_{19}$ (*M1, M2, M3, M4, M5,* and *M6*). The SEM graph of *M1* shows very tiny but fused grains coming together. As the doping is increased, the particles seem to enlarge in size, but voids are seen now. With more doping content in *M3*, the particles have changed their shape from oval (*M1*) to Rice-like (*M3*). Further, with increased doping, more fused grains can be seen in the graph. Due to the electrostatic and magnetic interactions between ferrite particles, doping results in grain clusters with an uneven size distribution. Figure 4.3 shows EDX spectra of $Ba_{0.2}Sr_{0.8}Co_xMg_xFe_{12-2x}O_{19}$ hexaferrite for samples *M1* and *M2*. EDAX of *M1* clarifies that there is no content of Mg found in the sample since x = *0.0*. *M2* shows that Mg content is present in the given synthesized sample.

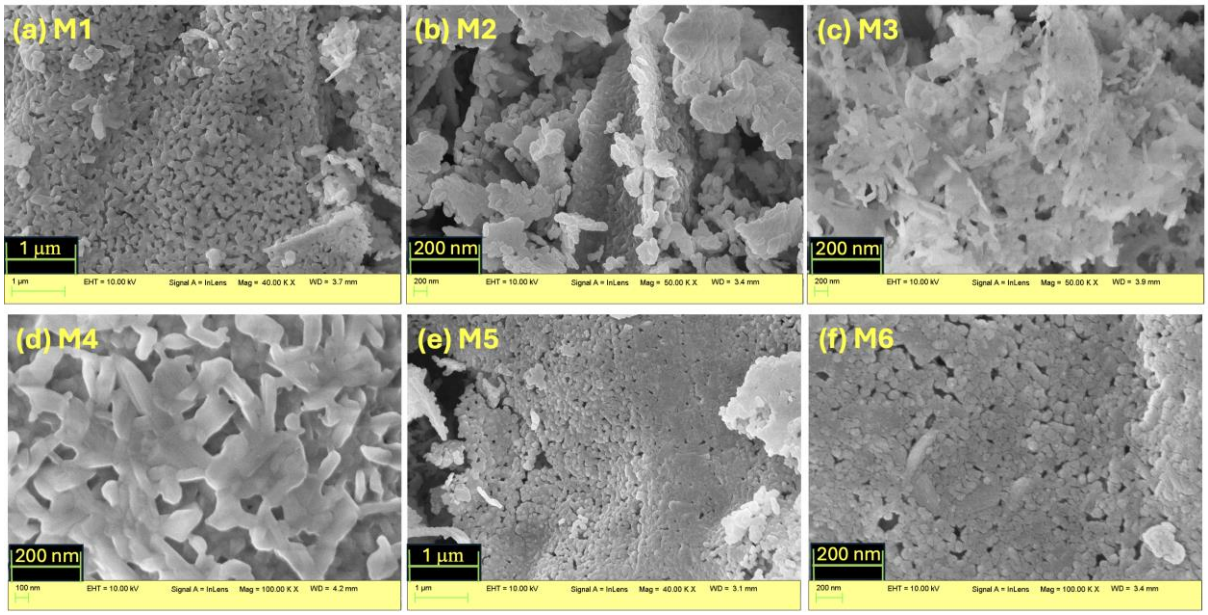

Figure 4.2: SEM Micrographs of Ferrite Samples: $Ba_{0.2}Sr_{0.8}Co_xMg_xFe_{12-2x}O_{19}$ (*M1, M2, M3, M4, M5* and *M6*)

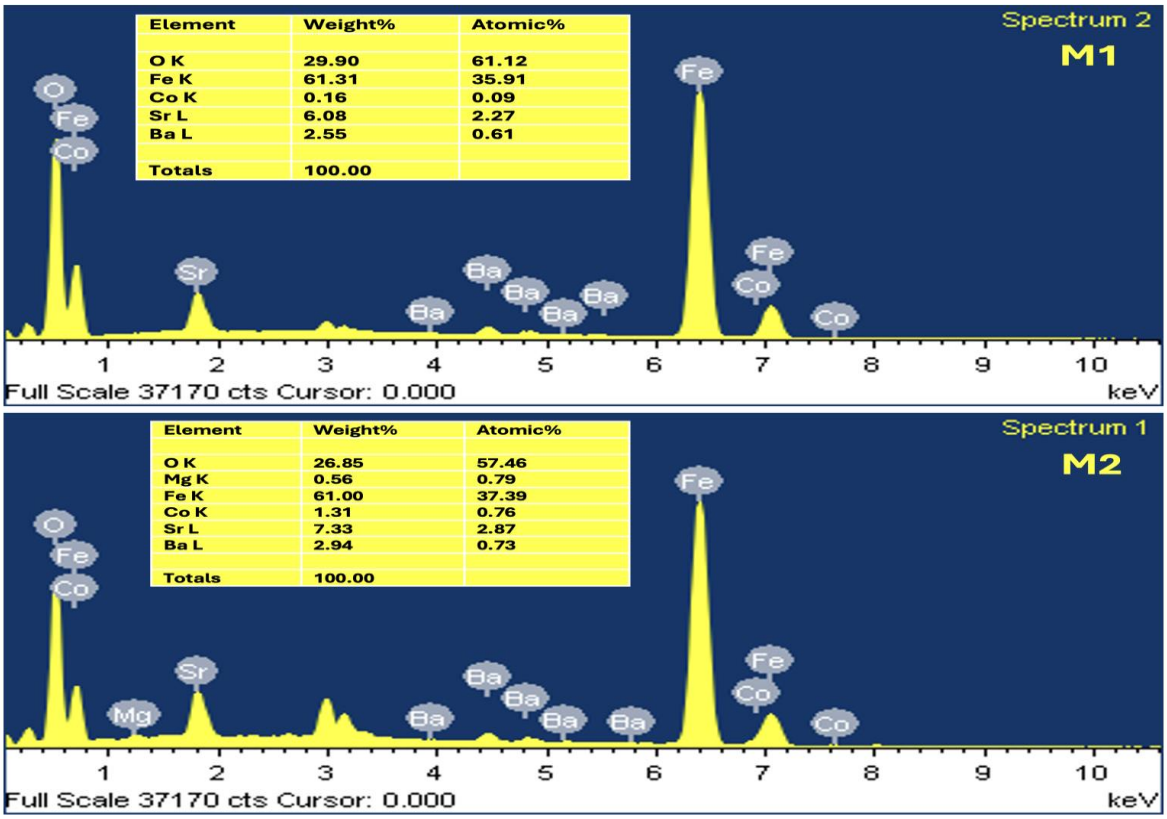

Figure 4.3: EDX Spectra $Ba_{0.2}Sr_{0.8}Co_xMg_xFe_{12-2x}O_{19}$ Hexaferrite for Samples *M1* and *M2*

4.1.2 Electrical Analysis

4.1.2.1 Dielectric permittivity

The relevant mathematical equations for electrical parameters have already been mentioned in the earlier section 3.1.1. There were measurement uncertainties in the low-frequency region, thus the plots are drawn from 100 Hz to 2 MHz (*M1* values are plotted from 10 Hz to 2 MHz due higher set of values in lower frequency).

Figure 4.4 depicts two distinct plots with frequencies ranging from 100 Hz to 2 MHz: (a) dielectric permittivity for samples *M2* to *M6* and (b) dielectric permittivity for samples *M1*. Similarly, Figure 4.5 depicts two distinct plots: (a) dielectric loss for samples *M2* to *M6* and (b) dielectric loss for samples *M1*. As illustrated in Figure 4.4 (a), (b) ε' exhibits dispersion in the low-frequency spectra, but it becomes frequency-independent beyond 10 kHz in all samples. It has been found that the declines non-monotonically with frequency, but it shows no dependency on doping content, the highest being for the undoped sample *M1*, which is around 450 at 200 Hz, and amongst doped, the highest for *M3* is around 80 at 90 Hz.

Maxwell-Wagner's interfacial polarization model is commonly utilized to explain the dielectric properties of hexaferrite, particularly the reduction in dielectric permittivity values as the frequency increases.

The Maxwell-Wagner interfacial polarization model postulates that hexaferrite comprises conducting grains that are isolated from the insulating grain boundaries. While the grain boundaries hinder electrical conduction, they aid in polarization. During the sintering process of pellets, the air present within the furnace oxidizes the grain boundaries to a greater extent than the interior of the grains [159]. As a result, the grain boundaries exhibit greater insulating characteristics compared to the bulk grains. During the conduction process, electrons tend to migrate towards the grain boundaries. However, when high resistance is encountered at the grain boundaries, electrons accumulate at these regions, leading to polarization, which contributes to a large Dielectric permittivity.

Verwey-de-Boer hopping is a phenomenon that explains the electrical conduction mechanism in ferrite materials [160]. Verwey proposed that electron hopping plays a crucial role in the conduction process, specifically between electrons of different ions of the same elements that were formed during the sintering process. The concentration of $Fe^{2+/}Fe^{3+}$ ions present in the ferrite material distinguishes it from other materials, but this concentration depends on various factors such as sintering time, temperature, etc. It is the Fe ions that cause the valence electrons to alternate between the +2 and +3 valence states, leading to most of the polarization. This electron hopping results in the displacement of charges in the direction of the sinusoidal applied electric field.

As previously discussed in Figures 4.4 and 4.5, beyond a certain frequency, the Dielectric permittivity/loss reaches a steady-state value, which inhibits further electron hopping and exchange between the +2 and +3 valence states. The highest dielectric permittivity in sample *M1* is associated with the greatest concentration of ferrous ions on the octahedral sites.

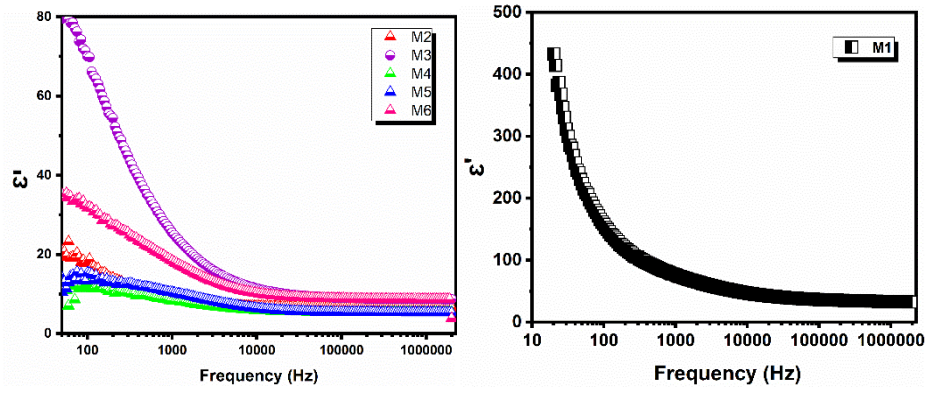

Figure 4.4: Variation of Dielectric Spectra of Real Component Ferrite Sample $Ba_{0.2}Sr_{0.8}Co_xMg_xFe_{12-2x}O_{19}$ (a) *M2, M3, M4, M5* and *M6* (b) *M1* Function of Frequency

The hopping of electrons between octahedral sites is widely recognized as the mechanism that provides ferrites with their conductivity and polarization.

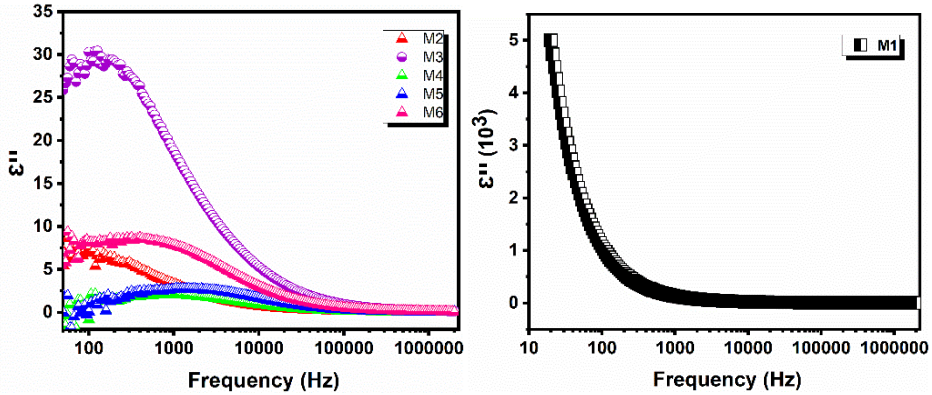

Figure 4.5: Variation of Dielectric Spectra of Imaginary Component of Ferrite Sample $Ba_{0.2}Sr_{0.8}Co_xMg_xFe_{12-2x}O_{19}$ (a) *M2, M3, M4, M5* and *M6* (b) *M1* Function of Frequency

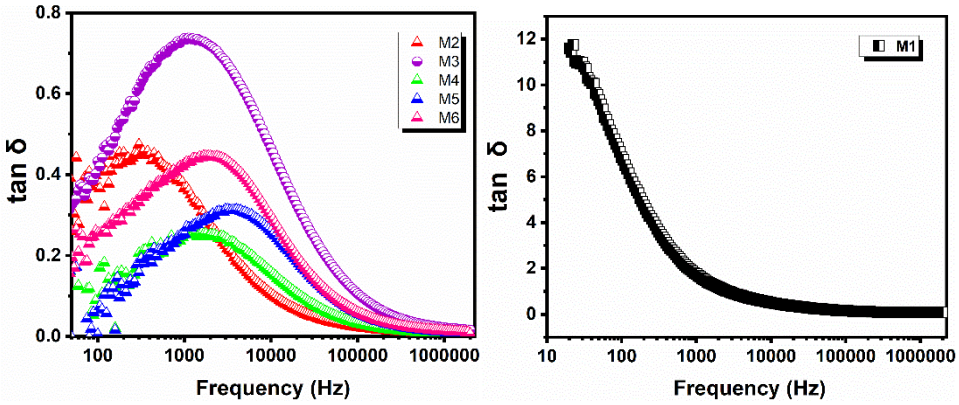

Figure 4.6: Variation of Dielectric loss Tangent of Ferrite Sample: $Ba_{0.2}Sr_{0.8}Co_xMg_xFe_{12-2x}O_{19}$ (a) *M2, M3, M4, M5* and *M6* (b) *M1* Function of Frequency

Now, illustrated in Figure 4.5 (a), (b), ε'' exhibits dispersion in the low-frequency spectra along with a weak peak at the start. However, it becomes frequency-independent beyond 10 kHz in all samples. It has been found that the ε'' declines non-monotonically with frequency.

The highest value of ε'' can be seen for the undoped sample *M1*, which is around 550 at 200 Hz, and amongst the doped highest for *M3* is around 30 at 200 Hz.

Figure 4.6 (a), (b) depicts the variation in $tan\ \delta$. Doping results in peaking behavior in the samples, *M1* doesn't show any peak, whereas the highest peak is observed for the *M3* sample, which is around 0.7 at 2000 Hz. But it could be seen from the figure that the value of loss tangent for all doped samples at higher frequency come together to stay around 0.0-0.1. However, doping peaks are seen to shift toward the mid-frequency region.

The phenomenological theory of dielectrics proposed by Koop is known as Koop's phenomenological model, and it aims to explain the behavior of dielectric materials under the influence of an alternating electric field.

One of the important properties of dielectric materials is dielectric loss, which is characterized by the tangent of the loss angle (*tan δ*). The loss angle is the phase difference between the applied electric field and the resulting polarization of the dielectric material.

According to Koop's model, the dielectric loss in a material is related to the mobility of the charge carriers (e.g., electrons ions) within the material. When an electric field is applied, the charge carriers start to move, and this motion generates an electric current within the material. The current, in turn, produces an opposing electric field that opposes the applied field. This opposing field leads to a phase difference between the applied field and the polarization, which is reflected in the value of the loss angle.

Koop's model explains the drop in the value of *tan δ* by considering the behavior of charge carriers under an electric field. As the frequency of the applied field increases, the mobility of the charge carriers decreases. This reduced mobility leads to a decrease in the magnitude of the current generated within the material, which, in turn, reduces the magnitude of the opposing field. As a result, the phase difference between the applied field and the polarization decreases, leading to a decrease in the value of *tan δ*.

In summary, Koop's phenomenological model explains the drop in the value of *tan δ* with increasing frequency of the applied electric field by considering the behavior of charge carriers within the dielectric material [161].

4.1.2.2 Electric modulus analysis

This study helps to elucidate the relaxation process and minimize the influence of electrode polarization.

M′ and *M″* are the real and imaginary parts of the complex electric modulus and are calculated using equation 3.8 and equation 3.9 respectively (from section 3.3.2).

The graph in Figure 4.7 shows the frequency-dependent behavior of the modulus (*M)* as an expansive, asymmetric peak in the imaginary part of the graph and a sigmoidal shape in the real component of the modulus. [162-163]. In Figure 4.7 (a), the variation of the real component of the modulus (*M′)* is taken vs the logarithmic scale of frequency. It is confined to a low value (tending towards zero) for a lower frequency region for *M1*, then increases to a certain value as the frequency is increased and then saturates in a high-frequency regime. This behavior can be seen in all the doped samples. It is also observed from the graph that the plots tend to saturate at a certain point for all the samples, with the lowest for the pure/undoped *M1* sample at around 0.015 and the maximum for *M4* and *M5* at around 0.19. The applied electric field has an impact on the charge carriers as it is applied. The absence of the restoring force, which regulates the movement of these charge carriers, has an impact on these conclusions. This

pattern shows that conductive grains are necessary for electrical properties. As the Co and Mg content increase, a corresponding increase in M' can be observed from undoped to doped samples, but the trend is nonlinear to the increase in dopant percentage.

The divergence in the plots of the imaginary component of modulus in the frequency domain provides information about several charge transport techniques, including electrical transport, conductivity, relaxation, and ion dynamics, Figure 4.7 (b). It can be seen from the graph of M'' that as the doping content increases, the peaks of each sample can be seen to reach their highest point; a peak of *M5* owes the highest value. Also, a shift of peaks towards the high-frequency region can be observed as the doping percentage is changed.

Ions can successfully hop from one site to another over extended distances in the low-frequency domain. The peaks in M'', however, show that the ions do not follow the longer hopping at higher frequencies but rather are constrained to their finite potential wells. The area where the peaks are found shows a transition from long-range mobility to a shorter one, with an increase in frequency in line with it. The hopping mechanism for electrical conduction is thus represented by the modulus spectrum. Thus, the peak frequency represents the conduction relaxation time, and the movement of the peak frequency Co-Mg dopants towards the high-frequency area denotes a shortening of the relaxation period.

As was previously mentioned, the release of charge pathways as a result of a frequency increase is also a cause of conductivity relaxation. Asymmetric and broad peaks with dopants provide further proof that the samples lack Debye-type relaxation. Figure 4.7 (c) shows the Cole-Cole plot (M' vs. M'') of the sample $Ba_{0.2}Sr_{0.8}Co_xMg_xFe_{12-2x}O_{19.}$ The charts show that the samples contain asymmetric semi-circles. The semicircular arc's intercept increases with doping, which also causes the arc to move toward a low-frequency regime.

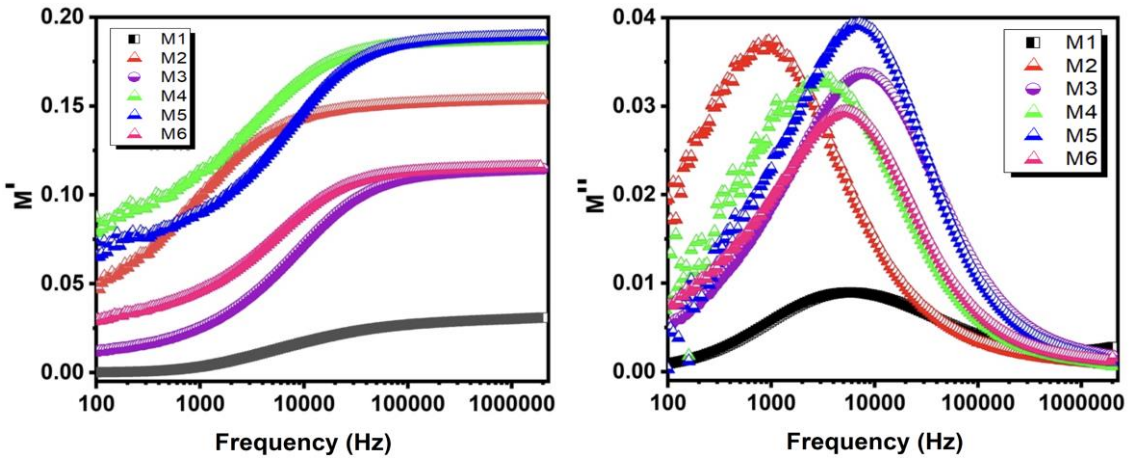

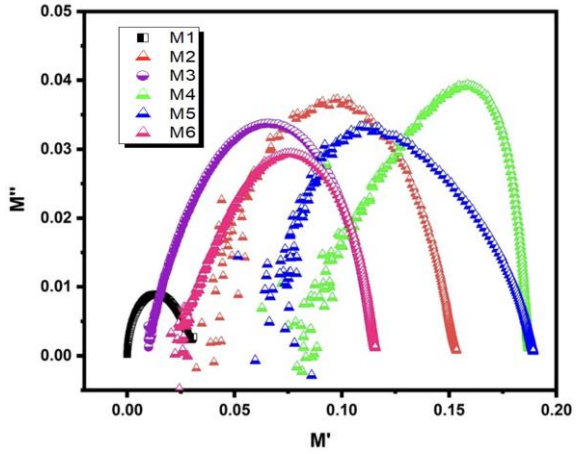

Figure 4.7: Variation of Modulus (a) Real Part, (b) Imaginary Part of Ferrite Sample $Ba_{0.2}Sr_{0.8}Co_xMg_xFe_{12-2x}O_{19}$ (*M1, M2, M3, M4, M5* and *M6*) as a Function of Frequency (c) Cole-Cole Plot (or Nyquist Plot) of Ferrite Sample

In the sample, *M1* grain boundaries play a vital role, whereas in the sample, *M4* grains dominate. However, in samples, *M2, M3, M5, and M6* grains, as well as grain boundaries, are actively participating. The distribution of relaxation time is illustrated by the modification of the semicircle's maxima for the maximum frequency with doping. The non-Debye form of relaxation is supported by this distribution.

4.1.2.3. Complex impedance spectra

An impedance analysis can reveal more about a material's resistance (Z′) and reactance (Z″) and are calculated using equation 3.11 and equation 3.12, respectively (from section 3.3.3).

The behavior of polycrystalline materials in terms of impedance is heavily influenced by bulk grains and grain borders. As the relaxation times for the impedances of bulk grains and grain borders are different, they can be dealt with in different ways.

The complex impedance spectrum is a crucial instrument for assessing the electrical characteristics of the samples. In this study, the resistive (real) and reactive (imaginary) impedance components that oversee the applied AC field's conduction process are explored. Figure 4.8 (a) shows the variation of the real portion of impedance (Z′) concerning frequency.

The variation of Z′ vs. frequency is depicted in Figure 4.8 (a). It has been observed that when frequency increases, *Z′* gradually decreases until it almost achieves a constant value after 10 kHz frequency. The samples' dipole polarisation effects might be to blame for this fall in *Z′* value. With doping, the value for *Z′* is varying, the highest being for *M2* around 0.55 at 110 Hz frequency.

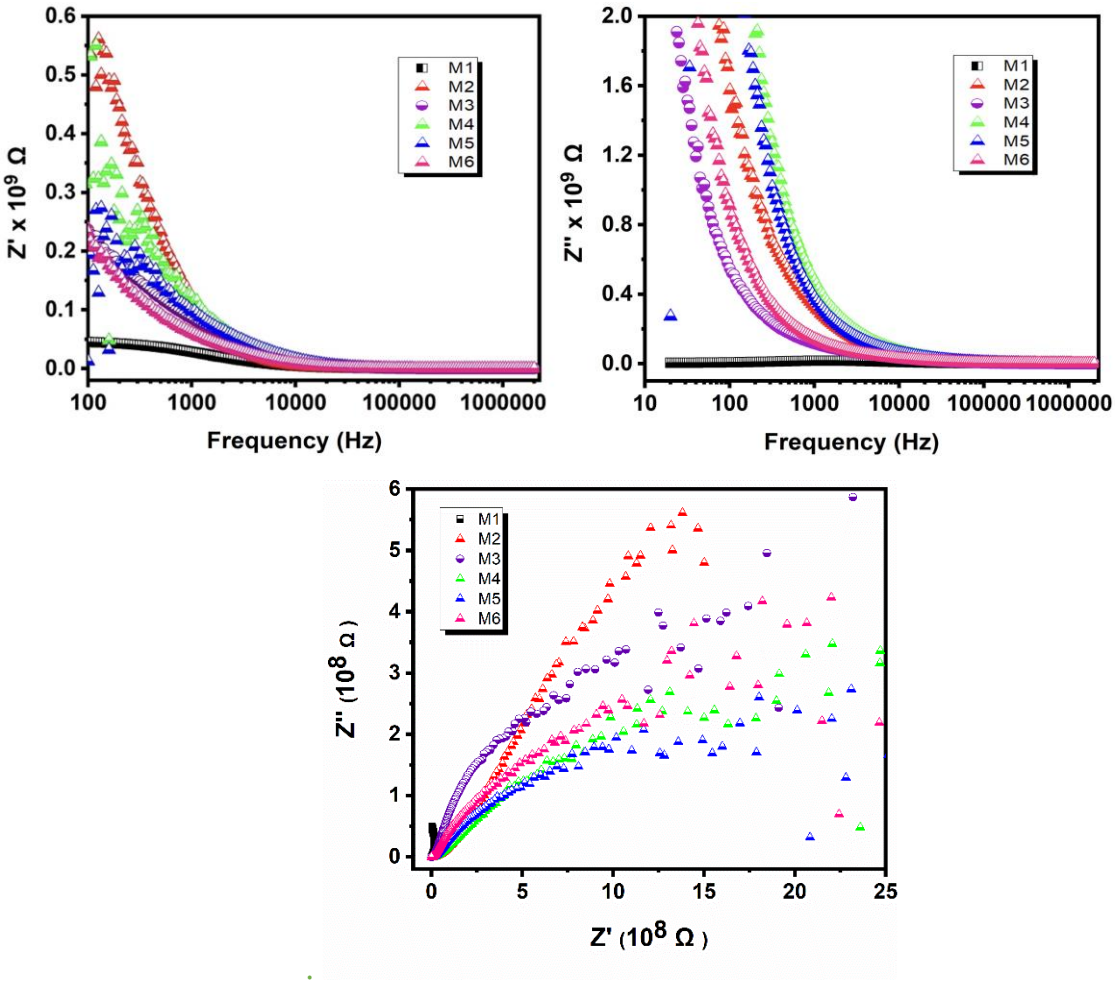

Figure 4.8: Dispersion in the (a) Dielectric Impedance Real (Z′), (b) Dielectric Impedance Imaginary (Z″) (c) Dielectric Impedance Real (Z′) Part Versus Dielectric Impedance Imaginary (Z″) Part of $Ba_{0.2}Sr_{0.8}Co_xMg_xFe_{12-2x}O_{19}$ (*M1, M2, M3, M4, M5* and *M6*) as a Function Frequency

The change in *Z″* with the variation in frequency has been explored to better understand the effect of space charges, as Figure 4.8 (b) illustrates. The imaginary components have been found to fall sharply at a lower frequency regime after 10 kHz, and all values saturate within the same range. For sample *M1*, the value does not vary much with frequency and remains almost constant for the complete test range. However, for all the doped samples, the highest value is around 2.0 within the frequency band of 80 to 1500 Hz.

The curves in Figure 4.8 (c) plot of *Z″* versus *Z′* for each sample have a semi-circular shape with the center of the circle being lower than the x-axis, depicting the non-Debye relaxation process.

For doped compositions, the depression of the arc shows variations from *M1, M2, M3, M4, M5 and M6*. Sample *M1 li*es in the high-frequency region. Hence, grains contributing, *M2* the samples cover the mid-frequency region, stating that grains and grain boundaries are equally

active and contributing. The samples *M3, M4, M5, and M6* lie in the low-frequency region. Hence, grain boundaries seem to be contributing.

4.1.2.4 AC Conductivity

Valence electron hopping between Fe^{2+} and Fe^{3+} at Octahedral sites is the primary cause of the conduction mechanism in ferrites. Increased frequency leads to a rise in the hopping frequencies of charge carriers, which increases conductivity. This frequency-dependent conduction process may be explained by the polaron hopping model, as stated in [124].

According to the polaron hopping concept, the AC conductivity rises with rising frequency within the constrained range of polaron hopping. However, the conductivity tends to diminish for long-range polarisation hopping. According to [125], the conductivity phenomena in the case of band conduction are frequency-independent. Figure 4.9 shows the frequency-dependent AC conductivity curve for ferrite samples. According to the results of the current experiment, the AC conductivity starts to slowly rise once the applied AC field frequency surpasses 1 kHz. It behaves in a nearly frequency-independent manner below 1 kHz, and at this frequency, DC conductivity transforms into AC conductivity.

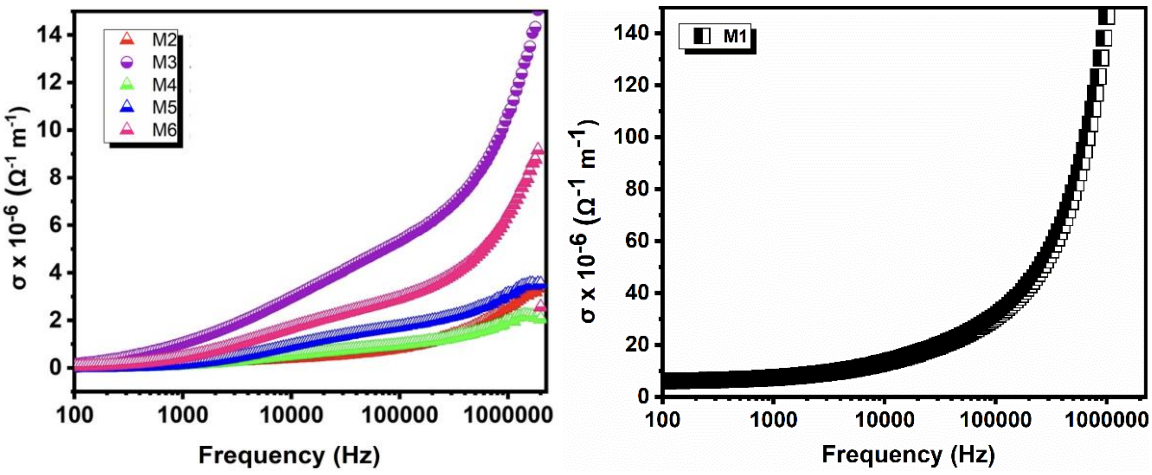

Figure 4.9: Variation of AC Conductivity Concerning Frequency for Ferrite Sample $Ba_{0.2}Sr_{0.8}Co_xMg_xFe_{12-2x}O_{19}$ (*M1, M2, M3, M4, M5* and *M6*)

The frequency-dependent AC conductivity is given in section 3.3.4 known as the Jonscher power law.

The Jonscher power law is useful for characterizing the behavior of dielectric materials over a wide range of frequencies. It is often used in the analysis of experimental data, particularly in studies of materials such as polymers, ceramics, and glasses. The law is named after A.K. Jonscher, who first proposed this relationship to describe the frequency-dependent behavior of the dielectric properties of materials [126].

The Jonscher power law (3.13) includes A, n as constants. Here A and n depend on what composition the sample owes. A has units of conductivity, and n is dimensionless. The second term, $A\omega^n$, quantifies the distribution in AC conductivity charts.

According to Funke [127], the number n has a physical significance: n < 1 suggests a sudden translational motion with hopping, whereas n > 1 denotes localized hopping between nearby places.

The value of n was determined by fitting the plots: *M1*- 0.3070, *M2* - 0.4423, *M3*- 0.5231, *M4*- 0.5071, *M5* - 0.5798, *M6* - 0.5551, suggesting a sudden translational motion with hopping. Because of this, it turns out that n is less than 1, which suggests that charge carriers are hopping in tandem with ac conductivity. The big values of n indicate a rather sudden jump in AC conductivity in the high-frequency range due to the abrupt increase in charge carriers in the aforementioned samples. Grain size affects high-frequency conductivity, as was previously discussed [164-165].

4.1.3 Magnetic analysis

As discussed before, it's a well-known fact that electronegativity determines cation occupancy in crystallographic sites, with more electronegative ions opting for larger octahedral locations compared to tetrahedral positions. Because of its electronegative characteristics, Mg^{2+} (1.31) prefers tetrahedral sites, although Co^{2+} (1.88) can occupy octahedral places. The site occupancy of cations can also be ascertained using the d-configuration and the kind of cations that are involved. While Mg^{2+} ions, with their d^0 configuration, may show no site preference, Co^{2+} ions, with their usual d^7 structure, can occupy octahedral locations, according to ligand field theory. The law of saturation is used to determine the M_s and H_a values of the synthesized samples. The hysteresis loops (room temperature) for all the samples are displayed in Figure 4.10. (M_r/M_s) ratio, saturation magnetization (M_s) anisotropy field (H_a), coercivity (H_c), and remanence magnetization (M_r) are enumerated in Table 4.3 which are calculated using Figure 4.11. that depicts M_s versus 1/ H^2 plots for all hexaferrite samples. Remanence magnetization, which is often large in M-type hexaferrite, implies substantial remanence and determines the continuing retention of magnetization after an applied field is removed. In addition, the inter-grain group development and magnetic hardness of the material are evaluated using the M_r/M_s ratio, whose value should range from 0 to 1. Materials with a significant squareness ratio ($0.5<M_r/M_s<1$) are more anisotropic, single-domain, and hard, while those with ($0.05<M_r/M_s<0.5$) have randomly oriented multi-magnetic domains [166].

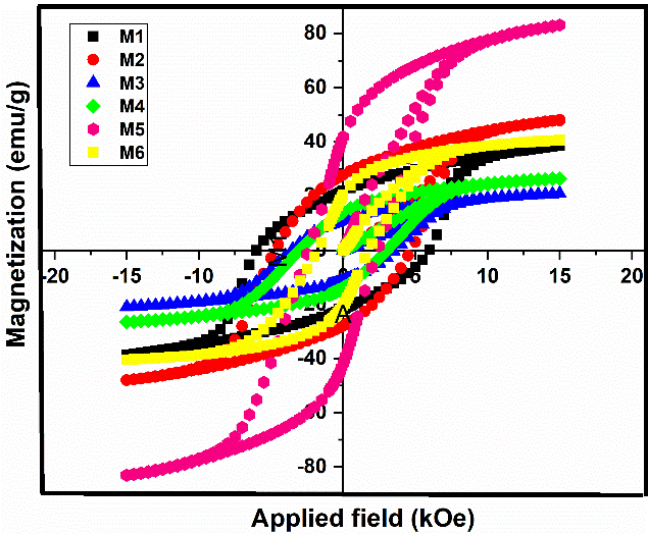

Figure 4.10: Hysteresis Loops of *M1, M2, M3, M4, M5* and *M6* Hexaferrite

In the present study M_r/M_s value for the *M1* and *M2* is larger than 0.5, indicating that the particles of the material are single-domain in nature. Conversely, *M3*, *M4*, *M5*, and *M6* show that the material contains multiple domains with $M_r/M_s<0.5$.

Table 4.3: Magnetic Parameters M_s, H_c H_a, M_r and M_r/M_s for Mg-Co/PANI Doped Hexaferrite Samples

Sample	M_s	H_c	H_a (kOe)	M_r	M_r/M_s
M1	41.77	5882.24	16.55	21.73	0.52
M2	40.25	4524.35	16.78	26.37	0.66
M3	22.17	3567.87	14.52	10.61	0.48
M4	28.09	3064.78	14.30	13.31	0.47
M5	87.58	2514.90	13.47	19.55	0.22
M6	42.16	1509.13	11.32	20.12	0.48

The pure sample *M1*, exhibits the greatest values of coercivity (5882 Oe), which is related to the absence of substituent cations in the crystal lattice. Both intrinsic and extrinsic factors readily explain the behavior of H_c [167]. The distribution of host and substituted cations throughout the five crystallographic sites inside the hexagonal crystal structure can be used to explain the magnetic moment of the synthesized composites, as expressed by the following expression [199],

$$M_S = M_a(2a+12k+2b)(\downarrow)-M_b\ 4f_1+4f_2\ (\downarrow) \qquad (4.1.1)$$

When non-magnetic ions or ions with weaker magnetic characteristics are substituted in the (4f1 ↓ + 4f2 ↓) lattice site, the overall magnetization increases. On the other hand, magnetism tends to decrease when these ions are replaced at (2a ↑ + 12k ↑ + 2b ↑) lattice sites.

It can be seen from the table that the low values of M_s are observed for *M3* (22.17 emu/g) and *M4* (28.09 emu/g) while the considerably high value of 87.58 emu/g is observed for *M5*. These low values of M_s can be attributed to site occupancy of more number of Co-Mg ions on a-site (spin-up sites) which reduces M_a more than M_b, thereby, the value (M_a-M_b) decreases, and hence M_s decreases. Similarly, Large M_s in *M5* is plausibly related to the occupancy of dopants Co-Mg on spin-down sites. However, further investigation is required to gain exact insights into the behavior.

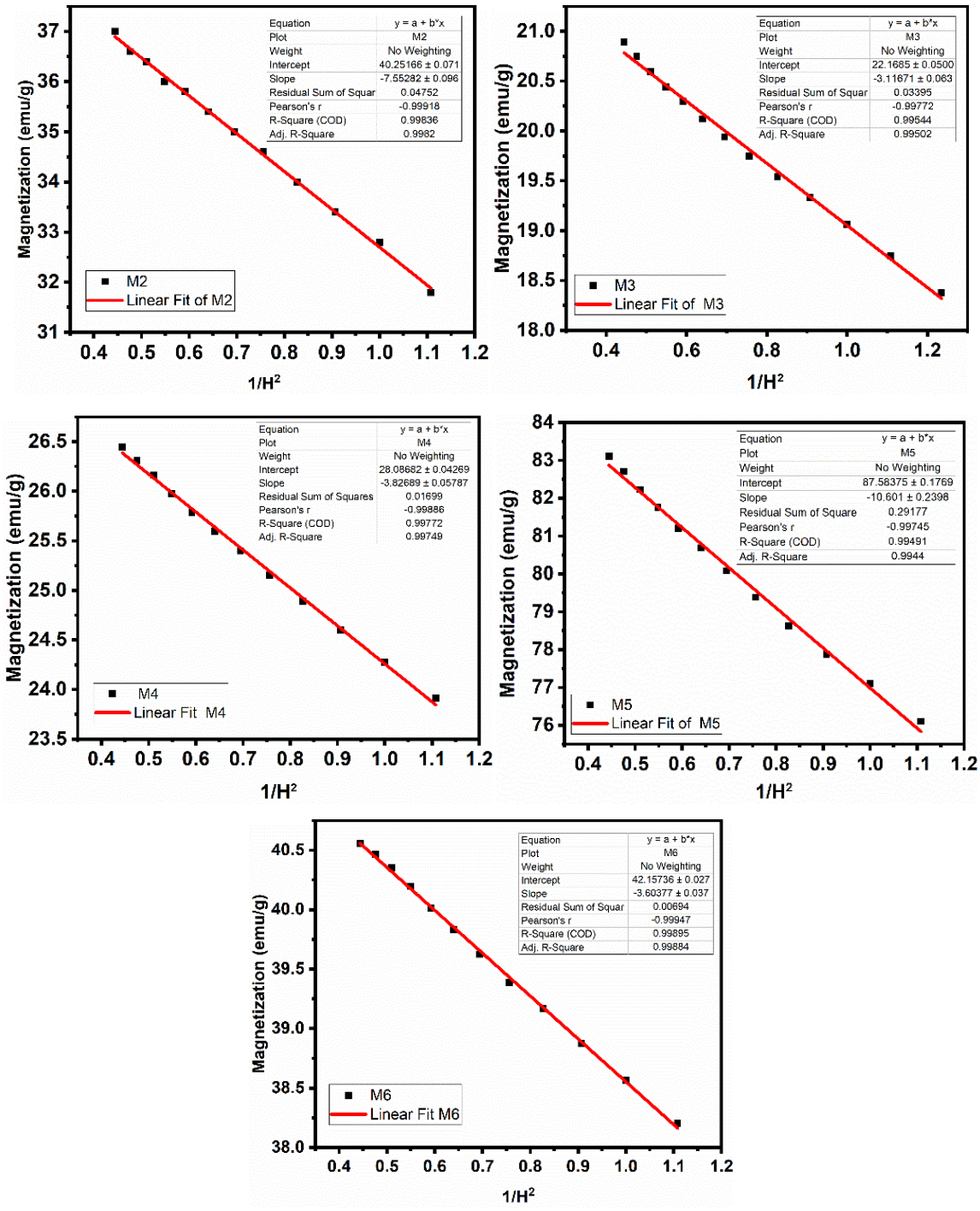

Figure 4.11: M_s Versus 1/ H² Plots for all Hexaferrite Samples

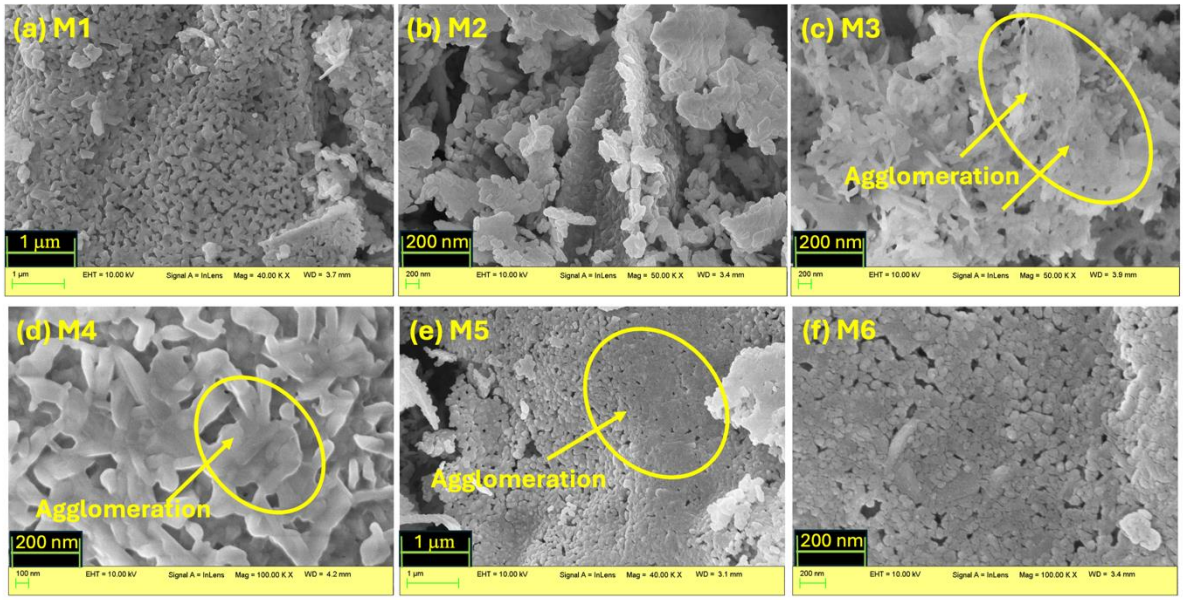

Figure 4.12: SEM Micrographs of Ferrite Samples: $Ba_{0.2}Sr_{0.8}Co_xMg_xFe_{12-2x}O_{19}$ (*M1, M2, M3, M4, M5* and *M6*) and its Correlation with Magnetic Data

As seen from the micrographs (Figure 4.12) the porosity is seen drastically decreasing from sample *M2* to *M6*, which can be one of the reasons that H_c is being lowered down from 4524 Oe to 1509 Oe. Also along with lowered porosity, as the doping is increased good agglomeration is seen in samples *M3, M4*, and *M5*, again contributing to reduced H_c. The table it can observe that M_s values are lower for the *M3* and *M4* samples, though porosity is reduced, with good agglomeration and connectivity, one of the reasons might be the site occupancy of the dopants as discussed earlier.

4.1.4 Electromagnetic Characteristics

4.1.4.1 Complex Permeability and Complex Permittivity

Figure 4.13 shows graphs of the dielectric permittivity(ε′) and dielectric loss (ε″) as functions of frequency. Both the dielectric permittivity and loss exhibit a nonmonotonic increase with the doping of Co^{2+} and Mg^{2+} ions. Initially for ε′, the value seems to increase from *M1* to *M2*, then drastically decrease from *M2* to *M3*, then increase from *M3* to *M5*, and then drop a little for *M6*. For all the samples, there seems a decrease in the value of the dielectric permittivity with increasing frequency. Especially noticing a dip in each sample at around 10 GHz frequency, exhibiting a relaxation process. However, sample *M1* does not go with this trend. It has a relaxation peak at around 8.9 GHz followed by a weak dip at around 9.7 GHz and a minor relaxation peak at around 11.6 GHz. It is visible that wherever the sample *M1* possesses relaxation peaks it has resonance peaks in the corresponding ε″ graph. It can be also seen that values for ε′ are decreasing, the lowest being for samples *M3*, and the highest being for *M5*.

The highest value of 7.1 at around 8.56 GHz frequency, is observed for M5 in ε′ plot. Sample M6 just shows minor changes in values following the same pattern. The behavior of *M1* is altogether different from other samples in ε″ trend. There is a major relaxation peak in *ε″* at around 10.2 GHz for all the samples besides *M1*, these samples also possess weak relaxation peaks at around 10.88 GHz and 11.6 GHz in *ε″* graph.

Figure 4.13 also represents plots of permeability (μ′)/magnetic loss (μ″) in the frequency spectrum with Co^{2+} and Mg^{2+} ions. There is an upward trend observed in all the samples as the frequency goes on increasing for μ′. The lowest value is observed as 0.4 for *M2* at 8.2 GHz, *M5* at 8.46 GHz and the highest is 1.9 at 12.4 GHz for M2 composition. Only Pure sample M1 depicts three deeps around 9 GHz, 9.8 GHz, and 11.2 GHz in μ′ plot and possesses resonance peaks in the corresponding μ″ plot. All the samples besides *M1*, stay in the same range of values throughout the test frequency, which seems to increase with frequency. For μ″, samples *M2*, and *M3* stay in the same range even if the frequency is increasing, *M5* possesses a relaxation peak at the very start of frequency but then stays in the range of 0.2 to 0.3 even if the frequency is increased.

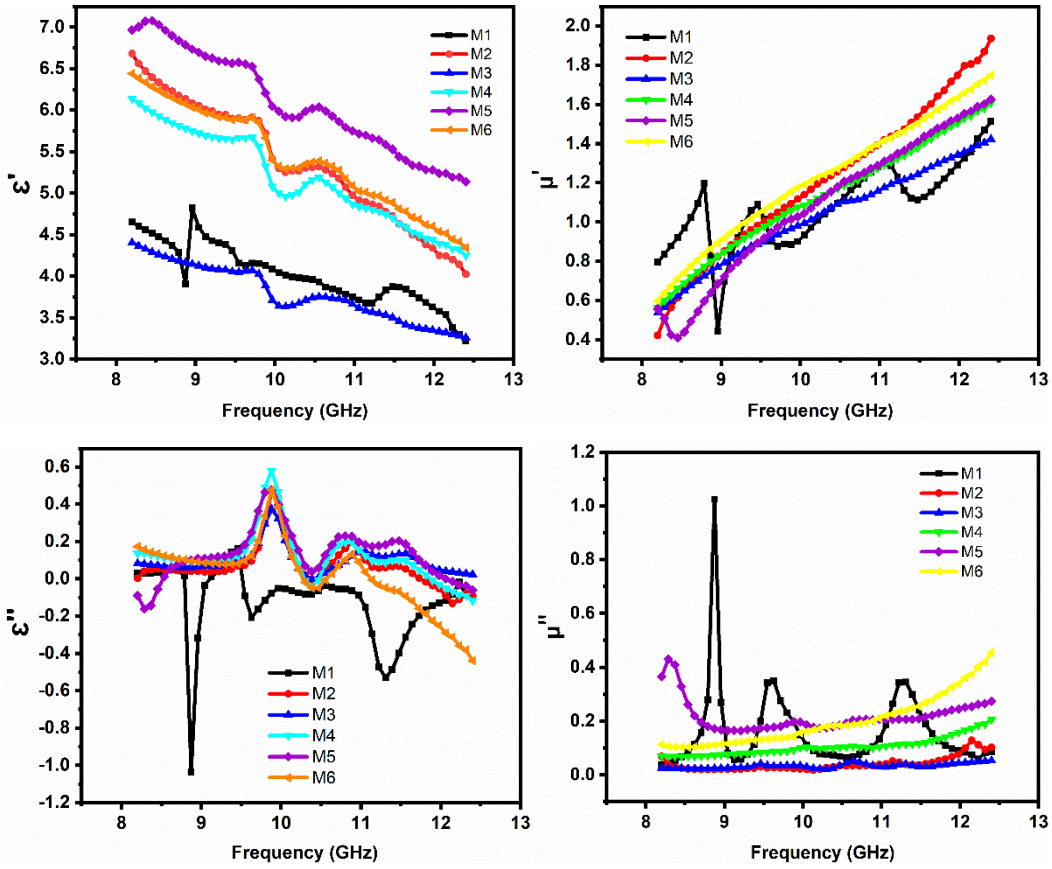

Figure 4.13: Dependence of ε′, ε″, μ′, μ″ on Frequency in Ferrite Compositions *M1, M2, M3, M4, M5* and *M6*

In the microwave regime, the complex permittivity and permeability are influenced by several factors, including porosity, electron spin, grain size distribution charge accumulation at grain boundaries, and dipole polarization [168]. Dielectric polarisation in ferrites is caused by electron hopping in Fe^{2+}/Fe^{3+} [169]. The porosity provides a barrier to the field flow and deters polarisation. Exchange resonance between Fe^{2+}/Fe^{3+} ions and ferromagnetic resonance controls the mechanism of complex permeability [170-171].

4.1.4.2 Microwave absorption in $Ba_{0.2}Sr_{0.8}Co_xMg_xFe_{12-2x}O_{19}$

Examining a material's reflection loss is one method of determining its microwave absorption capability. Equations 3.16 and 3.17 are used to determine the RL of the compositions. This section will examine how different factors affect the material's microwave-absorbing capacity. These variables include the degree of reflection loss, impedance matching, and material thickness ($\lambda/4$).

4.1.4.3 Quarter Wavelength Mechanism

The graphs of RL dependent on the frequency at different simulated thicknesses can be utilized to investigate the phenomenon of microwave absorption. Figures 4.14 (a), (b) to 4.22 (a), (b) show RL plots of the ferrite compositions $Ba_{0.2}Sr_{0.8}Co_xMg_xFe_{12-2x}O_{19}$ for RL $\geq$ -10 dB. The parameters such as matching frequency/thickness, bandwidth, and frequency range can be inferred from Figures 4.14 (a), (b) to 4.22 (a), (b) which is summarised in Table 4.4.

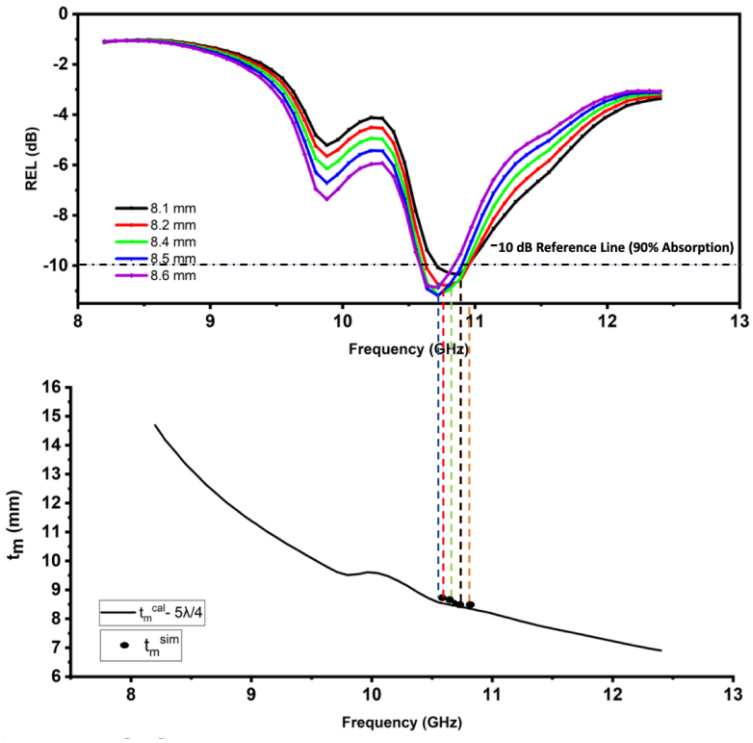

Figure 4.14: (a) Dependence of RL on Frequency in *M4* Composition and (b) t^{sim} and t^{cal} Versus Frequency for 5λ/4 in M4 Composition

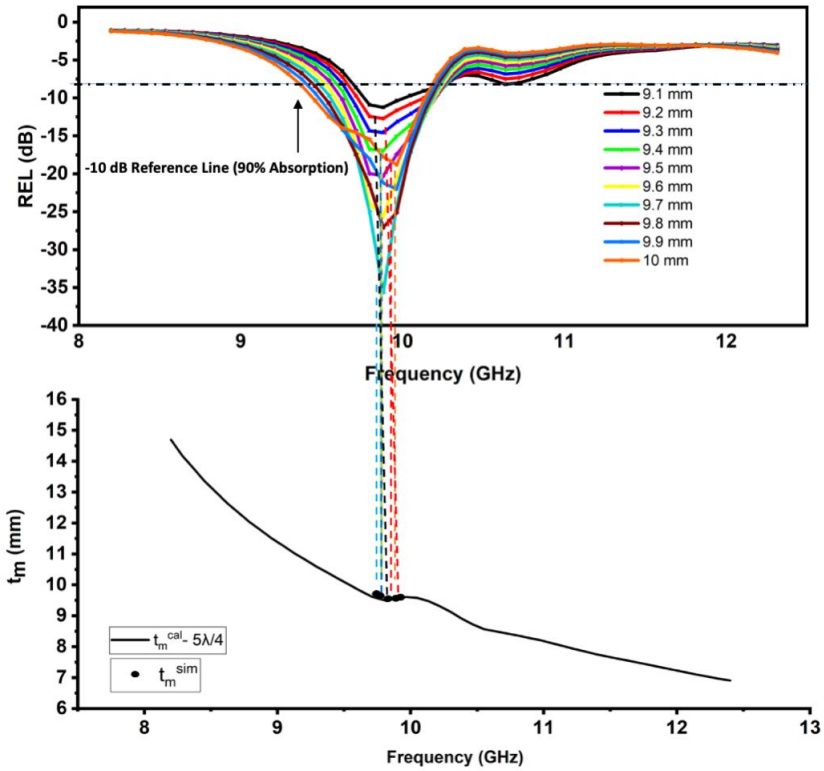

Figure 4.15: (a) Dependence of RL on Frequency in *M4* Composition and (b) t^{sim} and t^{cal} Versus Frequency for 5λ/4 in *M4* Composition

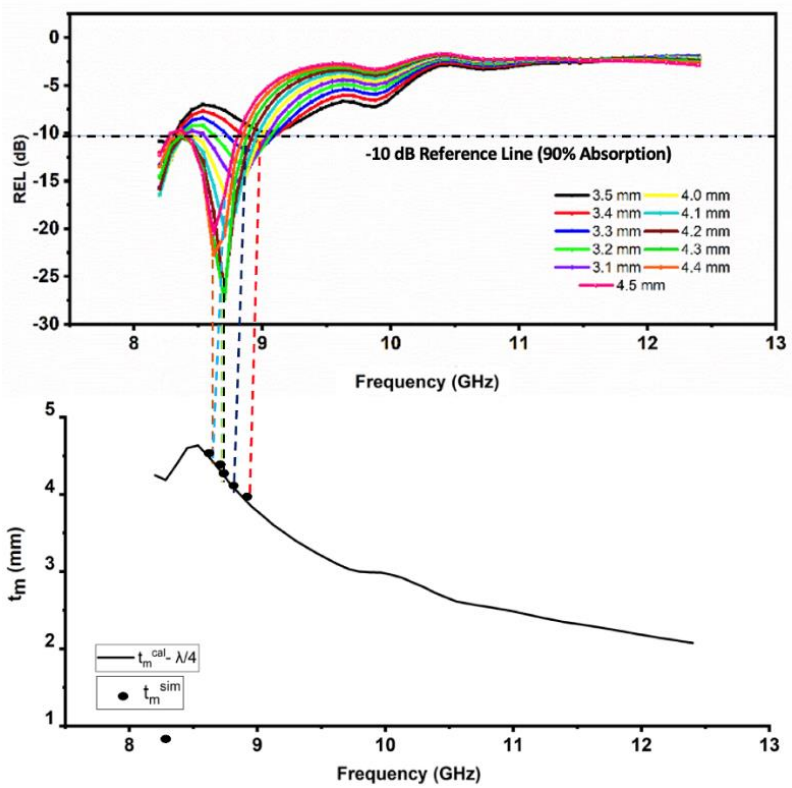

Figure 4.16: (a) Dependence of RL on Frequency in *M5* Composition and (b) t^{sim} and t^{cal} Versus Frequency for λ/4 in *M5* Composition

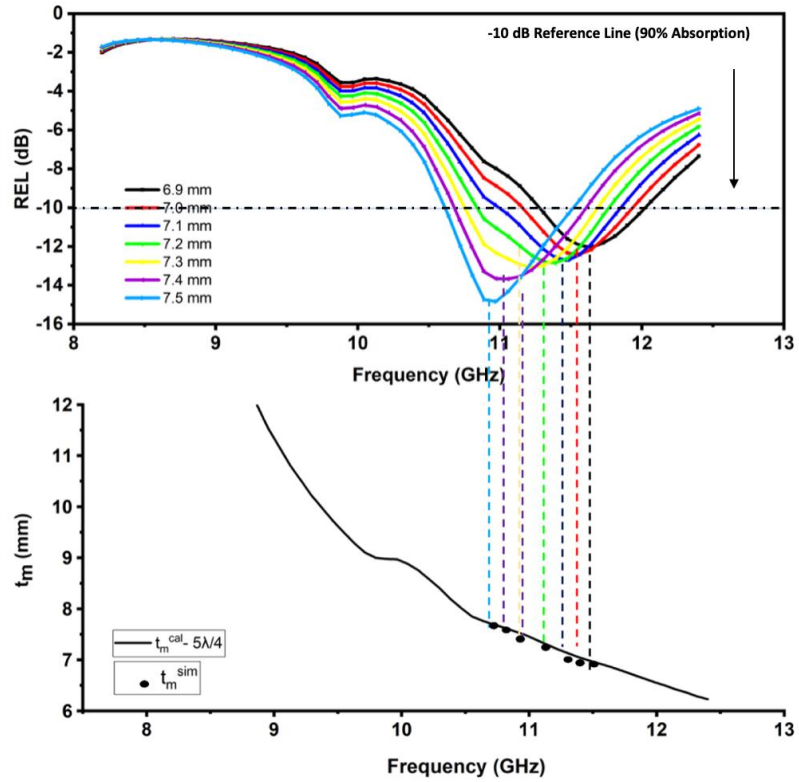

Figure 4.17: (a) Dependence of RL on Frequency in *M5* Composition and (b) t^{sim} and t^{cal} Versus Frequency for 5λ/4 in *M5* Composition

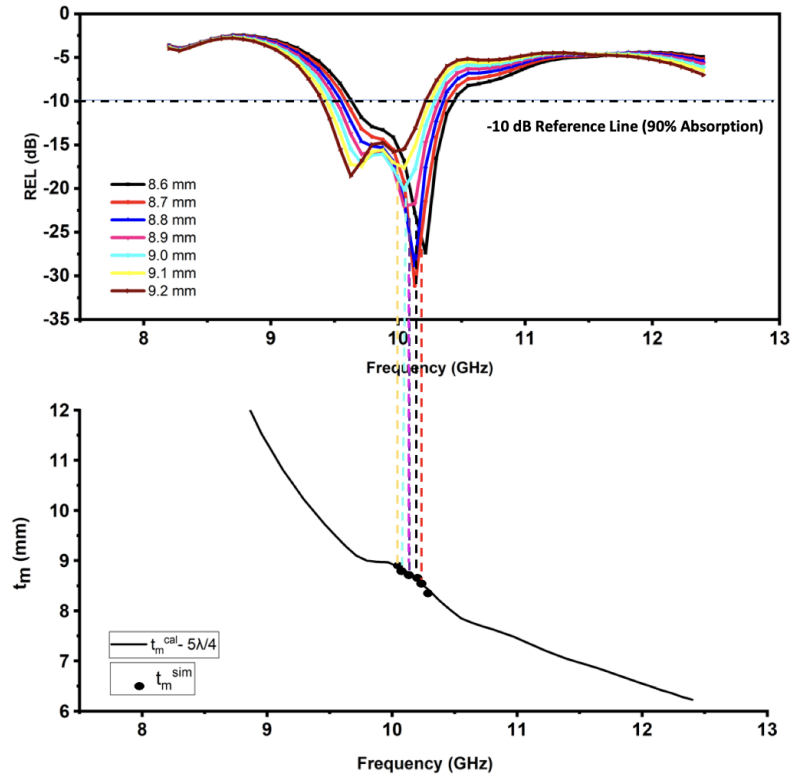

Figure 4.18: (a) Dependence of RL on Frequency in *M5* Composition and (b) t^{sim} and t^{cal} Versus Frequency for 5λ/4 in *M5* Composition

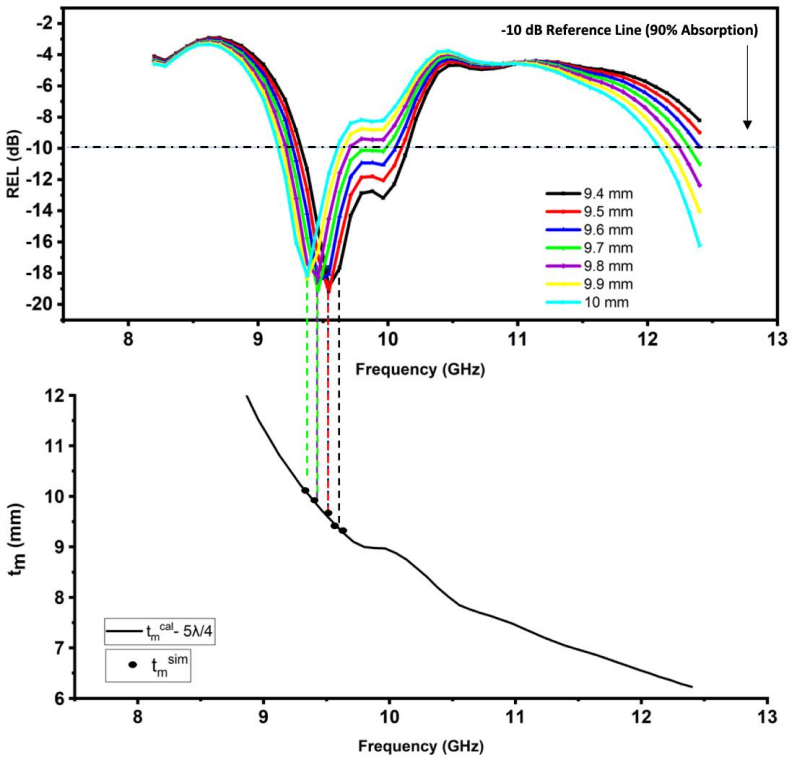

Figure 4.19: (a) Dependence of RL on Frequency in *M5* Composition and (b) t^{sim} and t^{cal} Versus Frequency for 5λ/4 in *M5* Composition

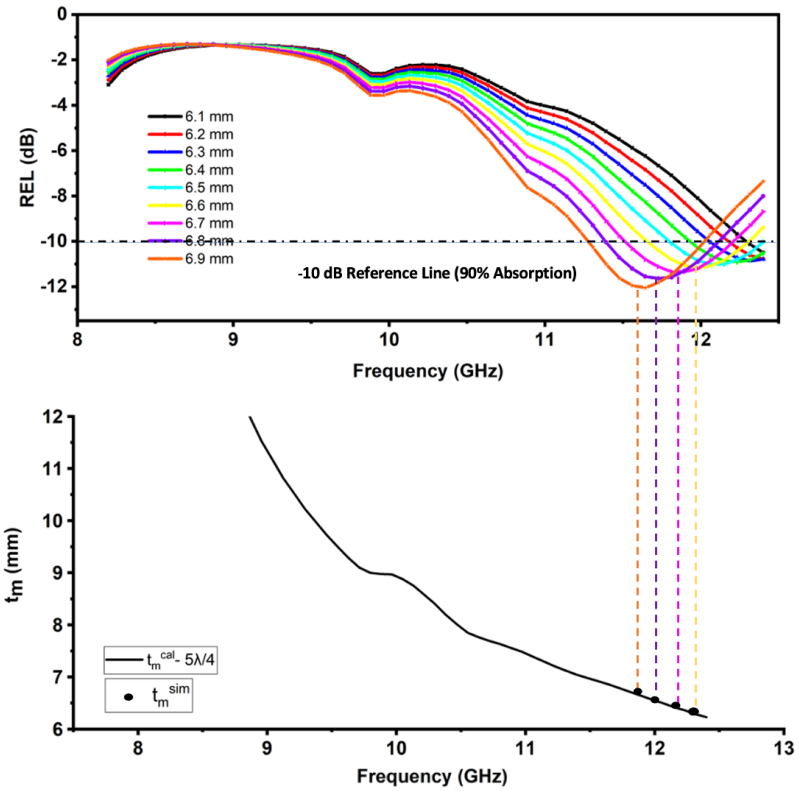

Figure 4.20: (a) Dependence of RL on Frequency in *M6* Composition and (b) t^{sim} and t^{cal} Versus Frequency for 5λ/4 in *M6* Composition

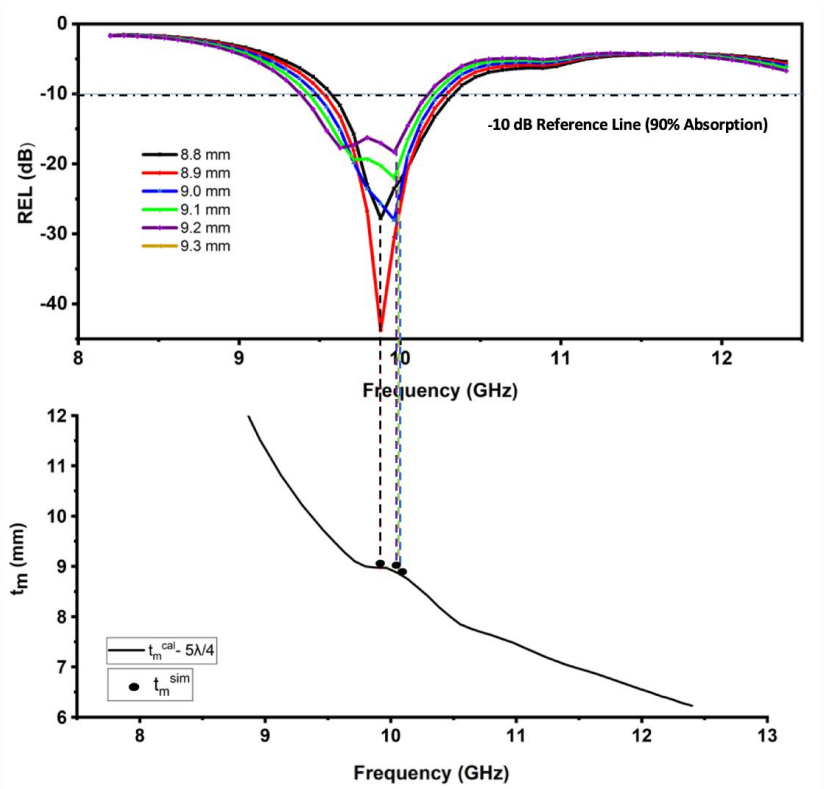

Figure 4.21: (a) Dependence of RL on Frequency in *M6* Composition and (b) t^{sim} and t^{cal} Versus Frequency for 5λ/4 in *M6* Composition

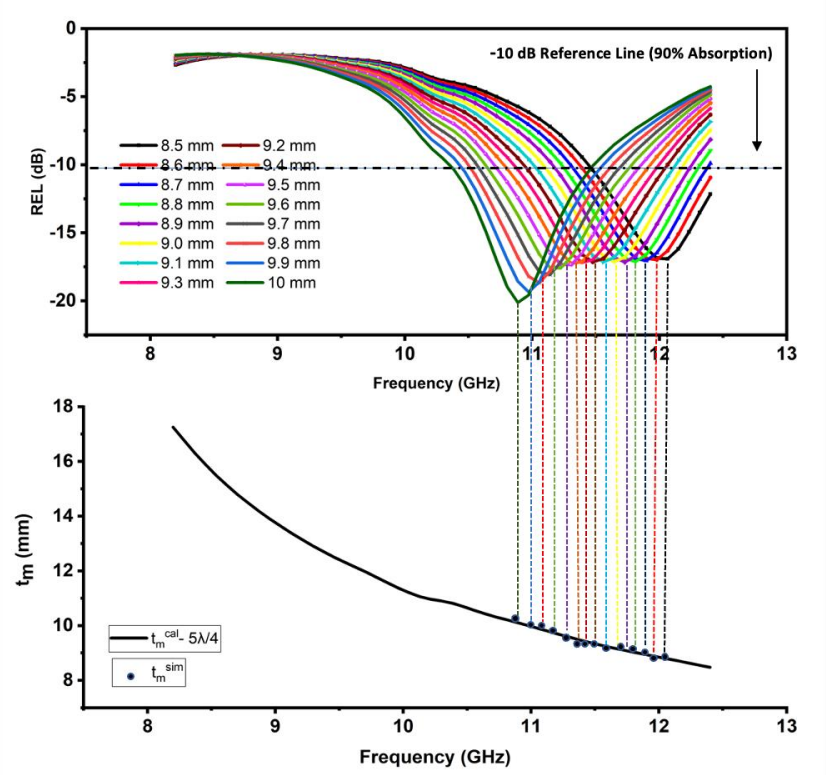

Figure 4.22: (a) Dependence of RL on Frequency in *M6* Composition and (b) t^{sim} and t^{cal} Versus Frequency for 5λ/4 in *M6* Composition

The highest RL dip of - 43.74 dB is observed in *M6* composition at 9.88 GHz frequency and 8.9 mm thickness. According to Table 4.4, the remaining compositions have RL values between -18.77 to -35.97 dB, 9.4 to 9.9 mm thickness (*M4)*, and -14.52 to -31.13 dB, 3.8 to 4.4 mm, 6.9 to 9.3 mm thickness (*M5*). All the plots (except Figure 4.21) illustrate how RL peaks shift toward the low-frequency spectra as thickness increases. This aligns with the quarter wavelength mechanism equation 3.16 in section 3.6 which states that the relationship between frequency and thickness is inversely proportional.

The RL peaks are observed in *M4* [Figure 4.14 (a), (b), Figure 4.15 (a), (b)], in the frequency band ranging from 10.63 to 10.97 GHz and 9.46 to 10.16 GHz at thicknesses from 8.1 to 8.6 mm and 9.1 to 10.0 mm, respectively. The RL peaks are shown for *M5* in [Figure 4.16 (a), (b) to Figure 4.19 (a), (b)], at thicknesses of 3.5 to 4.5 mm, 6.9 to 7.5 mm, 8.6 to 9.2 mm, and 9.4 to 10.0 mm in the frequency range of 8.2 to 8.97 GHz, 10.46 to 11.98 GHz, 9.26 to 10.88 GHz and 9.26 to 10.12 GHz respectively. The RL peaks are observed in *M6* [Figure 4.20 (a), (b), Figure 4.22 (a), (b)], in the frequency band ranging from 11.22 to 12.20 GHz, 10.63 to 11.96 GHz, 9.46 to 10.30 GHz and 9.12 to 10.26 GHz at thicknesses from 6.1 to 6.9 mm, 7.0 to 7.5 mm, 8.8 to 9.3 mm and 9.3 to 9.9 mm, respectively.

Equation 3.18 states that the simulated thickness (t_m^{sim}) is employed to compute RL, and n = 1, 3, 5, …., etc. is used to obtain the calculated thickness (t_m^{cal}) . To determine the link between RL peaks and the quarter wavelength mechanism, both parameters are investigated. Plots of the calculated thickness ($n\lambda/4$) in the frequency regime are displayed in Figures 4.14 (a), (b) to 4.22 (a), (b). By stretching a vertical line from RL peaks towards thickness–frequency graphs, the computed thickness ($n\lambda/4$) and the simulated thickness (t_m^{sim}) are compared. It follows from the plots that the $\lambda/4$ mechanism is satisfied in compositions with calculated thicknesses of $5\lambda/4$ and n = 5, for *M4* and *M6*, whereas *M5* composition is due to both $\lambda/4$ and $5\lambda/4$ values. For various matching thicknesses, *M4* composition has RL ≥-10 dB along with a frequency regime of 9.46 to 10.16 GHz. In this composition, the highest RL is observed at -35.97 dB at a thickness of 9.6 mm. In Table 4.4, a -10 dB broad bandwidth of 0.67 GHz for composition *M4*, 1.10 GHz for *M5*, and 0.98 GHz for *M6* is reported.

Here, in *M4* composition from 9.54 to 10.16 GHz and 9.46 to 10.13 GHz, respectively, -10 dB absorption bandwidths (AB) of 0.62 GHz and 0.67 GHz have been identified, matched by corresponding thicknesses of 9.8 mm and 9.9 mm. In *M5*, it can be noted that -10 dB absorption bandwidth (AB) of 1.10 GHz and 1.09 GHz are observed from 10.71 to11.81 GHz and 10.63 to 11.72 GHz with matching thicknesses of 7.1 and 7.2 mm respectively. *M6* owes -10 dB wide AB of 0.98 GHz from 10.46 to 11.44 GHz at 7.8 mm. Figure 4.23 depicts three-dimensional

(3D) plots of reflection loss at various frequencies and thicknesses for *M4, M5, and M6* samples. As can be seen in sample M4, the blue-violet area depicts RL peaks covering a thickness of around 9.6 mm and a frequency region of 9.6 to 9.8 GHz. Similarly, for samples *M5* and *M6*, the blue-violet shaded area with RL peaks and its corresponding thickness and frequency range can be cross-verified from Table 4.4.

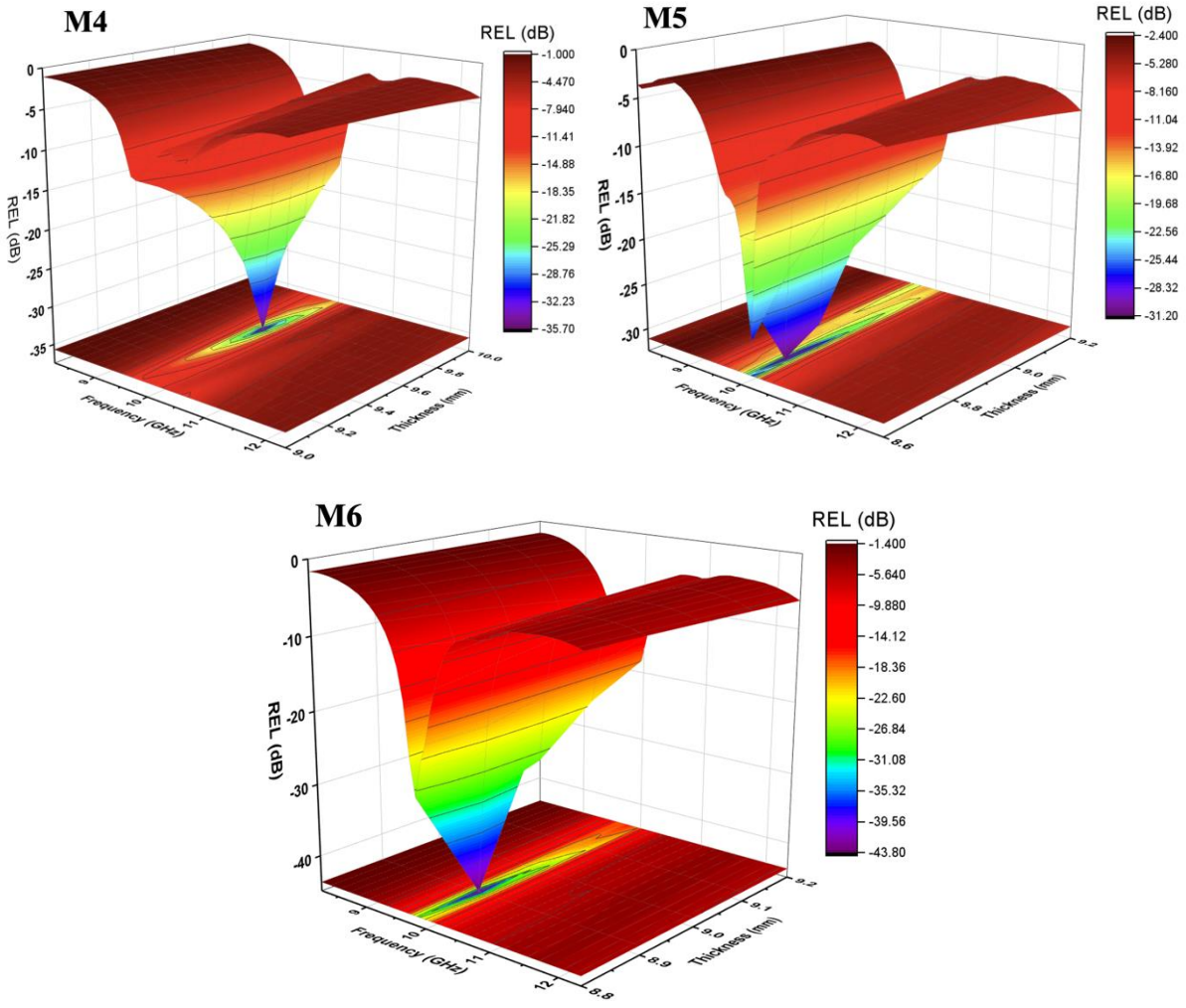

Figure 4.23: Three-dimensional (3D) Plots of Reflection loss at Various Frequencies and thicknesses for *M4, M5* and *M6* Samples

Table 4.4: Computed Parameters for Microwave Absorption (RL > -10 dB)

Co-Mg Content	Matching Thickness (mm)	Matching Frequency (GHz)	Maximum RL (dB)	Frequency band for RL >-10 dB (GHz)	Bandwidth for RL >-10 dB (GHz)	BWT	PBW
M4	9.4	9.88	-20.28	9.60-10.16	0.56	0.06	5.67
	9.5	9.88	-25.67	9.60-10.16	0.56	0.06	5.67

	9.6	9.80	-35.97	9.60-10.16	0.56	0.06	5.72
	9.7	9.88	-27.07	9.60-10.16	0.56	0.06	5.67
	9.8	9.96	-22.01	9.54-10.16	0.62	0.06	6.22
	9.9	9.96	-18.78	9.46-10.13	0.67	0.07	6.72
M5	3.8	8.20	-14.52	8.62-8.95	0.33	0.09	4.02
	3.9	8.20	-15.67	8.53-9.04	0.51	0.13	6.22
	4.0	8.79	-17.30	8.20-8.87	0.67	0.17	7.62
	4.1	8.70	-20.09	8.20-8.95	0.75	0.18	8.62
	4.2	8.70	-26.56	8.20-8.87	0.67	0.16	7.70
	4.3	8.70	-27.41	8.20-8.87	0.67	0.16	7.70
	4.4	8.62	-21.26	8.45-8.78	0.33	0.08	3.83
	6.9	11.56	-18.38	10.97-11.98	1.01	0.15	8.74
	7.0	11.39	-19.56	10.97-11.98	1.01	0.14	8.87
	7.1	11.31	-20.06	10.71-11.81	1.10	0.15	9.73
	7.2	11.22	-20.63	10.63-11.72	1.09	0.15	9.71
	7.3	11.06	-21.41	10.55-11.64	1.09	0.15	9.86
	7.4	10.89	-21.09	10.46-11.56	1.10	0.15	10.10
	7.5	10.89	-21.09	10.46-11.56	1.10	0.15	10.10
	7.7	10.64	-28.39	10.38-11.22	0.84	0.11	7.90
	8.1	10.38	-19.18	10.13-10.88	0.75	0.09	7.22
	8.6	10.22	-27.36	9.71-10.38	0.67	0.08	6.56
	8.7	10.13	-31.14	9.56-10.30	0.74	0.09	7.30
	8.8	10.13	-28.83	9.26-10.30	1.04	0.12	10.26
	8.9	10.05	-22.03	9.26-10.30	1.04	0.12	10.35
	9.0	10.05	-20.08	9.54-10.30	0.76	0.08	7.56
	9.1	10.05	-17.63	9.46-10.21	0.75	0.08	7.46
	9.2	9.63	-18.56	9.46-10.30	0.84	0.09	8.72
	9.3	9.63	-18.74	9.46-10.30	0.84	0.09	8.72
M6	7.0	11.64	-12.16	10.63-11.47	0.84	0.12	7.21
	7.5	10.97	-14.83	10.63-11.47	0.84	0.11	7.66
	7.8	10.89	-15.57	10.46-11.44	0.98	0.13	9.00
	8.0	10.64	-13.89	10.30-11.14	0.84	0.11	7.90
	8.3	10.30	-13.14	9.79-10.72	0.93	0.11	9.03
	8.6	9.88	-17.43	-	-	-	-

8.7	9.88	-21.14	9.62-10.3	0.68	0.08	6.88
8.8	9.88	-27.80	9.62-10.3	0.68	0.08	6.88
8.9	9.88	-43.75	9.54-10.26	0.72	0.08	7.29
9.0	9.96	-28.04	9.54-10.26	0.72	0.08	7.23
9.1	9.96	-22.00	9.46-10.13	0.67	0.07	6.72
9.2	9.96	-18.30	9.46-10.13	0.67	0.07	6.72

4.1.4.4 Impedance matching mechanism

The characteristic impedance of free space is $Z_o = (\mu/\varepsilon)^{1/2} = 377\ \Omega$, where μ/ε are permeability/ permittivity of free space and the impedance of the absorber is Z_{in}. Because of the disparity in their permittivity/permeability values, the absorber impedance differs from free space. Depending on the impedance inequality between Z_{in} and Z_o, when a microwave signal traveling through free space interacts with an absorber, some of the signal will be reflected from the absorber; the greater the difference, the more the reflection. The bulk of the reflected signal is left behind whereas just a small amount of the microwave signal enters the absorber due to the significant disparity between Z_{in} and Z_o. Because most of the signal is reflected, attenuation or absorption of the signal inside the absorber is minimal or meaningless, even if the absorber has maximal dielectric and magnetic loss. Thus, when designing the absorber, it is important to take the impedance matching of the absorber with free space into account [172-173].

The RL and impedance graphs (i.e., Z_{in}) with frequency regime for all compositions are displayed individually in Figures 4.24 and 4.25. In different compositions, impedance-matching conditions may arise in the form of RL peaks with $Z_{in} \sim Z_o$ (377) at specific frequencies that correspond to different matching thicknesses. Z_{in} values for compositions are listed in Table 4.5 and are derived from Z_{in} plots in the aforementioned figures.

The values of Z_{in} (Table 4.5) stay from 387 to 418 Ω for *M4*, 299 to 362 Ω, and 398 to 460 Ω for M5, which drifts away from the characteristic impedance value Z_o = 377 Ω. There is a problem with *M6,* for 8.8 mm thickness at 9.88 GHz frequency, RL = -27.797 dB, Z_{in} = 375.641 Ω, in proximity to Z_o = 377 Ω. Conversely, at 9.88 GHz, 8.9 mm thickness, a rather significant RL = -43.745 dB is recorded with Z_{in} = 374.90 (Figure 4.23 and Table 4.5, which is in proximity to Z_o = 377 Ω. Rather, in *M4,* there is an RL peak found at 9.88 GHz of -27.071 dB for 9.7 mm thickness, but Z_{in} = 383.29 Ω, which is far away from 377 Ω. Similarly, for *M5*, the RL peak is found at 10.13 GHz of -31.13 dB for 8.7 mm thickness, but Z_{in} = 362.15 Ω which is again away from 377 Ω.

It is explained by the fact that $|Z_{in}|$ (in equation 3.17) is a complex expression that uses both real and imaginary terms, such as Z_{real} and Z_{img}. As a result, Z_{real} and Z_{img} are computed using (equation 3.17), and the resulting graphs are displayed in the frequency and thickness domains for *M4*, *M5*, and *M6* composition (Figure 4.25). Likewise, Z_{real} and Z_{img} values for RL_{max} are calculated from plots and displayed in Table 4.5.

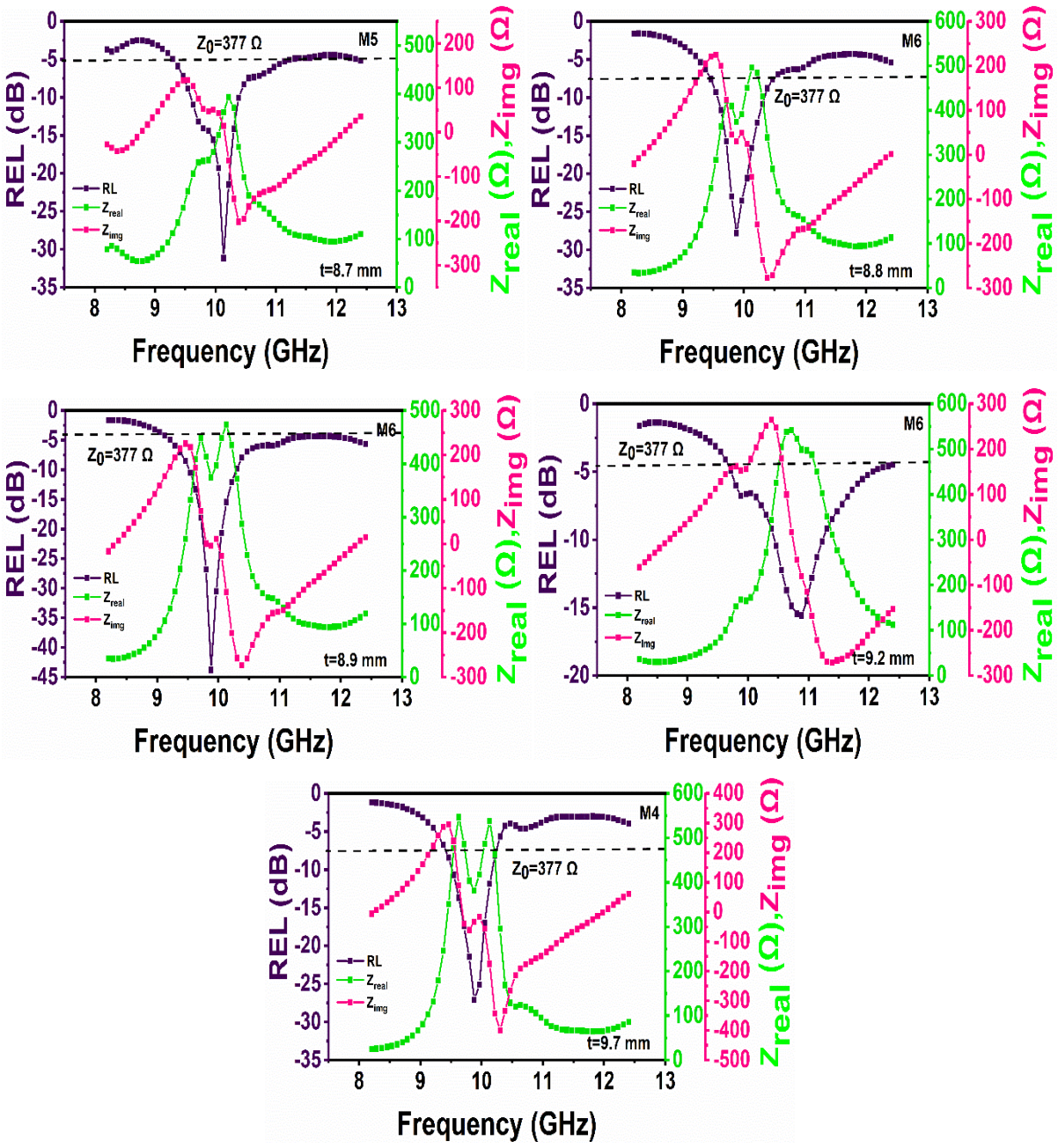

Figure 4.24: Dependence of RL, Z_{in}, Z_{real}, and Z_{img} on Frequency *M4, M5, M6* Composition

Table 4.5: Impedance Parameters of RL Peaks at Different thickness

Co-Mg Content	Matching Thickness (mm)	Matching Frequency (GHz)	Maximum RL (dB)	Z_{real} (Ω)	Z_{img} (Ω)	Z_{in} (Ω)
M4	9.4	9.88	-20.28	380.39	73.64	387.46
	9.5	9.88	-25.67	389.10	38.07	390.95
	9.6	9.80	-35.97	417.66	-18.89	418.08
	9.7	9.88	-27.07	381.85	-33.30	383.30
	9.8	9.96	-22.01	406.05	-55.09	409.77
	9.9	9.96	-18.78	386.86	-87.96	396.73
M5	3.8	8.20	-14.52	264.30	43.57	267.87
	3.9	8.20	-15.67	272.79	24.72	273.91
	4	8.79	-17.30	471.18	68.02	476.07
	4.1	8.70	-20.09	385.88	75.38	393.18
	4.2	8.70	-26.56	400.32	28.14	401.31
	4.3	8.70	-27.41	401.87	-21.99	402.47
	4.4	8.62	-21.26	322.49	26.39	323.57
	6.9	11.56	-18.38	479.91	9.16	479.99
	7	11.39	-19.56	461.62	25.25	462.31
	7.1	11.31	-20.06	459.33	11.05	459.47
	7.2	11.22	-20.63	454.28	-1.64	454.28
	7.3	11.06	-21.41	431.17	42.48	433.26
	7.4	10.89	-21.09	393.04	66.29	398.59
	7.5	10.89	-21.09	393.04	66.29	398.59
	7.7	10.64	-28.39	396.91	21.72	397.51
	8.1	10.38	-19.18	458.43	42.73	460.42
	8.6	10.22	-27.36	404.22	-19.51	404.69
	8.7	10.13	-31.14	361.89	13.86	362.16
	8.8	10.13	-28.83	360.71	-21.17	361.33
	8.9	10.05	-22.03	322.32	-8.85	322.44
	9	10.05	-20.08	317.36	-34.40	319.22
	9.1	10.05	-17.63	307.50	-57.56	312.85
	9.2	9.63	-18.56	298.63	14.94	299.01

	9.3	9.63	-18.74	299.38	-9.28	299.52
M6	7	11.64	-12.16	623.18	14.41	623.35
	7.5	10.97	-14.83	506.62	95.75	515.59
	7.8	10.89	-15.57	499.30	-80.68	505.78
	8	10.64	-13.89	551.01	-71.51	555.63
	8.3	10.30	-13.14	542.42	119.92	555.52
	8.6	9.88	-17.43	350.11	94.86	362.73
	8.7	9.88	-21.14	365.84	64.43	371.47
	8.8	9.88	-27.80	374.40	30.53	375.64
	8.9	9.88	-43.75	374.88	-4.40	374.91
	9	9.96	-28.04	393.28	-25.85	394.13
	9.1	9.96	-22.00	381.34	-60.25	386.08
	9.2	9.96	-18.30	363.01	-89.58	373.90

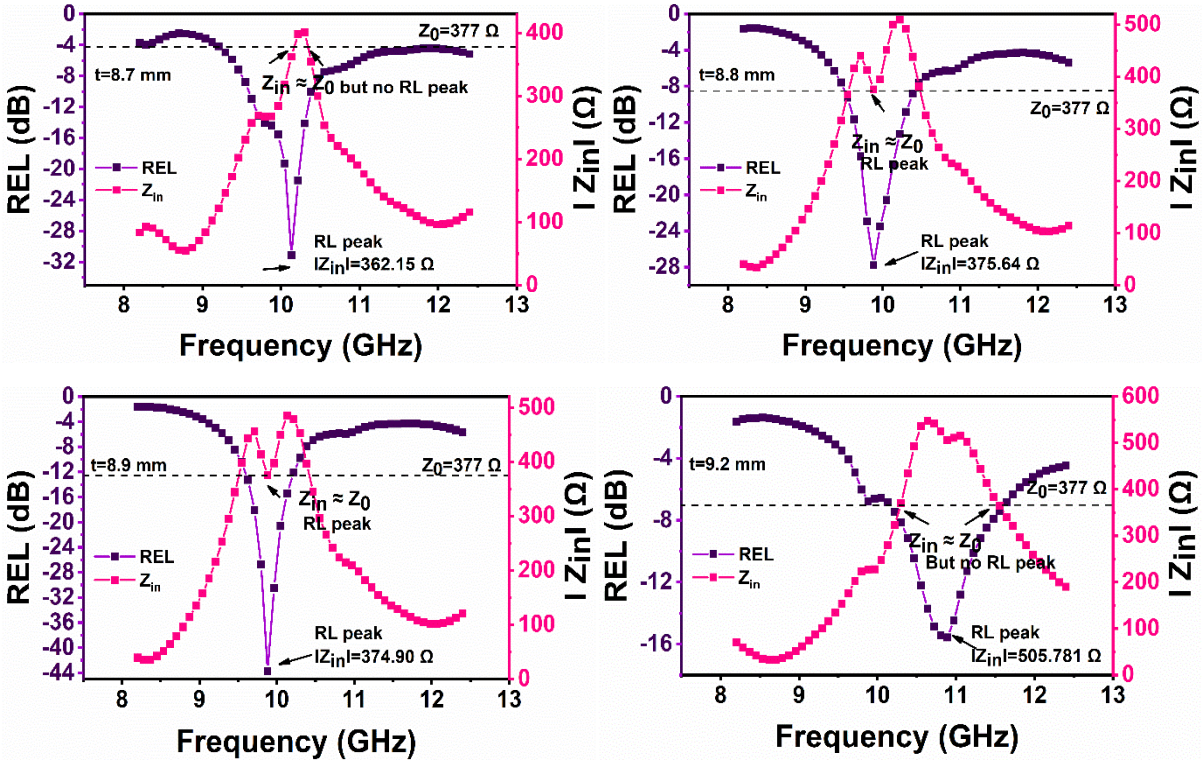

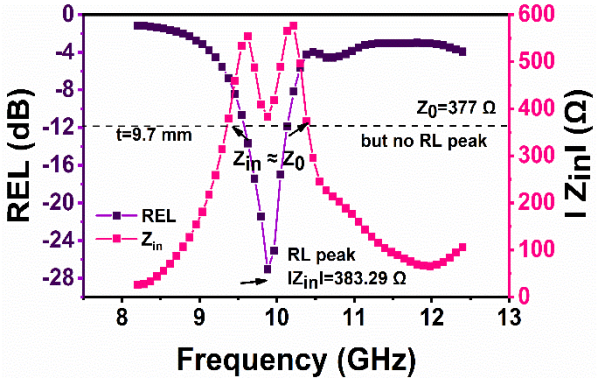

Figure 4.25: Dependence of RL and Z_{in} on Frequency in *M4, M5* and *M6* Composition

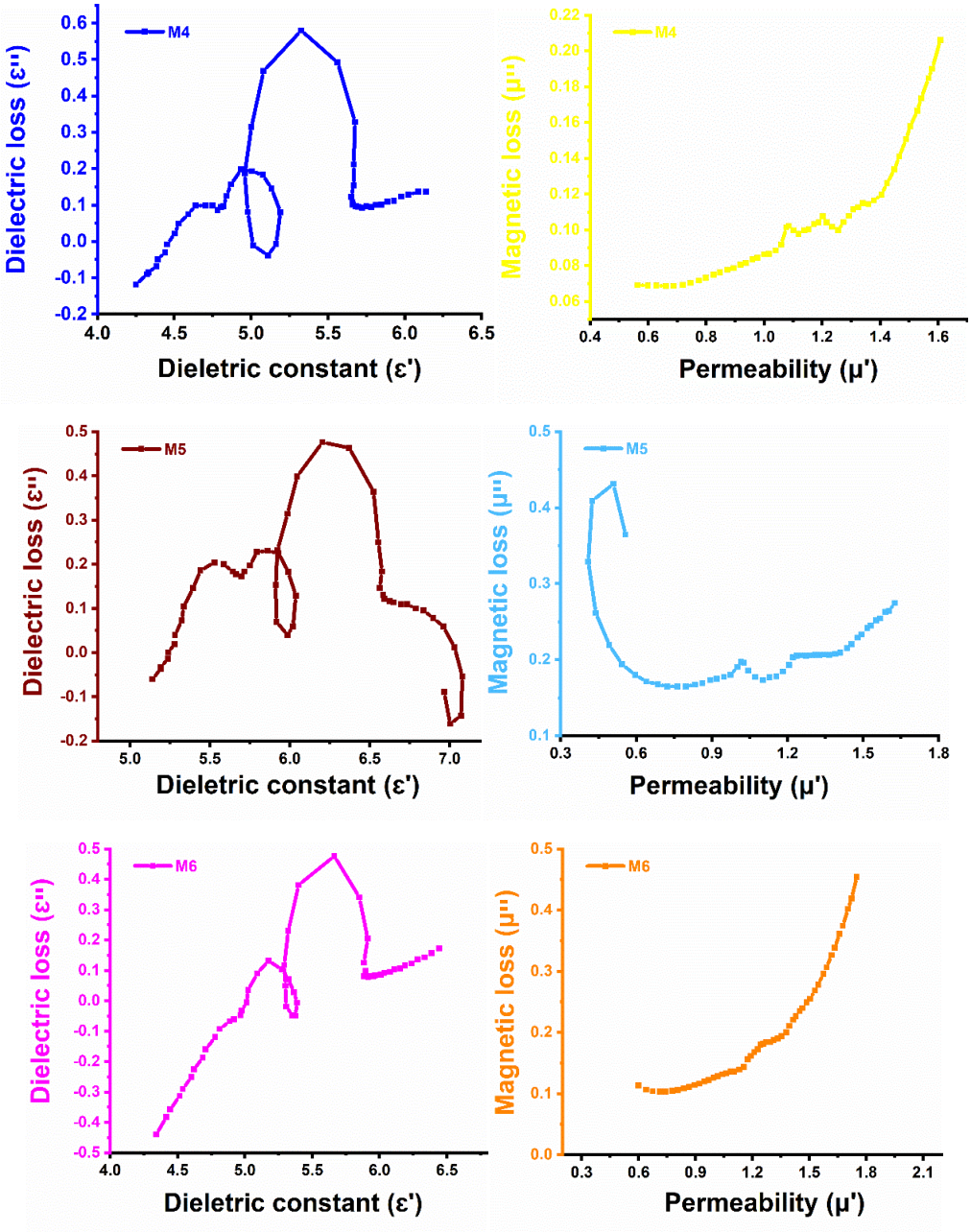

Figure 4.26: Cole–Cole plots in *M4, M5* and *M6* Compositions

Figure 4.26 shows Cole–Cole [174-175] plots to verify relaxation for compositions *M4*, *M5*, and *M6*. Plots show that a circle and a semicircle are visible in the midfrequency region for dielectric permittivity compositions of *M4*, *M5*, and *M6*. *M4* ε′ vs ε″ plots show a huge semicircle at around 9.88 GHz; this is the frequency where higher RL is captured for this composition. *M5* ε′ vs ε″ plots show a semicircle at around 10.22 GHz and a corresponding inverted semicircle in μ′ vs μ″ plot, this is the frequency where higher RL is captured for this composition. *M6* ε′ vs ε″ plots show a circle and a semicircle around the 9.88 GHz frequency range where the RL_{max} of this sample is noted. It suggests that in complex permittivity plots, dielectric relaxation is linked to peaks seen in ε′ vs ε″ spectra. Conversely, spin resonance and exchange resonance between Fe^{2+} and Fe^{3+} ions support the relaxation shown in complex permeability plots [176]. *M4* and *M6* μ′ vs. μ″ plots show weak inverted semicircles at mid-frequency regions depicting the relaxation process, but it may be dominated by impedance matching and quarter wavelength mechanism.

4.1.4.5. Eddy Current Loss

Typically, eddy current loss can be the source of magnetic loss in ferrites at the X-band and increase microwave absorption. The eddy current loss is computed using the following expression:

$$C_0 = \mu''(\mu')^{-2} f^{-1} \quad (4.1.1)$$

where the other variables were previously discussed, and C_0 is a constant.

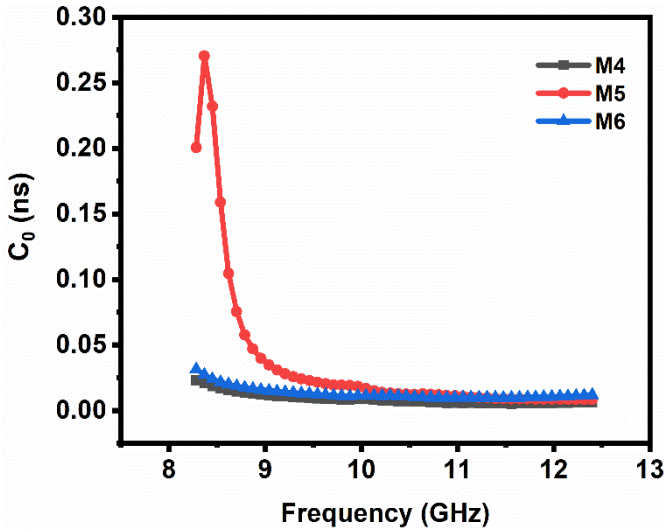

Figure 4.27: C_0 Versus Frequency Variation for Ferrite Compositions

The contribution of the eddy current loss to the magnetic loss is determined by the constant value of C_0 with frequency variation. If this value does not vary much with frequency, it indicates that the eddy current loss has contributed to the microwave absorption in the X-band

in the form of magnetic loss. The following Figure 4.27 shows the variation of eddy current loss for the *M4*, *M5*, and M6 samples.

M4 and *M6* remain constant for almost the test frequency, whereas sample *M5* remains constant from 9.5 to 12.4 GHz. Thus indicating that C_0 has contributed to microwave absorption in the given samples.

4.1.4.6 BWT/Percentage Bandwidth Ratio

The high bandwidth at low thickness for a typical RL or absorption dip is a crucial metric to design and characterize absorber behavior, in addition to the criterion RL≥-10. Rather than merely increasing RL, we need to concentrate on achieving a thin layer after hitting this RL limit. Because of this, the bandwidth-to-thickness ratio (BWT) and percentage bandwidth (PBW) in ferrite samples are estimated using relations discussed in section 3.8. Figure 4.28 shows the Bandwidth (%) variation with thickness in ferrite *M4*, *M5* and *M6* compositions.

Table 4.4 provides BWT for maximum RL with frequency. The BWT ranges between 0.06 to 0.07 for *M4*, 0.08 to 0.18 for *M5*, and 0.07 to 0.12 for *M6*. Hence, anything regarding doping cannot be concluded here. With values of 0.18 at 8.70 GHz and RL_{max} = -20.09, it is highest for *M5* at 4.1 mm thickness.

For composition *M4*, the PBW ranges from 5.67 to 6.72, for *M5*, it lies between 4.02 to 10.35, and for *M6*, it is between 6.72 to 9.03. The PBW is maximum for *M5*, at 10.05 GHz of matching frequency for 8.9 mm of thickness, with RL= -22.03 dB covering the broad bandwidth of 1.04 GHz.

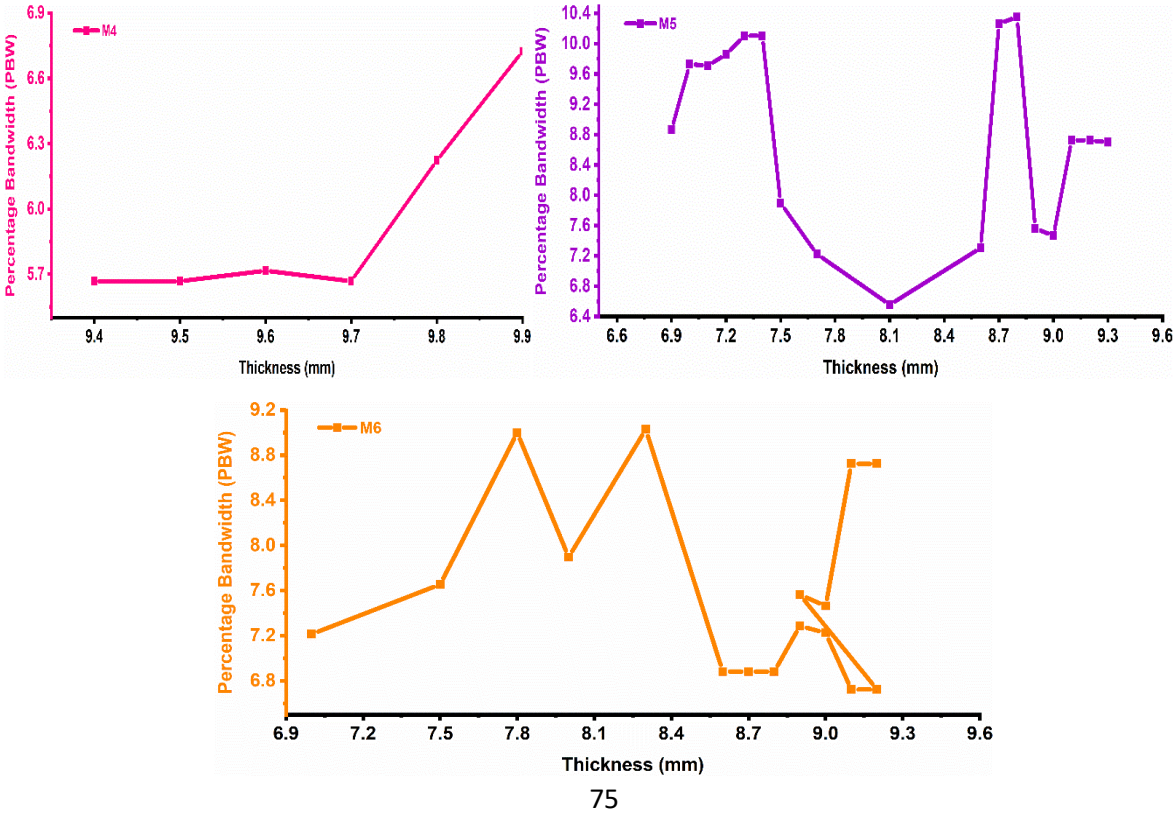

Figure 4.28: Bandwidth (%) Variation with thickness in Ferrite *M4, M5* and *M6* Compositions

4.2 Co^{2+}-Mg^{2+} substituted $Ba_{0.2}Sr_{0.8}Co_xMg_xFe_{12-2x}O_{19}$/PANI hexaferrite

In this section, we have synthesized a hexaferrite with Co and Mg substitutions with PANI as a matrix via the sol-gel technique. This composition hexaferrite will be given as $Ba_{0.2}Sr_{0.8}Co_xMg_xFe_{12-2x}O_{19}$/PANI. For composites, we are reporting only those samples in which significant results have been obtained. The sample names with the codes for each level of substitution in $Ba_{0.2}Sr_{0.8}Co_xMg_xFe_{12-2x}O_{19}$/PANI are given in Table 4.6

Table 4.6: The Assignment of Sample Names Corresponding to Various Substitution Levels in $Ba_{0.2}Sr_{0.8}co_xmg_xfe_{12-2x}o_{19}$/PANI Hexaferrite

Sample Composition $Ba_{0.2}Sr_{0.8}Co_xMg_xFe_{12-2x}O_{19}$	Sample Code Name	Sample Code (M-Series)
x = 0.0	$Ba_{0.2}Sr_{0.8}Fe_{12-2x}O_{19}$/PANI	MP1
x = 0.4	$Ba_{0.2}Sr_{0.8}Co_{0.4}Mg_{0.4}Fe_{11.2}O_{19}$/PANI	MP3
x = 0.8	$Ba_{0.2}Sr_{0.8}Co_{0.8}Mg_{0.8}Fe_{10.4}O_{19}$/PANI	MP5

4.2.1 Structural Analysis

4.2.1.1 Field Emission Scanning Electron Microscopy

The samples' grain morphology is shown in Figure 4.29 (a–c). The micrographs show that in the sample with zero doping, i.e., *MP1* fused grains lead to the creation of a massive grain. Along with these fused grains are the individual grains that are visible in the micrographs. With doping, the rice-like structure of the grain can be observed in *MP3* with more fused grains. But if the doping is increased, their rice-like structure is reduced and takes an oval shape. Though the observation of grain aggregation is there in all the samples, it is easy to detect individual grains too in doped samples, just like in pure sample *MP1*. Doping causes the ferrite particles to interact both magnetically and electrostatically, which causes grain clusters to have an uneven size distribution. The small individual grains become more noticeable in the grain clusters as doping levels rise. Voids are noticeably reduced in PANI composite samples (*MP1, MP2* and *MP3*) than that in pure ferrite samples (*M1, M2, M3, M4, M5* and *M6)*. Hence, it can be said that resistance that impedes the movement of charge carriers is also reduced here in these samples. Figure 4.30 shows the EDX spectra of $Ba_{0.2}Sr_{0.8}Co_xMg_xFe_{12-2x}O_{19}$ /PANI hexaferrite for samples *MP3* and *MP5*. From the figure, it can be varied that in sample *MP3*, the Mg content is lower than that in sample *MP5*.

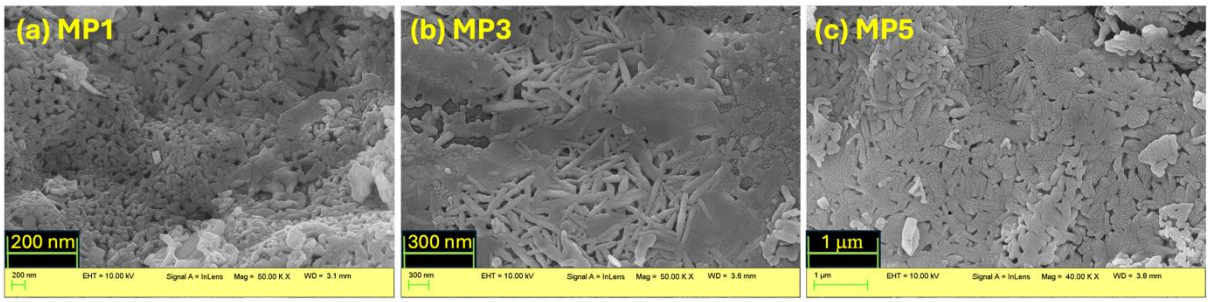

Figure 4.29: SEM Micrographs of Ferrite Samples: $Ba_{0.2}Sr_{0.8}Co_xMg_xFe_{12-2x}O_{19}$ /PANI (*MP1, MP3, MP5*)

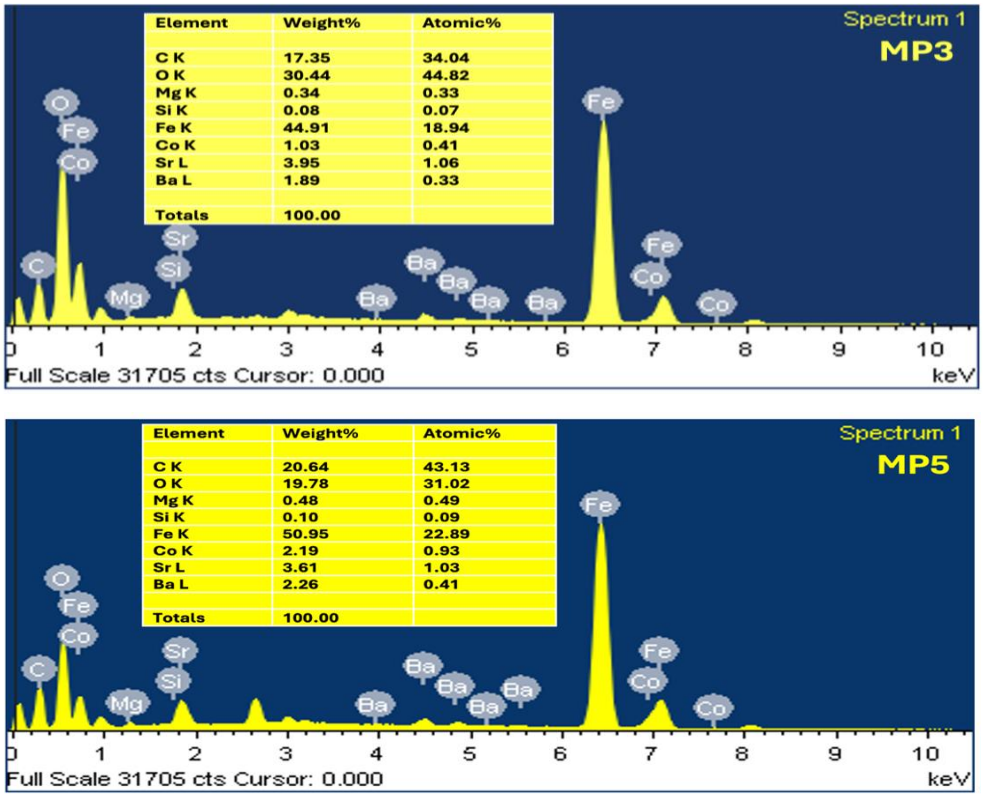

Figure 4.30: EDX Spectra $Ba_{0.2}Sr_{0.8}Co_xMg_xFe_{12-2x}O_{19}$ /PANI Hexaferrite for Samples *MP3* and *MP5*

4.2.2 Electrical Analysis

4.2.2.1 Dielectric permittivity

The relevant mathematical equations for electrical parameters have already been mentioned in the earlier section 3.1.1. With operational frequencies from 10 Hz to 2 MHz, Figure 4.31 and Figure 4.32 shows two different types of plots: 4.31 (a), (b) dielectric permittivity and 4.32 (a), (b) dielectric loss. Figure 4.31 illustrates how it exhibits dispersion in the overall frequency spectrum. Samples *MP1* and *MP3* have their highest value at around 1000 Hz frequency.

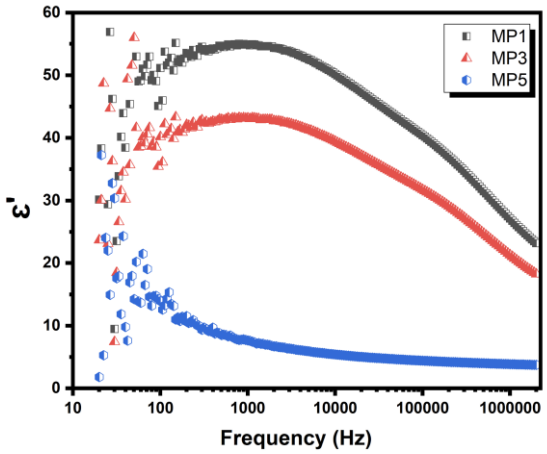

Figure 4.31: Variation of Dielectric Spectra of Sample $Ba_{0.2}Sr_{0.8}Co_xMg_xFe_{12-2x}O_{19}$ /PANI for a) Real Component (*MP1, MP3, MP5*)

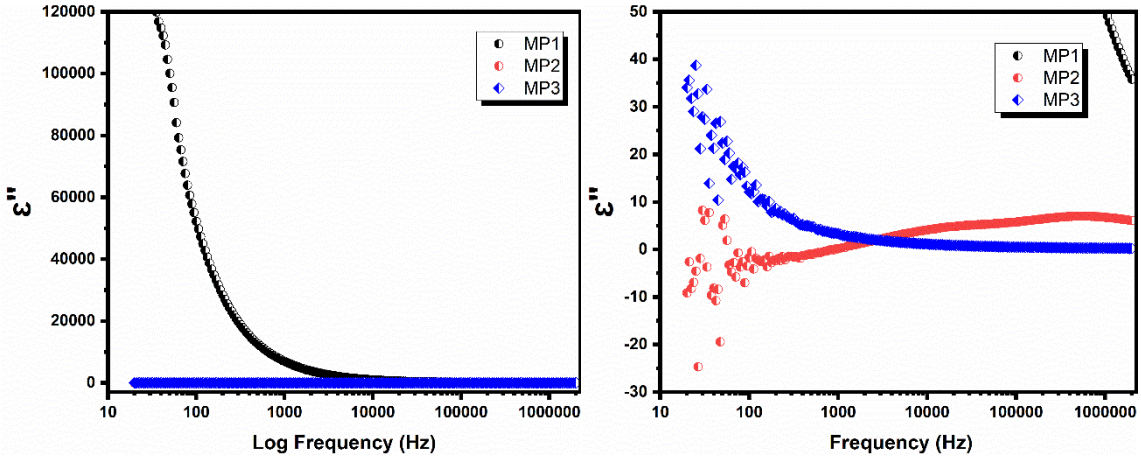

Figure 4.32: Variation of Dielectric Spectra of Imaginary Component of Ferrite Sample $Ba_{0.2}Sr_{0.8}Co_xMg_xFe_{12-2x}O_{19}$ (a) *MP1, MP5* (b) *MP3, MP5* Function of Frequency

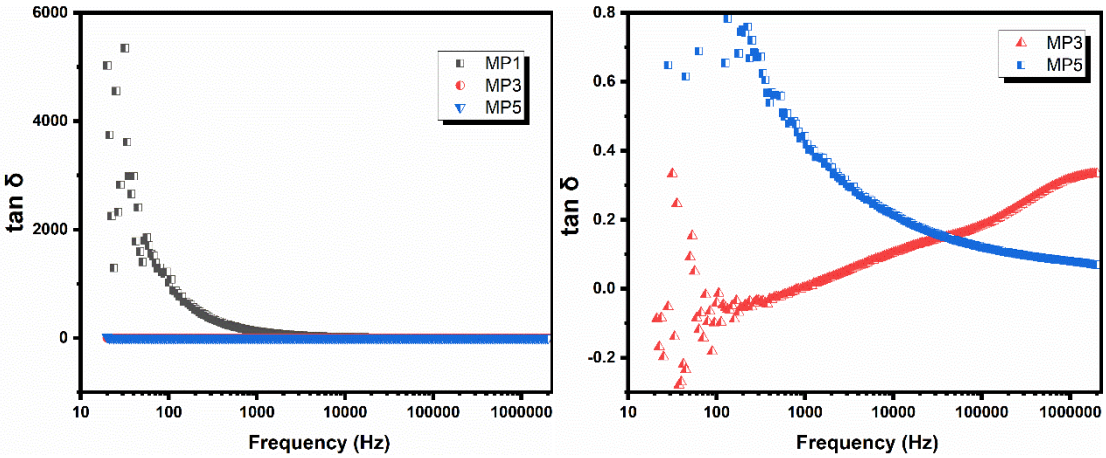

Figure 4.33: Variation of Dielectric loss Tangent of Ferrite Sample: $Ba_{0.2}Sr_{0.8}Co_xMg_xFe_{12-2x}O_{19}$/PANI a) *MP1, MP5* (b) *MP3, MP5* Function of Frequency

For *MP1*, it is around 55, for *MP3*, it is 41, but *MP5* has its highest value around 20 Hz, which is around 60. As the frequency is reduced, these values are reduced to 21, 18, and 2 for *MP1*, *MP3*, and *MP5* respectively. The Maxwell-Wagner interfacial polarisation model can be used to specify the dropping of dielectric permittivity values with decreasing frequency. This model is frequently used to explain hexaferrite's dielectric characteristics. However, it can be observed that even with doping of Co-Mg, these values have been reduced in *MP1*, *MP3*, and MP5. But, PANI as a matrix has increased the values of ε', from ferrites samples (*M1* to *M6*) to composite samples (*MP1*, *MP3, MP5*).

Figure 4.32 illustrates that *MP1* starts with a drastically high value ε'', whereas *MP3* starts with a negative value, and *MP5* starts with 40. However, the *MP1* sample reduces and follows a constant path after 10 kHz, whereas MP3 and MP5 follow a constant path after 50 kHz.

As previously mentioned in Figures 4.31 and 4.32, the Dielectric permittivity/loss reaches a steady state value after a specific frequency, which prevents electron hopping between Fe ions of +2 and +3 states. The maximum dielectric permittivity at *MP1* is associated with the highest ferrous ion concentration in the octahedral locations, while their quantity is negligible in the other doped samples.

From Figure 4.33, for undoped sample *MP1*, the maximum value of loss tangent is around 6000 and reduces sharply with a rise in frequency. However, for sample *MP3*, the value seems to rise with increasing frequency. Conversely, the *MP5* value seems to reduce. The highest value for sample MP3 at a lower frequency is around 0.4, and for *MP5*, it is around 0.8. This decrease in the value of $tan\ \delta$ is explained by Koop's phenomenological theory of dielectrics. Interface traps, interfacial polarisation, Fe^{2+}/Fe^{3+} content, structural oneness, stoichiometry, and, above all, the sintering circumstances are the factors that cause this variance.

The applied dynamic AC signal creates a fluctuating electric field across the ferrite interfaces, which causes all charge carriers to evacuate the confined area. The increase in frequency values causes this electrical field to fluctuate quickly, which forces a rapidly shifting field on the charge carriers and ultimately causes them to move away from the traps. This process increases the density of the charge carriers, and at this stage, the ascending charge paths are blocked by grain boundaries. Because less energy is required for the electron exchange between Fe2+ and Fe3+ ions at high frequencies, the loss tangent has a low value [161].

4.2.2.2 Electric modulus analysis

M' and M'' are the real and imaginary parts of the complex electric modulus and are calculated using equation 3.8 and equation 3.9 respectively (from section 3.3.2).

Figure 4.33 (a) shows the variation of the real component of the modulus (*M′*) vs the frequency and provides information on conductivity and Figure 4.33 (b) shows the variation of the imaginary component of the modulus (*M″*) vs the frequency

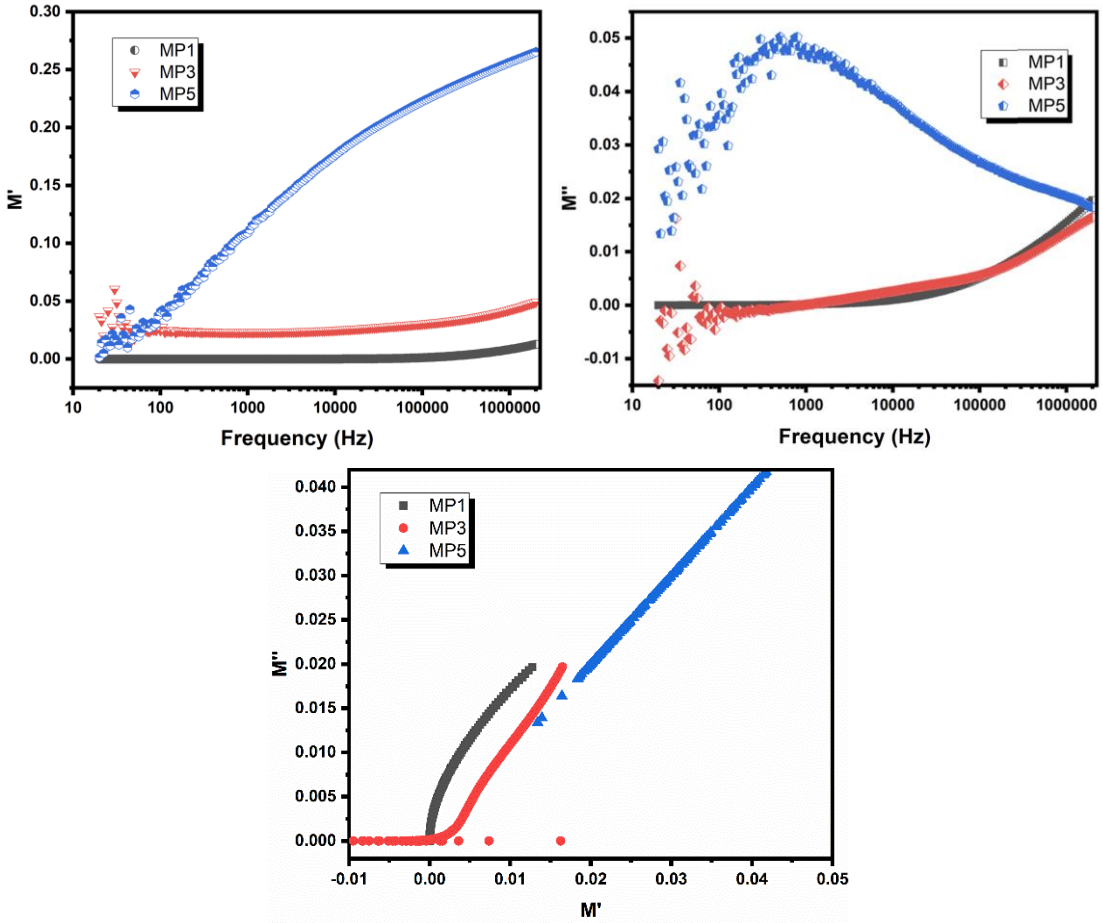

Figure 4.34: Variation of Modulus (a) Real Part, (b) Imaginary Part of Ferrite Sample $Ba_{0.2}Sr_{0.8}Co_xMg_xFe_{12-2x}O_{19}$/PANI (*MP1*, *MP3*, *MP5*) as a Function of Frequency (c) Cole-Cole Plot (or Nyquist Plot) of the Composite Sample

For *M′*, at lower frequencies, *MP1* can only be set to a lower value that tends to zero, and other samples stay at low values (non-zero). The Undoped sample seems to stay around 0.0 for the overall frequency range, but the other two do not. Sample *MP3* remains within the range of 0.05-0.06, and sample *MP5* starts with a low value of 0.0 and increases with frequency, reaching the value of 0.25. For *M″*, the undoped sample starts with a value of zero, *MP3* starts with a negative value, whereas *MP5* starts with 0.1. As the frequency increases, *MP1* and *MP3* seem to have increased, reaching the values of 0.02 and 0.018, respectively. But *MP5* shows a peaking behavior at around 500 Hz and then lowers down as the frequency is increased. In the low-frequency domain, ions can hop successfully over long distances between sites. However, the peaking behavior in *M″* indicates that the ions are restricted to the wells of their limiting potential rather than following the lengthier hopping for higher frequencies. As frequency rises,

the region where the peaks are found shows a change from long-range to short-range mobility. Thus, the modulus spectrum represents the hopping phenomenon for electrical conduction.

Figure 4.34 (c) shows the Cole-Cole plot (*M′* vs. *M″*) of the sample $Ba_{0.2}Sr_{0.8}Co_xMg_xFe_{12-2x}O_{19}$/PANI. The charts show that the samples contain asymmetric semi-circles. Incomplete smaller arcs for *MP1* and *MP3*, whereas a huge arc for *MP5* depicting grain boundaries playing a vital role as the doping is increased. The alteration of the maxima of the semicircle for the maximum frequency with doping is used to demonstrate the relaxation time distribution. This distribution supports the non-Debye form of relaxation.

4.2.2.3. Complex impedance spectra

Information regarding the polycrystalline materials' impedance performance, which is primarily caused by their bulk grains and grain boundaries, may be found in the details of their resistance (*Z′*) and reactance (*Z″*) and are calculated using equation 3.11 and equation 3.10, respectively (from section 3.3.3).

The impedance of the bulk grains and the impedance of the grain boundaries are treated differently because of their distinct relaxation durations. Figure 4.35 (a) shows how *Z′* fluctuates about log frequency. It has been observed that Z′ steadily decreases as the frequency increases until it almost achieves a constant value at a particular point after 5 kHz. The reduction in space charge polarization of the samples is accountable for this decrease in *Z′* value. For sample *MP5,* it seems to reduce and follow a constant path, but for undoped sample *MP1, it* almost stays in a similar range of values.

As seen in Figure 4.35 (b), the change in Z″ with the variation in frequency has been studied to better understand the impact of space charges. At a lower frequency regime, imaginary components have been found to fall sharply, and after 5 kHz, all values saturate in the same range. However, undoped sample *MP1* shows the same behavior as in *Z′* and stays in the same range of values.

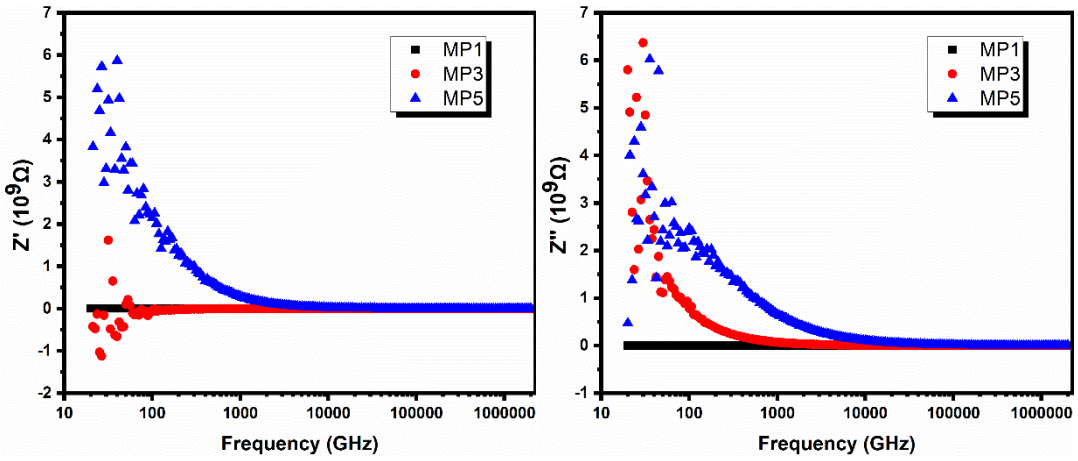

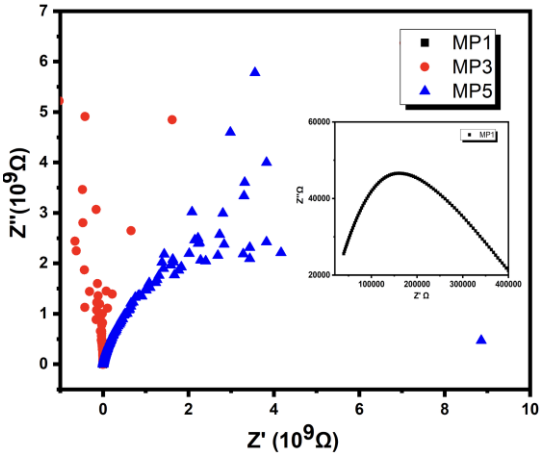

Figure 4.35: Variation in the (a) Dielectric Impedance Real (*Z′*) (b) Dielectric Impedance Imaginary (*Z″*) vs. Frequency (c) Variation in the Dielectric Impedance Real (Z′) Component Versus Dielectric Impedance Imaginary (*Z″*) Component for $Ba_{0.2}Sr_{0.8}Co_xMg_xFe_{12-2x}O_{19}$/PANI for (*MP1, MP3, MP5*)

In Figure 4.35 (c), for the graph of *Z″* vs *Z′*, every sample depicts a semi-circular arc, with a prominent curve for undoped sample *MP1*. For doped compositions, *MP3 and MP5*, the depression of the arc seems to increase but in sample *MP3* no significant variation can be seen. The low-frequency depressions are associated with the Maxwell-Wagner phenomenon, which is associated with interfacial polarisation at grain boundaries. In the sample, *MP1* grain boundaries are more actively participating and *MP3* grains as well as grain boundaries are more actively participating, whereas *MP5* grains, seem to be contributing.

4.2.2.4 AC Conductivity

The curve of AC conductivity in the composite samples as a function of frequency is shown in Figure 4.36. In the current study, it is observed that AC conductivity gradually rises after 5 kHz frequency for doped samples *MP3* and *MP5*, unlike undoped sample *MP1*. The behavior is nearly frequency-independent below 5 kHz, and DC conductivity changes to AC conductivity at this frequency. Doping Cu^{2+} and Mg^{2+} ions in place of Fe^{3+} ions hinders the Verwey hopping process as it restricts the conduction. The consequent decrease in conductivity is depicted in Figure 4.36, the highest being for *MP1*, followed by *MP3*, and the lowest for MP5.

Section 3.3.4 provides the frequency-dependent AC conductivity, also referred to as the Jonscher power law. When describing the behavior of dielectric materials throughout a broad frequency range, the Jonscher power law is helpful [126]. A and n are constants in the Jonscher power law. Here, A and n are determined by the sample's composition. While n is dimensionless, A has conductivity units. In AC conductivity charts, the distribution is quantified by the second term, $A\omega^n$. According to Funke [29], the number n has a physical

significance: n < 1 suggests a sudden translational motion with hopping, whereas n > 1 denotes localized hopping between nearby places.

The value of n was determined by fitting the plots: *MP1*- 0.2294, *MP3*- 0.2527, and *M5* - 0.5759 suggesting a sudden translational motion with hopping. Because of this, it turns out that n is less than 1, which suggests that charge carriers are hopping in tandem with ac conductivity.

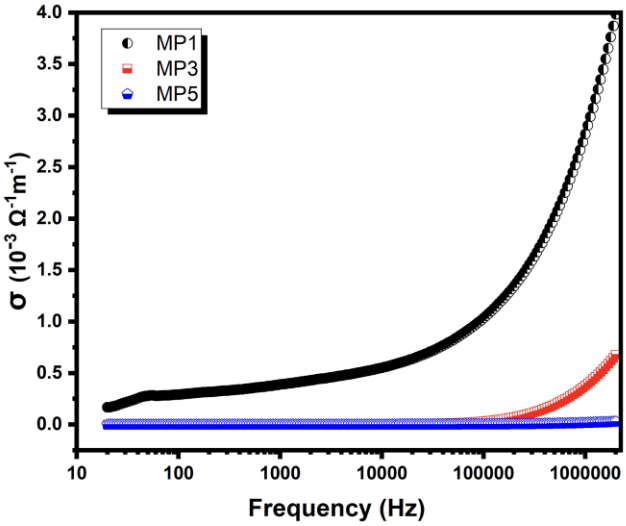

Figure 4.36: Variation of AC Conductivity for Composite Sample for $Ba_{0.2}Sr_{0.8}Co_xMg_xFe_{12-2x}O_{19}$/PANI for (*MP1*, *MP3*, *MP5*)

4.2.3 Magnetic analysis

The saturation magnetization (M_s), coercivity (H_c), anisotropy field (H_a), and squareness (M_r/M_s) ratio values are depicted in the table 4.7, and are derived from the M-H loops and Linear fits of samples *MP1*, *MP3*, and *MP5*. Figure 4.37 represents Hysteresis loops of *MP1, MP3,* and *MP5* hexaferrite. It can be deduced that the value of M_s increases in the *MP3* sample initially and then decreases in the *MP5* sample as the quantity of substitution increases. From the table, it can be seen that magnetization saturation first increases from *MP1* (44.54 emu/g) to *MP3* (46.82 emu/g) and is then decreased to *MP5* (36.00 emu/g). Electronegativity parameters and ligand field theory can assist in explaining this expected behavior, as was previously indicated. The observed decrease in M_s value (*MP3* to *MP5*), about 19%, might be explained by the replacement of Fe^{3+} at octahedral locations with non-magnetic (Mg^{2+}) and weakly magnetic (Co^{2+}) cations. It can also be said that the magnetic properties of the samples are influenced by the distribution of cations across crystallographic sites. Here, *MP1* (44.54 emu/g) and *MP3* (46.82 emu/g) exhibit relatively high saturation magnetization , likely due to favorable cation occupancy at spin-down sites, which enhances magnetization. In contrast, MP5 (36.00 emu/g) shows a lower which may be attributed to a higher concentration of cations

occupying spin-up sites, reducing the overall magnetic moment due to less efficient spin alignment.

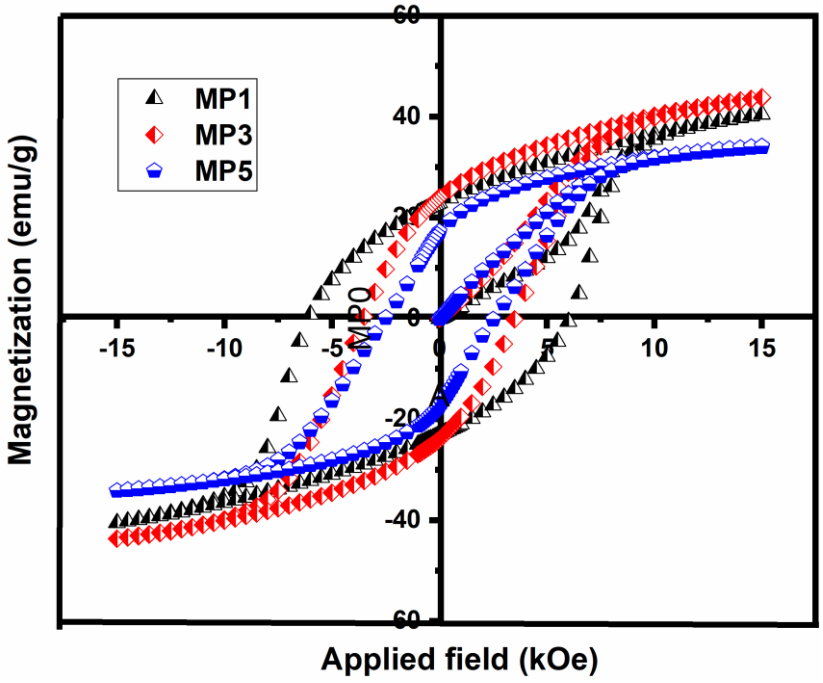

Figure 4.37: Hysteresis Loops of *MP1, MP3 and MP5* Hexaferrite

Table 4.7: Magnetic Parameters M_s, H_c H_a, M_r And M_r/M_s for Co-Mg/PANI Doped Hexaferrite Samples

Sample	M_s	H_c	H_a (kOe)	M_r	M_r/M_s
MP1	44.54	6112.67	17.49	22.78	0.50
MP3	46.82	3448.87	15.00	22.96	0.48
MP5	36.00	2396.44	13.27	16.86	0.46

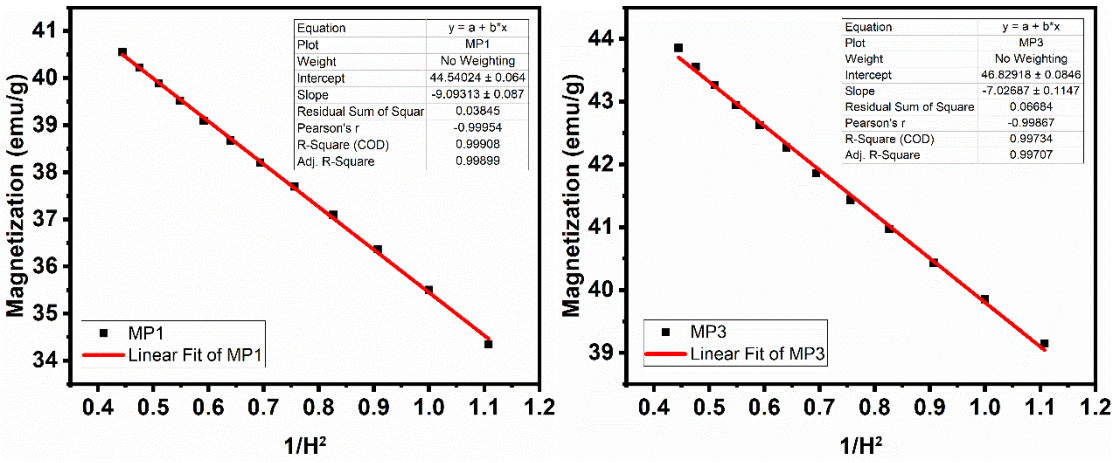

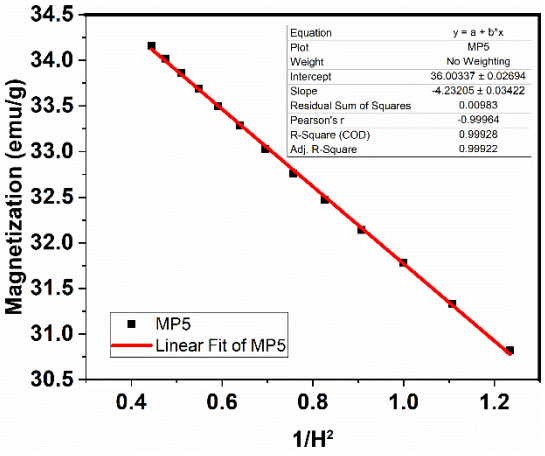

Figure 4.38: M_s Versus 1/ H^2 Plots for *MP1, MP3 and MP5* Hexaferrite Samples

Magnetization saturation is lowered as a result of a reduction in the magnetic moment and the strength of the superexchange interaction. The *MP1* sample's M-H curve is convex and smooth, as shown in Figure 4.37. It could be observed that the squareness ratio for *MP1,* i.e., for pure composite sample, is between ($0.5<M_r/M_s$) <1), implies single-domain, while for *MP3* and *MP5,* it is less than 0.5, implying randomly oriented multi-magnetic domains.

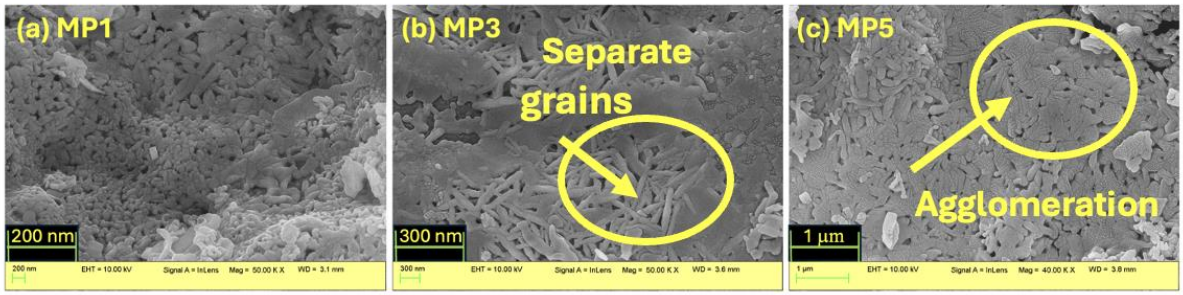

Figure 4.39: SEM Micrographs of Ferrite Samples: $Ba_{0.2}Sr_{0.8}Co_xMg_xFe_{12-2x}O_{19}$/PANI (*MP1, MP3, MP5*) and its Correlation with Magnetic Data

The pure composite sample (*MP1*) has the highest coercivity values (6112 Oe). H_c It is then seen decreasing with doping, 3448 Oe for *MP3* and 2396 Oe for *MP5*. As seen from the micrographs (Figure 4.39) the porosity is seen drastically decreasing from sample *MP1* to *MP5*, which can be one of the reasons that H_c is being lowered down from 6112.67 Oe to 2396.44 Oe. H_a it does not appear to have a significant impact on coercivity, indicating that H_a for *MP3* and *MP5* is equal to 15.00 kOe and 13.27 kOe, respectively. The remanence magnetization for *MP1* and *MP3* is nearly comparable. However, it decreases for *MP5*, with pure composite showing 22.7 emu/g and *MP3* and *MP5* showing 22.90 and 16.86 emu/g, respectively.

4.2.4 Electromagnetic Characteristics

4.2.4.1 Complex Permeability and Complex Permittivity

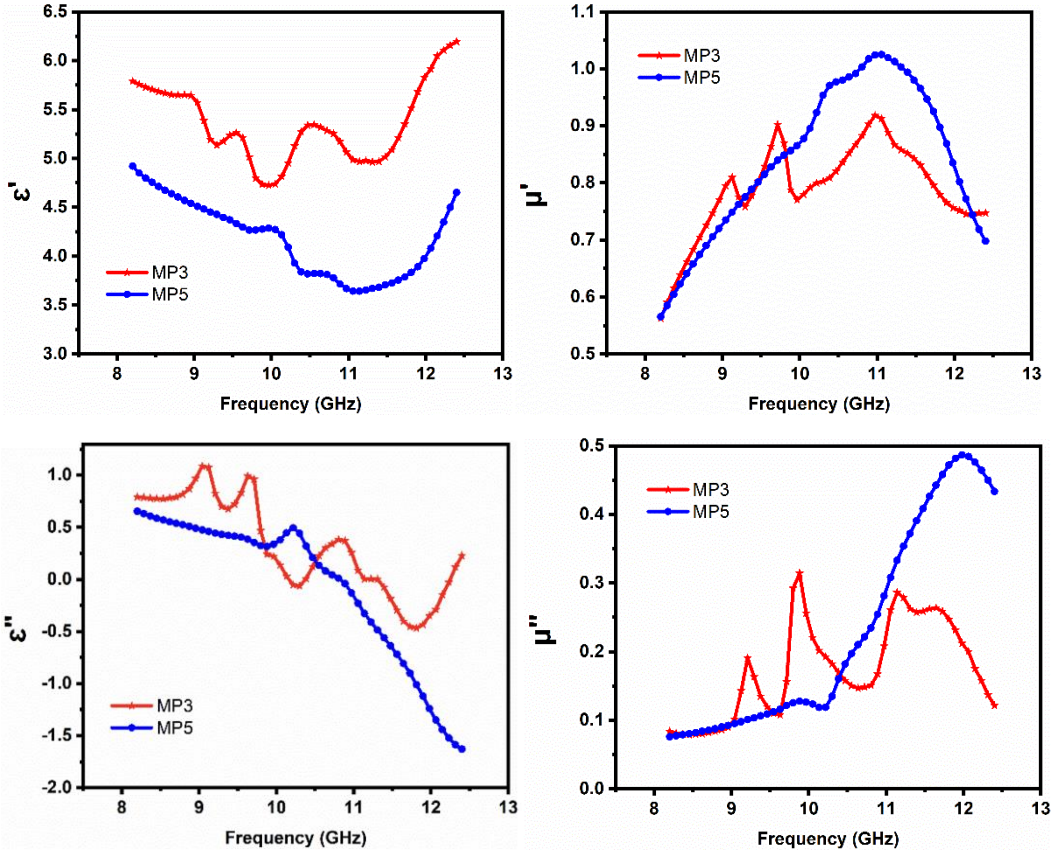

Figure 4.40: Dependence ε′, ε″, μ′ and μ″ on Frequency in Ferrite Compositions *MP3* and *MP5*

Plots of the dielectric permittivity (ε′) and dielectric loss (ε″) along with plots of the permeability (μ') /magnetic loss (μ") versus frequency are shown in Figure 4.40. Doping with Co^{2+}-Mg^{2+} ions results in a nonmonotonic decrease in the Dielectric permittivity/loss. For ε′, the value decreases with doping with multiple peaks for sample *MP3* and two weak peaks for *MP5*. Here, initially, the value seems to decrease, but after mid-frequency, there is an increase in values. In ε″, there are multiple relaxation peaks for sample *MP3*, but there seems to be a linear decrease in sample *MP5* with an increase in frequency, only one relaxation peak can be seen in this sample. In both μ′ and μ″, there are three resonance peaks for sample *MP3* and a high peak at a high-frequency region for *MP5* composition. If the ε′ and μ′ plots for both *MP3* samples are compared, then it can be observed that the dips in ε′ and μ′ plots match exactly with the peaks of ε″ and μ″ at the same frequencies. The highest value of ε′ observed is 6.2, which is for *MP3* at 12.4 GHz, ε″ is 1.1, which is again higher for the same sample at around 8.76 GHz. For *MP5*, the highest value of μ′ is observed, which is around 1.1 at 11.12 GHz, and μ″ is around 0.49 at 12.04 GHz.

In the microwave region, the complex permittivity/permeability depends on dipole polarisation, electron spin, porosity, grain, and grain size distribution, in addition to charge

accumulation at grain borders [168]. Dielectric polarisation in ferrites is caused by electron hopping in Fe^{2+}/Fe^{3+} [169]. The porosity provides a barrier to the field flow and deters polarisation. Exchange resonance between Fe^{2+}/Fe^{3+} ions and ferromagnetic resonance controls the mechanism of complex permeability [170]. Doping with Co-Mg modifies the polarisation and resonance, resulting in a decrease in Fe^{3+}. The pores in the compositions shown in the micrographs (Figure 4.39) are nonmagnetic voids that give rise to demagnetizing fields, which in turn alter the magnetization and polarisation related to complex permeability and permittivity.

4.2.4.2 Microwave absorption in $Ba_{0.2}Sr_{0.8}Co_xMg_xFe_{12-2x}O_{19}$ /PANI

Examining a material's reflection loss is one method of determining its microwave absorption capability. Equations 3.16 and 3.17 are used to determine the RL of the compositions. This section will examine how different factors affect the material's microwave-absorbing capacity. These variables include the degree of reflection loss, impedance matching, and material thickness ($\lambda/4$) [178-182].

4.2.4.3 Quarter Wavelength Mechanism

The graphic representations of RL dependent on frequency at different simulated thicknesses are used to investigate the phenomenon of microwave absorption. Figures 4.41 (a),(b) to 4.45 (a),(b) show RL plots of the ferrite compositions $Ba_{0.2}Sr_{0.8}Co_xMg_xFe_{12-2x}O_{19}$/PANI Ferrite composite. Table 4.8 presents the summarised data, and Figures 4.41 (a),(b) to 4.45 (a),(b) aid in inferring parameters matching frequency/thickness, bandwidth, and frequency range for an RL of -10 dB.

There was no absorption in the zeroth sample, i.e., *MP1*. The composition with *MP5* exhibits the largest RL dip of - 40.06 dB at 11.78 GHz frequency and 9.2 mm thickness. The other composition, i.e., *MP3* composition, owes RL values ranging from -11.00 to -19.70 dB (*MP3*), as shown in Table II. Plots illustrating how RL peaks shift towards the low-frequency spectra as thickness increases are displayed. This is in agreement with the quarter wavelength mechanism, which states that the relationship between frequency and thickness is inversely proportional.

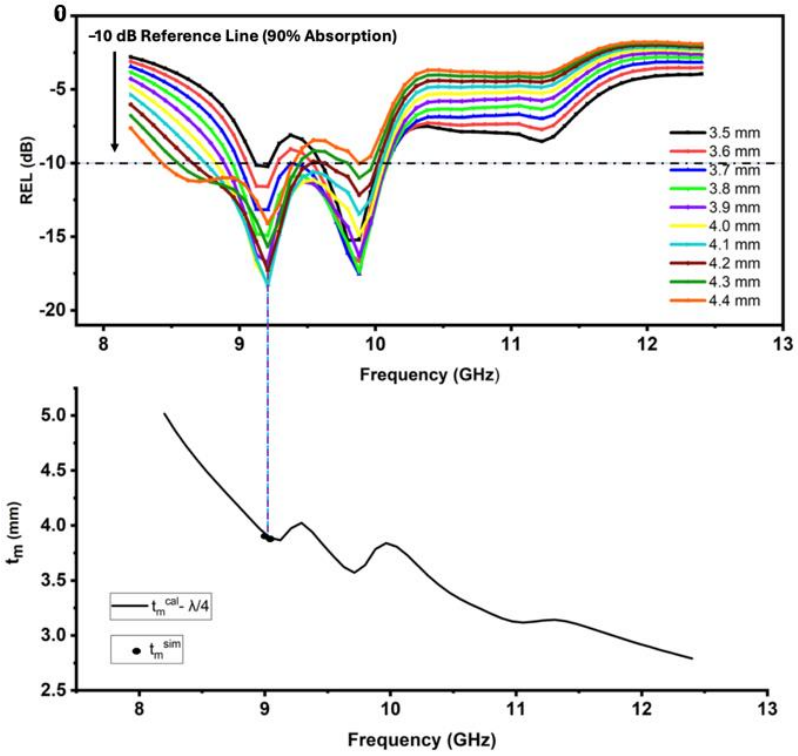

Figure 4.41: (a) Dependence of RL on Frequency in *MP3* Composition and (b) t^{sim} and t^{cal} Versus Frequency for λ/4 in *MP3* Composition

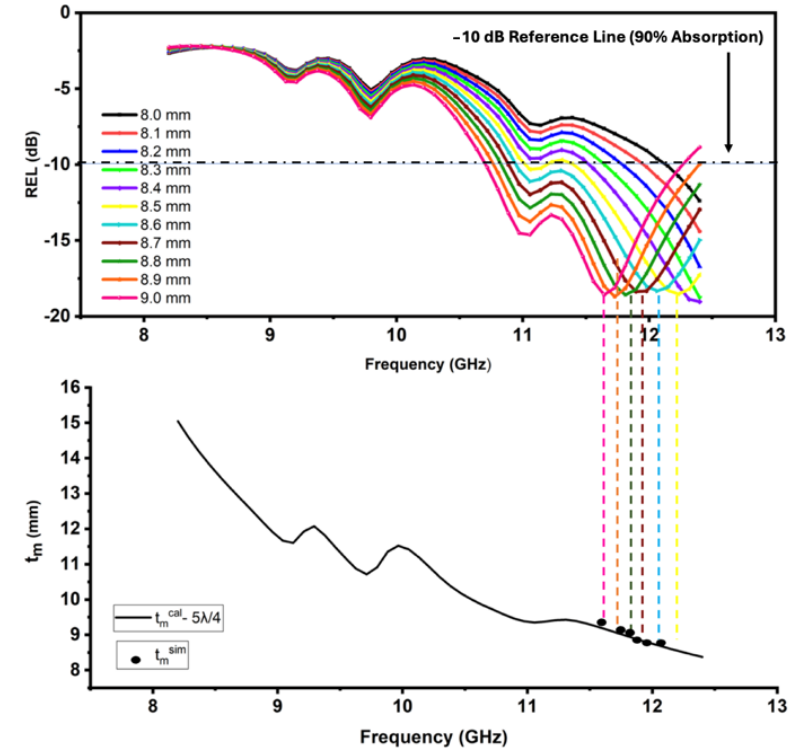

Figure 4.42: (a) Dependence of RL on Frequency in *MP3* Composition and (b) t^{sim} and t^{cal} Versus Frequency for 5λ/4 in *MP3* Composition

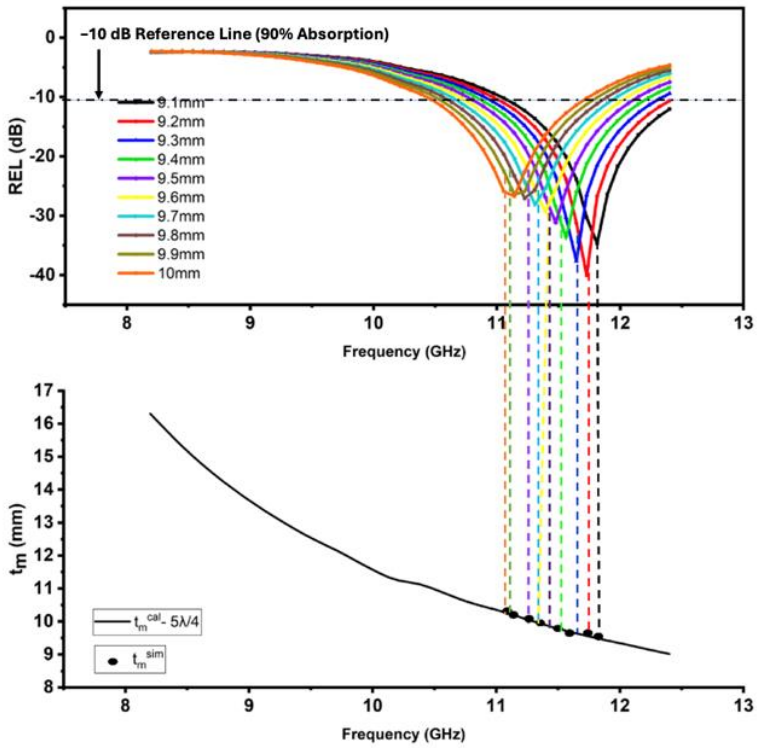

Figure 4.43: (a) Dependence of RL on Frequency in *MP3* Composition and (b) t^{sim} and t^{cal} Versus Frequency for 5λ/4 in *MP3* Composition

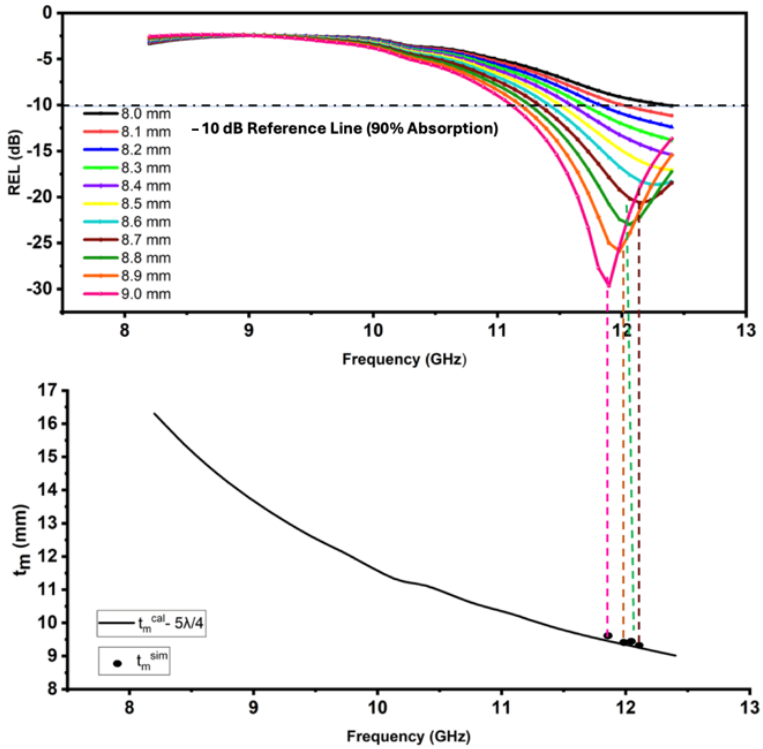

Figure 4.44: (a) Dependence of RL on Frequency in *MP5* Composition and (b) t^{sim} and t^{cal} Versus Frequency for 5λ/4 in *MP5* Composition

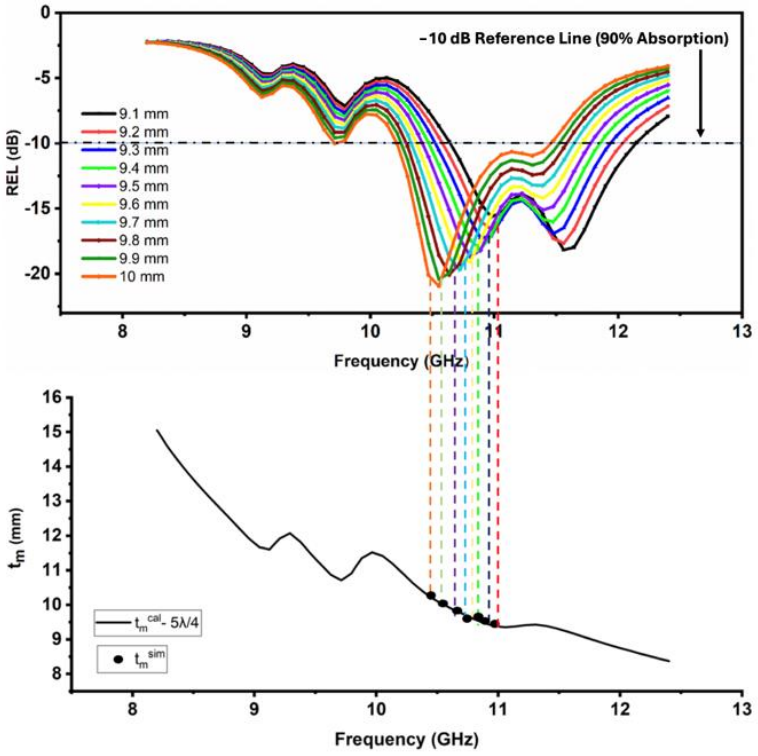

Figure 4.45: (a) Dependence of RL on Frequency in *MP5* Composition and (b) t^{sim} and t^{cal} Versus Frequency for 5λ/4 in *MP5* Composition

The RL peaks shown for composition *MP3* are given in Figure 4.41 (a), (b), Figure 4.42 (a), (b) and Figure 4.43 (a), (b), at thicknesses of 3.5 to 4.4 mm, 8.0 to 9.0 mm and 9.1 to 10.0 mm, respectively, in the frequency range of 8.36 to 11.22 GHz, 11.56 to 12.23 and 10.20 to 12.40 GHz. It is interesting to know that, for *MP3* composition, Figure 4.41(a), (b)shows the multi-RL peaks with RL ≥ -10 dB from 8.2 to 12.4 GHz and 3.5 to 4.4 mm thickness. The frequency region spanning from 10.28 to 12.4 GHz and 10.44 to 12.40 GHz at thicknesses of 8.0 to 9.0 mm and 9.1 to 10.0 mm, respectively, is where the RL peaks are seen in *MP5* [Figure 4.44 (a), (b), Figure 4.45 (a), (b)]. The multi-RL peaks with RL > -10 dB for *MP5* composition from 8.2 to 12.4 GHz and 9.1 to 10.0 mm thickness are shown in Figure 4.44 (a), (b). But for *MP5* composition, thicknesses 8.0 to 9.0 mm show incomplete RL curves. Figure 4.46 depicts three-dimensional (3D) plots of reflection loss at various frequencies and thicknesses for *MP3* and *MP5* samples. As can be seen from the 3-D plots the darker blue-violet area shows RL peaks covered thicknesses and corresponding frequency range. These values can be cross-verified from Table 4.8.

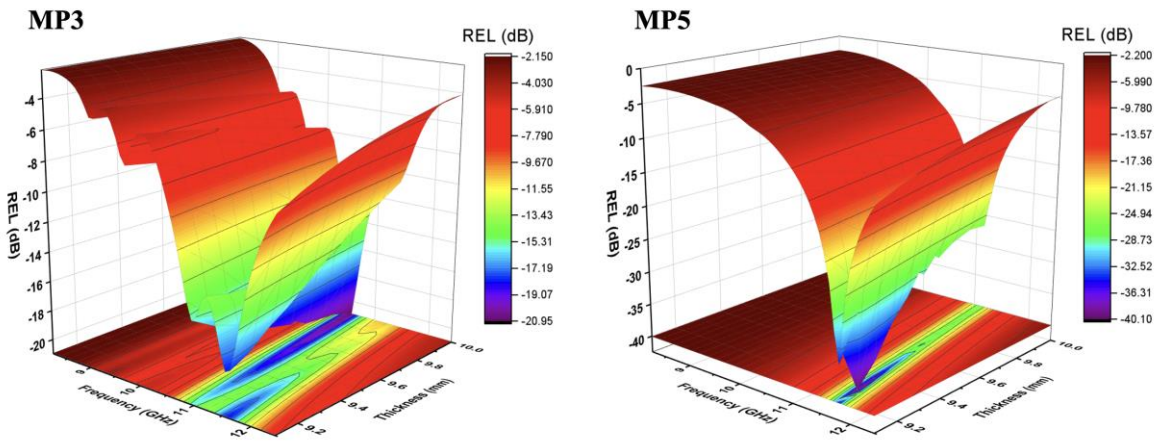

Figure 4.46: Three-dimensional (3D) Plots of Reflection loss at Various Frequencies and Thicknesses for *MP3* and *MP5* Samples

Table 4.8: Computed Parameters for Microwave Absorption (RL >-10 dB)

Co-Mg content	Matching Thickness (mm)	Matching Frequency (GHz)	Maximum RL (dB)	Frequency Band for RL > -10 dB (GHz)	Bandwidth for RL > -10 dB (GHz)	BWT	PBW
MP3	3.1	11.22	-11.01	11.05-11.22	0.17	0.05	1.51
	3.2	9.80	-11.32	11.14-11.30	0.16	0.05	1.63
	3.3	9.88	-12.18	9.7-9.88	0.18	0.05	1.82
	3.4	9.80	-14.00	9.7-9.96	0.26	0.08	2.65
	3.5	9.88	-15.21	9.12-9.96	0.84	0.24	8.50
	3.6	9.88	-16.66	9.12-10.04	0.92	0.26	9.31
	3.7	9.88	-17.53	9.04-10.04	1.00	0.27	10.12
	3.8	9.88	-17.37	8.96-10.04	1.08	0.28	10.93
	3.9	9.21	-16.74	8.96-10.04	1.08	0.28	11.73
	4.0	9.21	-18.12	8.87-10.04	1.17	0.29	12.71
	4.1	9.21	-18.32	8.87-9.96	1.09	0.27	11.84
	4.2	9.21	-17.28	8.70-9.96	1.26	0.30	13.68
	4.3	9.21	-15.69	8.62-9.96	1.34	0.31	14.55
	4.4	9.21	-14.10	8.45-9.37	0.92	0.21	9.99
	4.5	9.21	-12.68	8.36-9.29	0.93	0.21	10.10
	4.6	9.29	-10.71	8.24-9.29	1.05	0.23	11.30
	4.7	8.37	-12.37	8.20-8.70	0.50	0.11	5.98
	4.8	8.28	-13.03	11.05-11.30	0.25	0.05	3.02

	4.9	8.20	-13.72	11.05-11.30	0.25	0.05	3.05
	8.4	12.40	-19.03	11.46-12.4	0.94	-	-
	8.5	12.23	-18.53	10.80-12.4	1.60	-	-
	8.6	12.06	-18.32	10.72-12.4	1.68	-	-
	8.7	11.90	-17.13	10.88-12.4	1.52	-	-
	8.8	11.81	-18.59	10.88-12.4	1.52	-	-
	8.9	11.73	-18.70	10.88-12.31	1.43	-	-
	9.0	11.73	-18.11	10.72-12.23	1.51	0.17	12.88
	9.1	11.56	-18.16	10.72-12.40	1.68	-	-
	9.2	11.48	-17.30	10.63-12.06	1.43	-	-
	9.3	10.89	-17.25	10.55-11.98	1.43	0.15	13.13
	9.4	10.89	-18.12	10.55-11.81	1.26	0.13	11.57
	9.5	10.89	-18.12	10.55-11.98	1.43	0.15	13.13
	9.6	10.80	-19.08	10.38-11.64	1.26	0.13	11.66
	9.7	10.72	-19.70	10.38-11.56	1.18	0.12	11.01
	9.8	10.64	-7.52	10.30-11.56	1.26	0.13	11.85
MP5	8.2	12.40	-12.38	11.89-12.4	0.51	-	-
	8.3	12.40	-13.80	11.72-12.4	0.68	-	-
	8.4	12.15	-14.29	11.39-12.40	1.01	-	-
	8.5	12.40	-17.07	11.39-12.40	1.01	-	-
	8.6	12.23	-18.63	11.47-12.4	0.93	-	-
	8.7	12.15	-20.63	11.39-12.40	1.01	-	-
	8.8	12.06	-22.98	11.30-12.40	1.10	-	-
	8.9	11.98	25.88	11.22-12.40	1.18	-	-
	9.0	11.90	-29.67	11.14-12.40	1.26	-	-
	9.1	11.81	-34.68	11.05-12.40	1.35	0.15	11.43
	9.2	11.73	-40.06	10.97-12.40	1.43	0.16	12.19
	9.3	11.64	-37.65	10.97-12.40	1.43	0.15	12.28
	9.4	11.48	-28.54	10.88-12.23	1.35	0.14	11.76
	9.5	11.48	-31.17	10.80-12.06	1.26	0.13	10.98
	9.6	11.39	-29.32	10.72-11.98	1.26	0.13	11.06
	9.7	11.31	-28.13	10.63-11.89	1.26	0.13	11.14
	9.8	11.22	-27.05	10.63-11.81	1.18	0.12	10.51

Equation 3.16 states that the simulated thickness (t_m^{sim}) is used to compute RL, and n = 1,3,5,..., etc. is used to obtain the calculated thickness (t_m^{cal}) from (3.16). To determine the link between RL peaks and the quarter wavelength mechanism, both parameters are examined. Plots of the calculated thickness ($n\lambda/4$) in the frequency regime are displayed in Figs. 4.41(b) to 4.45 (b). By stretching a vertical line from RL peaks towards thickness–frequency graphs, the calculated thickness ($n\lambda/4$) and the simulated thickness (t_m^{sim}) are compared. Plots seem to suggest that *MP3* compositions with calculated thickness $\lambda/4$ of n = 1, 5 satisfy the $\lambda/4$ mechanism, while composition *MP5* is solely dependent on $5\lambda/4$ values.

For *MP3* composition, the frequency range of 8.36 to 11.22 GHz, 11.56 to 12.23 GHz, and 10.20 to 12.40 GHz has RL > -10 dB along with thicknesses of 3.5 to 4.4 mm, 8.0 to 9.0 mm, and 9.1 to 10.0 mm, respectively. This composition exhibits the maximum RL of -19.70 dB with a thickness of 9.7 mm In Table II, the -10 dB a broad bandwidth of 1.51 GHz and 1.43 GHz are reported from 10.72 to 12.4 GHz, and 10.88 to 12.4 GHz at 8.9 and 9.0mm respectively. Thicknesses 9.3 and 9.5 mm of *MP3* also show a broad AB of 1.43 GHz. The RL values associated with -10 dB are observed for *MP3* at thicknesses ranging from 3.1 to 4.9 mm and 8.0 to 10.0 mm. *MP3* has a broader AB compared to *MP5*. For the *MP5* case, -10 dB absorption bandwidth (AB) of 1.43 GHz, 1.35 GHz, and 1.26 GHz are observed from 10.97 to 12.4 GHz, 11.05 to 12.4 GHz, and 11.14 to 12.4 GHz with the matching thickness of 9.2 to 9.3 mm, 9.1 and 9.4 mm and 9.5 to 9.7 mm respectively.

4.2.4.4 Impedance matching mechanism

$Z_o = (\mu/\varepsilon)^{1/2} = 377\ \Omega$, is the characteristic impedance of free space, where μ/ε is the permeability/permittivity of the space and the impedance of the absorber is Z_{in}. Because of the difference in their permittivity/permeability values, absorbers have different impedances from free space. When a microwave signal traveling through free space interacts with an absorber, some of the signal will be reflected from the absorber, depending on the impedance inequality between Z_{in} and Z_o; the greater the difference, the greater the reflection.

Due to the large difference between Z_{in} and Z_o, only a small fraction of the microwave signal enters the absorber, leaving the majority of the reflected signal behind. This means that even if the absorber has the maximum dielectric and magnetic loss, the attenuation/absorption of the signal inside the absorber is negligible because the majority of the signal is reflected. For this reason, it is important to take free space and impedance matching into account when designing the absorber.

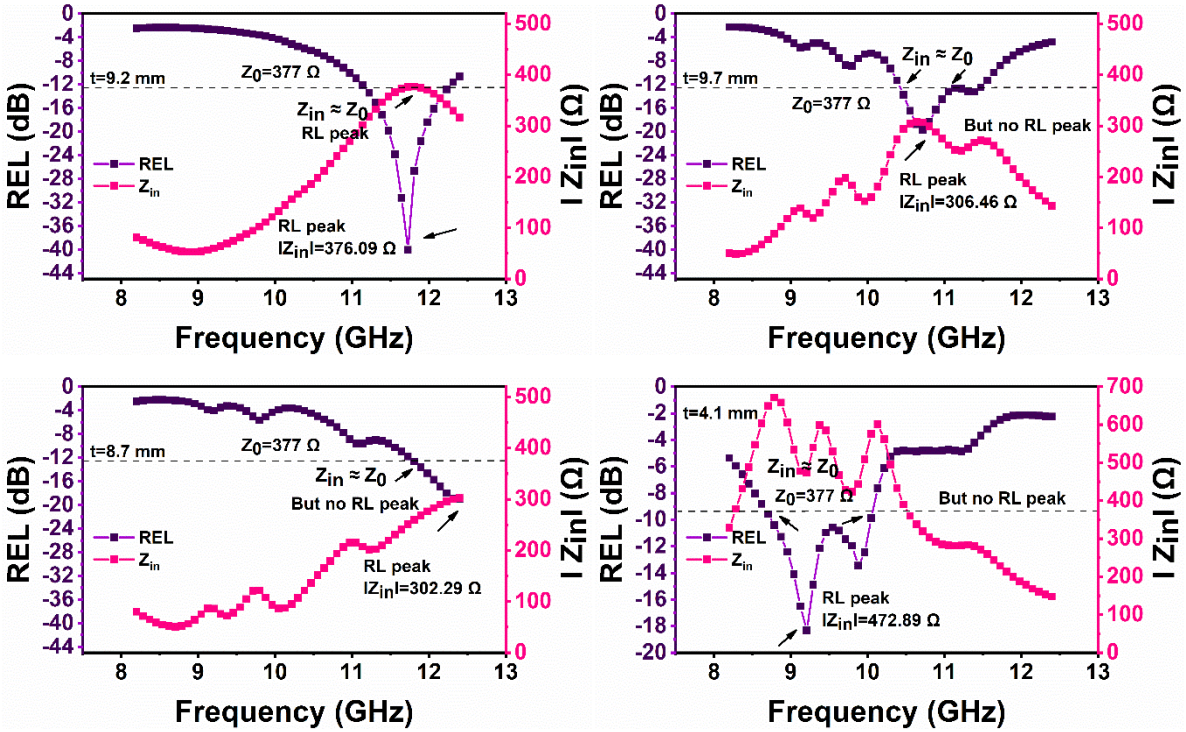

Figure 4.47: Dependence of RL and Z_{in} on Frequency in *MP3, MP5* Composition

Figures 4.47 and Figures 4.48 show different graphs for RL and impedance, i.e., Z_{in}, with frequency regimes for both compositions. In both of these compositions, impedance-matching conditions may arise in the form of RL peaks with $Z_{in} \sim Z_o$ (377) at specific frequencies that correspond to different matching thicknesses.

Z_{in} values for compositions are listed in Table 4.9 and are derived from Z_{in} plots in the aforementioned figures. There is an existence of impedance matching condition for *MP5*, for 9.2 mm thickness, matching frequency of 11.72 GHz, RL is - 40.061 dB with Z_{in} = 376.09 Ω. For *MP3* composition, the values of Z_{in} (Table 4.9) are from 284 to 301 Ω for an 8.1 to 10.0 mm thickness and 387 to 672 Ω for a thickness of 3.1 to 4.9 mm, which drifts away from the characteristic impedance value Z_o = 377 Ω. In *MP3* composition, there seems to be a problem, though the highest RL values from the table can be noted as -18.31 dB, -19.03 dB, and -19.70 dB for 4.1 mm, 8.4 mm, and 9.7 mm, but the values of Z_{in} are 472.89 Ω, 302.29 Ω and 306.46 Ω respectively, which drifts away from Z_o = 377 Ω.

It is demonstrated by the fact that $|Z_{in}|$ (in Equation 3.17) is a complex expression that uses both real and imaginary terms, such as Z_{real} and Z_{img}. Therefore, Z_{real} and Z_{img} are computed from (Equation 3.16), and their corresponding curves are displayed in the domain of thickness and frequency for *MP3* and *MP5* composition, which are shown in Figure 4.48.

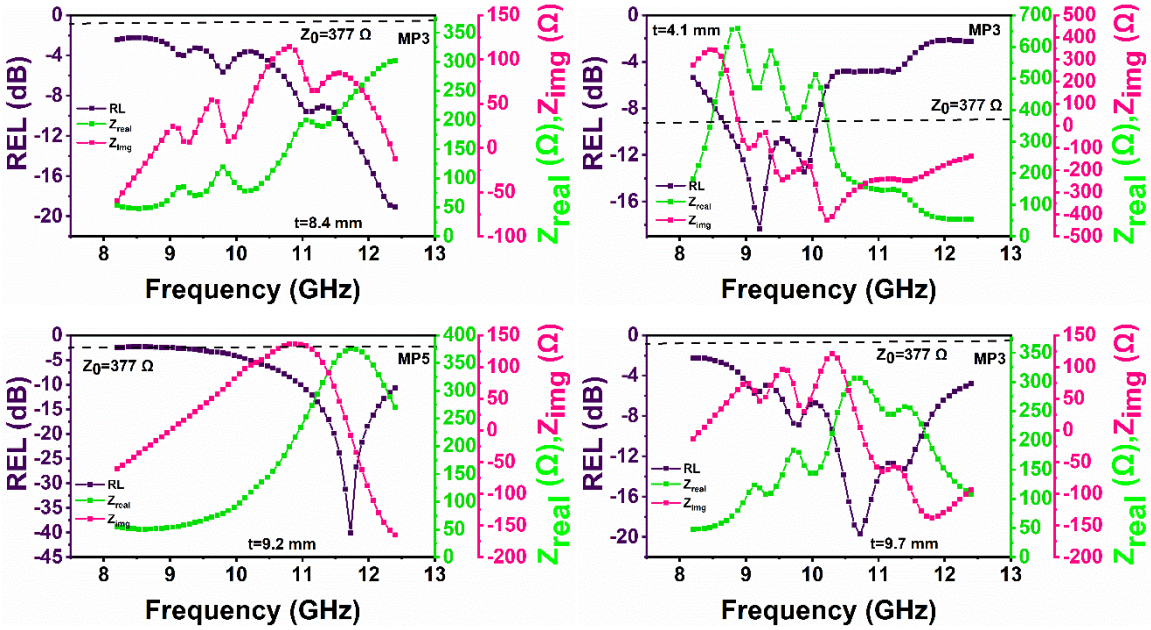

Figure 4.48: Dependence of RL, Z_{in}, Z_{real}, and Z_{img} on Frequency *MP3, MP5* Composition

Likewise, Z_{real} and Z_{img} values for RL_{max} are calculated from plots and displayed in Table 4.9. It makes it clear that composition MP5 has the highest RL value with Z_{real} = 376.023 and Z_{img} = -7.4, it is quite close to 377 Ω and zero in comparison to other compositions. As a result, between the two compositions, the highest RL, RL_{max} = -40.06 dB at 11.72 GHz. *MP3* compositions have lower RL_{max} values than *MP5* due to a greater offset of Z_{real} and Z_{img} values from 377 Ω and/or zero. While the impedance mechanism quantifies more substantially at *MP5*, the quarter wavelength mechanism is met in both compositions. It can also be noted that the addition of PANI as a matrix in the composite samples has improved the RL range considerably from that of ferrite samples without PANI.

Table 4.9: Impedance Parameters of RL Peaks at Different thickness

Co-Mg Content	Matching Thickness (mm)	Matching Frequency (GHz)	Maximum RL (dB)	Z_{real} (Ω)	Z_{img} (Ω)	Z_{in} (Ω)
MP3	3.1	11.22	-11.01	672.61	0.07	672.61
	3.2	9.80	-11.32	402.61	218.56	458.11
	3.3	9.88	-12.18	385.24	193.23	430.98
	3.4	9.80	-14.00	482.89	137.77	502.16
	3.5	9.88	-15.21	456.58	122.64	472.76
	3.6	9.88	-16.66	480.19	72.90	485.69
	3.7	9.88	-17.53	491.01	17.50	491.33

	3.8	9.88	-17.37	487.57	-38.61	489.09
	3.9	9.21	-16.74	481.07	69.69	486.09
	4.0	9.21	-18.12	483.16	12.16	483.31
	4.1	9.21	-18.32	471.01	-42.15	472.89
	4.2	9.21	-17.28	447.51	-88.92	456.26
	4.3	9.21	-15.69	416.69	-125.87	435.29
	4.4	9.21	-14.10	382.47	-152.72	411.83
	4.5	9.21	-12.68	347.90	-170.50	387.44
	4.6	9.29	-10.71	342.33	-216.09	404.83
	4.7	8.37	-12.37	602.31	71.73	606.57
	4.8	8.28	-13.03	566.87	93.53	574.53
	4.9	8.20	-13.72	520.62	119.04	534.05
	8.4	12.40	-19.03	302.05	-12.09	302.29
	8.5	12.23	-18.53	297.66	-9.67	297.82
	8.6	12.06	-18.32	295.65	-6.36	295.72
	8.7	11.90	-17.13	288.07	26.07	289.25
	8.8	11.81	-18.59	297.75	-5.01	297.80
	8.9	11.73	-18.70	298.99	-9.09	299.13
	9.0	11.73	-18.11	299.62	-33.23	301.46
	9.1	11.56	-18.16	294.64	-10.27	294.81
	9.2	11.48	-17.30	286.90	-9.91	287.08
	9.3	10.89	-17.25	290.99	31.98	292.74
	9.4	10.89	-18.12	294.62	12.75	294.89
	9.5	10.89	-18.12	294.62	12.75	294.89
	9.6	10.80	-19.08	301.54	-1.59	301.54
	9.7	10.72	-19.70	306.43	4.52	306.46
	9.8	10.64	-7.52	700.86	350.02	783.40
MP5	8.2	12.40	-12.38	235.96	43.86	240.01
	8.3	12.40	-13.80	252.87	34.20	255.18
	8.4	12.15	-14.29	262.23	45.91	266.22
	8.5	12.40	-17.07	284.44	4.15	284.47
	8.6	12.23	-18.63	294.92	7.88	298.39
	8.7	12.15	-20.63	312.89	2.27	312.90
	8.8	12.06	-22.98	327.08	-2.19	327.09

8.9	11.98	25.88	340.93	-5.52	340.97
9.0	11.90	-29.67	354.04	-7.05	354.11
9.1	11.81	-34.68	365.60	-7.59	365.68
9.2	11.73	-40.06	376.02	-7.41	376.10
9.3	11.64	-37.65	385.07	-5.89	385.12
9.4	11.48	-28.54	385.94	27.13	386.89
9.5	11.48	-31.17	398.44	0.09	398.44
9.6	11.39	-29.32	403.25	4.75	403.28
9.7	11.31	-28.13	405.88	10.41	406.02
9.8	11.22	-27.05	407.21	17.32	407.58

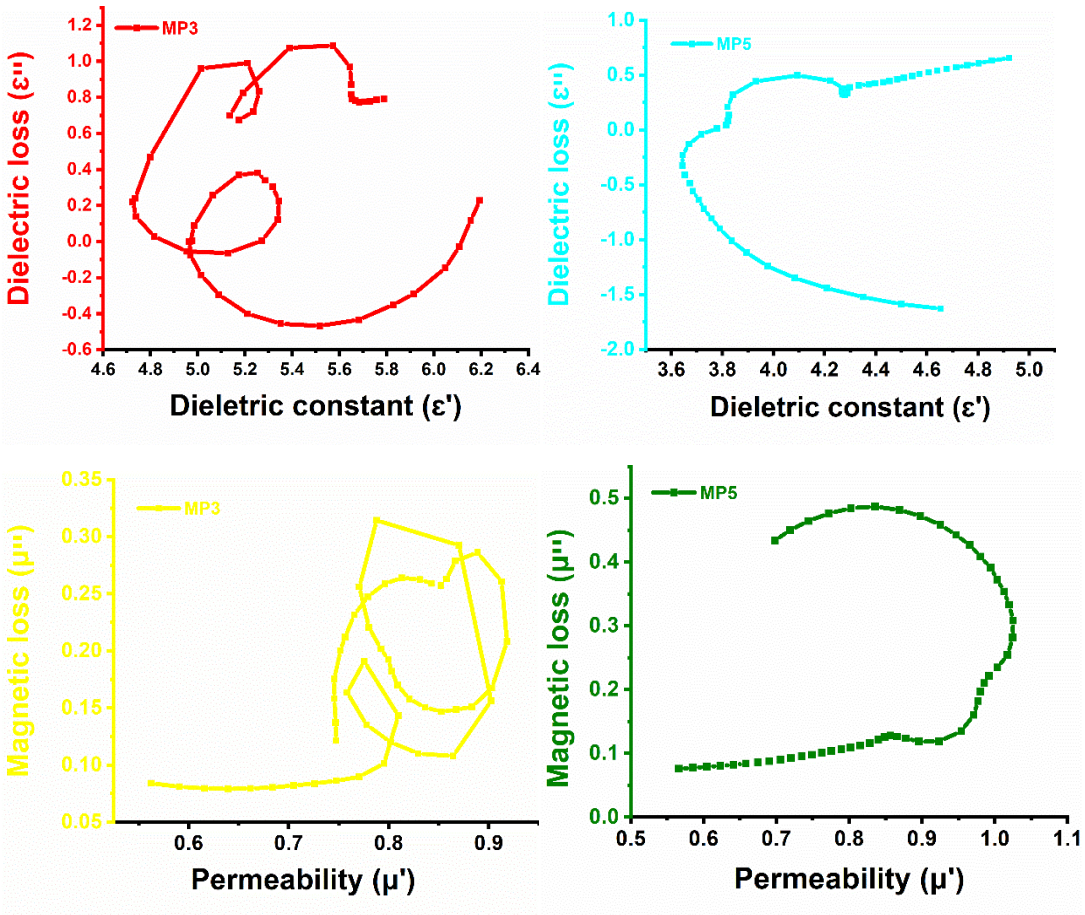

Figure 4.49: Cole–Cole Plots in *MP3* and *MP5* Compositions

Figure 4.49 shows Cole–Cole [174], [175] plots to verify relaxation for compositions *MP3* and *MP5*. But no prominent effect of the Cole-Cole plot is seen concerning the RL peaks here. Though multiple relaxations are shown in ε′ vs. ε″ plots and inverted semicircles in μ′ vs. μ″ plots, the relaxation process may be dominated by impedance matching and quarter wavelength mechanism.

4.2.4.5. Eddy Current Loss

The role of the eddy current loss in the magnetic loss contribution is also discussed in the previous section (4.1.4.5**)**. For the given test frequency, the value of C_0 does not remain constant. So, it can be concluded here that the eddy current loss does not contribute much to the microwave absorption.

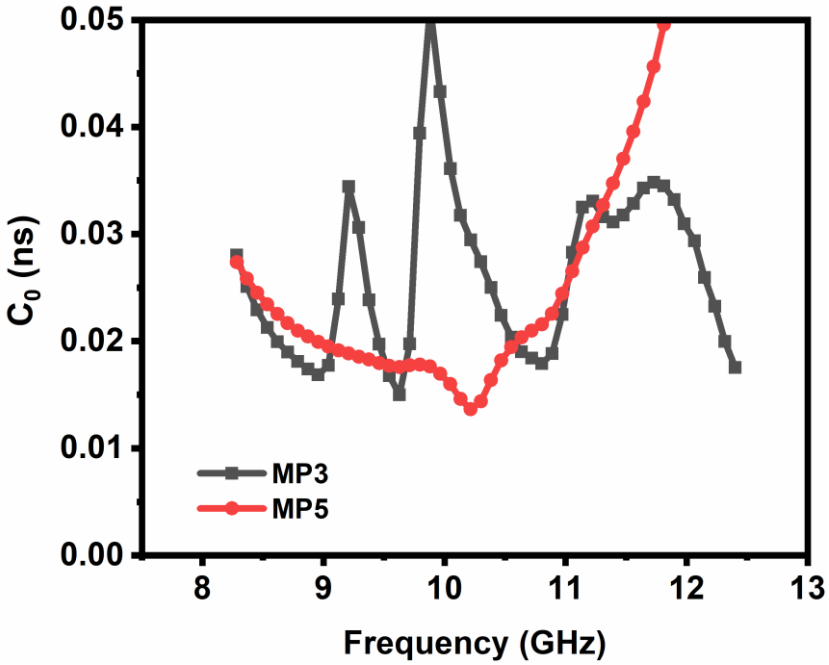

Figure 4.50: C_0 Versus Frequency Variation for Compositions *MP3* and *MP5*

4.2.4.6. BWT/Percentage Bandwidth Ratio

The relations used to estimate the bandwidth-to-thickness ratio (BWT) and percentage bandwidth (PBW) in ferrite samples are already discussed in section 3.8.

Table 4.8 depicts BWT for maximum RL with frequency, *MP3* shows greater BWT values than *MP5*. This shows that with doping of Co-Mg, BWT has decreased. It has the highest value of 0.31 at 4.3 mm thickness, matching frequency of 9.21 GHz, RL = -15.69 dB with the AB of 1.34 GHz.

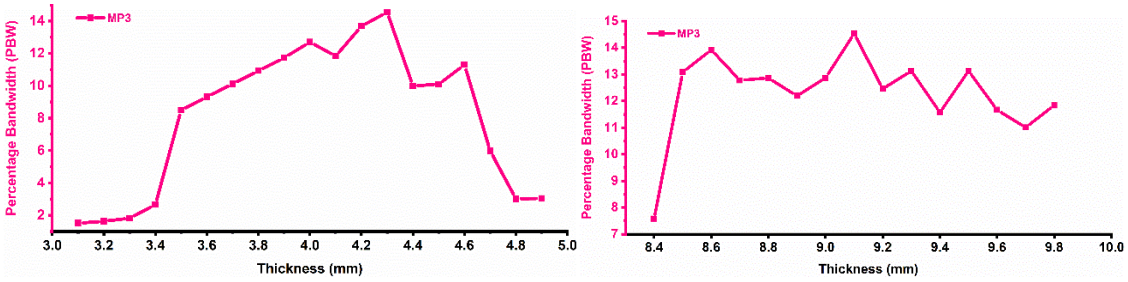

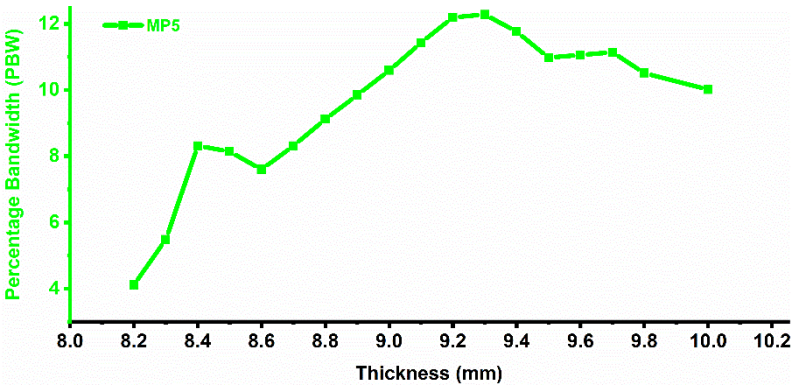

Figure 4.51: Bandwidth (%) Variation with thickness in Ferrite /PANI Compositions

Figure 4.51 above shows two PBW graphs for *MP3*, one from a thickness of 3 to 5 mm and the other from 8.3 to 10 mm. For *MP5*, the third plot of PBW is for thickness 8 to 10 mm.

The PBW is More or less the same for both compositions and shows no prominent change due to doping. It can be noted that the PBW ranges between 1-14.55 %.

4.3 Co^{2+}-Cu^{2+} substituted $Ba_{0.2}Sr_{0.8}Co_xCu_xFe_{12-2x}O_{19}$ hexaferrite

In this section, we have synthesized a hexaferrite with Co and Cu substitutions via the sol-gel technique. This composition hexaferrite will be given as $Ba_{0.2}Sr_{0.8}Co_xCu_xFe_{12-2x}O_{19}$. The sample names with the codes for each level of substitution in $Ba_{0.2}Sr_{0.8}Co_xCu_xFe_{12-2x}O_{19}$ are given in Table 4.10

Table 4.10: The Assignment of Sample Names Corresponding to Various Substitution Levels in $Ba_{0.2}Sr_{0.8}Co_xCu_xFe_{12-2x}O_{19}$ Hexaferrite

Sample Composition $Ba_{0.2}Sr_{0.8}Co_xCu_xFe_{12-2x}O_{19}$	Sample Code Name	Sample Code (C-Series)
x = 0.0	$Ba_{0.2}Sr_{0.8}Fe_{12-2x}O_{19}$	C1
x = 0.2	$Ba_{0.2}Sr_{0.8}Co_{0.2}Cu_{0.2}Fe_{11.6}O_{19}$	C2
x = 0.4	$Ba_{0.2}Sr_{0.8}Co_{0.4}Cu_{0.4}Fe_{11.2}O_{19}$	C3
x = 0.6	$Ba_{0.2}Sr_{0.8}Co_{0.6}Cu_{0.6}Fe_{10.8}O_{19}$	C4
x = 0.8	$Ba_{0.2}Sr_{0.8}Co_{0.8}Cu_{0.8}Fe_{10.4}O_{19}$	C5

4.3.1 Structural Analysis

4.3.1.1 X-ray Analysis

The traces of XRD are displayed in Figure 4.52 for prepared samples. All of the aforementioned samples' Bragg peaks appear to be clearly defined, indicating good crystallinity among the specimens. The captured peaks of the sample were compared with the JCPDS#51-1879; the results are shown in the table below. Using the below-provided equations, the unit cell volume and lattice parameters a, c (where a = b) of the synthesized samples were calculated using

equations 3.1 and 3.2 from section 3.2.1 The secondary peak (2 1 4) of the sample was compared with the JCPDS#86-0550 (hematite).

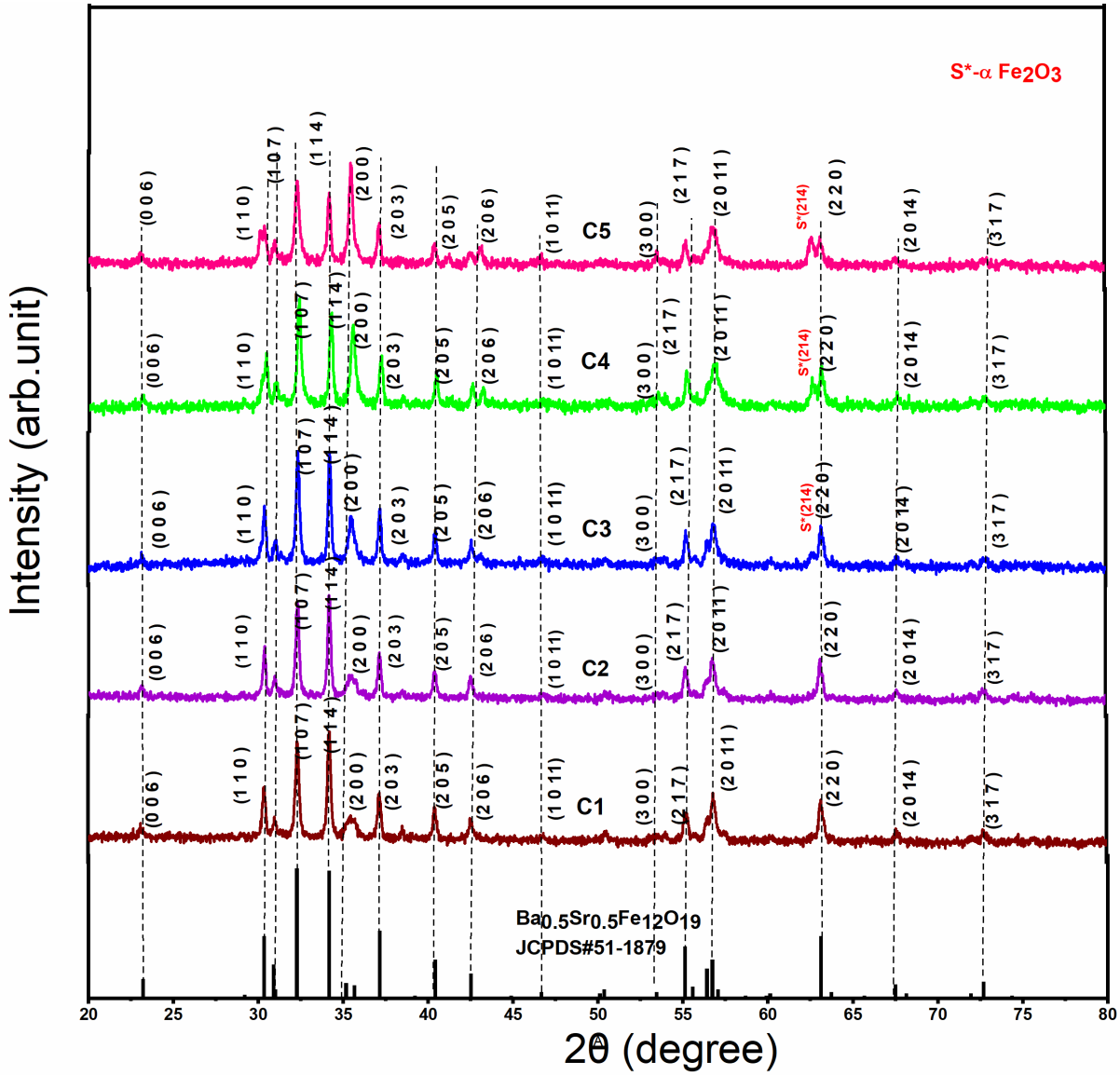

Figure 4.52: X-ray Diffraction Trends of M -type $Ba_{0.2}Sr_{0.8}Co_xCu_xFe_{12-2x}O_{19}$ (*C1, C2, C3, C4 a*nd *C5*) Hexaferrite

Table 4.52 lists the computed structural parameters of the prepared samples. The table below shows that doping of Co-Cu does alter cell volume and lattice constants (*a*, *c*) of samples *C1* to *C5*, the crystallite size goes on decreasing with doping content in samples. Also, it can be verified from the table that lattice constant a varies much more than c. The samples' c/a ratio matches the standard value of 3.93, and the crystallite size stays within 73.13-52.24 nm [18-20].

Table 4.11: Cu-Co content, Lattice Parameters, Unit Cell Volume, Crystallite Size, and Ratio c/a for Ferrite Sample $Ba_{0.2}Sr_{0.8}Co_xCu_xFe_{12-2x}O_{19}$ [*C1, C2, C3, C4 a*nd *C5*]

Co-Cu	Lattice parameters		Ratio	Unit cell vol.	Crystallite Size
Content (x)	a=b (Å)	c (Å)	c/a	V (Å) ^{3}	D_{xrd} (nm)
C1	5.8911	23.1831	3.9353	696.7584	73.1303
C2	5.8913	23.1822	3.9350	696.7786	72.1492
C3	5.8921	23.1821	3.9344	696.9649	58.2741
C4	5.8942	23.1823	3.9331	697.4678	52.2458
C5	5.8933	23.1820	3.9336	697.2458	58.2741

4.3.1.2Field Emission Scanning Electron Microscopy

The samples' grain morphology is shown in Figure 4.53 (a–e). The micrographs show that in the sample with zero doping, i.e., *C1* fused grains lead to the creation of a massive grain. Additionally visible are tiny individual grains, as shown in Figure 4.53 (a-e), with a smaller magnification factor observed in micrometers. Though the observation of grain aggregation is there in all the samples, it is easy to detect individual grains too in doped samples, unlike pure samples. Due to electrostatic as well as magnetic interactions among the ferrite particles, doping results in grain clusters exhibiting an irregular size distribution. As doping levels are increased, the tiny individual grains are more pronounced in the clusters of grains, giving the grain a prominent rice shape. The arrangement of grains has certain spaces that could resist or impede the movement of charge carriers. Now, the grain boundaries are higher, and the resistance to the applied field will be greater as grain size decreases, changing the process of charge transport.

An EDX analysis was conducted to determine the elemental composition of the synthesized $Ba_{0.2}Sr_{0.8}Co_xCu_xFe_{12-2x}O_{19}$ compounds. Figure 4.54 displays the EDX spectra acquired for samples *C4* and *C5*. As observed in the spectra, the elemental composition of *C4* it consists of less percentage of Cu than that in the *C5* sample. The weight and atomic percentages of all elements present in the final compositions are provided in the Figure 4.54.

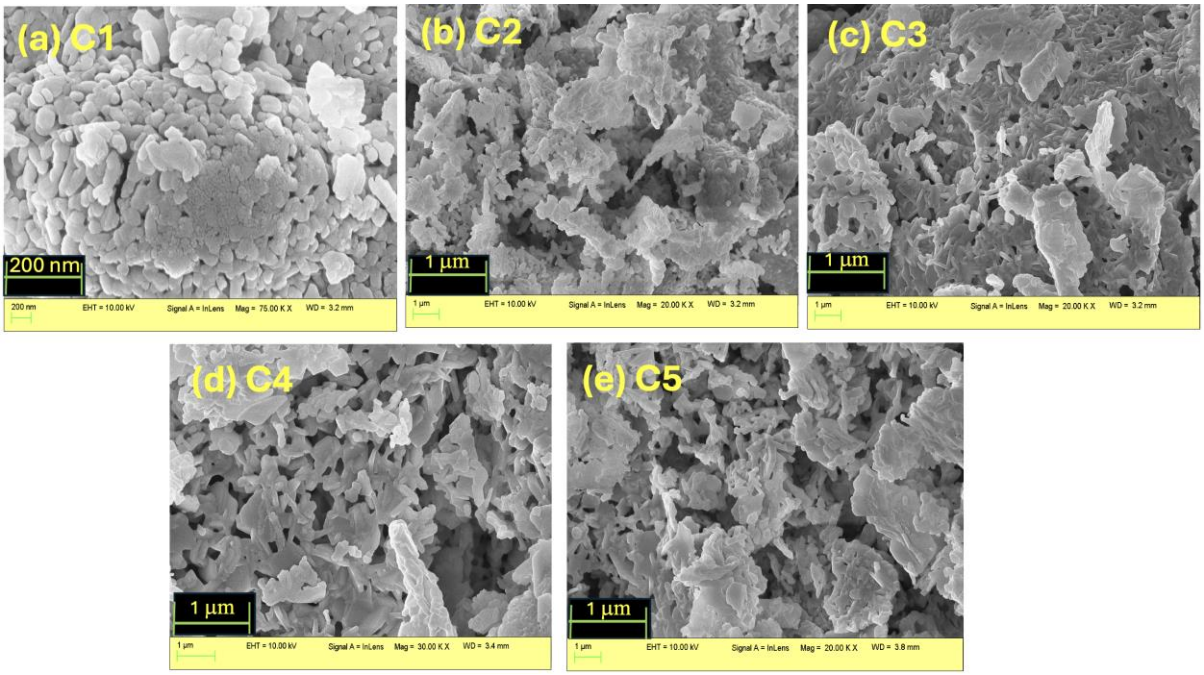

Figure 4.53: SEM Micrographs of Ferrite Samples: $Ba_{0.2}Sr_{0.8}Co_xCu_xFe_{12-2x}O_{19}$ (*C1, C2, C3, C4* and *C5*)

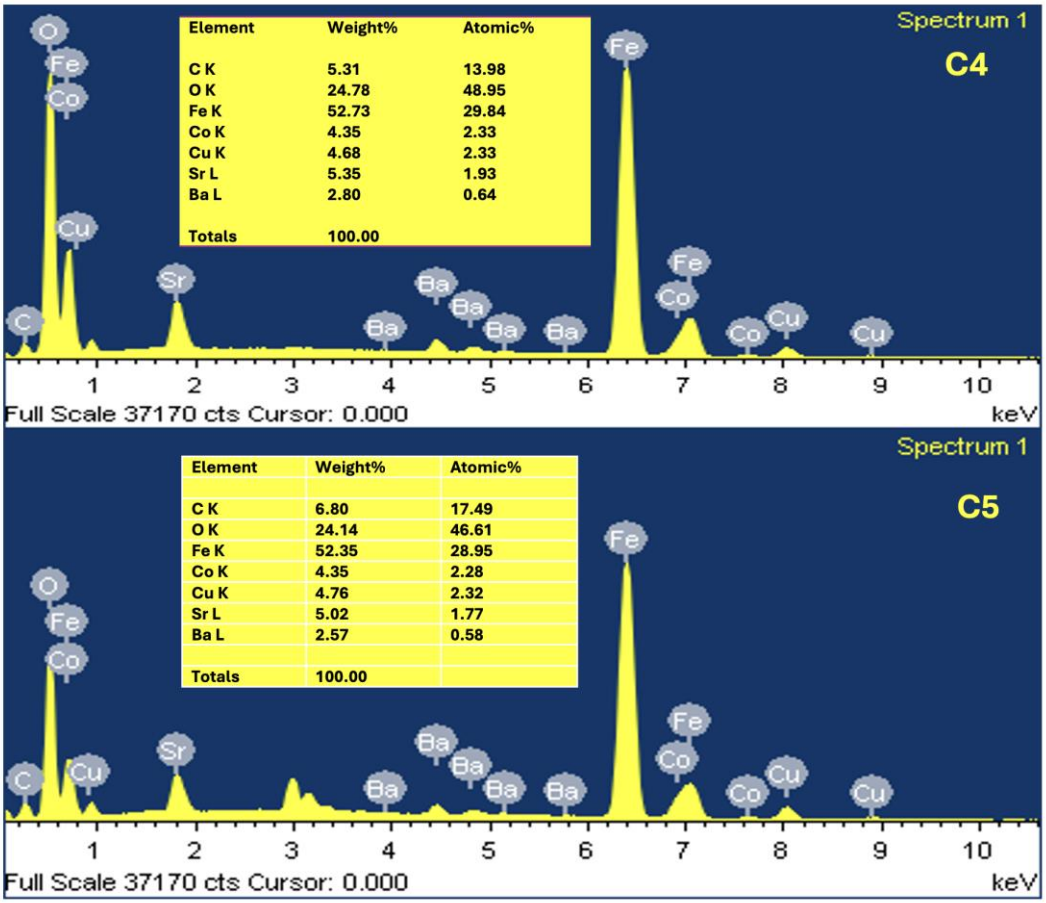

Figure 4.54: EDX Spectra $Ba_{0.2}Sr_{0.8}Co_xCu_xFe_{12-2x}O_{19}$ Hexaferrite for Samples *C4* and *C5*

4.3.2 Electrical Analysis

4.3.2.1 Dielectric permittivity

All necessary mathematical relations for electrical parameters viz-a-viz, $\varepsilon', \varepsilon''$ and $tan\delta$ have been mentioned in the previous section 3.1.1.

There were measurement uncertainties in the low-frequency region, thus the plots are drawn from 100 Hz to 2 MHz. With operational frequencies from 100 Hz to 2 MHz, Figures 4.55 and 4.56 show two different types of plots: dielectric permittivity and dielectric loss. Figure 4.55 illustrates how it exhibits dispersion in the spectrum of low frequencies, and it becomes frequency-independent beyond 10 kHz in each sample. It has been found that the graph declines non-monotonically (non-linearly) as the Cu content increases from *C1* to *C5*. From the data, it can also be seen that the highest value of the dielectric permittivity in the low-frequency regime is for *C4*, now, even if the frequency is increased, the highest value ε' is found for the same sample. The lowering of dielectric permittivity values with decreasing frequency can be specified using the interfacial polarization model of Maxwell Wagner. This model is often imposed to elaborate the dielectric properties of hexaferrite.

In light of this approach, hexaferrite contains grains that are conducting, which are disconnected from the insulating grain boundaries. The porosity between the grains prevents electrical conduction but helps in polarization. In the process of sintering the pellets, the air present inside the furnace oxidizes the grain boundary more than the interior of the grains. Due to this, there is a more insulating character in grain boundaries than in bulk grains. During the process of conduction, electrons hop toward grain boundaries. But when there is strong resistance provided by the boundaries of the grains, electrons accumulate at grain boundaries, inducing polarization that results in a dielectric permittivity with elevated values. It is commonly known that electrons can hop between octahedral locations, which indeed gives ferrites their conductivity and polarization.

Verwey-de-Boer hopping elaborates on the electrical conduction which occurs in ferrites [160]. According to Verwey, the hopping of electrons plays a major role in the conduction process. This hopping primarily occurs between electrons of several ions made of the same element that was created throughout the sintering process. The concentration of Fe^{2+}/Fe^{3+} ions in ferrite material differentiates it from the other materials. However, this concentration relies on several variables, including sintering time, temperature, etc. Fe ions that drive valence electrons to bounce between the +2 and +3 states of valency contribute towards the polarization. Charges are displaced due to this hopping in the applied electric field's direction.

As discussed before in Figures 4.55 and 4.56, after a certain frequency, the Dielectric permittivity/loss approaches a steady state number, making it impossible for the electron hopping to continue between Fe ions of +2 and +3 states. The largest ferrous ion concentration at the octahedral positions is correlated with the highest dielectric permittivity at *C1*, yet in the remaining doped samples, their amount is minimal.

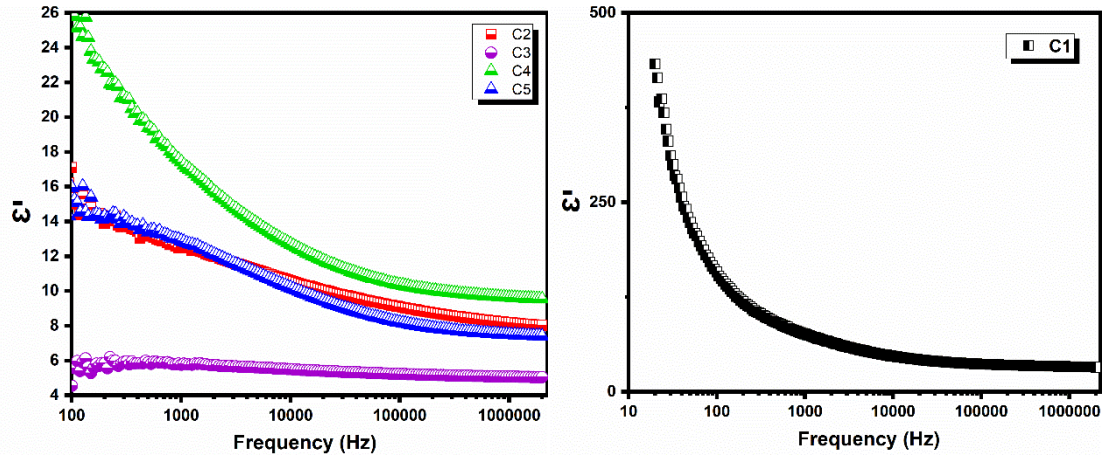

Figure 4.55: Variation of Dielectric Spectra of Real Component Ferrite Sample $Ba_{0.2}Sr_{0.8}Co_xCu_xFe_{12-2x}O_{19}$ (a) *C2, C3, C4, C5,* (b) *C1* Function of Frequency

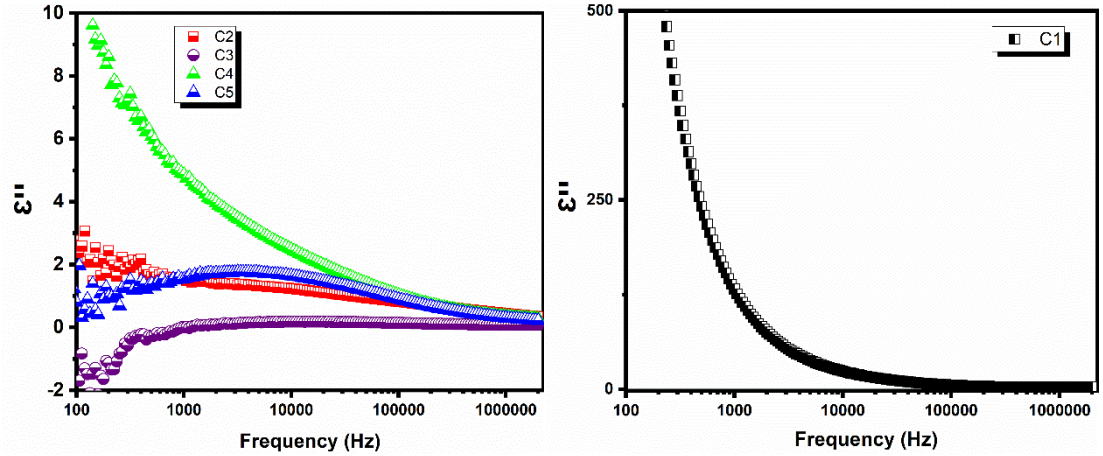

Figure 4.56: Variation in the Ferrite Sample's Dielectric Spectra of Imaginary Part $Ba_{0.2}Sr_{0.8}Co_xCu_xFe_{12-2x}O_{19}$ (a) *C2, C3, C4, C5,* (b) *C1* function of Frequency

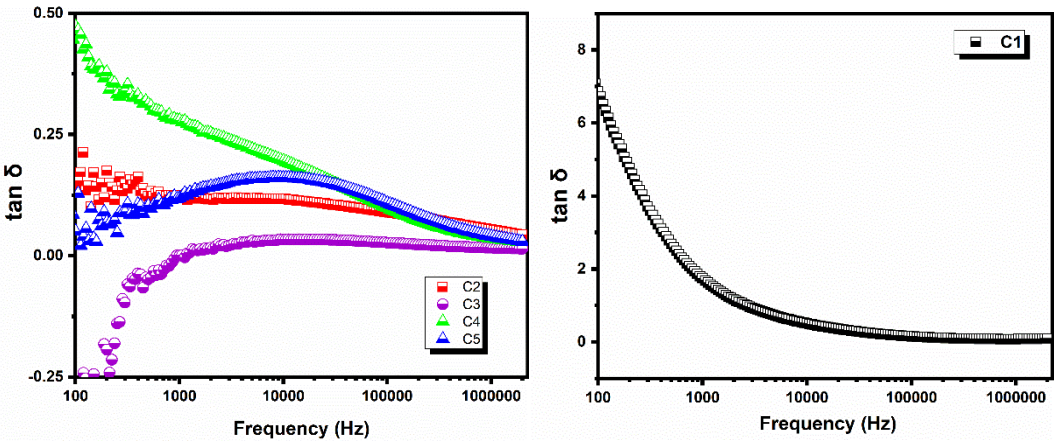

Figure 4.57: Variation of Ferrite Sample's Dielectric loss Tangent $Ba_{0.2}Sr_{0.8}Co_xCu_xFe_{12-2x}O_{19}$ (a) *C2, C3, C4, C5,* (b) *C1* Function of Frequency

From Figure 4.57, for undoped sample *C1*, the maximum value of loss tangent is around seven and reduces sharply with a rise in frequency. For samples *C2* and *C4*, the values decrease with a rise in frequency, whereas for *C3* at initial frequencies, it increases and stabilizes at a constant value as it crosses 10 kHz. The sample *C5* is the only sample where, at first, the value of loss tangent increases with frequency and then decreases with frequency. It is evident from the above figure that the value of loss tangent for all doping samples at higher frequency come together to stay around 0.0-0.08.

The phenomenological theory of dielectrics proposed by Koop accounts for this drop in the value of *tan* δ [161]. Factors responsible for this variation are interface traps, interfacial polarization, Fe^{2+}/Fe^{3+}content, structural oneness, stoichiometry, and, most importantly, the sintering conditions. In sample *C5*, peaking behavior can be seen at the mid-frequency regime. The cause of peaking behavior in *tan* δ is related to traps created at the interfaces and the interfacial polarization. These interfaces are formed at the time of the sintering in the samples that cause interfacial polarization, and charge carriers tend to bind in these traps. Across the ferrite interfaces, an electric field is produced by the applied AC signal that is dynamic, and this fluctuating field leads all charge carriers to leave the restricted territory. This rapidly fluctuating electrical field, due to the rise in frequency values, imposes a fast-changing field on the charge carriers, finally resulting in charge carriers moving away from the traps. The charge carriers' density is raised by this procedure, and at this point, grain boundaries provide obstruction to the rising charge pathways. The loss tangent has a low value because the energy needed for the electron exchange between Fe^{2+} and Fe^{3+} ions is smaller for high values of frequency.

4.3.2.2 Electric modulus analysis

This investigation aids in the resolution of the relaxation technique and reduces the impact of electrode polarization.

M' and M'' are the real and imaginary parts of the complex electric modulus and are calculated using equation 3.8 and equation 3.9 respectively (from section 3.3.2).

Figure 5.58 illustrates the characteristic feature of M along the frequency as a broad, asymmetric peak in the imaginary portion of the electric modulus graph [162-163]. Figure 5.58 (a) shows the variation of the real component of the modulus *(M')* vs the log of frequency and provides information on conductivity. At lower frequencies, it can only be set to a lower value that tends to zero for *C1*, and it also stays at low values (non-zero) among doped samples. The non-linear increment in M' with frequency is also visualized in all samples. It is observed that as the doping in the sample is increased, the M' value is increased for *C2*, being maximum for *C3*, but again, there is an overall decrease even if the doping is increased for *C4* and *C5*. The charge carriers are influenced by the applied electric field. However, these conclusions are influenced by the lack of the restoring force that controls the movement of these charge carriers. This pattern implies that conductive grains are necessary for electrical characteristics.

The information concerning charge transport methods, such as electrical transport, conductivity relaxation, and ion dynamics, is provided by the variations in the plots of the imaginary component electric modulus in the frequency domain, Figure 4.58 (b). The graph of M″ illustrates how each sample's peaks rise to their greatest peak as the level of doping increases; the peak with the highest value is one with *C5*, i.e., the maximum doped sample.

Ions can successfully hop from one site to another over extended distances in the low-frequency domain. However, the peaking behavior in M″ shows that the longer hopping is not followed by the ions for higher frequencies rather, they are limited to the wells of their limited potential. The area where the peaks are detected indicates a transition from long-range to short-range mobility as frequency increases. The hopping phenomenon for electrical conduction is thus represented by the modulus spectrum. Here, the peak frequency illustrates the conduction relaxation period and frequency peak shifting depicts the samples have a shorter relaxing period.

As previously said, conductivity relaxation is additionally associated with the charge carriers that were released as a result of an increase in frequency. The samples' lack of Debye-type relaxation is depicted by the asymmetric and board peaks observed with doping content.

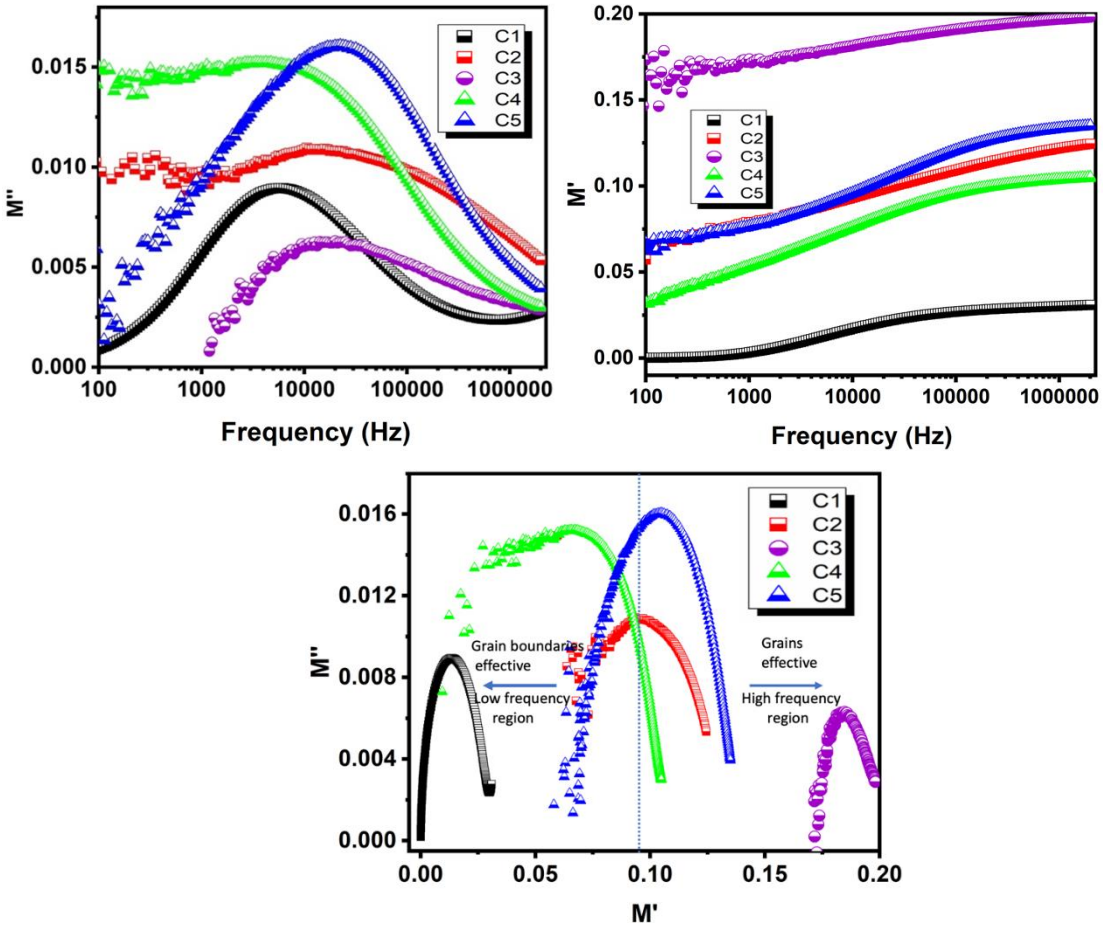

Figure 4.58: Electric Modulus Variation (a) Real Component, (b) imaginary Component of Ferrite Sample $Ba_{0.2}Sr_{0.8}Co_xCu_xFe_{12-2x}O_{19}$ as a Function of Frequency (c) Cole-Cole (*M′* vs *M″*) Plot of Ferrite Sample

Figure 4.58 (c) describes the Cole-Cole plot of $Ba_{0.2}Sr_{0.8}Co_xCu_xFe_{12-2x}O_{19}$. The asymmetric nature of distorted semi-circles has been observed. Co-Cu doping causes the semicircle to move towards a high-frequency domain, from *C1*, *C2*, and *C3*. It can be observed that doping causes an increase in the height of the semicircle, implying grains are more active than the boundaries of the grains. For *C1* and *C4*, grain boundaries are more effective, as can be seen in Figure 4.58 Similarly, *C3* grains are more effective. But as can be seen for *C2* and *C5*, grain boundaries, as well as grains, are collectively participating.

4.3.2.3. Complex impedance spectra

Details of resistance (Z′) and reactance (*Z″*) provide information about the Polycrystalline materials' impedance performance principally caused by their bulk grains and grain boundaries. Given that they have different relaxation times, the bulk grains' impedance and grain boundaries' impedance are handled differently.

The fluctuation of *Z′* vs. frequency is depicted in Figure 4.59 (a). It has been noticed that when the frequency rises, Z′ continuously declines until it practically reaches a constant value at a

specific point. For the *C2* sample to the *C5* sample, *Z′* decreases with frequency and almost stays in a similar range of values.

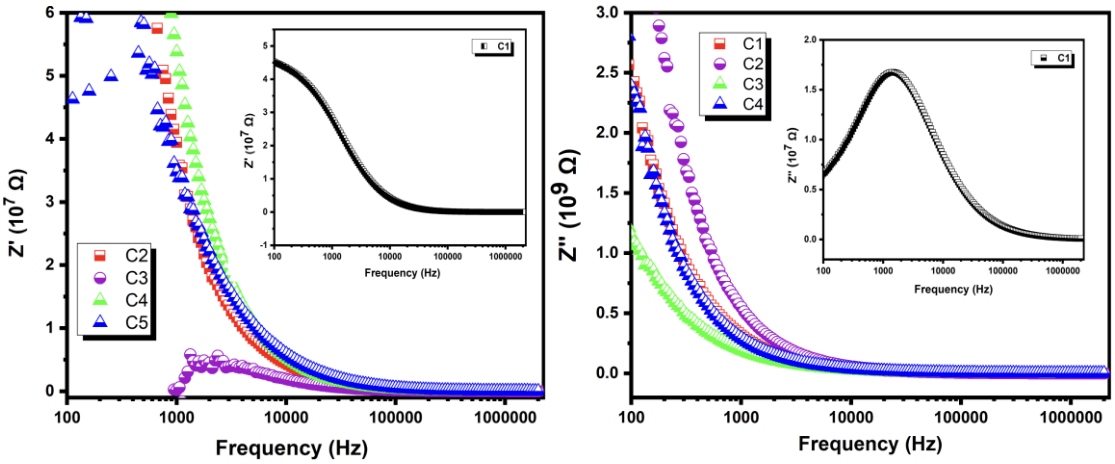

Figure 4.59: Variation In The (a) Dielectric Impedance Real (*Z′*), (b) Dielectric Impedance Imaginary (*Z″*) vs. Frequency ($Ba_{0.2}Sr_{0.8}Co_xCu_xFe_{12-2x}O_{19}$ for *C1, C2, C3, C4 and C5)*

To better comprehend the effect of space charges, the change in Z″ with the variation in frequency has been investigated, as shown in Figure 4.59 (b). It has been observed that there is a steep decrease in imaginary components at a lower frequency regime, and all the values saturate the same range after 10 kHz. The reduction in space charge polarization of the samples is accountable for this decrease in *Z″* value.

In Figure 4.60, for the graph of *Z″* vs *Z′*, every sample depicts a semi-circular arc, with a prominent curve for undoped *C1*. For doped compositions, *C4*, the depression of the arc seems to increase. The Maxwell-Wagner phenomenon, related to interfacial polarization at grain boundaries, is linked to these low-frequency depressions. Semi-Circular arc, as shown for sample *C4*, can be seen as a part of a smaller circle compared to that for other compositions. Here, the semi-circle is shown in the low frequency where grain boundaries are more active. Now, *C2*, *C3*, and *C5* samples display curves in the high-frequency region, depicting grains as more active. The curve of *C1* displays a semicircle and is lying in a high-frequency region, where grains play a prominent role. As can be seen from the grain morphology, in Figure 4.53 (a) *C1*, the grains are fused, but no voids are visible on the contrary, in (e*) C5*, though the grains are fused, voids are prominently visible.

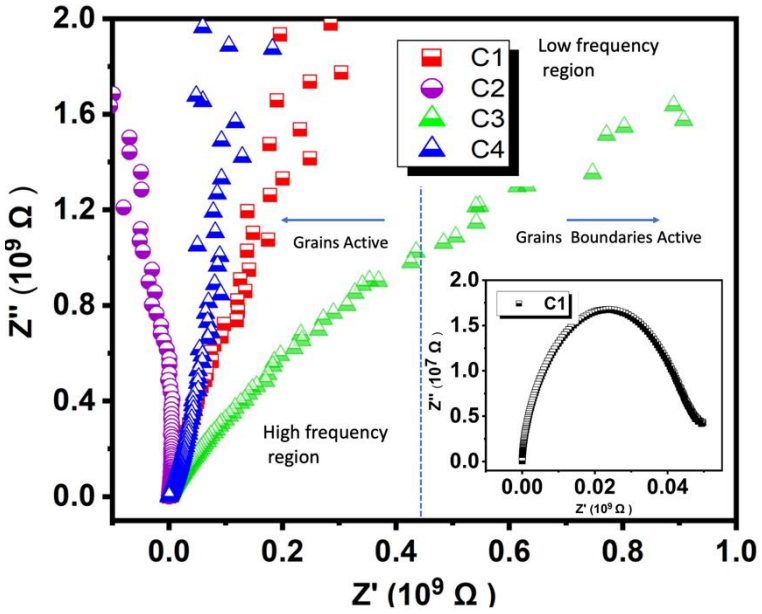

Figure 4.60: Variation in the (a) Dielectric Impedance Real (Z′) Component Versus Dielectric Impedance Imaginary (*Z″*) Component ($Ba_{0.2}Sr_{0.8}Co_xCu_xFe_{12-2x}O_{19}$ for *C1, C2, C3, C4 and C5)*

4.3.2.4 AC Conductivity

The main reason ferrites have AC conductivity is because of the valence electron hopping between Fe^{2+} and Fe^{3+} at Octahedral sites. The frequency increase boosts the charge carriers' hopping frequency, which raises conductivity. Applying the model of polaron hopping, the frequency-dependent conduction mechanism is explained in [124]. According to that model, for short-range polaron hopping, an upward trend in frequency causes a rise in AC conductivity, but for long-range polarization hopping, it decreases. The conductivity phenomena in band conduction are frequency-independent [125].

The curve of AC conductivity in the ferrite samples as a function of frequency is shown in Figure 4.61. In the current study, it is observed that AC conductivity gradually rises after 1 kHz frequency.

Below 1 kHz, it exhibits behavior that is almost frequency-independent, and at this frequency, DC conductivity is transitioned to AC conductivity. The Verwey hopping process is hampered by the doping of Cu^{2+} and Co^{2+} ions in place of Fe^{3+} ions because it limits the range of conduction at octahedral sites. Figure 4.61 shows the resulting drop in conductivity as a result of this. The Jonscher power law, as discussed in [126] expression provides the frequency-dependent AC conductivity, where σ_{dc} is dc conductivity, which is independent of frequency, here A and n are constants but temperature dependent and also depend on what composition the sample

owes.

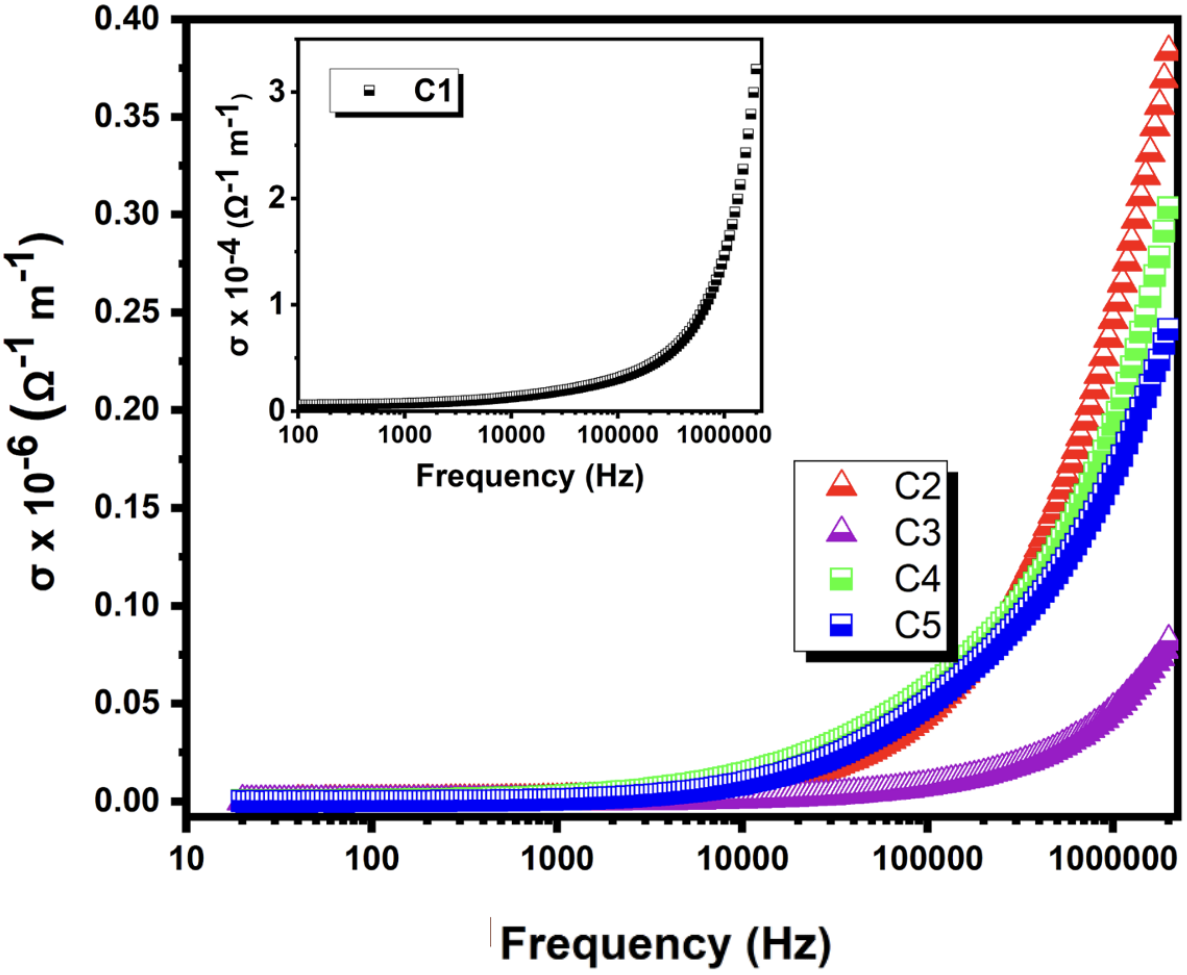

Figure 4.61: Variation of AC Conductivity for Ferrite Sample $Ba_{0.2}Sr_{0.8}Co_xCu_xFe_{12-2x}O_{19}$ for *C1, C2, C3, C4 and C5*

A has units of conductivity, and n is dimensionless. The second term, $A\omega^n$, quantifies the distribution in AC conductivity charts.

The value of n, according to Funke [127], has a physical meaning, where n < 1 denotes a translational motion with abrupt hopping, and n > 1 denotes localized hopping between surrounding locations. Here, n was calculated using fitting in the plots: *C1* - 0.3070, *C2* - 0.8261, *C3* - 0.9522, C*4* - 0.6213, *C5* - 0.8719. As a result, the value of n turns out to be smaller than 1, indicating that charge carriers are hopping along with ac conductivity. Because of the abrupt increase in charge carriers in the aforementioned samples in the high-frequency area, the large values of n imply a rather sharp rise in AC conductivity in that region. High-frequency conductivity is influenced by grains, as was previously addressed [164-165].

4.3.3 Magnetic analysis

As discussed earlier, the electronegativity of cations determines their occupancy at crystallographic sites; more electronegative ions select octahedral spots, which are larger than

tetrahedral positions. Cu^{2+} (1.359) can occupy tetrahedral sites since it is not as electronegative as Co2+ (1.88). The site occupancy of cations can also be ascertained using the d-configuration and the kind of cations that are involved. Cu^{2+} ions, with their d^9 configuration, show tetrahedral site preference. Co^{2+} ions, which usually have a d^7 configuration, can occupy octahedral locations, according to ligand field theory.

Moreover, Cu^{2+} ionic radii can ideally occupy tetrahedral locations since their radii are smaller (57 Å). Octahedral positions at the unit cell can be occupied by Co^{2+} (0.72 Å) ions due to their larger ionic radii compared to the host Fe^{3+} (0.64 Å) ions. The law of saturation is used to determine the M_s and H_a values of the synthetic composites, already discussed in Equation 3.15 section 3.4. Figure 4.62 shows the room-temperature hysteresis loops for each synthesized sample with a 25 kOe field applied. Table 4.12 lists M_r/M_s ratio, coercivity (H_c) , saturation magnetization, anisotropy field (H_a), and remanence magnetization (M_r).

Remanent magnetization, which is often large in M-type hexaferrite, suggests substantial remanence and determines the continued retention of magnetization after an applied field is removed. In addition, the inter-grain group development and magnetic hardness of the material are evaluated using the M_r/M_s ratio, whose value should range from 0 to 1 as discussed previously. Materials with a significant squareness ratio ($0.5<M_r/M_s<1$) are more anisotropic, single-domain, and hard, while those with ($0.05<M_r/M_s<0.5$) have randomly oriented multi-magnetic domains [166].

In the present study M_r/M_s value for the *C1*, *C2*, *C3*, *C4*, and *C5* samples is larger than 0.5, indicating that the particles of the material are single-domain in nature. The saturation magnetization (41.77 emu/g) is at its lowest in a pure sample *C1*; as cations are substituted, this value improves. Table 4.12 shows a 31.87% increase in M_s from 41.77 emu/g (*C1*) to 55.09 emu/g (*C2*), as per the data. Now, there is only a slight change in M_s as the doping is increased, the value of 54.80 emu/g (*C3*) has increased by 31.18% from 41.77 emu/g (C1). In the next sample, there is a swift increase in magnetization saturation by 82% for the (*C4*) sample. For 47.26 emu/g (*C5*), the M_s value is improved by 13.14%. The increased M_s values may be attributed to ions taking up the spin-down sites.

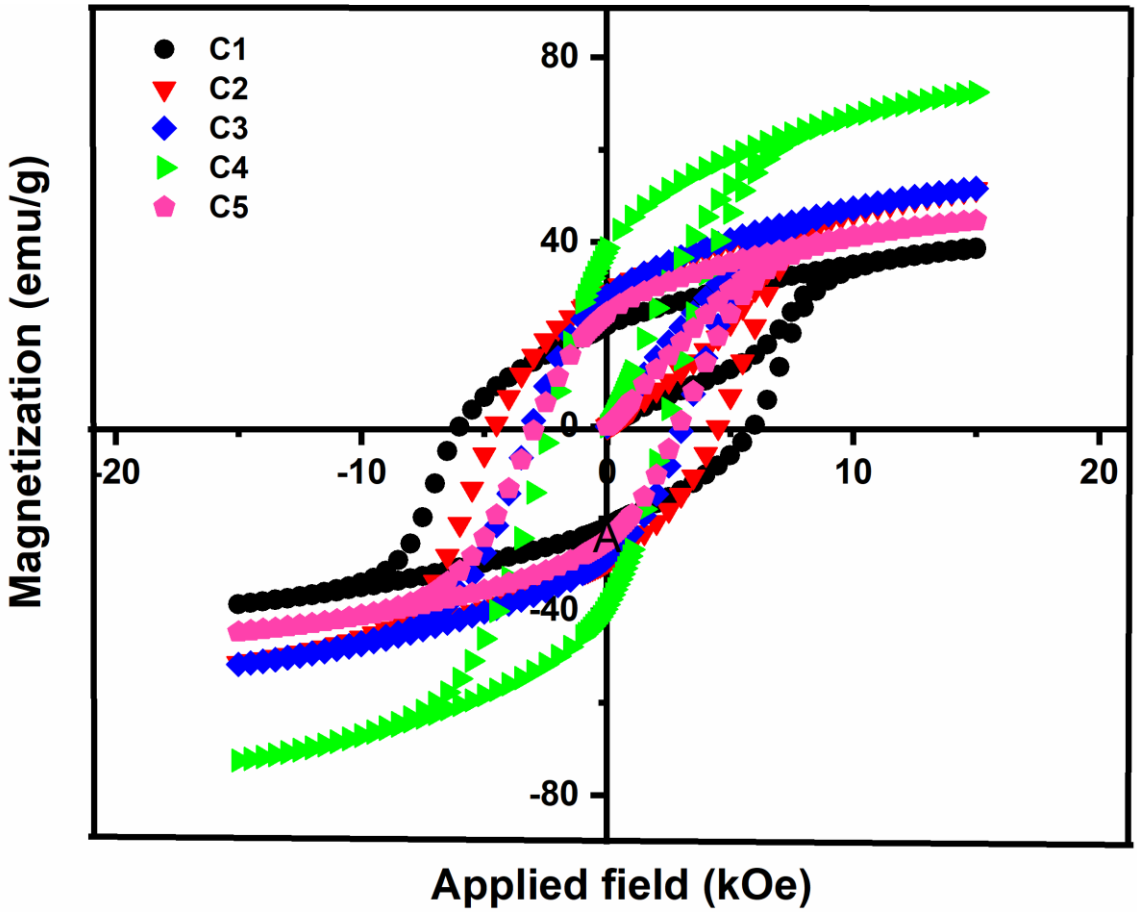

Figure 4.62: Hysteresis Loops of *C1, C2, C3, C4,* and *C5* Hexaferrite

Table 4.12: Magnetic Parameters M_s, H_c H_a, M_r and M_r/M_s for Cu-Co Doped Hexaferrite Samples

Sample	M_s	H_c	H_a (kOe)	M_r	M_r/M_s
C1	41.77	5882.43	16.55	20.93	0.50
C2	55.09	4549.37	15.56	28.26	0.51
C3	54.80	3154.98	14.40	27.53	0.50
C4	76.17	2841.67	13.39	38.94	0.51
C5	47.27	2382.45	14.17	24.75	0.52

The table shows an increase in M_s from 41.77 emu/g (*C1*) with an increase in doping content, but this increase is not linear. A pure sample (*C1*) exhibits the greatest values of coercivity (5882 Oe), which is related to the absence of substituent cations in the crystal lattice. Both intrinsic and extrinsic factors readily explain the behavior of H_c [167]. The H_c value decreases from 5882 emu/g (*C1*), 4549 emu/g (*C2*), 3154 emu/g (*C3*), 2841 emu/g (*C4*), and 2382 emu/g (*C5*) being the lowest.

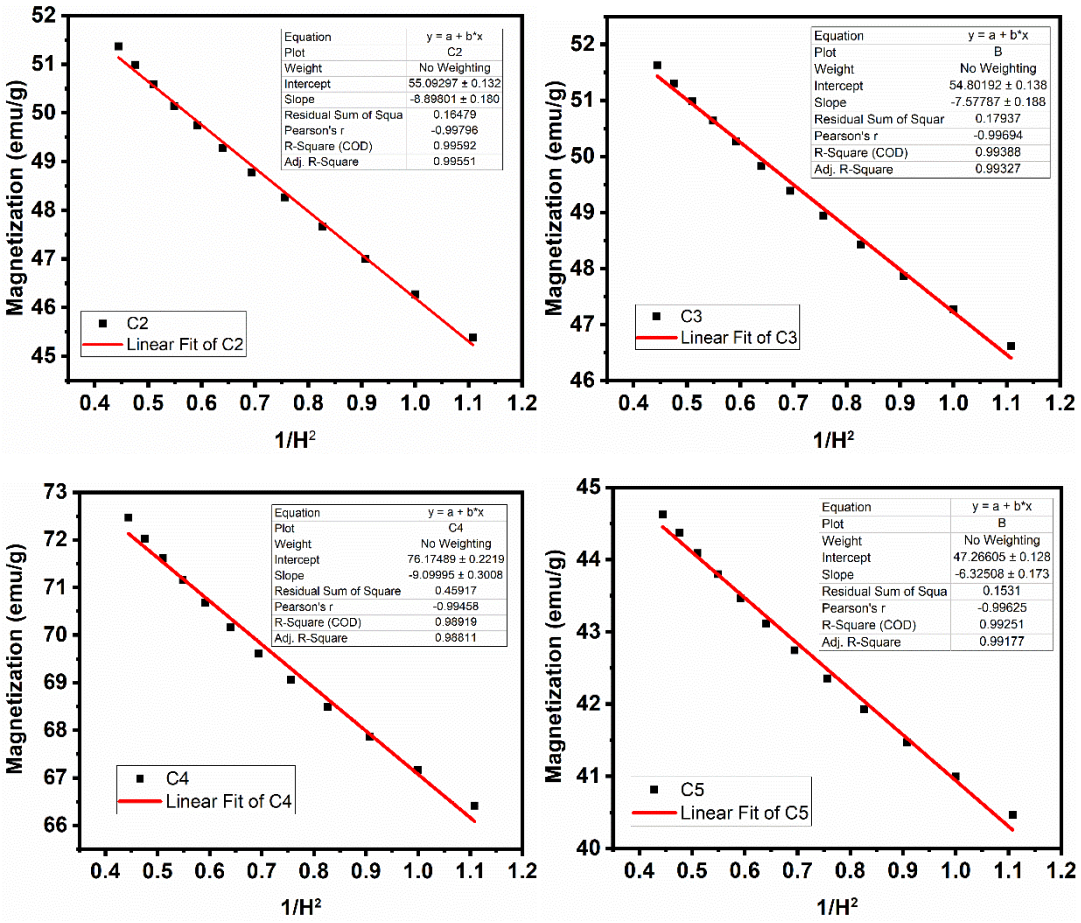

Figure 4.63:

M_s Versus 1/ H^2 Plots for *C2, C3, C4* and *C5* Hexaferrite Samples

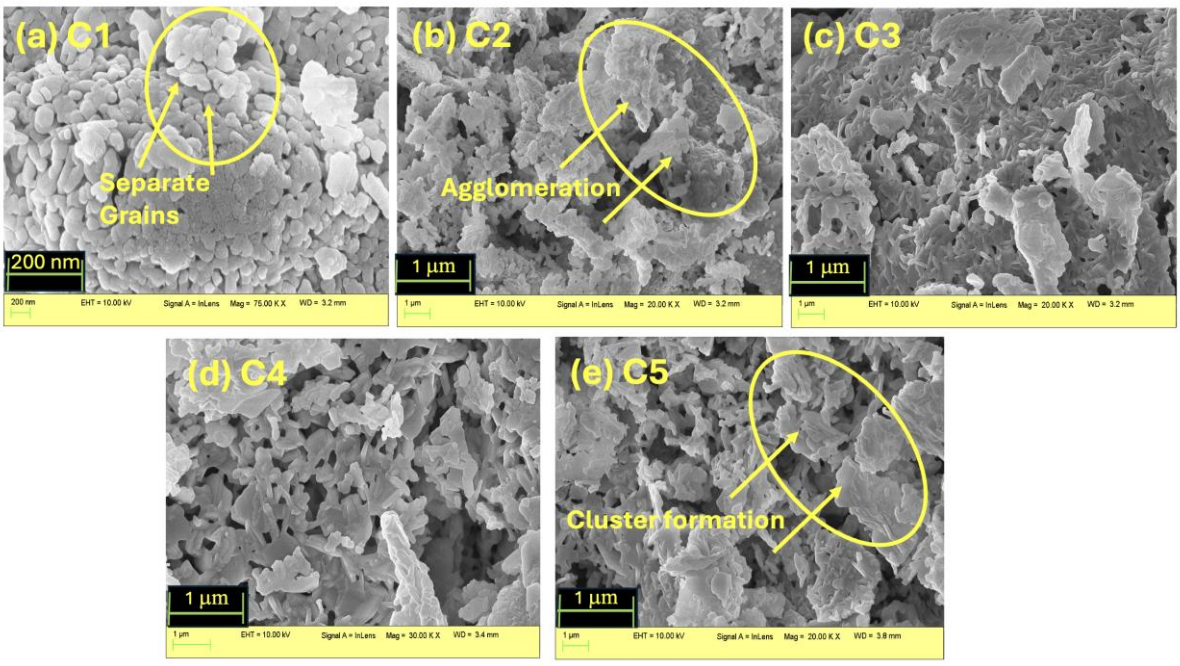

Figure 4.64: SEM Micrographs of Ferrite Samples: $Ba_{0.2}Sr_{0.8}Co_xCu_xFe_{12-2x}O_{19}$ (*C1, C2,*

***C3, C4* and *C5*) and its Correlation with Magnetic Data**

The increase in M_s from *C1* to *C5* can be concluded by comparing SEM (Figure 4.64**)** plots with Table 4.12 (magnetic data). For pure samples, individual grains can be seen. Here, separate particles can be noticed, but porosity is on the higher side. As doping is introduced, the agglomeration increases. Hence, magnetization saturation is lowest for pure/undoped samples. With the increase in doping for *C3* and *C4*, there is only a slight change in the M_s value but it stays on the higher side. As the doping level is moved further, more agglomeration and cluster formation are observed. This cluster formation is one of the key reasons for M_s improvement and is one of the key reasons that H_c it is decreased, whereas H_a does not show a prominent change with doping [183-185].

4.3.4 Electromagnetic Characteristics

4.3.4.1 Complex Permeability and Complex Permittivity

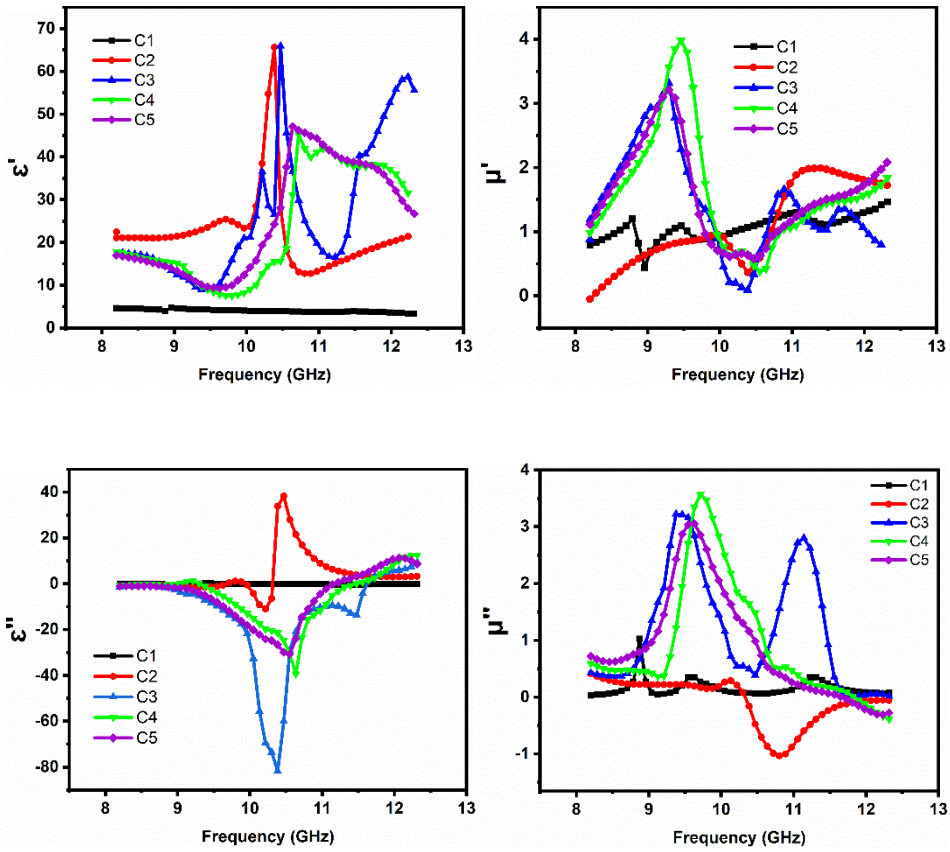

Figure 4.65: Dependence of ε', ε'', μ'and μ'' on Frequency in *C1, C2, C3, C4* and *C5* Ferrite Compositions

Figure 4.65 illustrates plots of dielectric permittivity (ε') and dielectric loss (ε'') versus frequency.

The prepared samples' complex permittivity and permeability values are considerably high, which is attributed to instrumental/ measurement error. Therefore, further calculations for Reflection loss and microwave absorption are not reported.

4.4 Co^{2+}-Cu^{2+} substituted $Ba_{0.2}Sr_{0.8}Co_xCu_xFe_{12-2x}O_{19}$/PANI hexaferrite

In this section, we have synthesized a hexaferrite with Co and Cu substitutions, along with PANI as a matrix, via the sol-gel technique. This composition hexaferrite will be given as $Ba_{0.2}Sr_{0.8}Co_xCu_xFe_{12-2x}O_{19}$/PANI. For composites, we are reporting only those samples in which significant results have been obtained. The sample names with the codes for each level of substitution in $Ba_{0.2}Sr_{0.8}Co_xCu_xFe_{12-2x}O_{19}$/PANI are given in Table 4.13

Table 4.13: The Assignment of Sample Names Corresponding to Various Substitutions Levels in $Ba_{0.2}Sr_{0.8}Co_xCu_xFe_{12-2x}O_{19}$ /PANI Hexaferrite

Sample Composition $Ba_{0.2}Sr_{0.8}Co_xCu_xFe_{12-2x}O_{19}$	Sample Code Name	Sample Code (C-Series)
x = 0.4	$Ba_{0.2}Sr_{0.8}Co_{0.4}Cu_{0.4}Fe_{11.2}O_{19}$/PANI	CP3
x = 0.8	$Ba_{0.2}Sr_{0.8}Co_{0.8}Cu_{0.8}Fe_{10.4}O_{19}$/PANI	CP5

4.4.1 Structural Analysis

4.4.1.1 Field Emission Scanning Electron Microscopy

Figure 4.66 (a-b) displays the grain morphology of the samples. The micrographs demonstrate that the fused grains in samples *CP3* and *CP5* combine to form huge grains. Even though both samples exhibit grain agglomeration, it is also effortless to identify individual grains in the samples. Doping causes grain clusters to have an uneven size distribution because of both magnetic and electrostatic interactions between the ferrite particles. The grain takes on a noticeable platelet-like form as doping levels rise. Also, it can be seen that the little individual grains become more noticeable in the grain clusters. Certain gaps in the grain arrangement may prevent or hinder the flow of charge carriers. Now, since the grain boundaries are higher, the resistance to the applied field will be greater as grain size decreases, changing the process of charge transport.

Figure 4.67 depicts the EDX spectra of $Ba_{0.2}Sr_{0.8}Co_xCu_xFe_{12-2x}O_{19}$/PANI hexaferrite for samples *CP3* and *CP5*. It can be seen from the EDAX table that as the doping increases, the Cu content rises from 3.52 to 5.94 (% weight) from sample *CP3* to *CP5*.

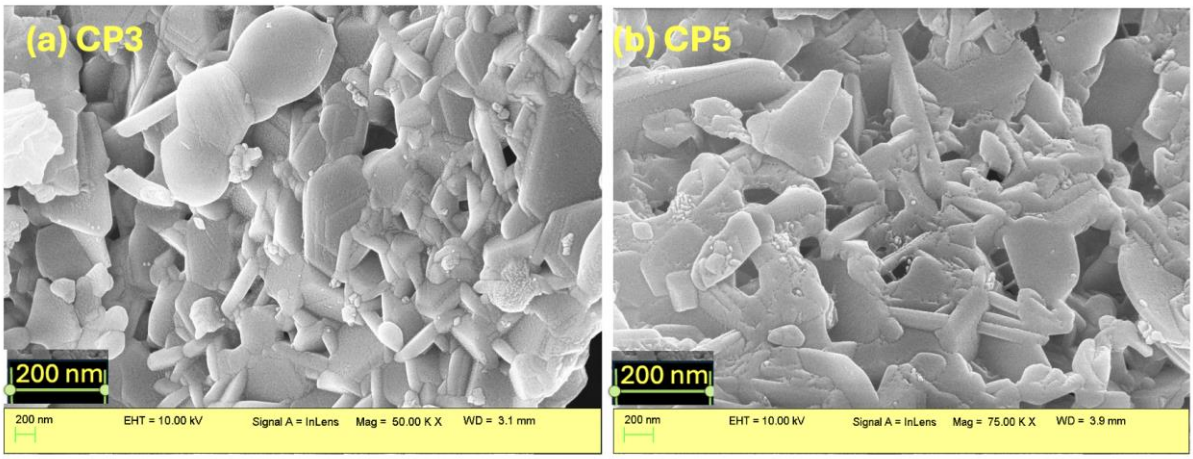

Figure 4.66: SEM Micrographs of Ferrite Samples: $Ba_{0.2}Sr_{0.8}Co_xCu_xFe_{12-2x}O_{19}$ /PANI (*CP3*, *CP5*)

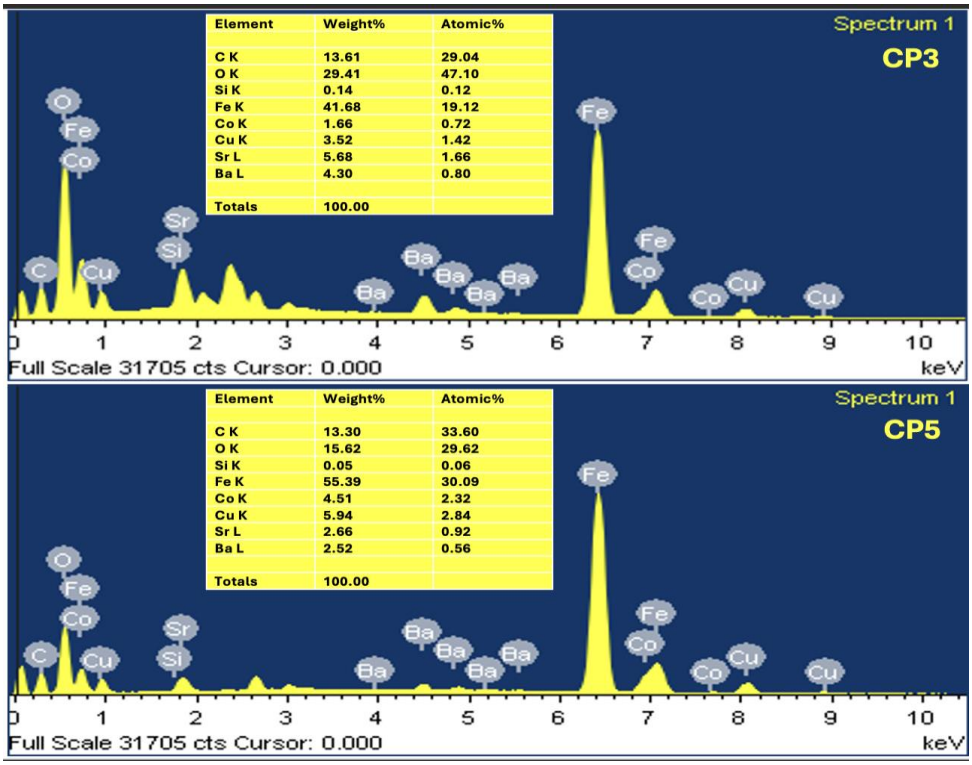

Figure 4.67: EDX Spectra $Ba_{0.2}Sr_{0.8}Co_xCu_xFe_{12-2x}O_{19}$/PANI Hexaferrite for Samples *CP3* and *CP5*

4.4.2 Electrical Analysis

4.4.2.1 Dielectric permittivity

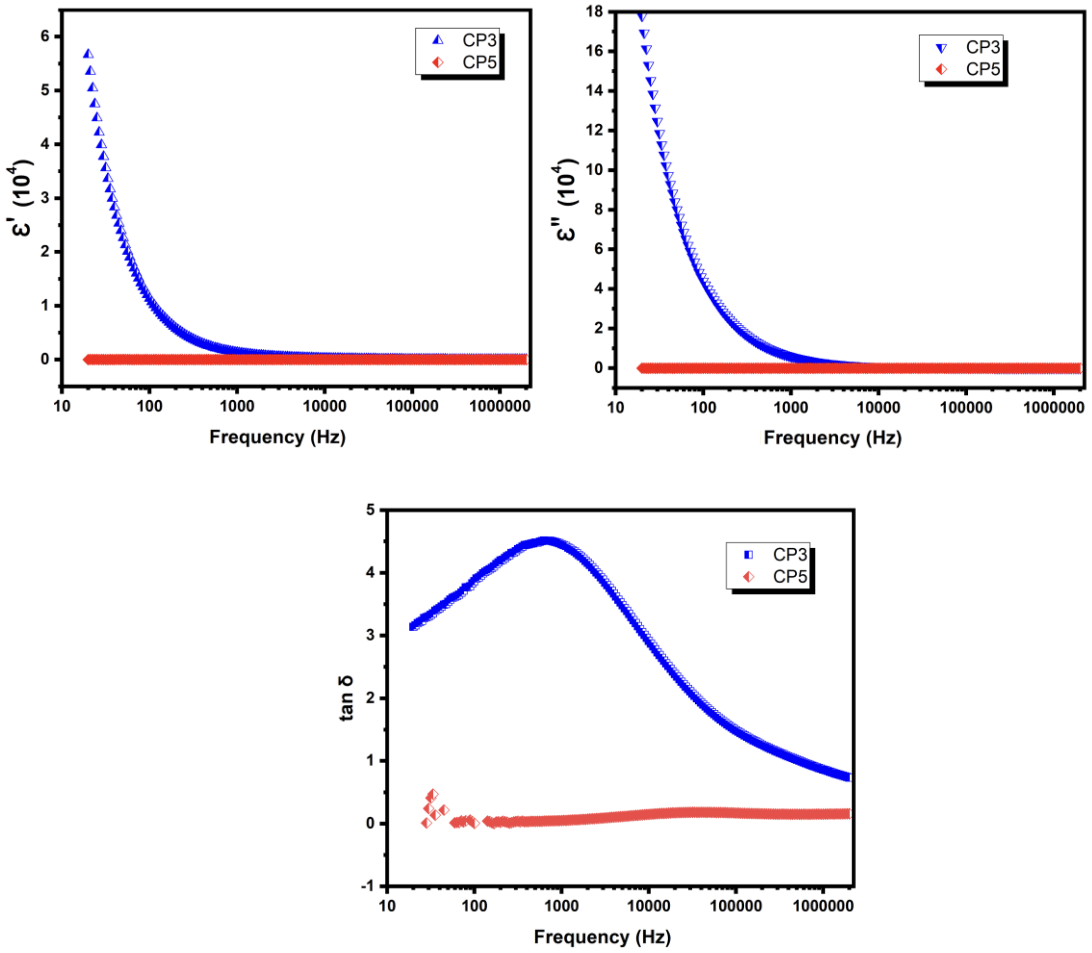

Figure 4.68: Variation of Dielectric Spectra of Ferrite Composite Sample $Ba_{0.2}Sr_{0.8}Co_xCu_xFe_{12-2x}O_{19}$ /PANI (*CP3, CP5*) a) Real Component b) Imaginary Component as a Function of Frequency (c) Variation of Dielectric loss Tangent

Figure 4.68 displays two distinct plot types: dielectric permittivity(ε′) and dielectric loss (ε′′). It displays the distribution in the low-frequency spectrum for *CP3* and becomes frequency-independent beyond 10 kHz, as shown in Figure 4.68 (a), (b). But for *CP5*, it shows the same behavior for the overall range of frequency.

For sample *CP3*, it has been discovered that the graph declines non-monotonically. The plot depicts that this sample has its highest dielectric permittivity value in the low-frequency range, but the value decreases as the frequency is raised. The ε′ highest value is 5.89 for *CP3* at 10 Hz. After it starts decreasing, it stays for a constant range of 0 to 0.5. The Maxwell-Wagner interfacial polarisation model can be used to specify the dropping of dielectric permittivity values with decreasing frequency. This model is frequently applied to elucidate hexaferrite's dielectric characteristics. Similarly, ε′′ shows the same behavior as ε′, i.e., a declining trend

after crossing a certain frequency. The highest value, 18 at 10 Hz, for ε″ is observed for the *CP3* sample. Once it started declining, it stayed in the range 0 to 1 for both the samples.

According to this approach, conducting grains that are separated from insulating grain boundaries can be found in hexaferrite. The boundaries between the grains aid in polarisation but inhibit electrical conduction. The air in the furnace during the pallet sintering process oxidizes the grain boundaries more than the grain interiors [151]. Grain boundaries, therefore, have a stronger insulating quality than bulk grains. Electrons hop in the direction of grain boundaries during conduction. However, in situations where the grain boundaries provide considerable resistance, electrons gather at these boundaries, causing polarization and an elevated Dielectric permittivity. As previously mentioned in Figure 4.68 (a), (b), for *CP3*, the Dielectric permittivity/loss approaches a steady state number after a certain frequency, which prevents electron hopping and electron exchange with the +2 and +3 states from occurring. The highest dielectric permittivity is connected with the ferrous ion concentration at the octahedral locations. It is well known that ferrites' conductivity and polarisation are caused by the ability of electrons to hop between octahedral sites.

Figure 4.68 (c) depicts the loss tangent plots for both samples. For sample *CP3,* the loss tangent value is approximately 4.5, around 800 to 900 Hz. As frequency increases, it exhibits peaking behavior in the mid-frequency band and abruptly decreases as frequency increases, depicting a relaxation process around the 500 to 1500 Hz frequency range. In contrast, sample *CP5*'s *tan* δ value shows constant behavior across the complete frequency range. The figure above makes it clear that, for all *CP3,* the loss tangent value maintains close to 1, but for *CP5,* it stays on the lower side, at 0.1- 0.2. This decrease in $tan\delta$ value is explained by Koop's phenomenological theory of dielectrics [161]. Interface traps, interfacial polarisation, content Fe^{2+}/Fe^{3+}, structural oneness, and stoichiometry are a few factors; nonetheless, the key to all of them is the sintering circumstances.

4.4.2.2 Electric modulus analysis

This study helps clarify the relaxation process and minimizes the effects of electrode polarization. M' and M'' are the real and imaginary parts of the complex electric modulus and are calculated using equation 3.8 and equation 3.9 respectively (from section 3.3.2). Figure 4.69 (b) displays the distinctive feature of M'' as a broad, asymmetric peak in the imaginary part of the electric modulus plot across different frequencies [162-163].

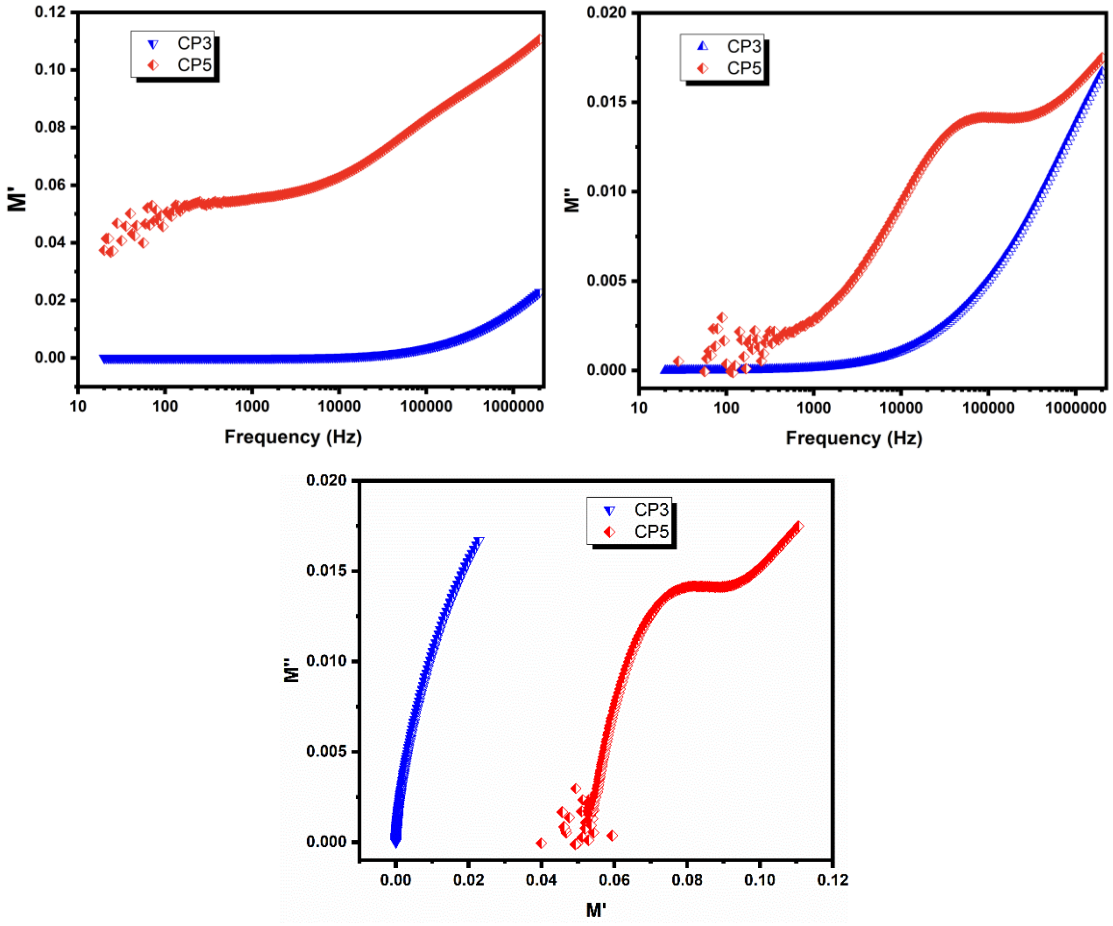

Figure 4.69: Variation of Modulus (a) Real Part, (b) Imaginary Part of Ferrite Composite $Ba_{0.2}Sr_{0.8}Co_xCu_xFe_{12-2x}O_{19}$ / PANI (*CP3*, *CP5*) as a Function of Frequency (c) Cole-Cole Plot (or Nyquist Plot)

In Figure 4.69 (a), the relationship between the real component of the modulus (*M'*) and frequency is shown, offering insights into conductivity. For sample *CP3*, it increases from 0.04 to 0.11. The non-linear increment in *M'* with frequency is also visualized in both samples. However, *CP5* shows the same trend around value 0.001 from 10 Hz till 1 MHz and then increases, touching 0.02 for the highest test frequency. The changes in the plots of the imaginary component of the electric modulus in the frequency domain, as shown in Figure 4.69 (b), provide insights into charge transport mechanisms, including electrical transport, conductivity relaxation, and ion dynamics. Though *M''* depicts a rising trend along the test frequency, it shows a relaxation peak around 10 kHz to 1 MHz. In the low-frequency range, ions can effectively move from one site to another over long distances. However, the peak observed in *M''* indicates that at higher frequencies, ions do not engage in longer hopping; instead, they remain confined to the wells of their finite potential. It can also be noted that doping Co-Cu has decreased the values of *M'* and *M''* from *CP3* to *CP5*. The applied electric field affects the charge carriers, but the results are impacted by the lack of a restoring force that

regulates their movement. This suggests that conductive grains are essential for electrical properties. As mentioned earlier, conductivity relaxation is also linked to the charge carriers released due to an increase in frequency. The absence of Debye-type relaxation in the samples is indicated by the observed asymmetric and broad peaks related to doping content.

Figure 4.69 (c) presents the Cole-Cole plot for $Ba_{0.2}Sr_{0.8}Co_xCu_xFe_{12-2x}O_{19}$/PANI. As can be seen in the *CP3* sample, it looks like a part of a huge semicircle, whereas the *CP5* composition shows two distorted semicircles one after the other. Co-Cu doping has shifted the semicircles from high-frequency region to low-frequency region, implying grains boundaries becoming more effective than grains. Sample *CP3* depicts grains as more active, but *CP5* implies grain boundaries plays a major role in it.

4.4.2.3. Complex impedance spectra

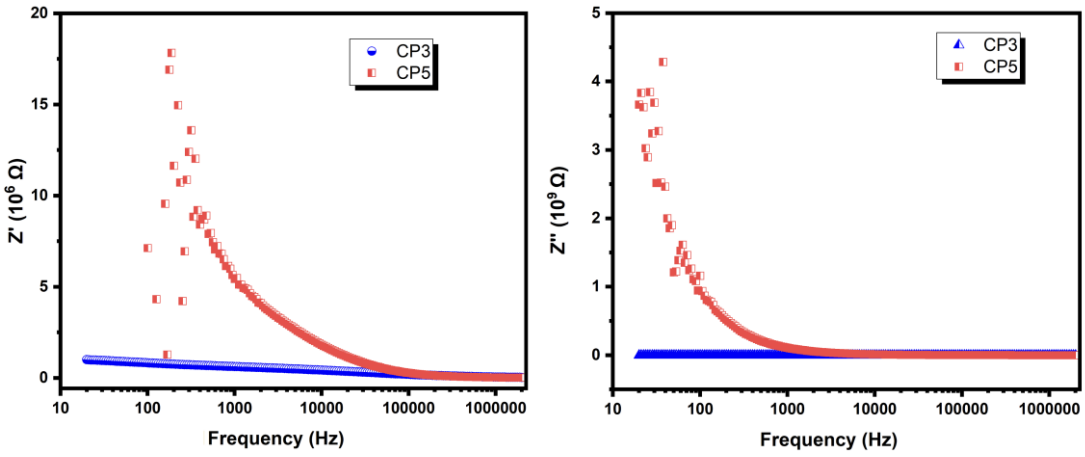

Figure 4.70: Dispersion in the (a) Dielectric Impedance Real (Z'), (b) Dielectric Impedance Imaginary (Z'') for Ferrite Composite Sample $Ba_{0.2}Sr_{0.8}Co_xCu_xFe_{12-2x}O_{19}$ /PANI for (*CP3, CP5)*

In Polycrystalline materials, impedance performance is primarily influenced by their bulk grains and grain boundaries. Details of resistance (Z') and reactance (Z'') are provided by their impedance analysis, Figure 4.70 shows the plots of impedance spectra. The impedance of grain borders and bulk grains is treated differently because of their distinct relaxation times. From the figure above, sample *CP3* shows a decrease in the value of (Z') and reactance (Z'') as the frequency increases. The highest value achieved by this sample is 18 for Z' *at* around 300 Hz frequency and 4.2 for Z'' at around 80 Hz. This drop in Z' value could be explained by the samples' dipole polarisation effect as well as the space charge polarisation effect.

But for sample *CP5*, there is not much change in the behavior with very weak relaxation for (Z') and almost constant behavior for (Z'').

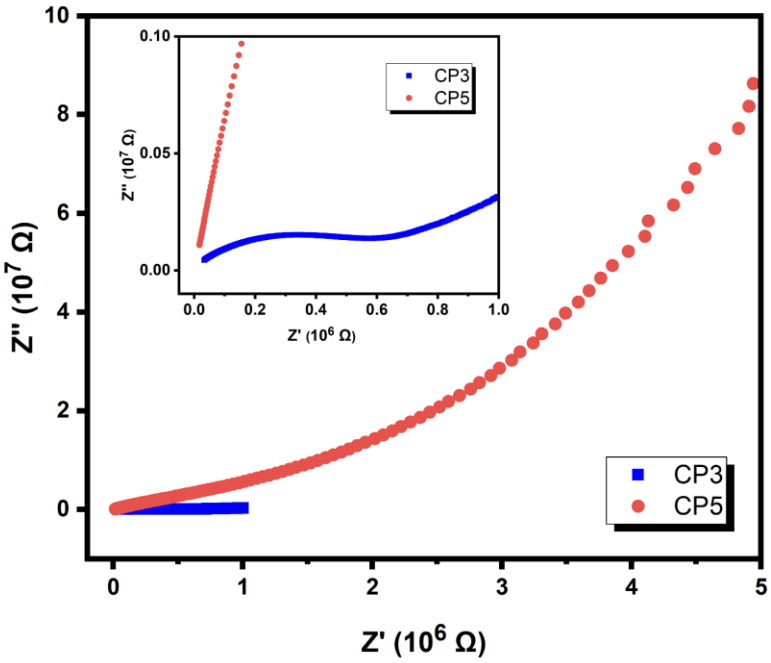

Figure 4.71: Variation in the Dielectric Impedance Real (Z′) Component Versus Dielectric Impedance Imaginary (*Z″*) Component for Ferrite Composite Sample $Ba_{0.2}Sr_{0.8}Co_xCu_xFe_{12-2x}O_{19}$ / PANI for (*CP3, CP5)*

In Figure 4.71, for the graph of *Z″* vs *Z′*, *CP3* shows very small values that are only for high-frequency regions depicting only grains active in this sample. However, sample *CP5* seems to increase exponentially so no comments can be given for this sample.

4.4.2.4 AC Conductivity

As discussed earlier, the valence electron hopping between Fe^{2+} and Fe^{3+} at octahedral sites is the primary cause of ferrites' AC conductivity. Conductivity is increased because the frequency increase accelerates the hopping frequency of the charge carriers. In [124], the frequency-dependent conduction mechanism is described using the polaron hopping model. In that scenario, an increasing trend in frequency results in an increase in AC conductivity for short-range polaron hopping. However, a decrease in AC conductivity is observed for long-range polarisation hopping. Band conduction conductivity phenomena are independent of frequency [125].

Figure 4.72 depicts sample *CP3* possessing higher values for AC conductivity as compared to sample *CP5*. Hence, it can be concluded here that with Co-Cu doping, the conductivity is decreased. *CP3*, below 80 Hz, and *CP5*, below 80 kHz, exhibit behavior that is almost frequency-independent, and at this frequency, DC conductivity is transitioned to AC conductivity.

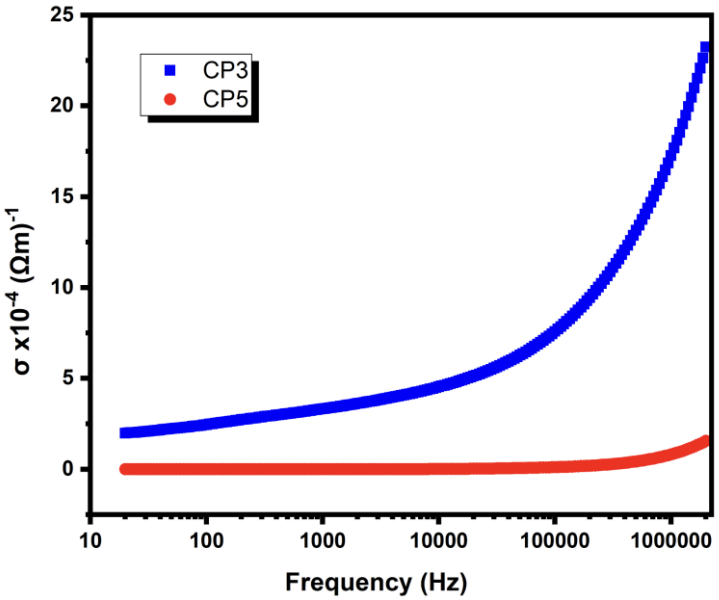

Figure 4.72: Variation of AC Conductivity for Ferrite Composite Sample $Ba_{0.2}Sr_{0.8}Co_xCu_xFe_{12-2x}O_{19}$ /PANI (CP3, CP5)

The Jonscher power law is already discussed in section 3.3.4. According to this law, n has a physical meaning, where n < 1 denotes a translational motion with abrupt hopping, and n > 1 denotes localized hopping between surrounding locations. Here, n was calculated using fitting in the plots: for *CP3*, *n* = 0.1940, and *CP5*, n = 1.1169. For *CP3*, n is smaller than 1, indicating that charge carriers are hopping along with ac conductivity. For *CP5*, n is greater than 1, which gives the idea that there is a localized hopping between surrounding locations.

4.4.3 Magnetic analysis

Figure 4.73 shows the room-temperature hysteresis loops for all synthesized ferrite samples. Table 4.14 lists the (M_r/M_s) ratio, coercivity (H_c), saturation magnetization (M_s) anisotropy field (H_a) and remanence magnetization (Mr).

Table 4.14: Magnetic Parameters M_s, H_c H_a, M_r and M_r/M_s for Cu-Co/PANI Doped Hexaferrite Samples

Sample	M_s	H_c	Ha (kOe)	Mr	M_r/M_s
CP1	44.54	6112.67	17.49	22.78	0.50
CP3	50.72	3136.47	15.79	21.26	0.42
CP5	6.28	2258.82	13.62	3.36	0.53

The M-H curves of the hexagonal ferrites composites *CP1* (is same as the *MP1* sample, values taken from section 4.5) *CP3* and *CP5* are displayed in Figure 4.73 at room temperature with a 25 kOe applied field. The magnetic properties that were ascertained using M-H curves are listed in the table. All prepared specimens had a linear relationship, as demonstrated by the M-H loop in Figure 4.73, with a rapid increase in M_s at low-applied fields that slows down at high-applied fields. Figure 4.74. shows M_s versus $1/H^2$ plots for *CP3* and *CP5* hexaferrite samples From the table, it is observed that M_r/M_s the ratio is between 0.5 and 1 for samples *CP1* (0.5096) and *CP5* (0.5349), implying more anisotropic, single-domain, and hard, whereas for sample *CP3* (0.4191), it is less than 0.5 implying randomly oriented multi-magnetic domains.

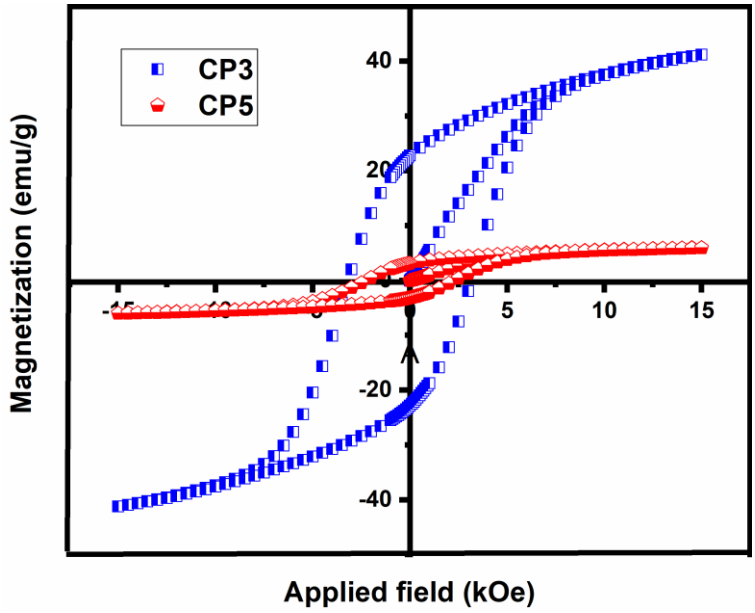

Figure 4.73: Hysteresis Loops of *CP3* and *CP5* Hexaferrite

In a pure x = 0.0 sample, which is *CP1* (i.e *MP1* section 4.2.3) the saturation magnetization is 41.54 emu/g, this value rises as cations are substituted in *CP3* composition, M_s being 50.71 emu/g. the increase from *CP1* to *CP3* is around 13%, may be due to favorable cation occupancy at spin-down sites, which enhances magnetization. But as further substitution was done, the M_s seen have decreased drastically (only for this sample and may require further investigation for such behavior).

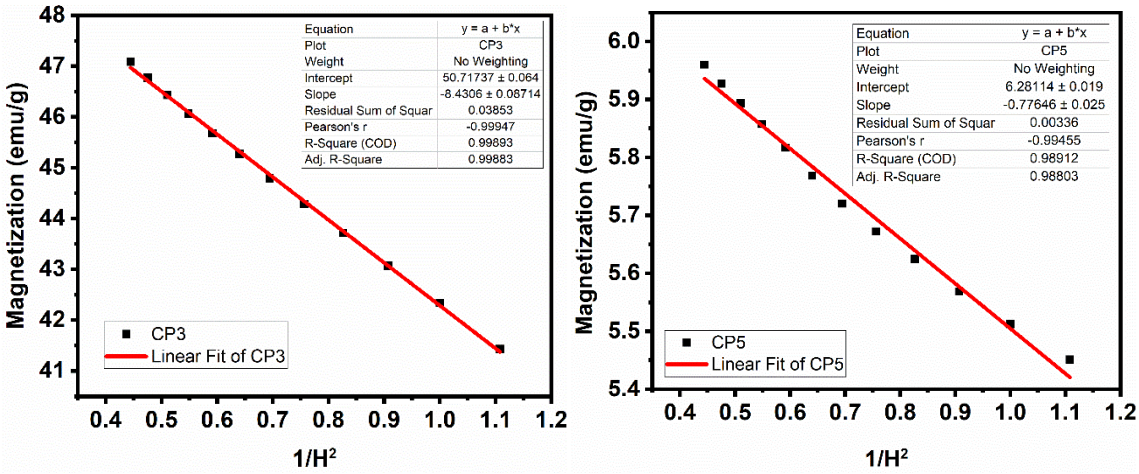

Figure 4.74: M_s Versus 1/ H^2 Plots for *CP3* and *CP5* Hexaferrite Samples

The highest coercivity values (6112 Oe) are seen in pure composite samples, which are associated with the crystal lattice's lack of substituent cations. Further, with doping in samples *CP3* and *CP5*, the value of H_c is seen decreasing with doping content, 3136 Oe and 2258 Oe, respectively. No prominent change in H_a is observed, but it is seen decreasing with doping content, being 17.49 kOe, 15.79 kOe, and 13.61 kOe for pure sample, *CP3*, and *CP5*, respectively. Figure 4.75 shows SEM micrographs of ferrite samples: $Ba_{0.2}Sr_{0.8}Co_xCu_xFe_{12-2x}O_{19}$ /PANI [*CP3* and *CP5*] and its correlation with magnetic data. As can be seen from the SEM images shown below, the *CP3* sample shows very less void compared to *CP5*, this might be one of the reasons for H_c being lowered drastically in *CP5*.

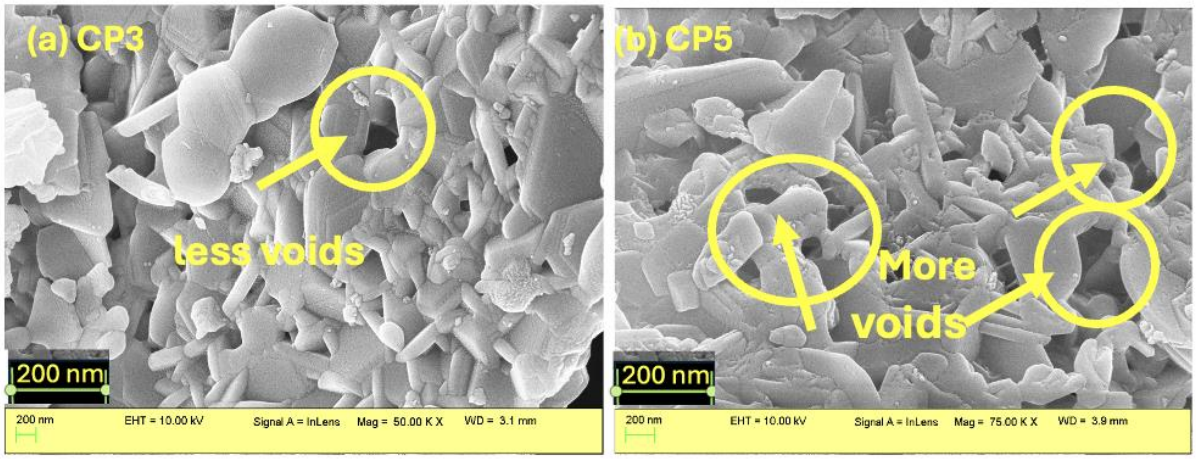

Figure 4.75: SEM Micrographs of Ferrite Samples: $Ba_{0.2}Sr_{0.8}Co_xCu_xFe_{12-2x}O_{19}$ /PANI (*CP3* and *CP5*) and its Correlation with Magnetic Data

4.4.4 Electromagnetic Characteristics

4.4.4.1 Complex Permeability and Complex Permittivity

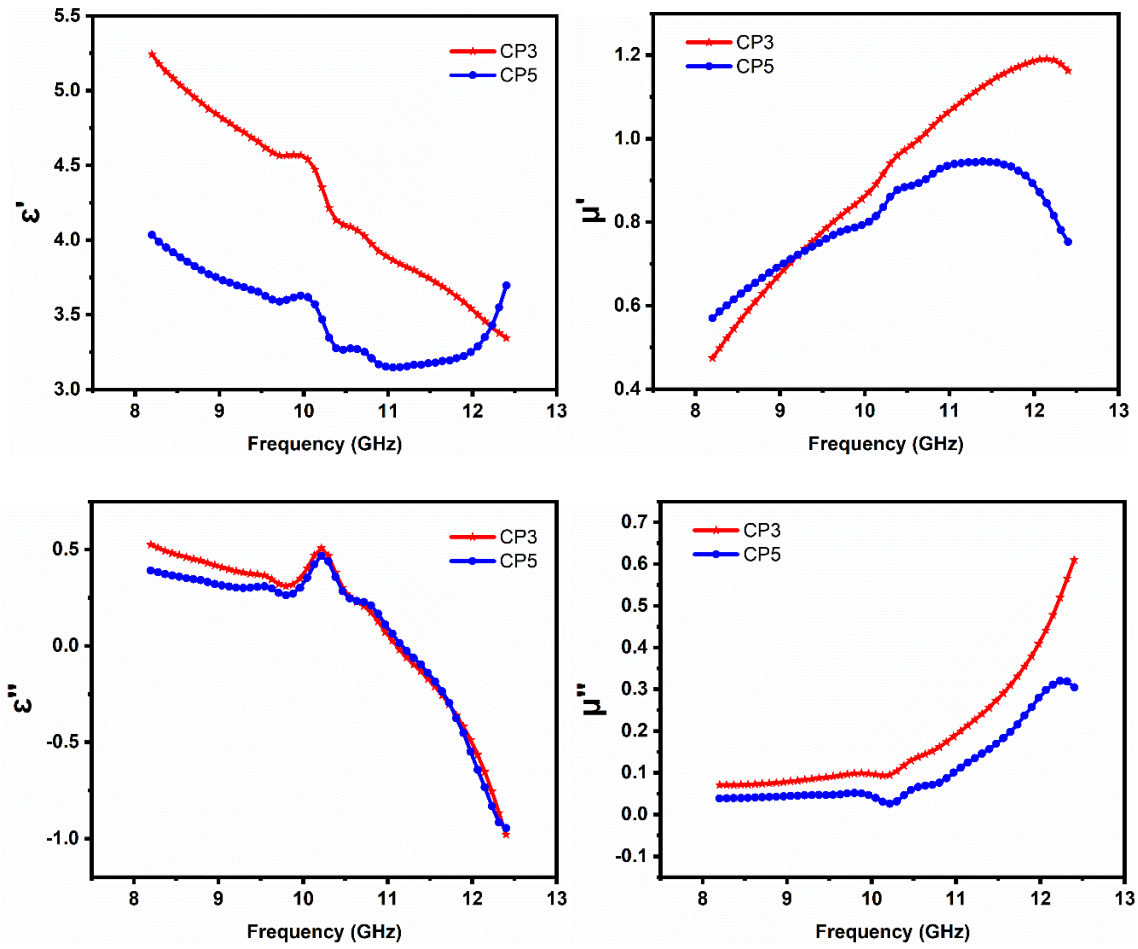

Figure 4.76: Dependence of ε', ε'', μ'and μ'' on Frequency in Ferrite Compositions *CP3* and *CP5*

Plots of the dielectric permittivity(ε') and dielectric loss (ε'') versus frequency are shown in Figure 4.76. The Dielectric permittivity/loss decreases non-monotonically with the doping of Co^{2+}-Cu^{2+} ions. The dielectric permittivity values show dispersion from the range 8.2 to 12.4 GHz, whereas the loss doesn't show the same trend till 10.2 GHz but then shows dispersion above this range to 12.4 GHz.

In low-frequency region, the values scale to highest ε' and ε'', but ε'' is at its lowest for highest frequency. The highest value of ε' is observed for *CP3* composition at 8.2 GHz, which is 5.32, and for ε'', the highest value noted is 0.48, which also is for the *CP3* sample and is around 10.38 GHz.

For *CP3* composition, a peaking behavior is observed for both parameters at around the frequency region of 10 to 11 GHz. Similarly, for *CP5* composition, ε' is showing the same rising trend at around 12.4 GHz.

Plots of the permeability (μ') /magnetic loss (μ'') versus frequency are shown in Figure 4.76. For both compositions, the values (μ') show a wide dispersion over the complete frequency range whereas (μ'') shows dispersion from around 10.2 to 12.4 GHz. Though the overall value

for both parameters is increasing with frequency, with Co^{2+}- Cu^{2+} doping, the values have decreased. The values of μ' depict a sharp rise at around 11 GHz, and this reaches the highest point for *CP3* in the given test frequency. Composition *CP3* owes maximum μ' as well as μ" value in the high-frequency regime, 1.2 and 0.62, respectively. There is a rise initially but a fall in the values of μ' curve at around 11.5 to 12.4 GHz frequency.

In the microwave region, the complex permittivity/permeability depends on dipole polarisation, electron spin, porosity, grain, and grain size distribution, in addition to charge accumulation at grain boundaries. Dielectric polarisation in ferrites is caused by the electron hopping in Fe^{2+}/Fe^{3+} [169]. The porosity provides a barrier to the field flow and deters polarisation. Exchange resonance between Fe^{2+}/Fe^{3+} ions and ferromagnetic resonance controls the mechanism of complex permeability.

4.4.4.2 Microwave absorption in $Ba_{0.2}Sr_{0.8}Co_xCu_xFe_{12-2x}O_{19}$/PANI

Examining a material's reflection loss is one method of determining its microwave absorption capability. Equations 3.16 and 3.17 are used to determine the RL of the compositions. This section will examine how different factors affect the material's microwave-absorbing capacity. These variables include the degree of reflection loss, impedance matching, and material thickness (λ/4) [178-182].

4.4.4.3 Quarter Wavelength Mechanism

The condition for the occurrence of quarter wavelength or λ/4 mechanism is already discussed in 3.7.1. Figures 4.77 (a), (b) to 4.79 (a) illustrate reflection loss (RL) diagrams for various compositions of $Ba_{0.2}Sr_{0.8}$ $Co_xCu_xFe_{12-2x}O_{19}$/PANI ferrite. Figures 4.77 (a), (b) to 4.79 (a) aid in determining parameters such as frequency/thickness correlation, bandwidth, and frequency range corresponding to RL values of -10 dB. Table 4.15 provides a concise summary of these findings.

There was no absorption found for *CP1*, i.e. $Ba_{0.2}Sr_{0.8}CoCuFe_{12}O_{19}$/PANI composite sample. The highest RL dip of -20.12 dB is observed in *CP3* composition at 10.88 GHz frequency and 10 mm thickness. *CP5* composition owes a partial RL Plot wherein the -10 dB line is cut only at one frequency, so the table does not depict any corresponding bandwidth.

The RL plots of *CP3*, illustrate that RL peaks shift towards the low-frequency spectra from the high-frequency spectra as thickness is increased. This is in line with the quarter wavelength mechanism (Equation 3.18), which states that the relationship between frequency and thickness is inversely proportional.

Figures 4.77 (a), (b), and Figures 4.78 (a), (b) show the RL values for *CP3* composition for reflection loss ≥ -10 dB for 7.8 to 10 mm thickness at the frequency range of 10 to 12.5 GHz.

The RL peaks are observed in CP3 [Figures 4.77 (a), (b), Figures 4.78 (a), (b)] in the frequency band ranging from 11.88 to 12.4 GHz and 10.88 to 12.4 GHz at thicknesses from 7.4 to 8.4 mm and 8.5 to 10 mm, respectively.

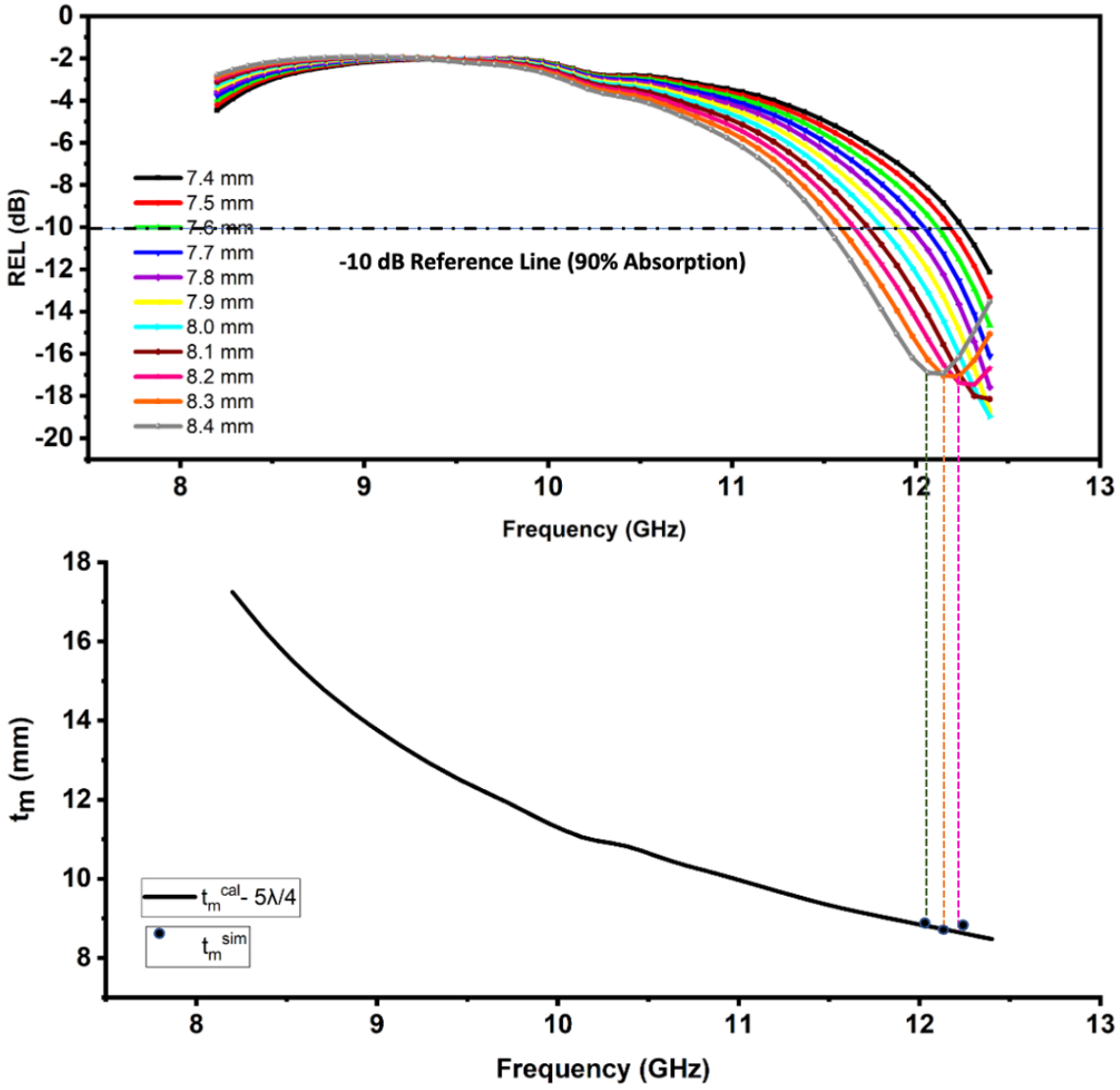

Figure 4.77: (a) Dependence of RL on Frequency in *CP3* Composition and (b) t^{sim} and t^{cal} Versus Frequency for 5λ/4 in *CP3* Composition

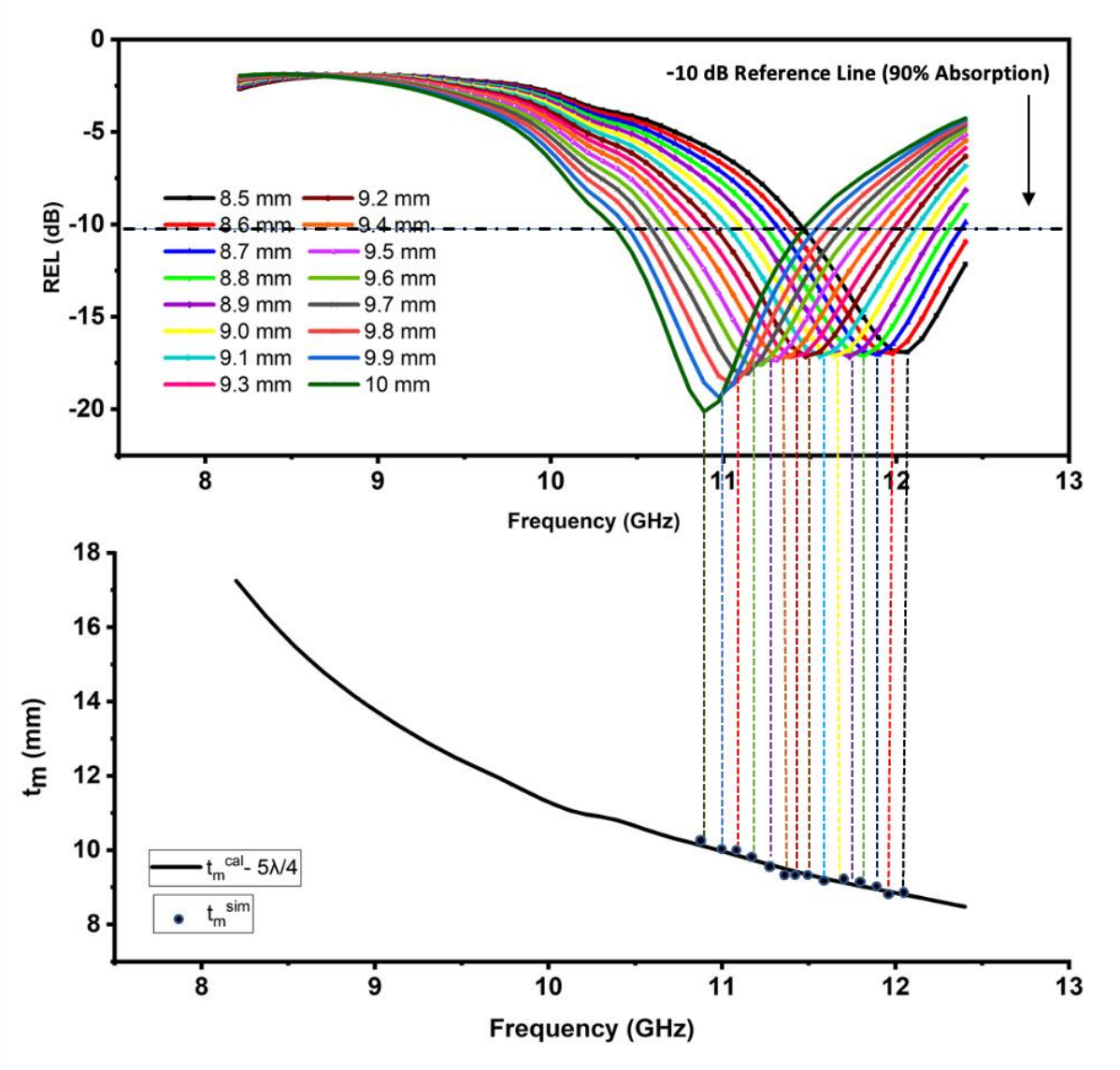

Figure 4.78: (a) Dependence of RL on Frequency in *CP3* Composition and (b) t^{sim} and t^{cal} Versus Frequency for 5λ/4 in *CP3* Composition

As per reference (3.16), Reflection Loss (RL) is computed using the simulated thickness (t_{sim}), while the calculated thickness (t_{cal}) is derived from equation (3.18) with n = 1, 3, 5, etc. These two parameters are analyzed to explore the relationship between RL peaks and the quarter-wavelength mechanism.

Figures 4.77 (a), (b) and Figures 4.78 (a),(b) depict plots of the calculated thickness (nλ/4) across different frequency ranges. A comparison between the calculated thickness (nλ/4) and the simulated thickness (t_{sim}) involves drawing vertical lines from RL peaks onto thickness-frequency plots. These plots indicate that the λ/4 mechanism is satisfied in CP3 compositions, where the calculated thickness is 5λ/4 with n = 5.

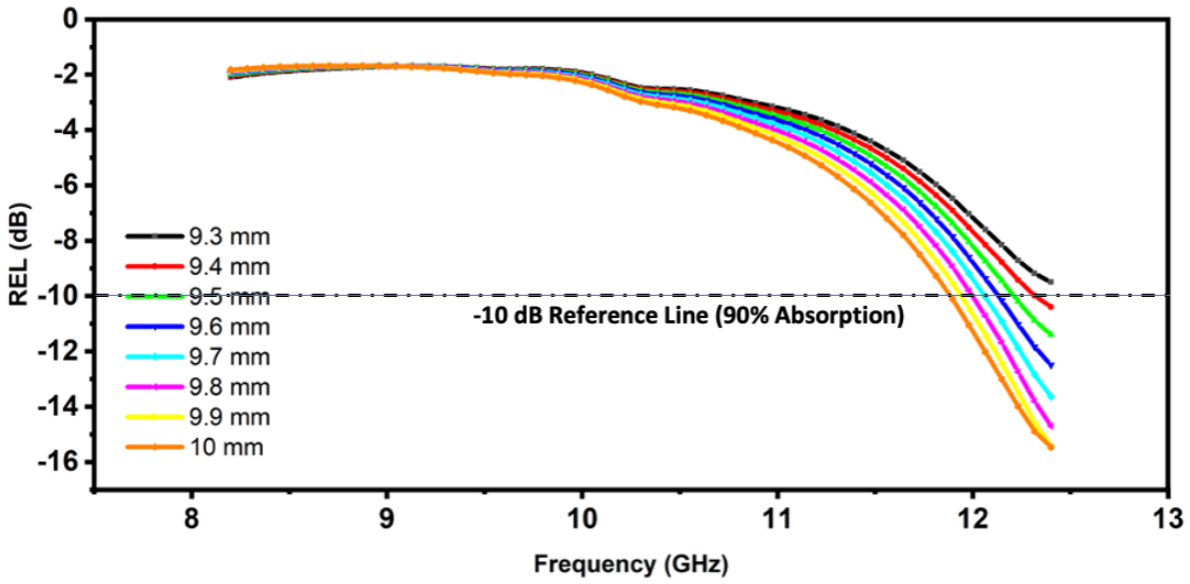

Figure 4.79: (a) Dependence of RL on Frequency in *CP5* Composition

The RL graph for *CP5* shows partial RL peaks, so anything regarding the λ/4 mechanism cannot be concluded here. Figure 4.80 shows three-dimensional (3D) plots of reflection loss at various frequencies and thicknesses for *CP3* and *CP5* samples. As can be seen from the graphs, the darker blue-violet region shows the RL peaks covering corresponding thickness and frequency which can be cross-verified from Table 4.15.

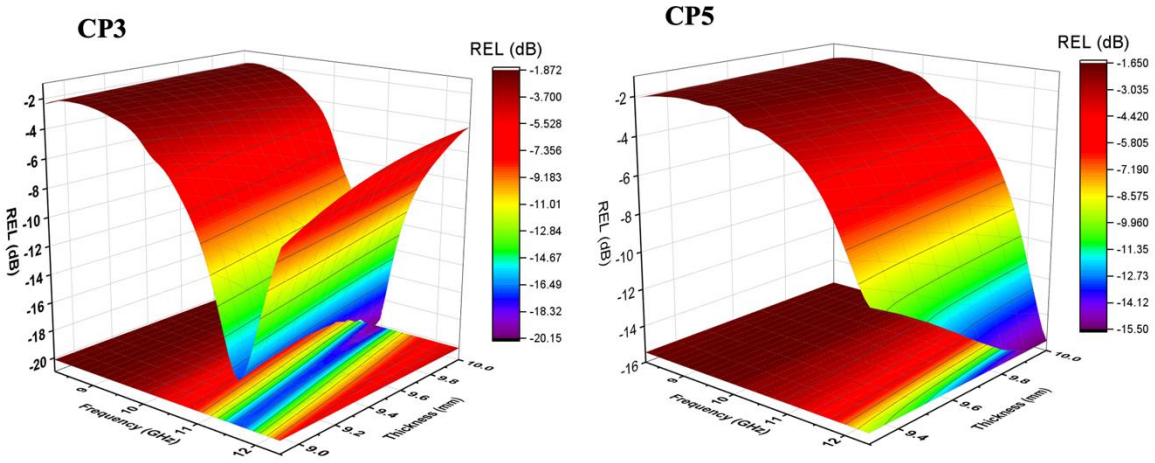

Figure 4.80: Three-Dimensional (3D) Plots of Reflection loss at Various Frequencies and thicknesses for *CP3* and *CP5* Samples

Table 4.15: Computed Parameters for Microwave Absorption (RL More Than -10 dB)

Co-Cu content	Matching Thickness (mm)	Matching Frequency	Maximum RL (dB)	Frequency Band for RL>-10 dB (GHz)	Bandwidth for RL >-10 dB (GHz)	BWT	PBW
CP3	7.5	12.32	-11.83	-	-	-	-
	7.6	12.4	-14.65	-	-	-	-
	7.7	12.4	-16.11	-	-	-	-
	7.8	12.4	-17.58	-	-	-	-
	7.9	12.4	-18.71	-	-	-	-
	8.0	12.4	-18.96	-	-	-	-
	8.1	12.4	-18.14	-	-	-	-
	8.2	12.32	-17.46	-	-	-	-
	8.3	12.23	-17.07	-	-	-	-
	9.2	11.48	-17.14	10.97-11.98	1.01	0.11	8.80
	9.3	11.39	-17.18	10.88-11.98	1.10	0.12	9.66
	9.4	11.31	-17.26	10.80-11.89	1.09	0.12	9.64
	9.5	11.31	-17.34	10.72-11.81	1.09	0.11	9.64
	9.6	11.22	-17.59	10.63-11.72	1.09	0.11	9.71
	9.7	11.14	-18.08	10.63-11.64	1.01	0.10	9.07
	9.8	11.06	-18.67	10.55-11.56	1.01	0.10	9.14
	9.9	10.97	-19.35	10.38-11.47	1.09	0.11	9.93
	10.0	10.89	-20.13	10.38-11.47	1.09	0.11	10.01
CP5	9.5	12.4	-11.39	-	-	-	-
	9.6	12.4	-12.48	-	-	-	-
	9.7	12.4	-13.63	-	-	-	-
	9.8	12.4	-14.68	-	-	-	-
	9.9	12.4	-15.39	-	-	-	
	10.0	12.4	-15.45	-	-	-	

In Table 4.15, a broad bandwidth (BW) of 1.10 GHz can be noted for 9.3 mm thickness. Here for *CP3* composition, -10 dB absorption bandwidth (AB) of 1.01 GHz to 1.09 GHz can be seen for matching thickness of 9.2 to 10 mm.

4.4.4.4 Impedance matching mechanism

The characteristic impedance of free space, $Z_o = (\mu/\varepsilon)^{1/2} = 377\ \Omega$, where μ/ε are the permeability and permittivity of free space, respectively, differs from the impedance of the absorber, Z_{in}.

The absorber's impedance varies from that of free space due to differences in its permeability and permittivity values. When a microwave signal propagates through free space and encounters an absorber, a portion of the signal reflects off the absorber depending on the impedance mismatch between Z_{in} and Z_o; greater differences result in more reflection.

Because of the significant disparity between Z_{in} and Z_o, only a small fraction of the microwave signal penetrates the absorber, while the majority reflects. Consequently, even if the absorber exhibits high dielectric and magnetic loss, the actual attenuation or absorption of the signal within the absorber remains minimal or insignificant due to extensive reflection.

Thus, it is crucial to consider impedance matching between the absorber and free space during absorber design to optimize its effectiveness.

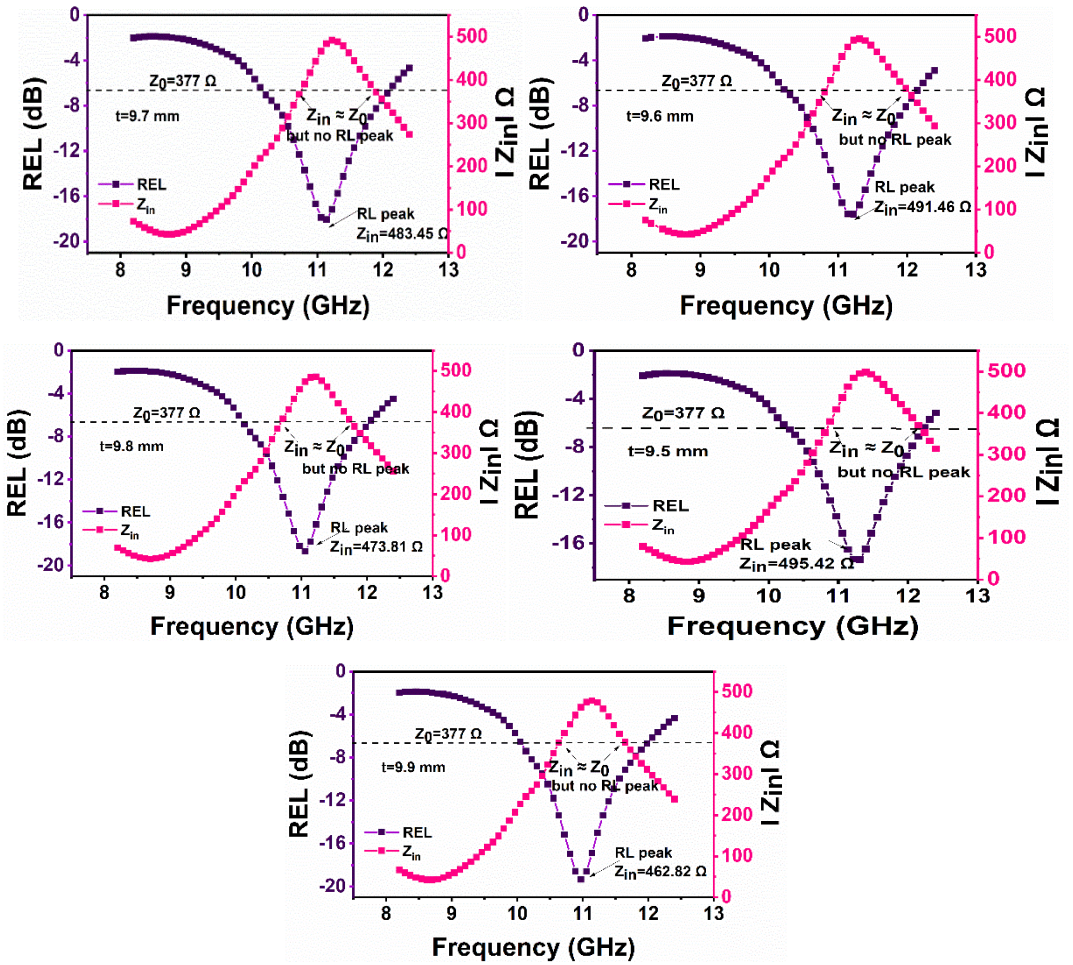

Figure 4.81: Dependence of RL and Z_{in} on Frequency in *CP3* Composition

Table 4.16 lists Z_{in} values of compositions which are obtained from plots of Z_{in} in the mentioned figures. For *CP3* composition, the values of Z_{in} (Table 4.16) are from 302 to 344 Ω for a

thickness 7.5 to 7.6 mm, and 400 to 495 Ω for a thickness of 7.8 to 10.0 mm, in both cases it drifts away from the characteristic impedance value Z_o = 377 Ω . Now if the RL at 7.5 mm and 7.8 mm is compared, it is noticed that RL for later is on the higher side (-17.58 dB) than the prior (-11.83 dB) since Z_{in} for 7.5 mm drifts away more than that at 7.8 mm.

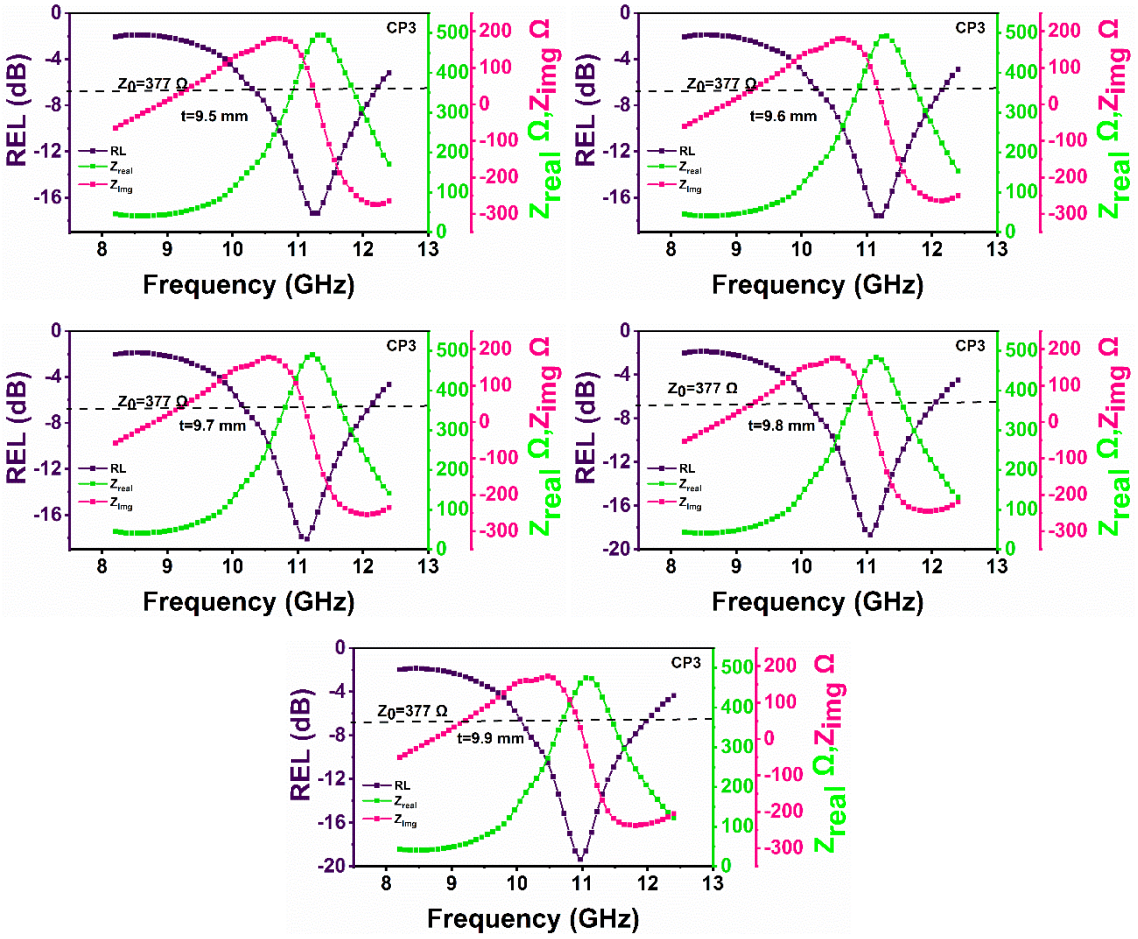

Figure 4.82: Dependence of RL, Z_{in} , Z_{real} , and Z_{img} on Frequency for *CP3*

There is an issue with | Z_{in} | in composition *CP3*, here it owes RL = -16.11 dB at 12.4 GHz frequency, 7.7 mm thickness with Z_{in} = 372.09 Ω (Table 4.16) that is in proximity to Z_o = 377 Ω . On the other hand, large RL = -20.12 dB is reported at 10.88 GHz, thickness 10 mm with Z_{in} = 450.73 Ω (Figure 4.81 and Table 4.16) which is more offset from Z_o = 377 Ω than Z_{in} = 372.09 Ω with RL = -16.11 dB. A similar situation is noted here, wherein RL = -19.34 dB at 10.97 GHz, thickness 9.9 mm is observed with Z_{in} = 462.82 Ω (more away from Z_o = 377 Ω). It is demonstrated by the fact that | Z_{in} | (in equation 3.17) is a complex expression that uses both real and imaginary terms, such as Z_{real} and Z_{img}. As a result, Z_{real} and Z_{img} are computed using (in equation 3.17), and the resulting curves are plotted in the frequency and thickness domains for the composition of *CP3*, Figure 4.82.

Table 4.16: Impedance Parameters of RL Peaks at Different thickness

Co-Cu content	Matching Thickness (mm)	Matching Frequency (GHz)	Maximum RL (dB)	Z_{real} (Ω)	Z_{img} (Ω)	Z_{in} (Ω)
CP3	7.5	12.32	-11.83	271.68	132.94	302.46
	7.6	12.40	-14.65	323.29	120.07	344.87
	7.7	12.40	-16.11	354.35	113.54	372.09
	7.8	12.40	-17.58	387.22	101.33	400.25
	7.9	12.40	-18.71	420.78	82.09	428.71
	8	12.40	-18.96	453.19	54.61	456.46
	8.1	12.40	-18.14	481.79	18.23	482.13
	8.2	12.32	-17.46	490.41	25.82	491.09
	8.3	12.23	-17.07	494.72	33.13	495.83
	9.2	11.48	-17.14	492.93	34.74	494.16
	9.3	11.39	-17.18	490.59	39.23	492.15
	9.4	11.31	-17.26	486.85	44.73	488.90
	9.5	11.31	-17.34	495.42	-2.82	495.42
	9.6	11.22	-17.59	491.43	5.92	491.46
	9.7	11.14	-18.08	483.21	15.46	483.46
	9.8	11.06	-18.67	473.21	23.92	473.82
	9.9	10.97	-19.35	461.74	31.70	462.82
	10.0	10.89	-20.13	449.10	37.99	450.70
CP5	9.5	12.40	-11.39	308.85	178.44	356.69
	9.6	12.40	-12.48	346.19	174.00	387.46
	9.7	12.40	-13.63	387.56	162.44	420.23
	9.8	12.40	-14.68	431.74	141.16	454.23
	9.9	12.40	-15.39	476.03	107.44	488.00
	10.0	12.40	-15.45	515.88	59.33	519.28

We discussed input impedance and λ/4 criterion that controls huge RL values in different compositions. In addition, absorption in the compositions may also be facilitated by the relaxation behaviors seen in the ε and μ spectra. There is a small semicircle in ε' vs ε'' plot of CP3 around 10.63 GHz and RL_{max}= -20.12 dB, 10.89 GHz matching frequency, 10 mm of thickness. Similarly, a small semicircle in μ' vs μ'' plot in *CP3* can be observed at the same frequency. Here it can be concluded that additional variables that affect microwave absorption

are the dielectric and magnetic loss.Figure 4.83 displays Cole-Cole [174-175] plots to verify relaxation for compositions *CP3* and *CP5*. The Dielectric permittivity/dielectric loss and permeability/magnetic loss charts show a semicircle at 10.63 GHz for *CP3* while the permeability/magnetic loss plots show a depressed semicircular arc at around the same frequency.

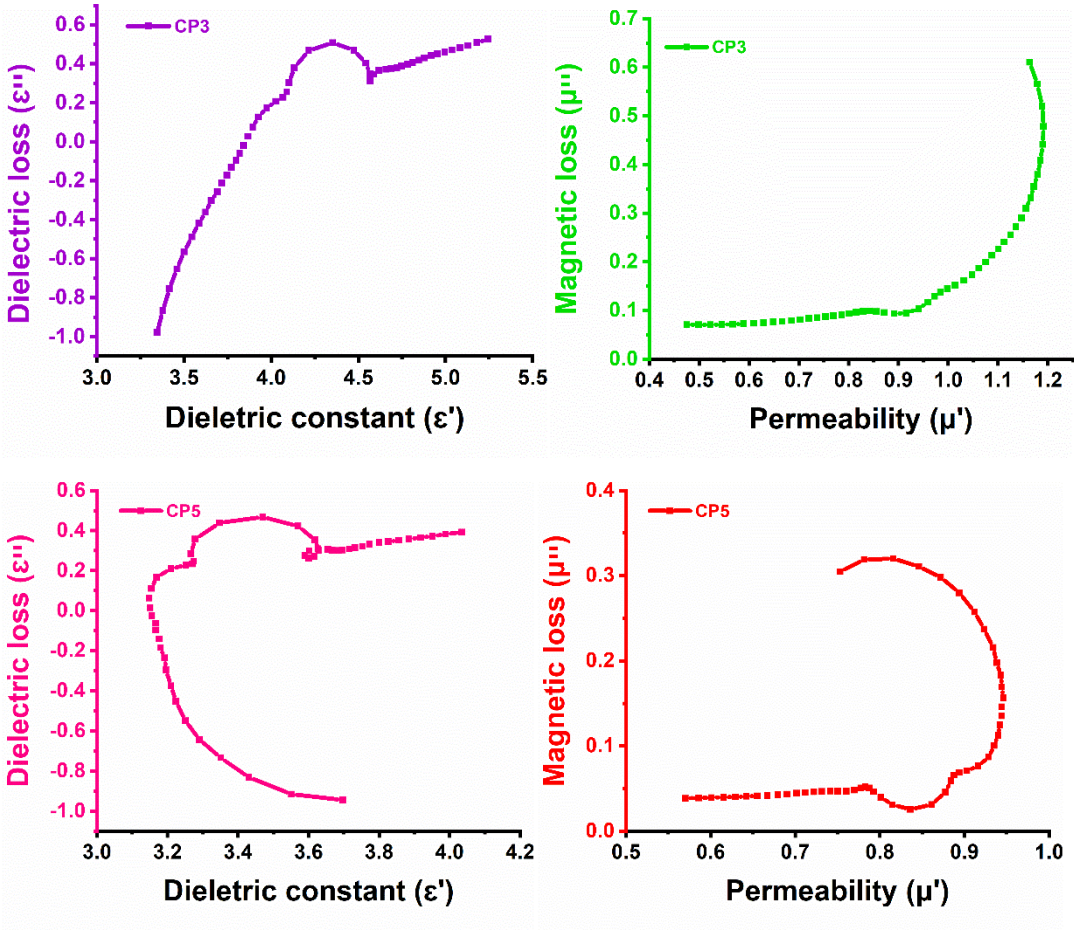

Figure 4.83: Cole–Cole Plots in *CP3* and *CP5* Compositions

It suggests that in complex permittivity plots, dielectric relaxation is linked to peaks seen in ε″ spectra. Conversely, spin resonance and exchange resonance between Fe^{2+} and Fe^{3+} ions support the relaxation shown in complex permeability plots [176-177]. For *CP5* as the RL peaks are not observed, hence there would be no comments on the constant/dielectric loss and permeability/magnetic loss plots of *CP5*.

4.4.4.5. Eddy Current Loss

The Eddy current loss can be the source of magnetic loss in ferrites and can lead to microwave absorption. The eddy current loss is computed using the formula (4.1.1) [35], where C_0 is a constant. The role of the eddy current loss in the magnetic loss contribution is determined by the constant value of C_0 with frequency variation. The constant value of C_0 with frequency variation indicates the contribution of the eddy current loss to the magnetic loss. Figure 4.84

given below depicts that the value of C_0 varies along the complete test frequency indicating that eddy current loss has not contributed here for microwave absorption.

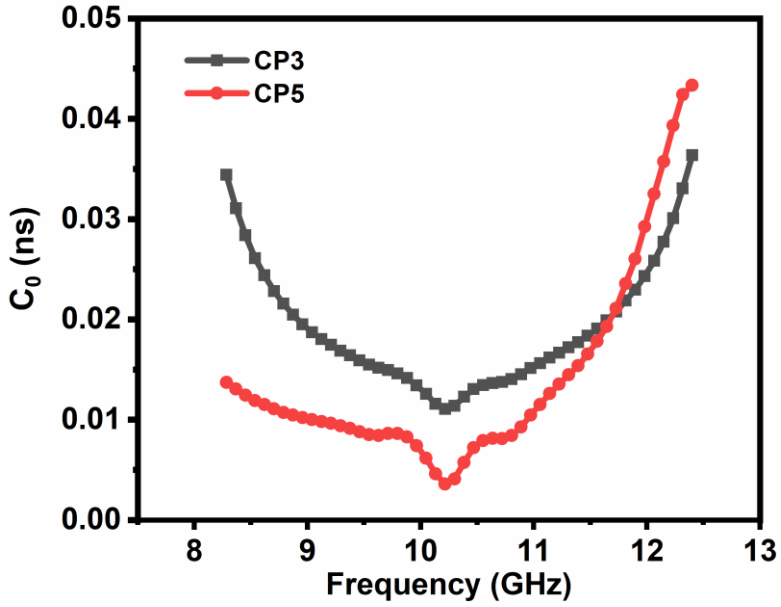

Figure 4.84: C_0 Versus Frequency Variation for Ferrite/PANI Compositions *CP3* and *CP5*

4.4.4.6. BWT/Percentage Bandwidth Ratio

In addition to the criterion $RL \geq -10$, a relevant parameter to design and characterize absorber behavior is the high bandwidth at low thickness for a typical RL or absorption dip. After reaching this RL limit, we must focus on getting a thin layer rather than just increasing RL. Because of this, the bandwidth-to-thickness ratio (BWT) and percentage bandwidth (PBW) in ferrite samples are estimated using relations discussed in section 3.8.

Table 4.15 ascribes BWT for maximum RL with frequency but here the effect of doping cannot be commented on since *CP5* composition has incomplete RL graphs. For *CP3*, it is highest with values of 0.12 at 11.48 and 11.31 GHz and RL_{max} = -17.18 and -17.26 dB.

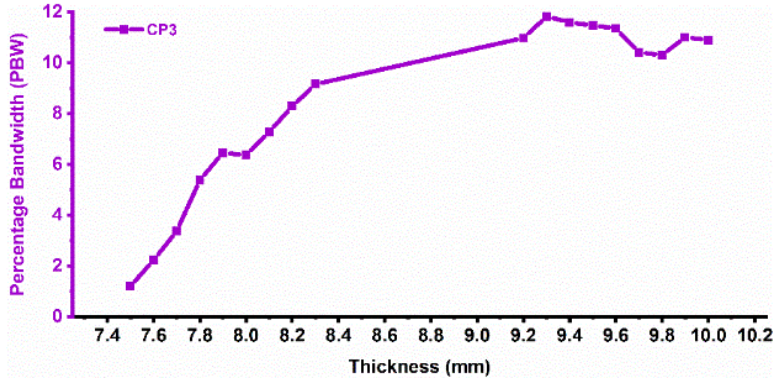

Figure 4.85: Bandwidth (%) Variation with thickness in Ferrite *CP3* Compositions

The PBW is highest for composition *CP3*, RL= -20.12 dB at 10.88 GHz of matching frequency for 10 mm of thickness. It can be noted that it's increasing with increasing thickness, and the PBW ranges between 1-12 %. Here, PBW behavior cannot be commented on since the CP5 sample does not show any PBW due to incomplete RL graphs.

4.5 Co^{2+}-Al^{3+} substituted $Ba_{0.2}Sr_{0.8}Co_xAl_xFe_{12-2x}O_{19}$ hexaferrite

In this section, we have synthesized a hexaferrite with Co and Al substitutions via the sol-gel technique. This composition hexaferrite will be given as $Ba_{0.2}Sr_{0.8}Co_xAl_xFe_{12-2x}O_{19}$. The sample names with the codes for each level of substitution in $Ba_{0.2}Sr_{0.8}Co_xAl_xFe_{12-2x}O_{19}$ are given in Table 4.17.

Table 4.17: The Assignment of Sample Names Corresponding to Various Substitutions Levels in in $Ba_{0.2}Sr_{0.8}Co_xAl_xFe_{12-2x}O_{19}$

Sample Composition $Ba_{0.2}Sr_{0.8}Co_xAl_xFe_{12-2x}O_{19}$	Sample Code Name	Sample Code (A-Series)
x = 0.0	$Ba_{0.2}Sr_{0.8}Fe_{12-2x}O_{19}$	A1
x = 0.4	$Ba_{0.2}Sr_{0.8}Co_{0.4}Al_{0.4}Fe_{11.2}O_{19}$	A2
x = 0.8	$Ba_{0.2}Sr_{0.8}Co_{0.8}Al_{0.8}Fe_{10.4}O_{19}$	A3
x = 1.2	$Ba_{0.2}Sr_{0.8}Co_{1.2}Al_{1.2}Fe_{9.6}O_{19}$	A4
x = 1.6	$Ba_{0.2}Sr_{0.8}Co_{1.6}Al_{1.6}Fe_{8.8}O_{19}$	A5
x = 2.0	$Ba_{0.2}Sr_{0.8}Co_2Al_2Fe_8O_{19}$	A6

4.5.1 Structural Analysis

4.5.1.1 X-ray Analysis

Figure 4.86 depicts the X-ray diffraction pattern of prepared hexaferrite samples $Ba_{0.2}Sr_{0.8}Co_xAl_xFe_{12-2x}O_{19}$ (*A1, A2, A3, A4, A5,* and *A6*) and the Bragg peaks of the prepared samples are well-defined. To determine Miller indices of the obtained peaks, Powder-X software has been used, and peaks matched with a typical standard pattern of Barium hexaferrite-$Ba_{0.5}Sr_{0.5}Fe_{12}O_{19}$ having space group P63/mmc (JCPDS card no 51-1879). The XRD investigation of the samples depicts the existence of the primary phase as M-type (hexagonal) along with minor traces of the secondary spinel phase ($BaFe_2O_4$) (JCPDS card no. 77-2337) and magnetite (Fe_3O_4) (JCPDS card no 86-1362).

The lattice parameters (a = b and c), the volume of the unit cell, and the crystallite size for the synthesized samples are calculated using equations 3.1, 3.2, and 3.3 from section 3.2.1 and specified in Table 4.18.

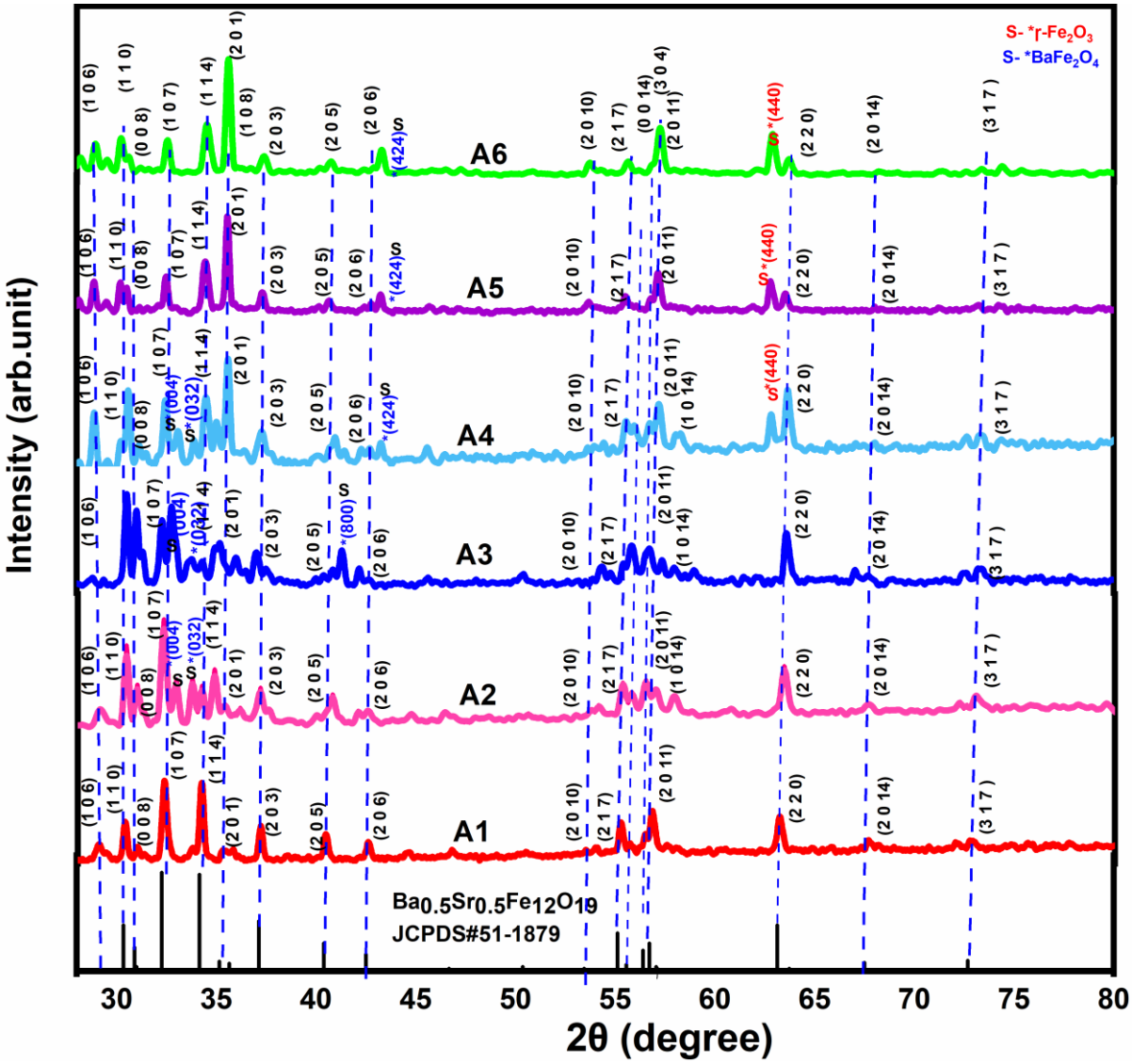

Figure 4.86: X-ray Diffractions of M -type $Ba_{0.2}Sr_{0.8}Co_xAl_xFe_{12-2x}O_{19}$ (*A1, A2, A3, A4, A5,* and *A6*) Hexaferrite

The calculated lattice parameters of the prepared samples are listed in Table 4.18. From the table, it can be seen that lattice parameter *a* is varied more as compared to that lattice parameter lattice parameter *c*. It can be seen from the table that lattice constants (*a*, *c*) and cell volume do not owe much change with doping of Co-Al from samples *A1* to *A4*, whereas a significant change in lattice parameters is observed in samples *A5* and A6. It is plausibly related to the difference in ionic radii of dopants Co^{2+} (0.72 Å), Al^{3+} (0.51 Å), and parent Fe^{3+} (0.64 Å) [186-187]. The *c/a* ratio of the samples agrees with the typical value of 3.98 reported by Wagner [188], and crystallite size remains in the narrow range of 15.36-17.74 nm.

Table 4.18: Co-Al Content, Lattice Constants, Ratio c/a and Unit Cell Volume Ferrite Sample $Ba_{0.2}Sr_{0.8}Co_xAl_xFe_{12-2x}O_{19}$ (*A1, A2, A3, A4, A5,* and *A6*)

Co-Al Content (x)	Lattice constant a =b (Å)	c (Å)	Ratio c/a	Unit cell vol. V (Å) ^{3}	Crystallite Size D_{xrd} (nm)
0.0	5.8811	23.1322	3.933	692.8903	15.3604
0.4	5.8823	23.1351	3.934	693.2600	15.3987
0.8	5.8813	23.1371	3.934	693.0842	15.6228
1.2	5.8817	23.1350	3.933	693.1156	17.7419
1.6	5.7893	23.2271	4.012	674.1826	16.7816
2.0	5.7884	23.1320	3.996	671.2135	16.7657

4.5.1.2 Field Emission Scanning Electron Microscopy

Figures 4.87 (a-f) display the grain morphology of the samples. The micrographs depict that fused grains result in the formation of a colossal grain in undoped sample *A1,* and small-size individual grains can also be seen as shown in Figure 4.87 with different magnification factors. The agglomeration of grain is observed with the doping of Co-Al content, and a non-uniform trend in grain size distribution has been observed in compositions. As the doping increases from *A1* to *A6,* needle-shaped along with hexagonal-shaped platelets can be noticed; Figure 34.87 (f) shows the formation of needle-shaped grains in *A6*. The doping causes the formation of grain clusters with non-uniform size distribution attributed to electrostatic effects and magnetic interaction between ferrite particles. The small size of individual grains is seen in the gain clusters; thus, grain size is inhibited with the doping at high doping levels.

The arrangement of grains has some voids within that could provide reluctance/hindrance to the flow of charge carriers. The smaller the size of grains, the more the grain boundaries and the larger the impediment/resistivity to the applied field, modifying the charge transport mechanism.

The EDX analysis particularly provides an estimation of an elemental presence as per specifications of mixed chemicals during synthesis. The EDX spectra of $Ba_{0.2}Sr_{0.8}Co_xAl_xFe_{12-2x}O_{19}$ samples *A1* and *A2* have been presented in Figure 4.88. It can be seen from EDX spectra that the Ba, Sr, and Fe elements are present in composition *A1* which is a pure sample, while Ba, Sr, Fe, Co, and Al elements are present in composition *A2*. The weight and atomic percentages of all elements present in the final compositions are provided in the graph presented in Figure 4.88.

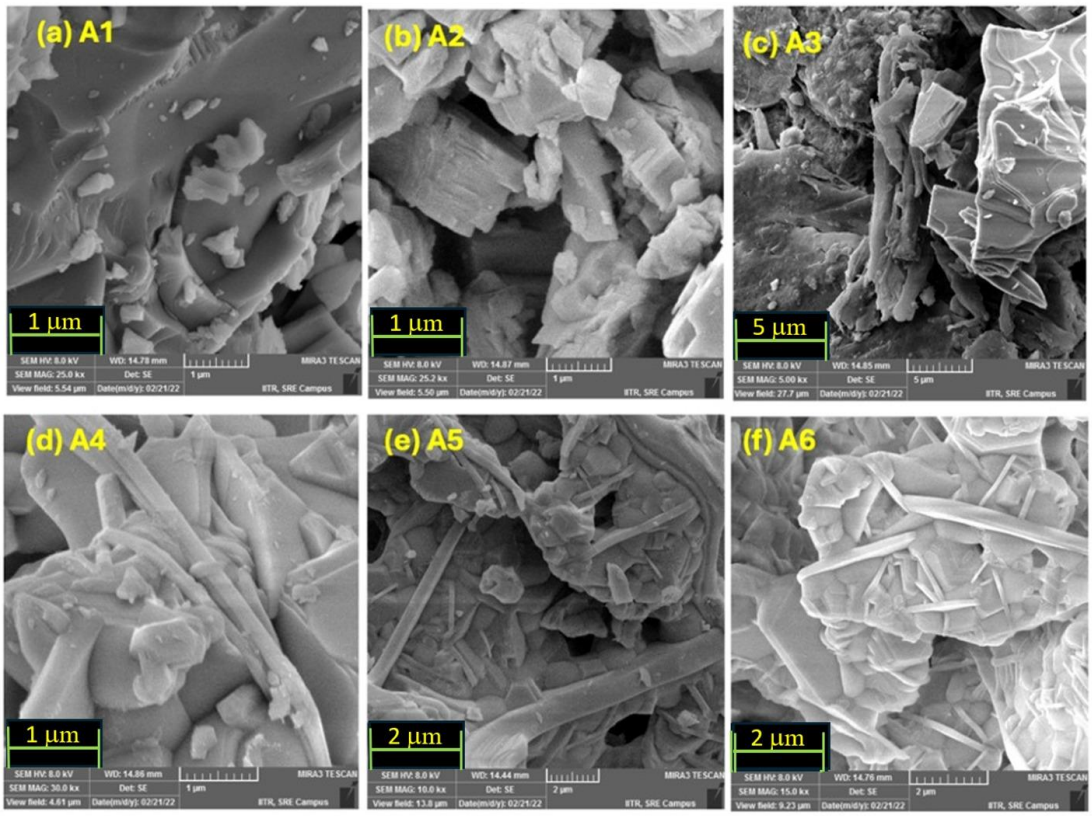

Figure 4.87: SEM Micrographs of Ferrite Samples: $Ba_{0.2}Sr_{0.8}Co_xAl_xFe_{12-2x}O_{19}$ (*A1*, *A2*, *A3*, *A4*, *A5*, and *A6*)

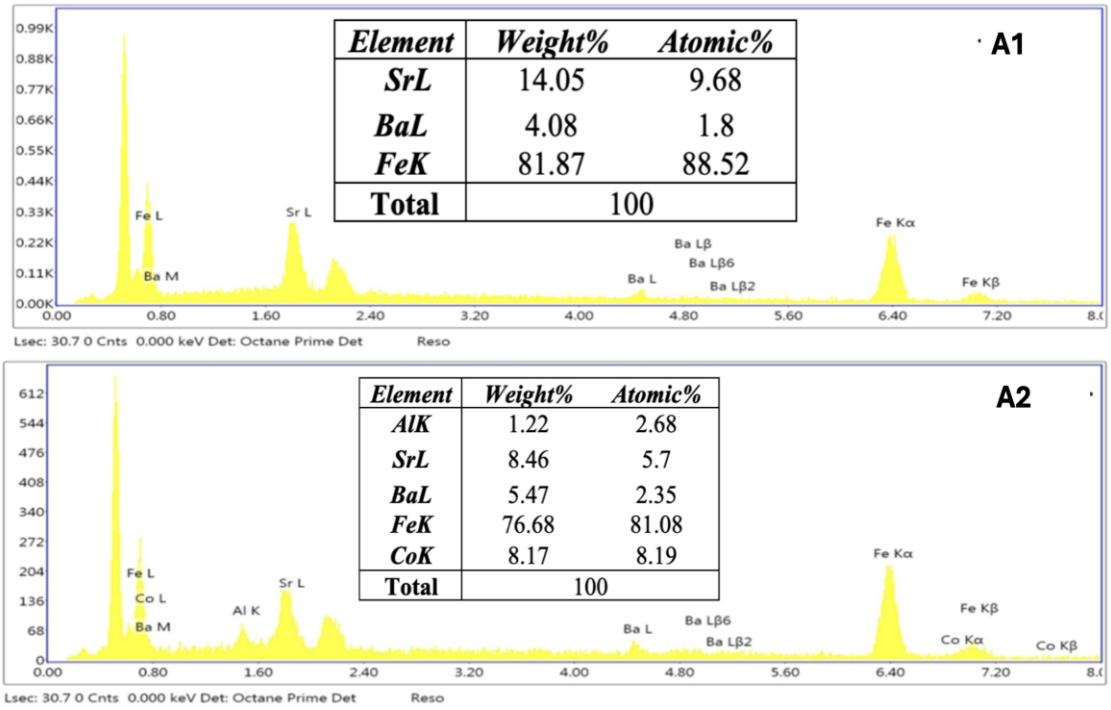

Figure 4.88: EDX Spectra of $Ba_{0.2}Sr_{0.8}Co_xAl_xFe_{12-2x}O_{19}$ Hexaferrite for Samples *A1* and *A2*

4.5.2 Electrical Analysis

4.5.2.1 Dielectric permittivity

The calculation for the real part of the dielectric permittivity (ε') is done using the formula (3.4) in section 3.3.1 and the calculations of the imaginary part of the dielectric loss (ε'') and dielectric loss tangent ($tan\delta$) have been performed from equation (3.5) and (3.6) from the same section.

Figure 4.89 demonstrates two types of plots with frequencies ranging from 100 Hz to 2 MHz, (a) the first real part accompanied by a dielectric permittivity and (b) the second, the imaginary part associated with dielectric loss. It can be seen from Figure 4.89 (a) that the value ε' shows dispersion with a fall in frequency in the low-frequency spectra, and it becomes independent of frequency after 2 kHz in all samples. It is observed that the value ε' decreases non-monotonically with an increase in doping of Co^{2+} and Al^{3+}, the lowest being for *A6* and the highest being for *A1*. The mechanism of dielectric mechanism is according to the Maxwell-Wagner model based on Koop's phenomenological theory [161].

The existence of highly conductive grains with insulating grain boundaries outgrows confined aggregation of charge due to the impact of an electric field, resulting in space charge polarization. A definite time is required for space charge carriers in the sinusoidal electric field to arrange themselves parallel to the field. When there is an unceasing increment in the field reversal frequency, there comes a point wherein the space charges are not able to stay in synchronism with the sinusoidal field. And it lags the field, henceforth reducing the dielectric permittivity of the material. In ferrite material, polarization can be related to the conduction process that takes place primarily because of the hopping conduction mechanism [189].

The electrical conduction that follows in ferrite materials is elaborated by the Verwey-de-Boer hopping technique [190]. Verwey interpreted that the process of conduction is primarily associated with the hopping of electrons. This hopping is mainly between the electrons of different ions of the same elements that were formed during the process of sintering. Ferrite material is distinguished by the concentration of its Fe^{2+}/ Fe^{3+}ions, but this concentration depends upon various factors such as sintering time, sintering temperature, etc. The main play of polarization is due to the Fe ions that lead valence electrons hopping within +2 and +3 states of valency. This hopping leads to the displacement of charges in the sinusoidal direction of the applied electric field [191-192].

As discussed before in Figure 4.89 (a) (b), Dielectric permittivity/loss reaches a steady state value after a certain frequency: the electron hopping accompanied by the electron exchange with +2 and +3 states is not able to follow it.

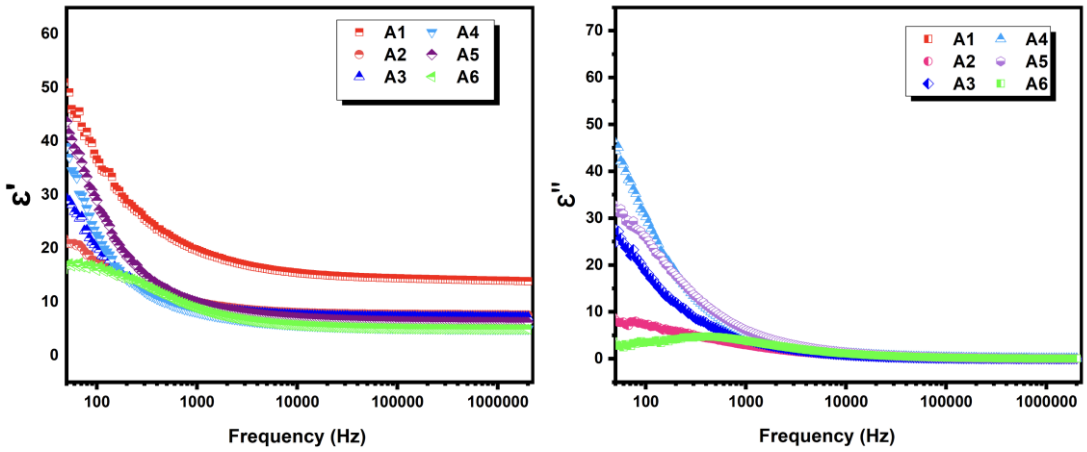

Figure 4.89: Variation of Dielectric Spectra of Ferrite Sample $Ba_{0.2}Sr_{0.8}Co_xAl_xFe_{12-2x}O_{19}$ for (*A1, A2, A3, A4, A5,* and *A6*) a) Real Component b) Imaginary Component as a Function of Frequency

The maximum dielectric permittivity in *A1* is associated with the highest concentration of ferrous ions on the octahedral sites, whereas this content is small in the rest of the samples of $Ba_{0.2}Sr_{0.8}Co_xAl_xFe_{12-2x}O_{19}$. It is also known that ferrites owe conductivity/polarization due to the hopping of electrons between octahedral sites.

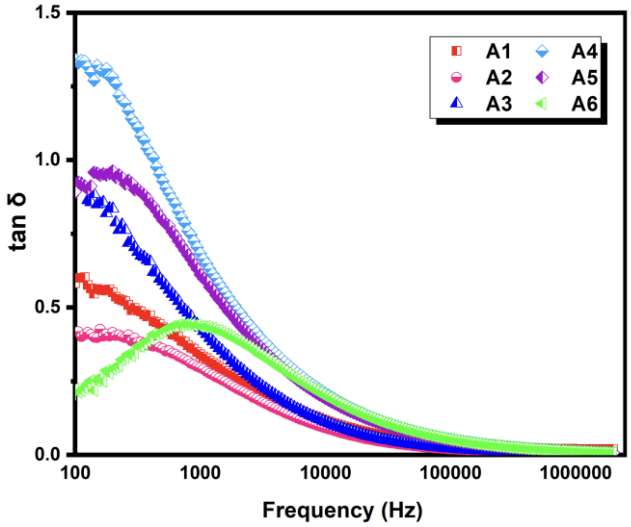

Figure 4.90: Variation of Dielectric loss Tangent of Ferrite Sample $Ba_{0.2}Sr_{0.8}Co_xAl_xFe_{12-2x}O_{19}$ (*A1, A2, A3, A4, A5,* and *A6*) as a Function of Frequency

Figure 4.90 attributes that the dielectric loss tangent decreases in its value with an increase in frequency in all samples. This decrease in the value of *tanδ* is explained by Koop's phenomenological theory of dielectrics [161]. The figure also shows well-defined pronounced peaks of tanδ in the low-frequency region. The doping of Co-Al causes an increase in loss tangent in *A3, A4,* and *A5,* and it is ~2 times in *A4* than in undoped sample *A1*. There is an

observation of a shift in the loss peaks towards a high-frequency regime attributed to dopants. The loss tangent depends on various factors, namely Fe^{2+}/Fe^{3+} content, interfacial polarization, interface traps, the stoichiometry of the sample, structural oneness, and finally, all these factors eventually depend on the sintering temperature.

Another reason for peaking behavior in $tan\ \delta$ is associated with interfacial polarization and traps formed among the interfaces. The interfaces/traps are formed during the sintering process in ferrites, which induces interfacial polarization (electric field), and charge careers are bounded in the traps. The applied AC signal forms a changing electric field across the interfaces of ferrite, and this varying field causes the charge careers to move away from the trapped region. The fast-changing electric field, owing to the increase in frequency, exerts rapid field on the charge careers, and ultimately, charge careers move away from the traps. This process increases the density of the charge career, and during this time, grain boundaries offer impediments to the increased charge careers. Thus, the energy requirement for electron exchange is greater, leading to greater energy loss, resulting in the high value of $tan\delta$. But grains are effective in the high-frequency region and assist the charge carriers. Thus, the energy requirement for electron exchange between Fe^{2+} and Fe^{3+} ions is on the lower side for high values of frequency, leading to small energy loss, and hence there is a low value of loss tangent [193]. The nature of ε', ε'' and $tan\ \delta$ is in accordance with work reported earlier [194-195].

4.5.2.2 Electric modulus analysis

The exercise on complex electric modulus helps us analyze the electrical behavior of the material. This approach helps us know about the nature of polycrystalline material and evaluates the electrical relaxation in ionic solids.

M' and M'' are the real and imaginary parts of the complex electric modulus and are calculated using equation 3.8 and equation 3.9 respectively (from section 3.3.2).

Typically, the peculiarity of M^* concerning frequency comprises an expansive, asymmetric peak in the graph of the imaginary part of the modulus and a sigmoidal shape for the real part of the modulus. Figure 4.91 (a) depicts the variation of the real part of the modulus (M′) vs frequency. It is confined to a low value (tending towards zero) for a lower frequency region, then increases linearly to a certain value. Thereafter, plots tend to saturate at a certain point for all the samples, being the lowest for the pure/undoped *A1* sample. As the electric field is applied, the charge carriers come under the influence of the applied electric field. But the lack of restoring force, which governs the mobility of these careers, influences these observations. This trend suggests the dependence of electrical properties on conductive grains. As the Co and

Al content increase, a corresponding increase in M' can be observed with a maximum for the *A6* sample.

As can be seen in Figure 4.91 (b), the divergence in the plots of the imaginary part of modulus in the frequency domain contributes to the information about charge transport mechanisms viz-a-viz electrical transport, conductivity, relaxation, and ion dynamics. It can be seen from the graph of M'' that as the doping content increases, the peaks of each sample can be seen to reach their highest point; a peak of *A4* owes the highest value.

In low-frequency regions, ions migrate over longer distances, i.e., ions can achieve successful hops from one site to another. But for higher frequencies, the peaks in M'' depict that the ions don't follow the longer hopping but rather are confined to their finite potential wells. The territory where the peaks are covered indicates the changeover from long-range mobility to a shorter one with the corresponding increase in frequency. Thus, the modulus spectrum signifies the hopping mechanism for electrical conduction. The peak frequency here portrays conduction relaxation time, and shifting of peak frequency Co-Al dopants towards high-frequency region implies a reduction in relaxation time.

As discussed previously, conductivity relaxation is also attributed to the release of charge careers (bounded in traps) under the influence of an increase in frequency. Further, asymmetric and broad peaks with dopants are indicative of the absence of Debye-type relaxation in the samples.

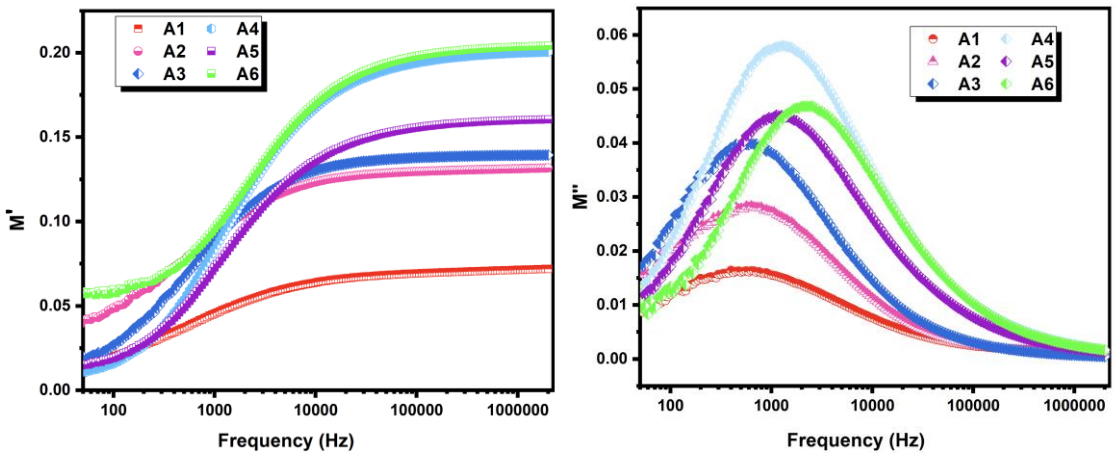

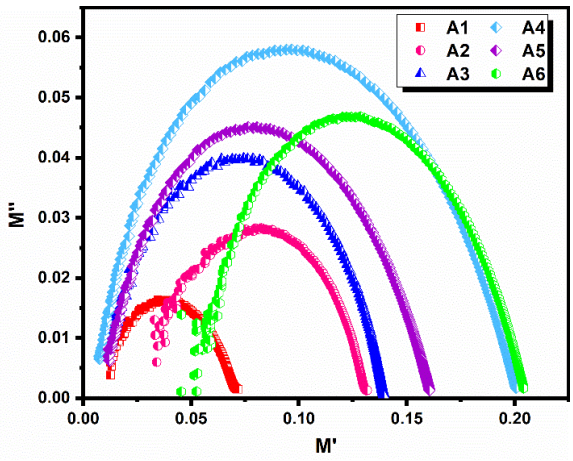

Figure 4.91: Electric Modulus Variation (a) real component, (b) imaginary component of ferrite sample $Ba_{0.2}Sr_{0.8}Co_xAl_xFe_{12-2x}O_{19}$ as a function of frequency (c) Cole-Cole (M' vs M'') plot of ferrite sample

Figure 4.91 (c) depicts the Cole-Cole plot (M' vs M'') of the sample $Ba_{0.2}Sr_{0.8}Co_xAl_xFe_{12-2x}O_{19}$. The plots demonstrate asymmetric semi-circles in the samples. The doping of Co-Al shifts the arc towards a low-frequency regime; the intercept of the semicircular arc increases with doping. Hence, grains contribute to the mechanism of electric transport, and the center of the arc is found to lie below the x-axis (M'), signifying non-Debye relaxation in the samples. The change in maxima of the semi-circle for the maximum frequency with doping illustrates the distribution of relaxation time. This distribution backs up the non-Debye type of relaxation [196].

4.5.2.3. Complex impedance spectra

The analysis of impedance provides us with information on resistance (Z') and reactance (Z'') in the material. The impedance behavior of polycrystalline materials is primarily due to bulk grains and grain boundaries. The impedance of bulk grains can be treated differently from grain boundaries since both have different relaxation times.

In the Cole-Cole plot, Z''(imaginary part of impedance) is plotted concerning Z'(real part of impedance), where the complex impedance is given by equation (3.10) in the 3.3.3 section. The resistive (real) and reactive (imaginary) parts of impedance are given by equations (3.11) and (3.12) respectively from the same section.

Figure 7 (a) shows the variation of the real part of impedance (Z') concerning frequency. It has been observed that Z' constantly decreases with an increase in frequency, and after a certain point, this value of Z' almost becomes constant. This reduction in the value of Z' can be due to the space charge and dipole polarization effect of the samples. From *A1* to *A3* samples, Z'

increases to a maximal value, and thereafter, it decreases with further doping: lowest value in sample *A6*.

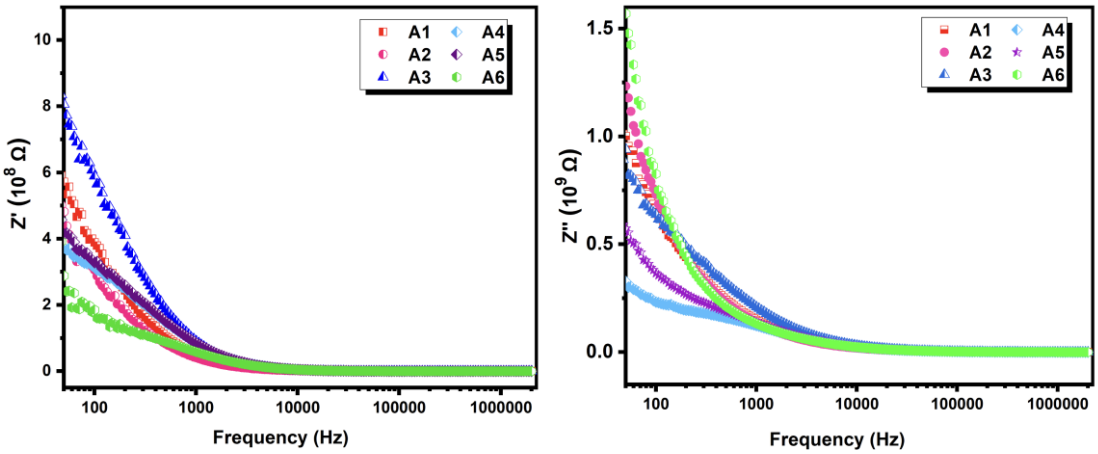

Figure 4.92: Dispersion in the (a) Dielectric Impedance Real (*Z′*), (b) Dielectric Impedance Imaginary (*Z″*) of $Ba_{0.2}Sr_{0.8}Co_xAl_xFe_{12-2x}O_{19}$ (*A1, A2, A3, A4, A5,* and *A6)* as a Function Frequency

Further, plots of all samples get coalesced with the lowest values at the high-frequency spectrum. It is attributed to the reduction of space charge polarization with the corresponding increment in frequency.

To understand the space charge effect in a better way, the change in the imaginary part of impedance has been investigated with the change in frequency, as shown in Figure 7.92 (b). There is a non-monotonic shift in *Z″* values along with the low-frequency regime with an increase in Al and Co content.

In Figure 4.93, the plot of *Z″* versus *Z′* for each sample shows a semi-circular arc in the curves. For doped compositions, there is depression of the arc for *A2*, *A3*, and *A4* from sample *A1*. But then, for sample A5, there is a slight rise in the height of the arc of the sample. These depressions in the high-frequency region are associated with dielectric polarization at grains. For *A2* and *A3*, individual grains, along with non-magnetic voids, can be seen in micrographs (Figure 4.87). However, clusters and grain agglomerate stem in *A4*, *A5*, and *A6*, while *A1* has a flat surface of colossal grain with a small size distinct grain over it.

The individual grain boundaries contribute to an increment in resistance (*Z′*) and render polarization enhancing the capacitance (*Z″*) in *A1*. On the contrary, grain cluster/agglomerate reduces the grain boundaries, thereby reducing both *Z′* and *Z″* in *A2*, *A3*, *A4*, *A5*, and *A6*. Among all compositions, there is a considerable decrease in Z′ for *A6*: *Z″- Z′* plot in *A6* moves towards high-frequency spectra, implying the contribution of grains.

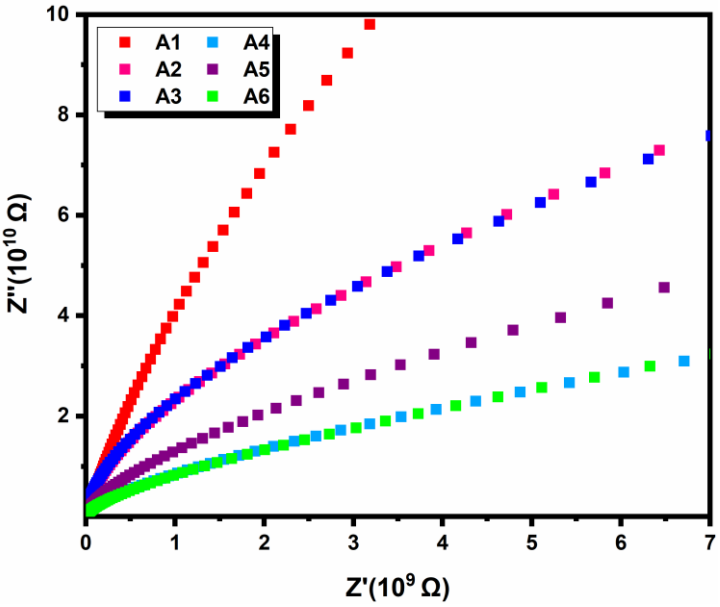

Figure 4.93: Dispersion in the (a) Dielectric Impedance Real (Z′) Part Versus Dielectric Impedance Imaginary (Z′′) Part of $Ba_{0.2}Sr_{0.8}Co_xAl_xFe_{12-2x}O_{19}$ (*A1, A2, A3, A4, A5,* and *A6)* as a Function Frequency

It elucidates the contribution of grains, which play an important role in the high-frequency regime for the impedance mechanisms in *A6*. *A1*, the plots occupy a position in the high-frequency regime, indicating the role of grains in the mechanisms. However, the role of grain boundaries is prevalent explicitly for *A2*, *A3*, *A4*, *A5*, and *A6*.

4.5.2.4 AC Conductivity

The conduction in ferrites is primarily reported due to the hopping of its valence electrons between Fe^{2+} and Fe^{3+} at Octahedral sites. The increase in frequency boosts the hopping frequency of charge carriers and causes an increase in conductivity. This frequency-reliant conduction mechanism is explained based on the polaron hopping model reported in [124]. Based on that model, AC conductivity increases with an increase in frequency for the limited range of polaron hopping. However, it shows a decreasing trend for long-range polarization hopping. In the case of band conduction, the conductivity phenomenon is frequency-independent [125].

Figure 4.94 depicts the plot of AC conductivity as a function of frequency in the ferrite samples. In the present investigation, it is seen that AC conductivity progressively increases after the 1 kHz frequency of the applied AC field. It shows nearly frequency- Independent behavior below 1 kHz and this frequency marks the transition from DC conductivity to AC conductivity. The doping of Al^{3+} and Co^{3+}. Ions in place of Fe^{3+} bounds the scope of conduction, hampering the Verwey hopping mechanism at octahedral sites.

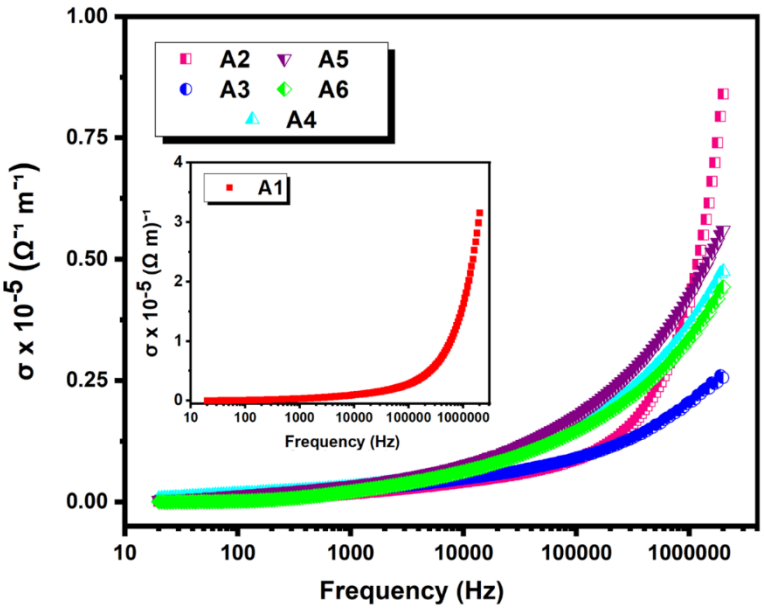

Figure 4.94: Variation of AC Conductivity Concerning Frequency for Ferrite Sample $Ba_{0.2}Sr_{0.8}Co_xAl_xFe_{12-2x}O_{19}$ (*A1)* (*A2, A3, A4, A5,* and *A6*)

This leads to a decrease in conductivity, which can be seen in Figure 4.94. The hopping frequency seems to alter to a lower frequency as Al and Co content increases.

The frequency-dependent AC conductivity is given in section 3.3.4 known as the Jonscher power law.

The Jonscher power law is useful for characterizing the behavior of dielectric materials over a wide range of frequencies. It is often used in the analysis of experimental data, particularly in studies of materials such as polymers, ceramics, and glasses. The law is named after A.K. Jonscher, who first proposed this relationship to describe the frequency-dependent behavior of the dielectric properties of materials [126].

According to Funke [127], the value of n has a physical meaning: $n < 1$ means that the electron hopping involves a translational motion with sudden hopping, whereas $n > 1$ means that the motion involves localized hopping between neighboring sites. The value of n was calculated by fitting the plots: *A1* - 0.514, *A2* - 0.4929, *A3* - 0.328, *A4* - 0.340, *A5* - 0.3828, *A6* - 0.5836. Thus, the value of n comes out to be less than 1, implying the mechanism of ac conductivity accompanied by the hopping of charge carriers.

The large values of n in samples *A1*, *A2*, and *A6* imply a relatively steep rise in the AC conductivity in the high-frequency region. Thus, there is a sudden rise in charge careers in the mentioned samples at the high-frequency region. As discussed before, grains contribute to conductivity in the high-frequency region. Micrographs depict colossal grain, fused grains, and grain clusters in *A1*, *A2*, and *A6*, respectively, which may cause an exponential increase in AC conductivity at the high-frequency region. Hence, an anomaly is seen between the fitting and

measured graph in these samples. However, it needs further investigation to ascertain the mechanism for this variation.

4.5.3 Magnetic analysis

The occupancy of cations in crystallographic sites is determined by their electronegativity; more electronegative ions choose octahedral locations, which are larger compared to tetrahedral positions. Al^{3+} (1.61) can occupy tetrahedral spaces because it is less electronegative than Co^{2+} (1.88) [197]. The d-configuration and the type of cations involved may also be used to determine the site occupancy of cations. Co^{2+}, which is typically d^7-configuration, can occupy octahedral positions, but according to ligand field theory, Al^{3+} ions, featuring d^0 configuration, exhibit no site preference. According to reports, Al^{3+} ions typically occupy tetrahedral sites, whereas Co^{2+} ions typically occupy octahedral sites. Furthermore, Al^{3+}ionic radii are (54 Å) relatively smaller, so it can be concluded that they preferably occupy tetrahedral positions. Co^{2+} (0.72 Å) ions can occupy octahedral sites at the unit cell because their ionic radii are bigger than those of the host Fe^{3+} (0.64 Å) ions [198].

The hysteresis loops (room temperature) for all synthesized ferrite samples are displayed in Figure 4.95. (M_r/M_s) ratio, saturation magnetization (M_s), anisotropy field (H_a), coercivity (H_c) and remanence magnetization (M_r) are enumerated in Table 4.19.

As seen in Figure 4.95, the M-H loop showed that all prepared specimens have a linear relationship and a fast increase in Ms at low-applied fields that slows down at high-applied fields. (M_r/M_s), (M_r) (H_c).

The continued retention of magnetization following the removal of an applied field is determined by Remanence magnetization, which is usually large in M-type hexaferrite, suggesting substantial remanence. The squareness ratio M_r/M_sratio, whose value should fall between 0 and 1, is also used to assess the material's magnetic hardness and inter-grain group development. Although materials with $0.05<M_r/M_s<0.5$ have randomly oriented multi-magnetic domains, those with a large squareness ratio ($0.5<M_r/M_s<1$) are more anisotropic, single-domain, and hard.

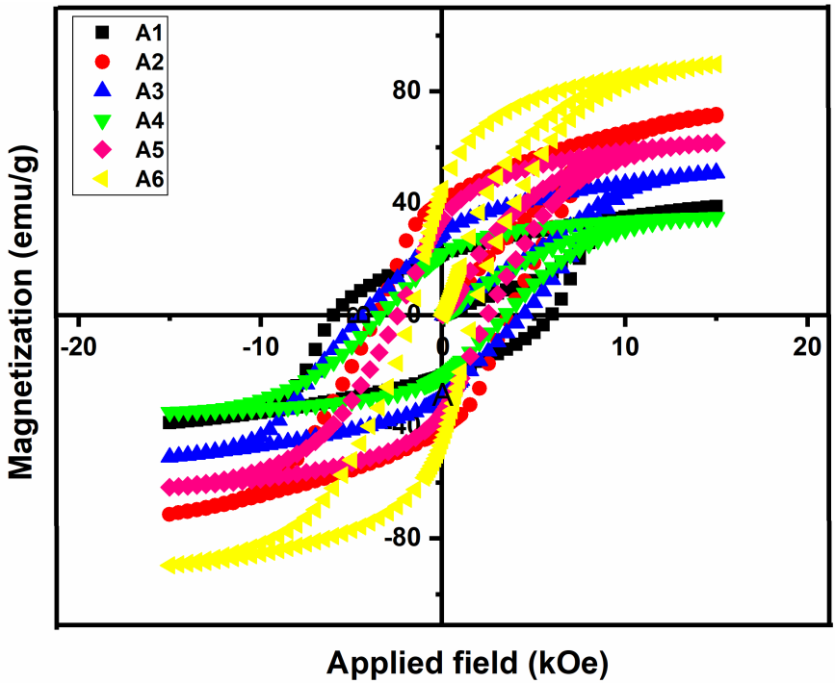

Figure 4.95: Hysteresis Loops of *A1, A2, A3, A4, A5* and *A6* Hexaferrite

In the present study, the M_r/M_s value for the *A1, A2, A3, A4,* and *A5* samples is larger than 0.5, indicating that the particles of the material are single-domain in nature. Conversely, A6 shows that the material contains multiple domains with $M_r/M_s<0.5$.

In a pure x = 0.0 sample (section 4.2.3) the saturation magnetization (41.77 emu/g) is at its lowest; this value rises as cations are substituted.

Table 4.19 depicts that M_s initially increases from 41.77 emu/g (*A1*) to 77.87 emu/g (*A2*), which is around 86% increase. Followed by 57.59 emu/g (*A3*), here, there is an increase of 38% from that of 41.77 emu/g (*A1*). These increased M_s values may be due to ions taking the spin-down sites. Sample x = 1.2 (*A3*) is the only sample where M_s is decreased and is by 7 %. Again, for *A5*, the saturation magnetization is 66.55 emu/g, and for *A6*, it is 95.35 emu/g. The table shows that M_s is increases from 41.77 emu/g (*A1*) to 95.35 (A6) as the doping content increases. A pure sample (*A1*) exhibits the highest value of coercivity (5882 Oe). H_c can be seen decreasing from 5882.25 (*A1*), 3812.16 (*A2*), 3607.38 (*A3*), 3205.98 (*A4*), 2428.87 (*A5*), and the lowest being for 1717.13 (*A6*). H_a does not seem to have any prominent effect on H_c. The table depicts that as M_s increases with doping, the H_c decreases, the only exception here is a sample (*A4*) where M_s is also seen to decrease. This may be explained by the fact that fewer magnetic Al^{3+} ions and Co^{2+} replace Fe^{3+} ions at octahedral sites or this may require further investigation.

Additionally, it is discovered that the value of M_s for *A6* is the greatest. The squareness ratio (M_r/M_s), the presence of secondary phases, and the SEM micrographs (Figure 4.97) may all be used to explain this saturation magnetization behavior.

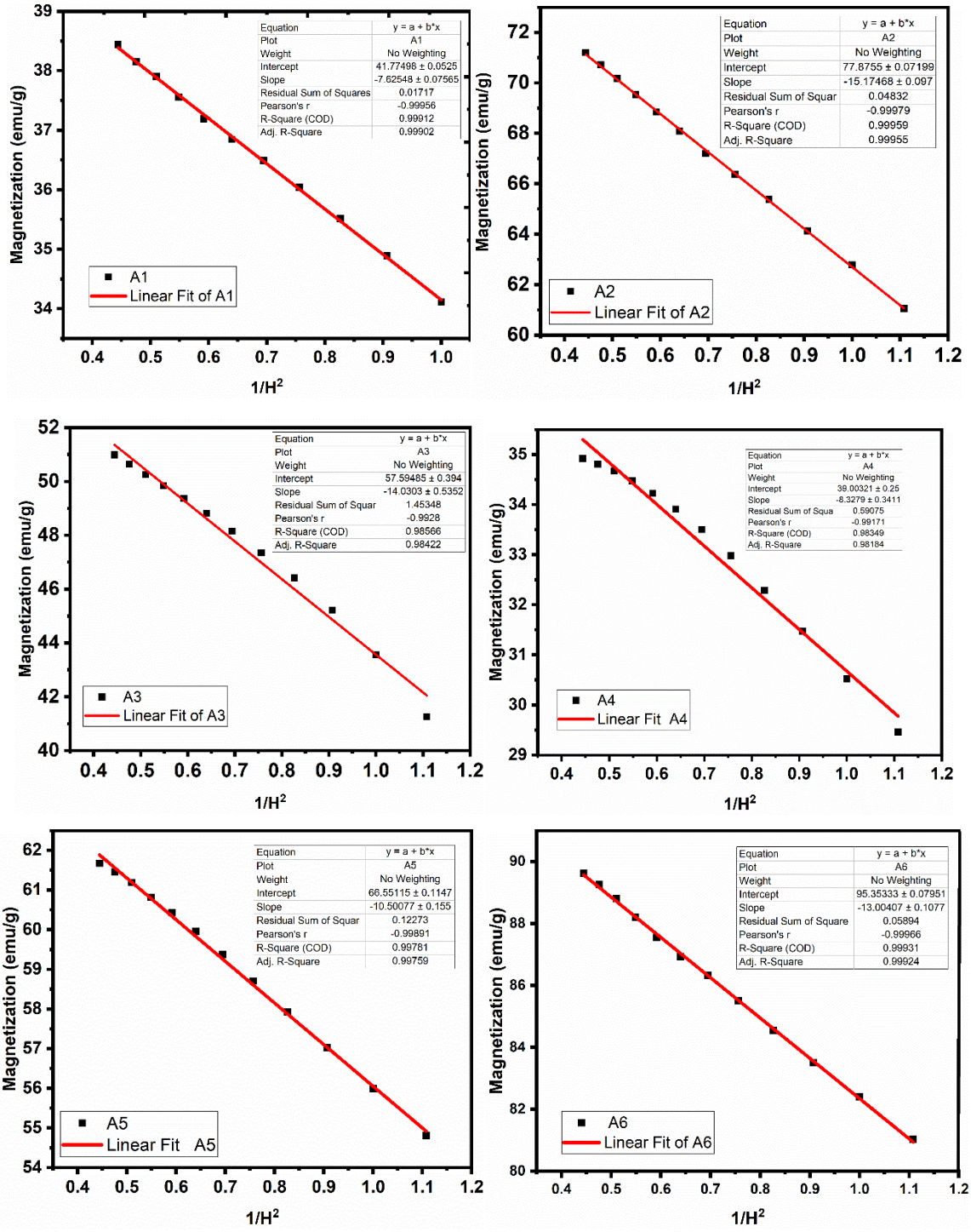

Figure 4.96: M_s Versus 1/ H^2 Plots for all Hexaferrite Samples

Table 4.19: Magnetic Parameters M_s, H_c, H_a, M_r and M_r/M_s for Al-Co Doped Hexaferrite Samples

Sample	M_s	H_c	H_a (kOe)	M_r	M_r/M_s
A1	41.77	5882.25	16.55	21.73	0.52
A2	77.88	3812.16	17.10	40.21	0.52
A3	57.59	3607.38	19.12	29.75	0.52

A4	39.00	3205.98	17.90	21.73	0.56
A5	66.55	2428.87	15.38	35.05	0.53
A6	95.35	1717.13	14.30	43.11	0.45

The rise in M_s from *A1* to *A6* may now be concluded by comparing the SEM plots 4.87 with Table 4.19 (magnetic data). For *A1* in the SEM graph, the particles are seen as separate from each other with very little agglomeration within the particles, so Ms is the lowest here. Good grain connectivity and better cluster formation within the grains are responsible for increased M_s in doped samples. As compared to *A1*, *A3* has better-connected grains but not as good as *A2*. So, M_s is on the higher side for *A2*.

The saturation Magnetization is maximum in the *A6* sample (95.35 emu/g) and coercivity is also lowest (1717). So it is attributed to the secondary phase as shown in the XRD graph, here magnetic phase is highest since magnetite is a soft magnetic material. Therefore it can be said that there is an exchange coupling between the M-phase and magnetic phase which enhances the saturation magnetization and reduces coercivity. It can be seen from the morphology that platelet-type grains are observed with doping and the size of these grains increases with an increase in doping. The connectivity is also improved in these samples, which causes a decrease in coercivity.

In sample *A2*, the saturation magnetization is significantly increased, which can be related to morphology and secondary phase. The morphology shows that there are formation of clusters in this sample which eases the flow of the applied field rendering the increase in the saturation magnetization. Secondly, the formation of the spinel phase in *A2* and good exchange coupling between M-phase and S-phase (Spinel-phase), increases the saturation magnetization to 77.87 emu/g.

Further, an increase in doping for *A3* and *A4* reduces the saturation magnetization reduces the saturation magnetization. This can be related to the competition between the exchange coupling of spinel phase and M-Phase as well as Morphology. As we can see in Fig.2, in sample *A3*, the spinel phase is significantly increased and the M-phase is rather reduced. So the exchange coupling can be more in this case which leads to a decrease in M_s.

Now the coupling between the primary phase and secondary phase observed in the samples can increase/decrease the saturation magnetization. The morphology as discussed before can increase the magnetization (i.e. grain connectivity). The site occupancy on tetrahedral sites increases the saturation magnetization but it reduces with occupancy on spin-up sites. The behavior of all these factors is complex and the competition between all these factors causes the non-linear variation between saturation magnetization.

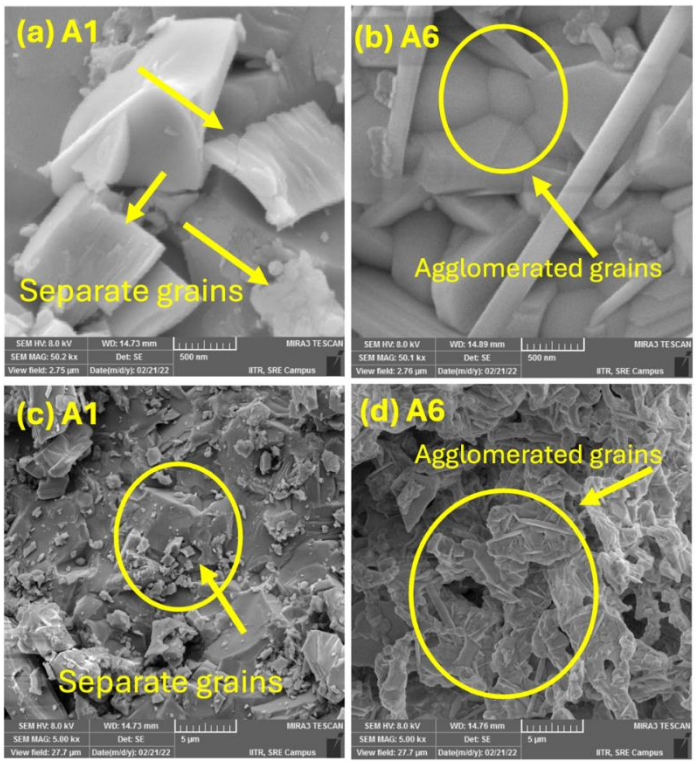

Figure 4.97: SEM Micrographs of Ferrite Samples: $Ba_{0.2}Sr_{0.8}Co_xAl_xFe_{12-2x}O_{19}$ (*A1, A2, A3, A4, A5 and A6*) and its Correlation with Magnetic Data

4.5.4 Electromagnetic Characteristics

4.5.4.1 Complex Permeability and Complex Permittivity

Plots of the dielectric permittivity (ε′) and dielectric loss (ε") against frequency are shown in Figure 4.98. When Co^{2+}- Al^{3+} ions are doped, the dielectric permittivity decreases nonmonotonically, however, for sample *A4* the value has increased. The dielectric loss does not show much variation with Co^{2+}- Al^{3+} ions doping. But in samples *A3* and *A4*, the loss was seen increasing non-monotonically. For compositions *A1*, *A2*, *A3*, and *A6*, the dielectric permittivity is not significantly affected by frequency. Moreover, sample *A5* shows a dip between the frequency of 10 to 11 GHz range and a sudden increase after crossing 11 GHz of frequency and again followed by a dip for the 11 to 12.4 GHz range. Multiple relaxation peaks can observed for samples *A1*, *A2*, *A4*, and *A6* in ε" plots. From Figure 4.98, it can be seen that the behavior of ε" these samples owe multiple peaks after certain frequency gaps, whereas sample *A3* does not show much dispersion. Sample *A4*, which possesses the highest value for ε", shows dual peaks, first between 8.5 to 9 GHz and the other between 10.2 to 11 GHz. The highest value of ε" achieved by sample *A4* is 7.2 at around 8.67 GHz. Sample *A5* does not show much trend in the overall frequency range besides a noticeable dip around 10.88 GHz.

The highest value ε′ is observed for sample *A4*, and it is around 7.4 at around 8.56 GHz. Similarly, for ε", *A4* composition stands out as possessing the highest value of around 1.5 at

9.21 GHz as well as 12.4 GHz. The other samples stay less than 1 for ε" and less than 4.5 for ε′ for complete test frequency.

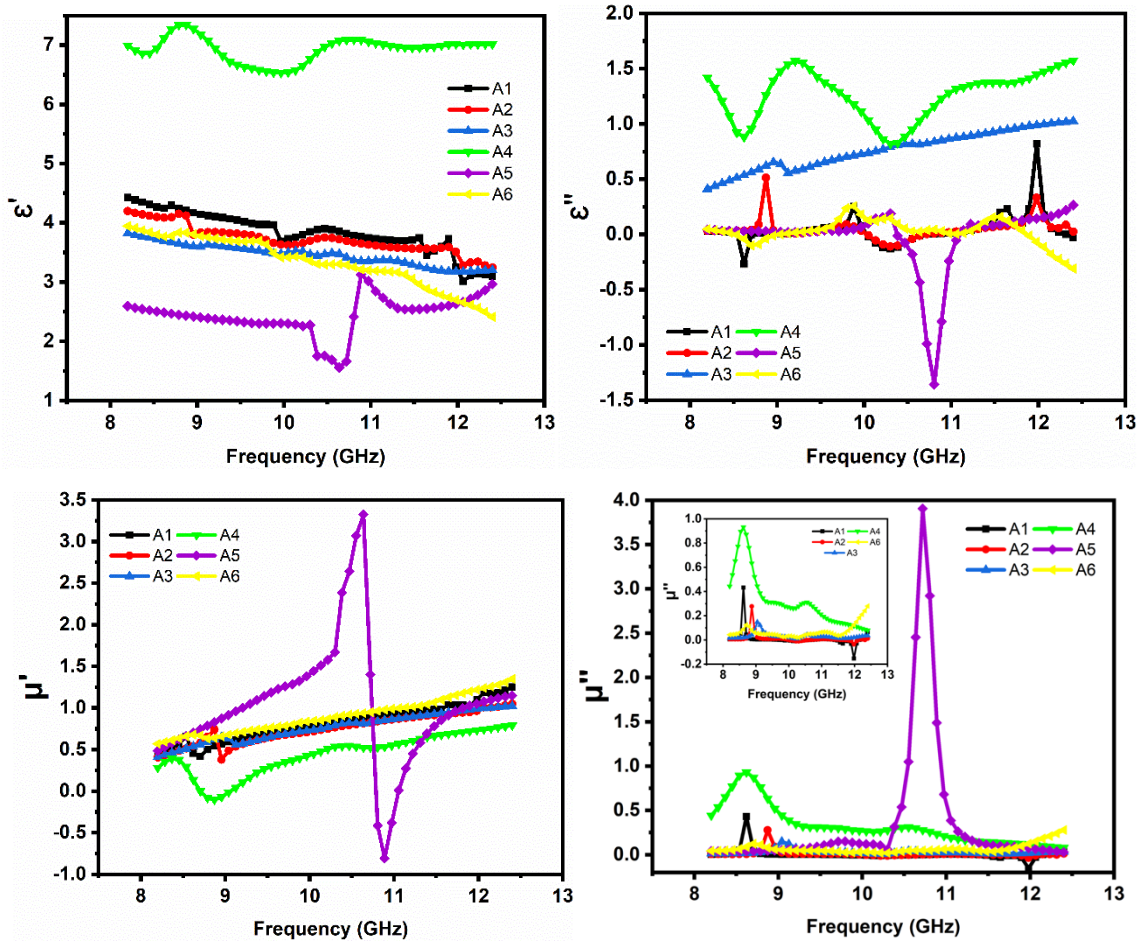

Figure 4.98: Dependence of ε', ε", μ'and μ" on Frequency in Ferrite Compositions *A1, A2, A3, A4, A5* and *A6*

Plots of permeability (μ')/magnetic loss (μ") in the frequency spectrum with Co^{2+}- Al^{3+} ions doping are shown in Figure 4.98. The results of μ' do not show a significant dispersion in the entire test frequency range for the doped compositions of *A1, A2, A3, A4,* and *A6*. A super high relaxation peak is observed for sample *A5* in the frequency range of 10.2 to 10.8 GHz. Similar behavior can be seen in μ" plots for the above-mentioned samples. Not much dispersion is observed for *A1, A2, A3, A4,* and *A6* samples. However, each sample possesses a relaxation peak at the start of the test frequency followed by weak peaks later. Sample *A5* exhibits a super high relaxation peak for μ", between 10.3 to 11.2 GHz frequency range. If *A5* values are kept aside, then the range of μ' stays below 1, but the *A5* sample possesses the highest value for μ', i.e., 3.4. Similarly, the range of μ" stays below 0.9, and the highest value is possessed by sample *A4*. If values of *A5* are taken into account, then Co^{2+}- Al^{3+} ions doping seems to have affected this sample prominently, with the μ" value of 4 as the highest. In the microwave region, the complex permittivity/permeability depends on dipole polarisation, porosity, electron spin grain

and grain size distribution, and space charge polarisation, in addition to charge accumulation at grain boundaries. Dielectric polarisation in ferrites is caused by the electron hopping in Fe^{2+}/Fe^{3+} [170-171].

4.5.4.2 Microwave absorption in $Ba_{0.2}Sr_{0.8}Co_xAl_xFe_{12-2x}O_{19}$

Examining a material's reflection loss is one method of determining its microwave absorption capability. Equations 3.16 and 3.17 are used to determine the RL of the compositions. This section will examine how different factors affect the material's microwave-absorbing capacity. These variables include the degree of reflection loss, impedance matching, and material thickness (λ/4).

4.5.4.3 Quarter Wavelength Mechanism

The phenomenon of microwave absorption is explored with plots of reflection loss dependent on the frequency at various simulated thicknesses. RL versus frequency plots at various thicknesses provide crucial insights into the microwave absorption properties of materials. These plots help in understanding how materials interact with electromagnetic waves and are essential for optimizing material design for various practical applications.

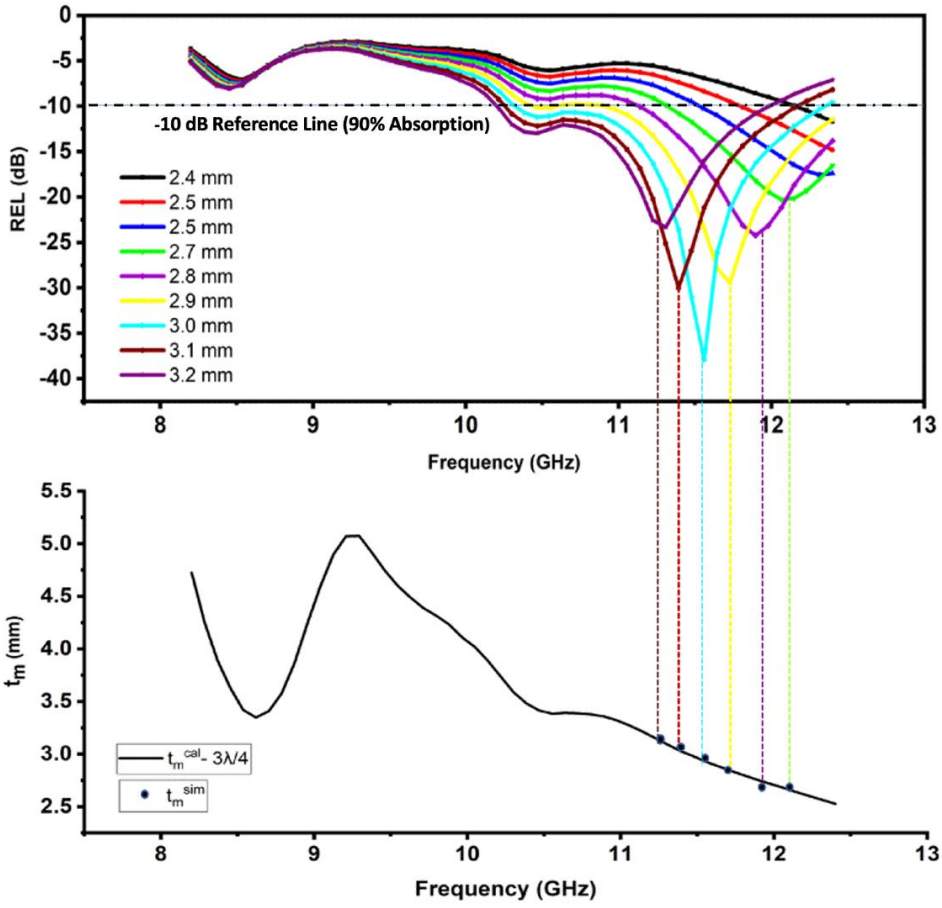

Figure 4.99: (a) Dependence of RL on Frequency in *A4* Composition (b) t^{sim} and t^{cal} Versus Frequency for 3λ/4 in *A4* Composition

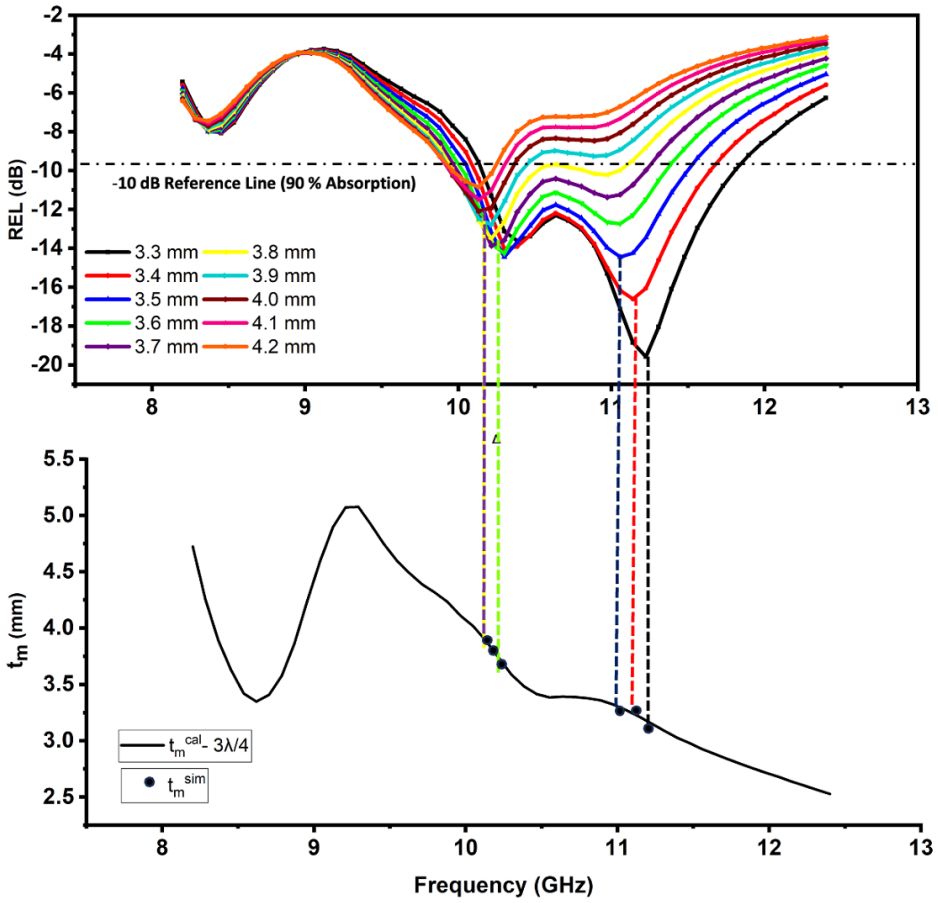

Figure 4.100: (a) Dependence of RL on Frequency in *A4* Composition (b) t^{sim} and t^{cal} Versus Frequency for 3λ/4 in *A4* Composition

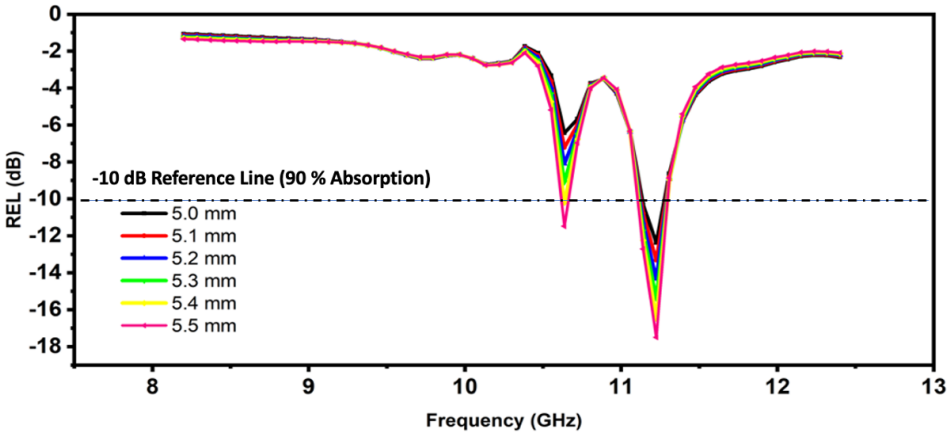

Figure 4.101: (a) Dependence of RL on Frequency in *A5* Composition

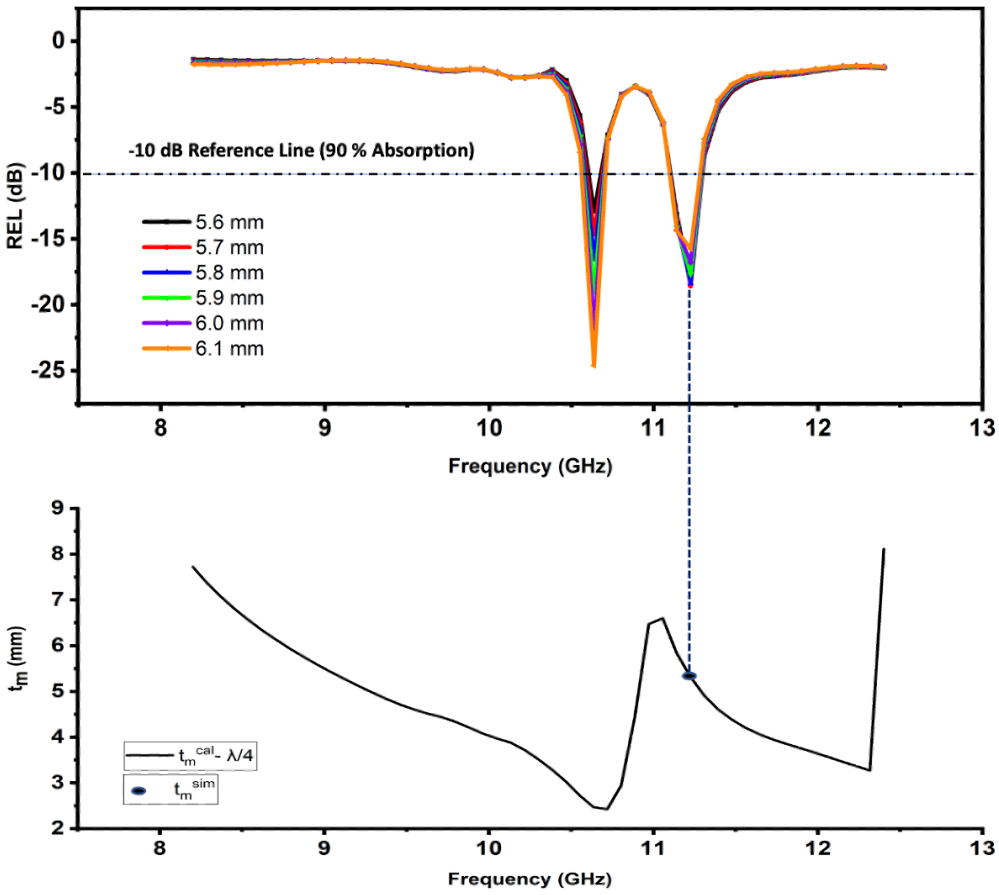

Figure 4.102: a) Dependence of RL on Frequency in *A5* Composition (b) t^{sim} and t^{cal} Versus Frequency for λ/4 in *A5* Composition

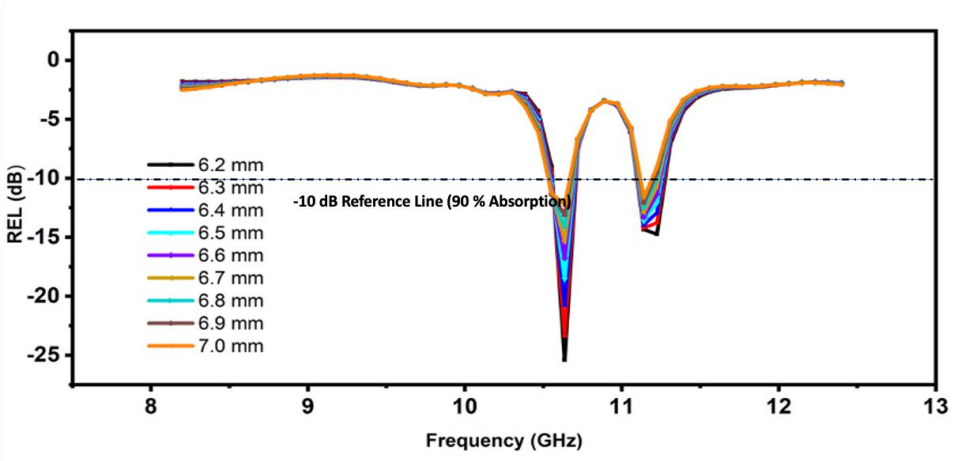

Figure 4.103: (a) Dependence of RL on Frequency in *A5* Composition

Figures 4.99 (a), (b) to Figure 4.103 (a), depict the RL plots $Ba_{0.2}Sr_{0.8}Co_xAl_xFe_{12-2x}O_{19}$ ferrite compositions. Table 4.20 presents the summarised values derived from these figures, which correspond to the frequency/thickness, bandwidth, and frequency range for RL of -10 dB.

A4 composition exhibits the largest RL peak of -30.99 dB at 1.48 GHz frequency and 3 mm thickness. But *A5* composition owes RL values ranging from 10.52 to 12.4 GHz, 5.4 to 6.7 mm

matching thicknesses as shown in table 4.20. Figure 4.99 depicts how RL peaks shift towards the low-frequency spectra as thickness increases. This is in line with the quarter wavelength mechanism which states that the relationship between frequency and thickness is inversely proportional.

The RL peaks are observed in *A4*, figure 4.99 (a), (b), in the frequency band ranging from 10.02 to 12.4 GHz and 10.04 to 11.98 GHz at thicknesses from 2.4 to 3.2 mm and 3.3 to 4.3 mm, respectively. In Figure 4.99, we can observe that initially, as the thickness is increased, the height of the RL peak is increased to a thickness of 3.0 mm, but from 3.1-3.2 mm, it is decreased. But in Figure 4.100, there is a decrease in the height of the RL peak with thickness increment, from 3.3 to 4.2 mm for sample *A4*. Now, even in Figure 4.101, there is an increase in the height of the RL peak with an increase in thickness, for 5.0 to 5.5 mm for *A5* sample. Figure 4.102 follows the same trend for sample A5, but in Figure 4.103 there is a decrease in the height of RL peaks with an increase in thickness for the same sample. The RL peaks are seen in the frequency band spanning from 10.02 to 12.40 GHz, covering the thickness of 2.4 to 3.2 mm and of 3.3 to 4.2 mm in A4 composition [Figure 4.99 (a), (b), Figure 4.100 (a), (b)], The RL peaks observed in *A5* composition are 5.0 to 5.5 mm, 5.6 to 6.1 mm, and 6.2 to 7 mm for the frequency band ranging from 11.14 to 11.22 GHz, 11.14 to 11.22 GHz, 10.52 to 11.22 GHz respectively.

Equation 3.18 states that the simulated thickness (t_m^{sim}) is used to calculate RL and that the calculated thickness (t_m^{cal}) can be obtained by solving equation 6 for n = 1, 3, 5,..., etc. To determine the association between RL peaks and the quarter wavelength mechanism, both parameters are investigated. Plots of the calculated thickness ($n\lambda/4$) in the frequency regime are shown in Figure 4.99 (a), (b) and Figure 4.100 (a), (b). By extending a vertical line from RL peaks towards thickness-frequency graphs, the estimated thickness ($n\lambda/4$) and the simulated thickness (t_m^{sim}) are compared.

It appears from the figures that the *A4* composition satisfies the $\lambda/4$ mechanism, with calculated thickness with $3\lambda/4$ values. Table 4.20 illustrates how the $\lambda/4$ mechanism in *A4* composition results in -10 dB bandwidth covering the range between 10.38 and 12.4 GHz and 2.4 and 3.2 mm thickness and range between 9.8 GHz to 11.86 GHz for 3.3 to 4.2 mm with n = 3. With a calculated thickness of $\lambda/4$, it appears from the figures that the composition of *A5* meets the $\lambda/4$ mechanism with n = 1. Table 4.20 shows how the *A5 c*omposition's $\lambda/4$ mechanism offers a -10 dB bandwidth that spans the 9.48 to 10.36 GHz and 8.6 to 9.2 mm thickness. Figure 4.104 Three-dimensional (3D) plots of reflection loss at various frequencies and thicknesses for all samples of *A4 and A5.* It can be seen from the plots that the blue-violet color portion depicts the RL peaks with their corresponding frequencies and thickness.

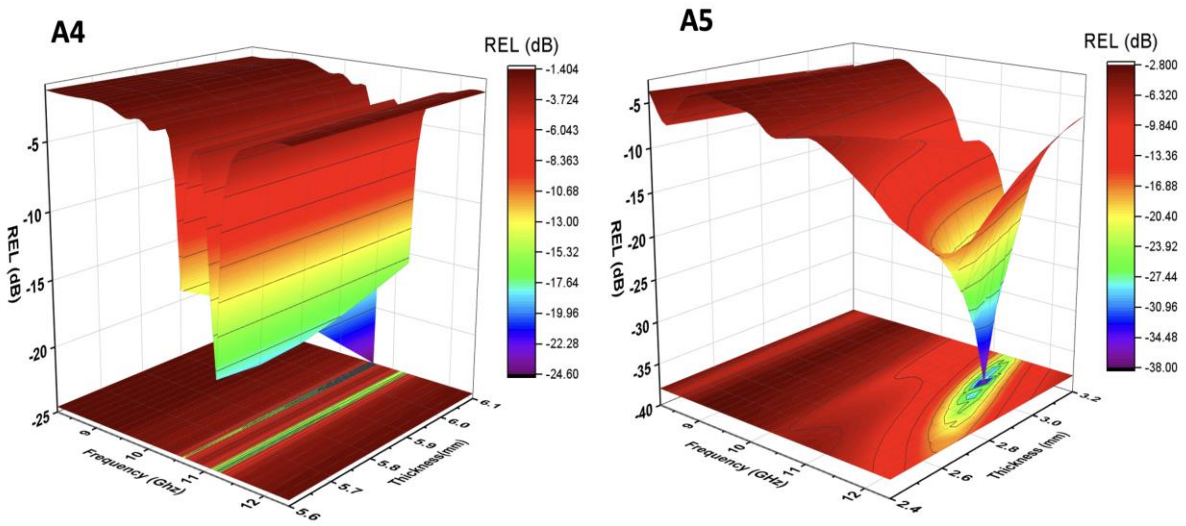

Figure 4.104: Three-dimensional (3D) Plots of Reflection loss at Various Frequencies

Table 4.19: Computed Parameters for Microwave Absorption (RL > -10 dB)

Co-Al content	Matching Thickness (mm)	Matching Frequency (GHz)	Maximum RL (dB)	Frequency Band for RL>-10 dB (GHz)	Bandwidth for RL>-10 dB (GHz)	BWT	PBW
A4	2.4	12.40	-11.69	-	-	-	-
	2.5	12.40	-14.83	-	-	-	-
	2.6	12.40	-17.41	-	-	-	-
	2.7	12.06	-20.26	-	-	-	-
	2.8	11.90	-24.23	11.14-12.4	1.26	0.45	10.59
	2.9	11.73	-29.47	10.97-12.4	1.43	0.49	12.19
	3.0	11.48	-30.99	10.38-12.4	2.02	0.67	17.60
	3.1	11.39	-30.01	10.30-12.14	1.84	0.59	16.15
	3.2	11.31	-23.33	10.21-11.98	1.77	0.55	15.65
	3.3	11.22	-19.58	10.21-11.72	1.51	0.46	13.45
	3.4	11.14	-16.61	10.12-11.56	1.44	0.42	12.93
	3.5	11.06	-14.45	10.12-11.47	1.35	0.39	12.21
	3.6	10.30	-14.26	10.04-11.30	1.26	0.35	12.23

	3.7	10.30	-13.58	10.04-11.13	1.09	0.29	10.58
	3.8	10.22	-13.49	10.04-11.05	1.01	0.27	9.89
A5	5.4	11.22	-16.50	11.14-11.22	0.08	0.01	0.71
	5.5	11.22	-17.49	11.14-11.22	0.08	0.01	0.71
	5.6	11.22	-18.25	11.14-11.22	0.08	0.01	0.71
	5.7	11.22	-18.56	11.14-11.22	0.08	0.01	0.71
	5.8	11.22	-18.35	11.14-11.22	0.08	0.01	0.71
	5.9	11.22	-17.69	11.14-11.22	0.08	0.01	0.71
	6.0	11.22	-16.77	11.14-11.22	0.08	0.01	0.71
	6.1	10.64	-24.60	10.63,11.14-11.22	0.08	0.01	0.75
	6.2	10.64	-25.39	10.63,11.14-11.22	0.08	0.01	0.75
	6.3	10.64	-23.35	10.63,11.14-11.22	0.08	0.01	0.75
	6.4	10.64	-20.76	10.63,11.14-11.22	0.08	0.01	0.75
	6.5	10.64	-18.56	10.52-10.63, 11.14-11.22	0.11 0.08	0.01 0.01	1.03 0.75
	6.6	10.64	-16.78	10.52-10.63, 11.14-11.22	0.11 0.08	0.01 0.01	1.03 0.75
	6.7	10.64	-15.33	10.52-10.63, 11.14-11.22	0.11 0.08	0.01 0.01	1.03 0.75

4.5.4.4 Impedance matching mechanism

The characteristic impedance of free space, $Z_o = (\mu/\varepsilon)^{1/2} = 377\ \Omega$, where μ/ε are the permeability and permittivity of free space, respectively, differs from the impedance of the absorber, Z_{in}. The absorber impedance differs from that of free space because of variations in their permeability and permittivity values. Depending on the impedance inequality between Z_{in} and Z_o, a portion of a microwave signal traveling through free space will be reflected from the

absorber when it interacts with the material; the greater the difference, the greater the reflection. The majority of the reflected signal is left behind, whereas only a small fraction of the microwave signal enters the absorber due to the significant disparity between Z_{in} and $Z_{o.}$ Because most of the signal is reflected, attenuation or absorption of the signal inside the absorber is minimal or insignificant, even if the absorber has maximal dielectric and magnetic loss. Thus, when designing the absorber, it is important to take into account the impedance matching of the absorber material with free space.

Figure 4.105, displays distinct graphs for impedance, RL, and Z_{in}, with frequency regimes for *A4* and *A5* composition. In these compositions, impedance-matching conditions may arise in the form of RL peaks with $Z_{in} \sim Z_o$ (377 Ω) at specific frequencies that correspond to different matching thicknesses. Table 4.21 lists Z_{in} values of compositions, which are obtained from plots of Z_{in} in the mentioned Figure 4.104. The composition A4 owes RL = -30.99 dB at 11.48 GHz frequency, 3.0 mm thickness with Z_{in} = 372.03 Ω, which is in proximity to Z_o = 377 Ω but in the same composition, a situation arises at RL = -30.01 dB at 11.39 GHz frequency, 3.1 mm thickness but Z_{in} = 354.74 Ω which is away from Z_o = 377 Ω. On the other side, a relatively large RL = -29.46 dB is reported at 11.72 GHz, 2.9 mm with Z_{in} = 402.77 which is more offset from Z_o = 377 Ω than Z_{in} = 372.02 Ω with RL = -30.98 dB. A similar situation arises in *A5* composition for 6.1 mm thickness, 10.63 GHz frequency with RL = -24.59 dB and Z_{in} = 385.70 Ω and at 6.2 mm thickness with same matching frequency but RL = -25.39 dB and Z_{in} = 406.13 Ω, more offset from Z_o =377 Ω.

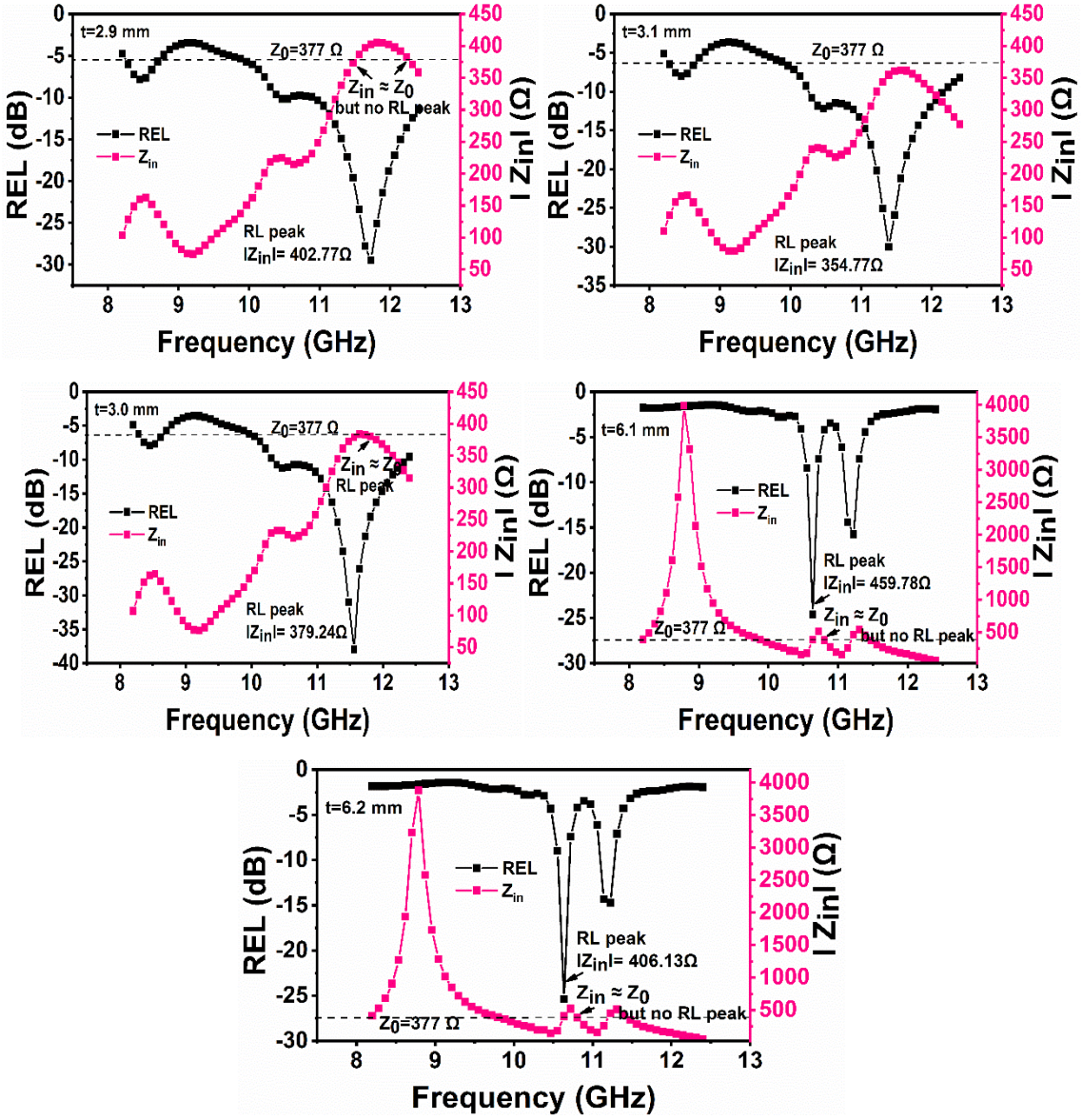

Figure 4.105: Dependence of RL and Z_{in} on Frequency in *A4* and *A5* Composition

It is explained by the fact that | Z_{in} | [in Equation (3.18)] is a complex expression that uses both real and imaginary terms, such as Z_{real} and Z_{img}. These are, therefore, computed from (3.18), and their corresponding curves are displayed in the domain of thickness and frequency for *A4* and *A5* composition in Figure 4.106.

It is evident from Table 4.20 that the maximum RL value around Z_{real} = 377 Ω and/or Z_{img} = 0 Ω was observed in composition *A4*. It has Z_{real} = 372.02 Ω, and Z_{img} = 20.399 Ω, which are comparatively near to 377 Ω, but the latter is the little higher side than zero. Composition *A5* shows comparatively lower RL_{max} values than composition *A4* because of a greater offset of Z_{real} and Z_{img} values from 377 Ω and/or zero. Co-Al modifies the input impedance Z_{in} (Z_{real} and Z_{img}) of compositions. According to Table 4.20, the composition of *A4* exhibits significant input impedance (impedance matching mechanism) values than those of *A5*.

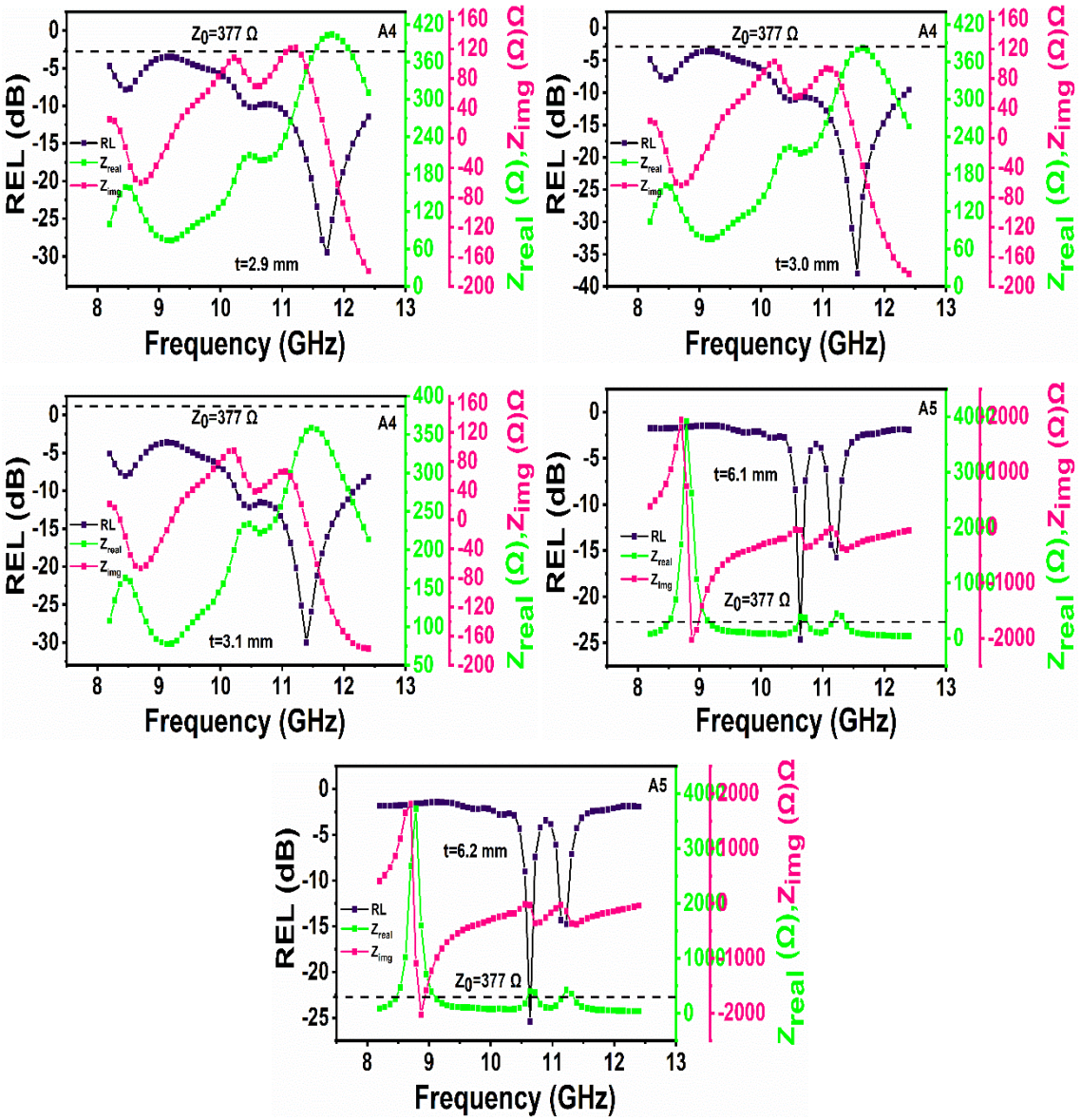

Figure 4.106: Dependence of RL, Z_{in}, Z_{real}, and Z_{img} on Frequency in *A4* and *A5* Composition

Table 4.21: Impedance Parameters of RL Peaks at Different thickness

Co-Al content	Matching Thickness (mm)	Matching Frequency (GHz)	Maximum RL (dB)	Z_{real} (Ω)	Z_{img} (Ω)	Z_{in} (Ω)
A4	2.4	12.40	-11.69	445.50	209.96	492.50
	2.5	12.40	-14.83	497.67	104.65	508.56
	2.6	12.40	-17.41	493.70	-12.04	493.85
	2.7	12.06	-20.26	449.38	34.63	450.71
	2.8	11.90	-24.23	425.63	8.23	425.71

	2.9	11.73	-29.47	402.75	-4.91	402.78
	3.0	11.48	-30.99	371.47	20.40	372.03
	3.1	11.39	-30.01	354.69	-6.09	354.74
	3.2	11.31	-23.33	334.46	-23.32	335.27
	3.3	11.22	-19.58	313.25	-34.56	315.15
	3.4	11.14	-16.61	288.03	-42.24	291.12
	3.5	11.06	-14.45	265.13	-48.72	269.56
	3.6	10.30	-14.26	255.38	-14.29	255.78
	3.7	10.30	-13.58	249.92	-33.88	252.21
	3.8	10.22	-13.49	246.77	-21.57	247.71
A5	5.4	11.22	-16.50	451.12	100.51	462.18
	5.5	11.22	-17.49	464.67	70.84	470.04
	5.6	11.22	-18.25	473.70	38.88	475.29
	5.7	11.22	-18.56	477.69	5.66	477.73
	5.8	11.22	-18.35	476.46	-27.65	477.27
	5.9	11.22	-17.69	470.17	-59.90	473.97
	6.0	11.22	-16.77	459.30	-90.05	468.05
	6.1	10.64	-24.60	383.14	-44.42	385.71
	6.2	10.64	-25.39	404.92	-31.45	406.14
	6.3	10.64	-23.35	427.96	-20.01	428.43
	6.4	10.64	-20.76	452.28	-10.27	452.39
	6.5	10.64	-18.56	477.85	-2.43	477.86
	6.6	10.64	-16.78	504.65	3.25	504.66
	6.7	10.64	-15.33	532.59	6.50	532.62

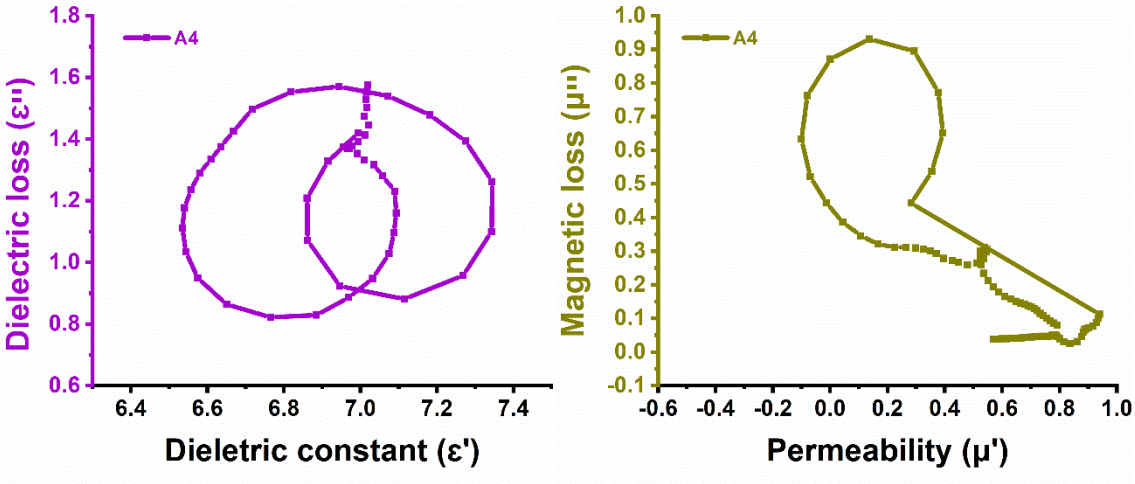

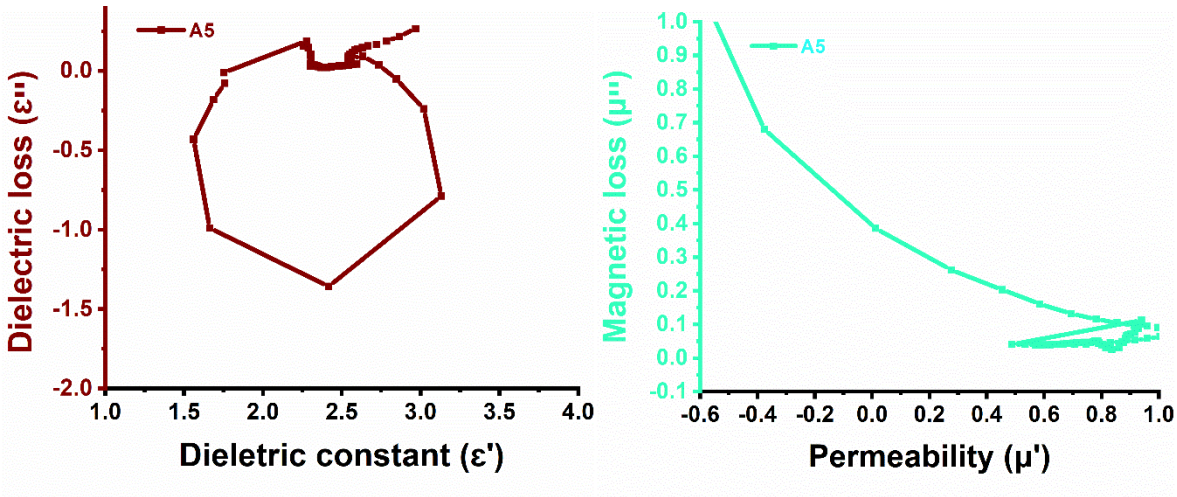

Figure 4.107: Cole–Cole Plots in *A4* and *A5* Compositions

Figure 4.107 shows Cole–Cole plots of *A4* and *A5* samples to verify relaxation in the compositions. But no prominent effect of the Cole-Cole plot is seen concerning the RL peaks here. Multiple relaxations and inverted semicircles can be seen in the plots above. Here, it can be said that the relaxation process may be dominated by impedance matching and quarter wavelength mechanism.

4.5.4.5. Eddy Current Loss

Eddy current loss can generally increase microwave absorption and contribute to magnetic loss in ferrites at the X-band. The contribution of the eddy current loss to the magnetic loss is determined by the constant value of C_0 with frequency variation. As can be seen from Figure 4.108, sample *A4* shows absorption from frequency band 10.30 to 12.40 GHZ, and C_0 for *A4* shows a constant value for the same frequency band verifying that here eddy current loss has contributed in the form of magnetic loss. For sample *A5* it is observed that absorption bandwidth is around 10.64 to 11.22 GHz and C_0 for *A5* also remains constant for almost 8.2 to 10.8 GHz. So it can be concluded that C_0 here might have contributed to absorption.

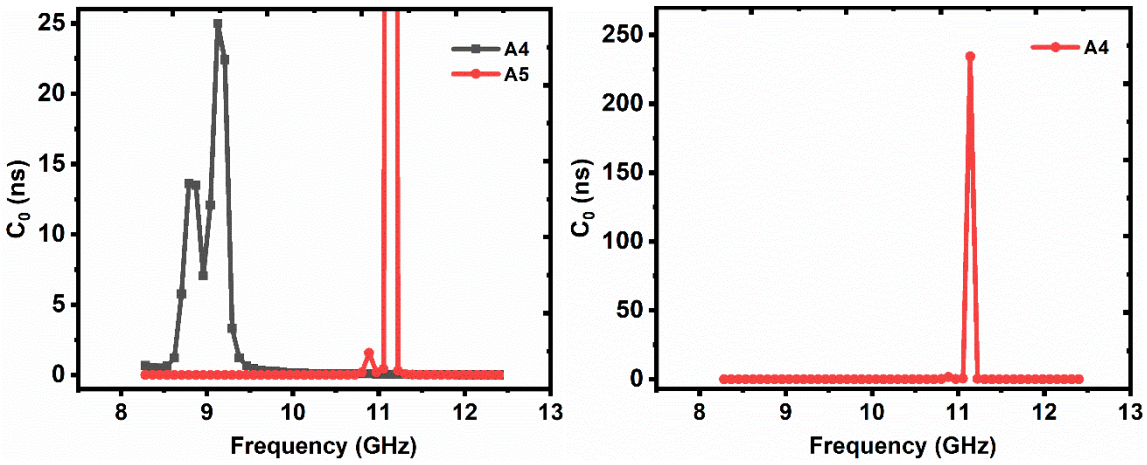

Figure 4.108: C_0 Versus f Variation for Ferrite Compositions *A4* and *A5*

4.5.4.6 BWT/Percentage Bandwidth Ratio

Besides the criterion of RL ≥ -10, an important factor in designing and assessing absorber performance is achieving a high bandwidth at low thickness for a typical RL or absorption dip. Once this RL threshold is met, the emphasis should shift to creating a thin layer rather than merely increasing the RL. Because of this, the bandwidth-to-thickness ratio (BWT) and percentage bandwidth (PBW) in ferrite samples are estimated using relations discussed in section 3.8.

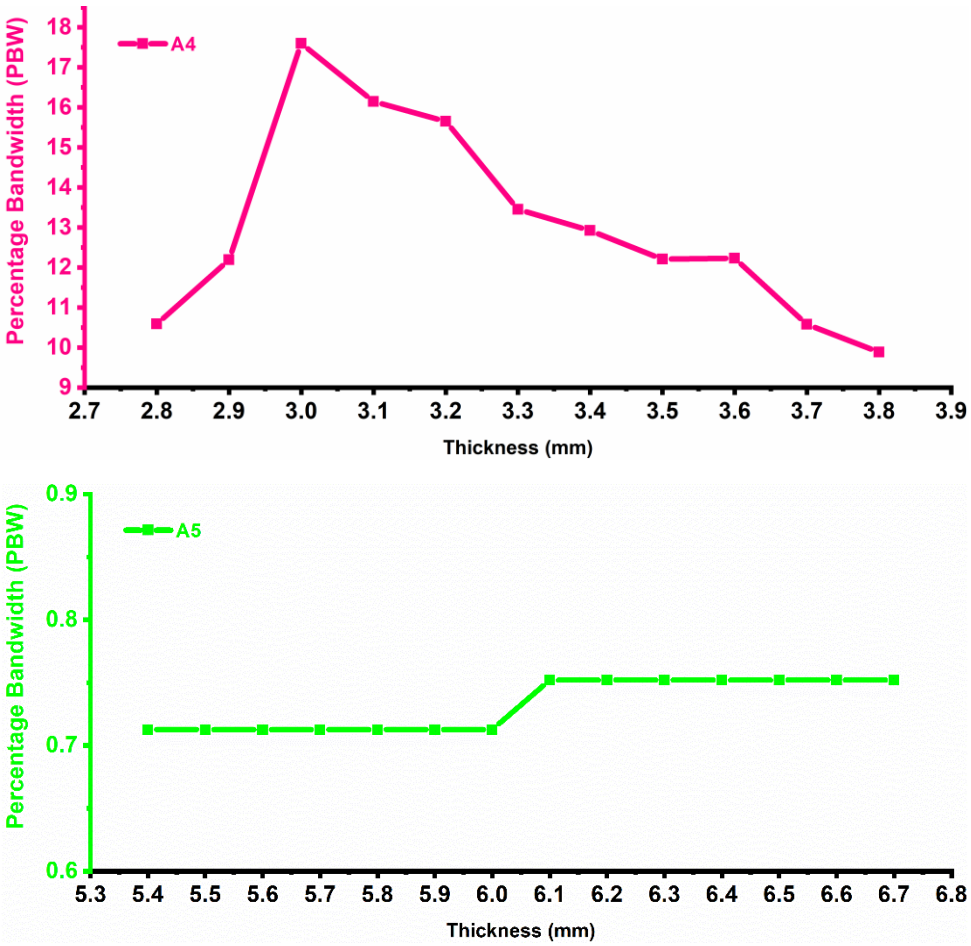

Figure 4.109: Bandwidth (%) Variation with thickness in Ferrite *A4 and A5* Compositions

Table 4.20 associates the bandwidth-to-thickness ratio (BWT) for maximum RL with frequency; however, Co-Al doping seems to have impacted sample *A4* as more BWT is observed for the *A4* sample than *A5*. For *A4*, the BWT is highest at 0.67, observed for the frequency band of 10.38 to 12.40 GHz, with RL values of -30.99 GHz and thickness of 3.0 mm, as can be seen from Figure 4.109. A broad bandwidth of 2.02 GHz is seen to be achieved here. PBW is also noted highest for the sample at the same frequency band and same thickness, which is 17.60 %. For the first few thicknesses starting from 2.8 mm, *A4* PBW seems to rise

but then falls from a thickness of 3.1 mm to 3.8 mm. However, the PBW of *A5* does not seem to impact much, as can be seen from the plot below.

4.6 Co^{2+}-Al^{3+} substituted $Ba_{0.2}Sr_{0.8}Co_xAl_xFe_{12-2x}O_{19}$ / PANI hexaferrite

In this section, we have synthesized a hexaferrite with Co and Cu substitutions with PANI via the sol-gel technique. This composition hexaferrite will be given as $Ba_{0.2}Sr_{0.8}Co_xAl_xFe_{12-2x}O_{19}$/PANI. For composites, we are reporting only those samples in which significant results have been obtained. The sample names with the codes for each level of substitution in $Ba_{0.2}Sr_{0.8}Co_xAl_xFe_{12-2x}O_{19}$/PANI are given in Table 4.22.

Table 4.22: The Assignment of Sample Names Corresponding to Various Substitutions Levels in $Ba_{0.2}Sr_{0.8}Co_xAl_xFe_{12-2x}O_{19}$/PANI Hexaferrite

Sample Composition $Ba_{0.2}Sr_{0.8}Co_xAl_xFe_{12-2x}O_{19}$ /PANI	Sample Code Name	Sample Code (A-Series)
x = 0.0	$Ba_{0.2}Sr_{0.8}Fe_{12-2x}O_{19}$ /PANI	AP1
x = 0.8	$Ba_{0.2}Sr_{0.8}Co_{0.8}Al_{0.8}Fe_{10.4}O_{19}$/PANI	AP3
x = 1.6	$Ba_{0.2}Sr_{0.8}Co_{1.6}Al_{1.6}Fe_{8.8}O_{19}$/PANI	AP5

4.6.1 Structural Analysis

4.6.1.1 Field Emission Scanning Electron Microscopy

Figure 4.110 shows the Micrographs of Ferrite Samples: $Ba_{0.2}Sr_{0.8}Co_xAl_xFe_{12-2x}O_{19}$/PANI *(AP3* and *AP5*). The grain agglomeration, it is also effortless to identify individual grains in the samples. Doping causes grain clusters to have an uneven size distribution because of both magnetic and electrostatic interactions between the ferrite particles. The grain takes on a noticeable platelet-like form as doping levels rise. Also, it can be seen that the little individual grains become more noticeable in the grain clusters. Certain gaps in the grain arrangement may prevent or hinder the flow of charge carriers. Now, since the grain boundaries are higher, the resistance to the applied field will be greater as grain size decreases, changing the process of charge transport. Figure 4.111 depicts the EDX spectra of $Ba_{0.2}Sr_{0.8}Co_xCu_xFe_{12-2x}O_{19}$/PANI hexaferrite for samples *AP5*.

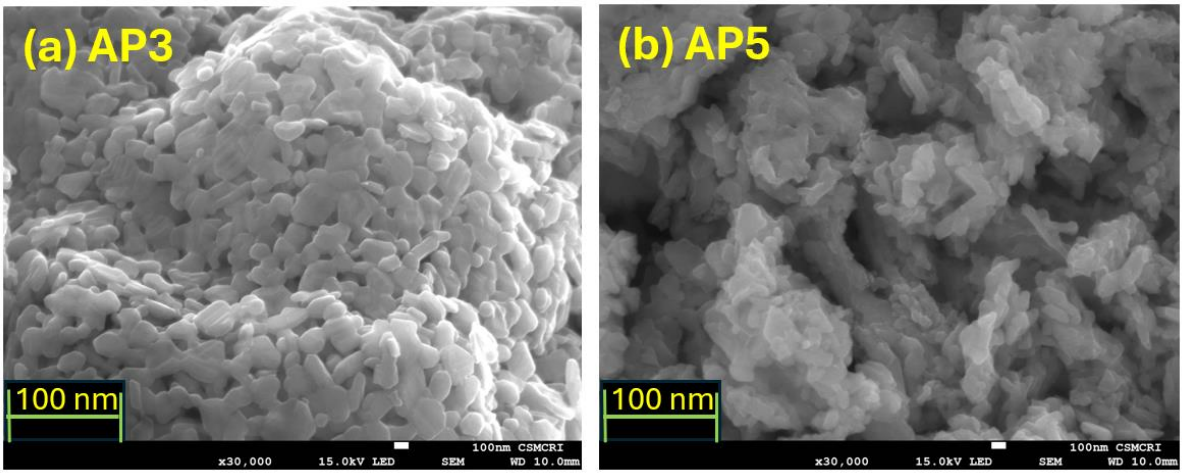

Figure 4.110: SEM Micrographs of Ferrite Samples: $Ba_{0.2}Sr_{0.8}Co_xAl_xFe_{12-2x}O_{19}$/PANI (*AP3* and *AP5*)

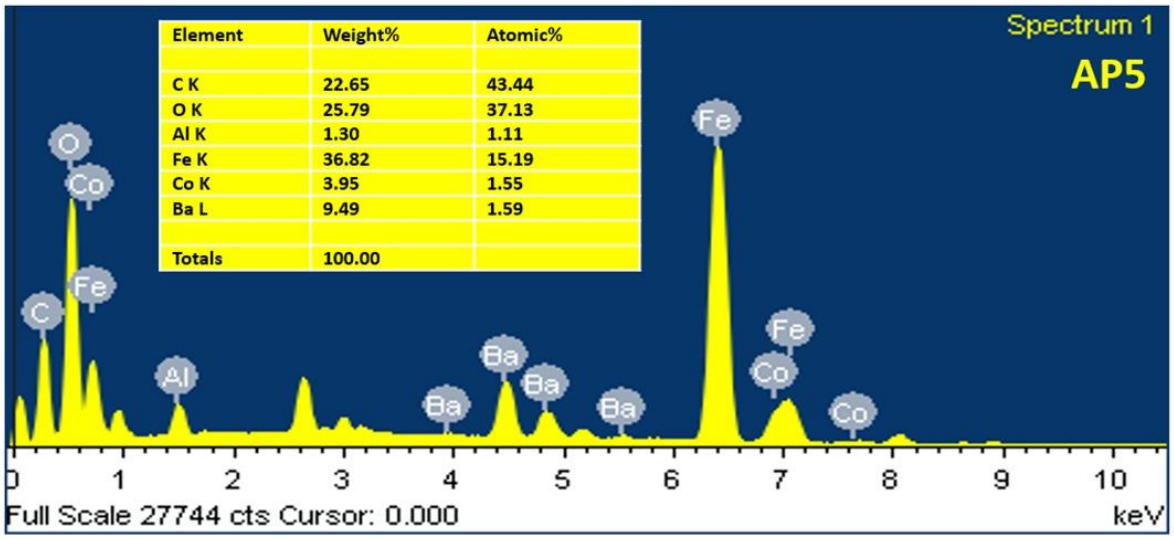

Figure 4.111: EDX Spectra $Ba_{0.2}Sr_{0.8}Co_xAl_xFe_{12-2x}O_{19}$/PANI (*AP3* and *AP5*)

4.6.2 Electrical Analysis

4.6.2.1 Dielectric permittivity

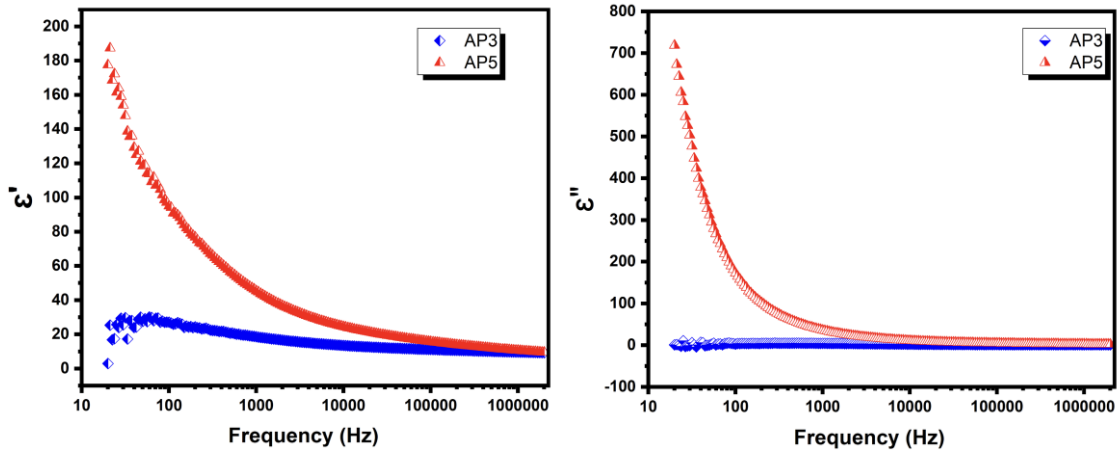

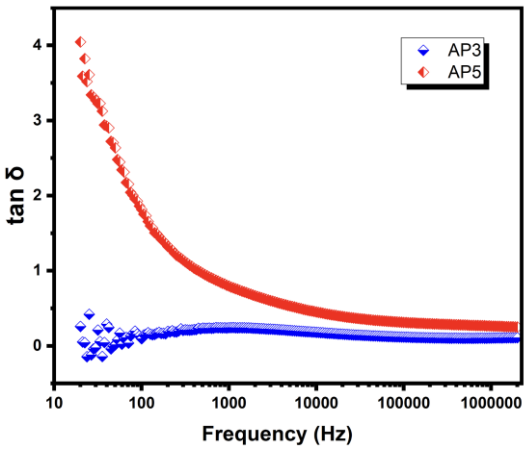

Figure 4.112: Variation of Dielectric Spectra of: $Ba_{0.2}Sr_{0.8}Co_xAl_xFe_{12-2x}O_{19}$/PANI *(AP3* and *AP5*) a) Real Component, b) Imaginary Component as a Function of Frequency, (c) Variation of Dielectric loss Tangent

With frequencies ranging from 10 Hz to 2 MHz, Figure 4.112 shows two different types of plots: (a) the first real component, which is accompanied by a Dielectric permittivity, and (b) the second, the imaginary part related to dielectric loss. Figure 4.112 (a) illustrates how the value ε' exhibits dispersion in the low-frequency spectra, becoming independent of frequency in all samples beyond 250 kHz as the frequency increases. With an increase in Co^{2+} and Al^{3+} doping, it is seen that the value ε' declines non-monotonically, starting with a low value of ε' = 32 for *AP3* and ε' = 196 for *AP5*. The Maxwell-Wagner model, which is based on Koop's phenomenological theory, describes the dielectric mechanism [190-192]][197]. However, in ε'' spectra, the value for *AP3* stays in the range of 0 to 20, but for sample *AP5*, the value starts with 730, declines with frequency, and stays in the same range as *AP3* after 7k Hz. This drastic rise in sample *AP5* value ε'' may be due to the addition of PANI, which has the inherent tendency to increase the dielectric loss.

Space charge polarisation results from highly conductive grains with insulating grain borders outgrowing restricted charge aggregation caused by the action of an electric field. Space charge carriers in a sinusoidal electric field have a specific amount of time to align themselves parallel to the field. The space charges eventually lose their ability to remain in synchronism with the sinusoidal field when the reversal applied field increases. From this point on, it trails the field, decreasing the material's Dielectric permittivity. Polarisation in ferrite materials can be linked to the conduction process, which is mostly caused by the hopping conduction mechanism. The Dielectric permittivity/loss, as previously mentioned in Figure 4.112 (a), (b), achieves a steady-state value at a specific frequency, beyond which electron hopping and electron exchange with +2 and +3 states cannot occur [192].

Figure 4.112 (c), shows that in both samples, the dielectric loss tangent's value drops as frequency increases. Koop's phenomenological theory of dielectrics explains this drop in the value of *tan δ*. Co-Al doping results in a rise in the loss of tangent, the highest being for the *AP5* sample. Fe^{2+}/Fe^{3+} content, interfacial polarisation, sample stoichiometry, interface traps, structural oneness, and, ultimately, sintering temperature are the parameters that determine the loss tangent.

4.6.2.2 Electric modulus analysis

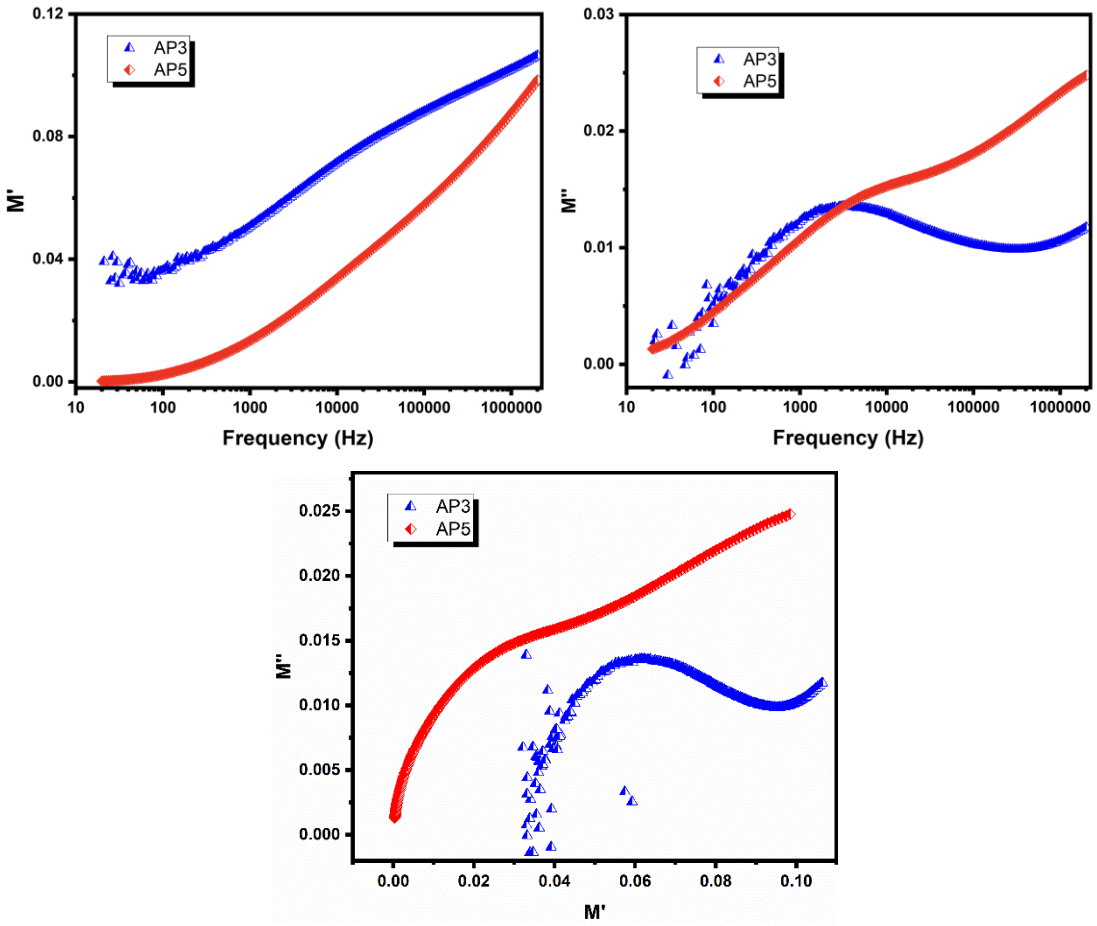

Figure 4.113: Variation of Modulus (a) Real Part, (b) Imaginary Part of Ferrite Sample $Ba_{0.2}Sr_{0.8}Co_xAl_xFe_{12-2x}O_{19}$ /PANI (*AP3, AP5)* as a Function of Frequency (c) Cole-Cole Plot (or Nyquist Plot)

The material's electrical behavior can be better understood by using the complex electric modulus exercise. In addition to assessing electrical relaxation in ionic solids, this method advances our understanding of the nature of polycrystalline materials.

M′ and *M″* stand for the real and imaginary parts of the complex electric modulus, respectively. The formulae are discussed earlier in section 3.3.2.

A sigmoidal form for the real part of the modulus and an expanding, asymmetric peak in the graph of the imaginary part of the modulus are typical characteristics of Modulus w.r.t

frequency. Figure 4.34 (*MP1* since it is the same sample *AP1*), the pure sample does not show any sigmoidal shape, but the other two doped samples of the composite with PANI, i.e., the figure above, show a slightly sigmoidal shape. The fluctuation of the real part of the modulus (*M′*) with the logarithmic frequency scale is shown in Figure 4.113 (a). For the lower frequency range, *AP3* is limited to a low value (tending toward zero) and then rises linearly to an approximate value of 0.09, whereas for *AP5*, it starts at 0.04 and increases to 0.09. The charge carriers are subject to the applied electric field's influence as it is applied.

Figure 4.113 (b) illustrates how the divergence in the imaginary part of modulus plots in the frequency domain adds to our understanding of the mechanisms underlying charge transport, including electrical transport, conductivity, relaxation, and ion dynamics. The *M″* graph shows that the peaks of each sample rise to their maximum point with an increase in doping concentration. *AP5* composition seems to have two weak peaks, one around 8k Hz and the other around 2 MHz however, *AP3* composition possesses a curve around 2 kHz.

The Cole-Cole plot (*M′* vs *M″*) of the sample *AP3* and *AP5* is shown in Figure 4.113 (c). For the two composite samples, two arcs are visible, the first one seems to be a whole semicircle, whereas the next one can termed as just the initial stage for a semicircle, or it can also be said the other arc is at a higher frequency degenerates into a segment. This depicts the process where the grain effect is replaced by the grain boundaries effect. The presence of two Nyquist semicircles in Figure 4.113 (c) naturally prompts us to assume that, similar to other systems, the grains effect and grain boundaries effect contribute to these Semicircles [200]. The activation energies calculated for both semicircles using Arrhenius law, however, point to a different scenario. Grain borders typically have an activation energy greater than the grains themselves [202]. Because of their high barrier, this was another reason why the grain boundaries in many ionic oxides could have a blocking effect. In contrast, the activation energy that the so-called grains create is higher than the activation energy of grain boundaries in the current situation, thus nullifying the barrier effect of grain boundaries [199-200].

4.6.2.3 Complex impedance spectra

Researchers may learn about the material's resistance (*Z′*) and reactance (*Z″*) through impedance analysis. The bulk grains and grain boundaries of polycrystalline materials are the main causes of their impedance behavior. Since the impedance of grain borders and bulk grains have distinct relaxation durations, they can be treated differently.

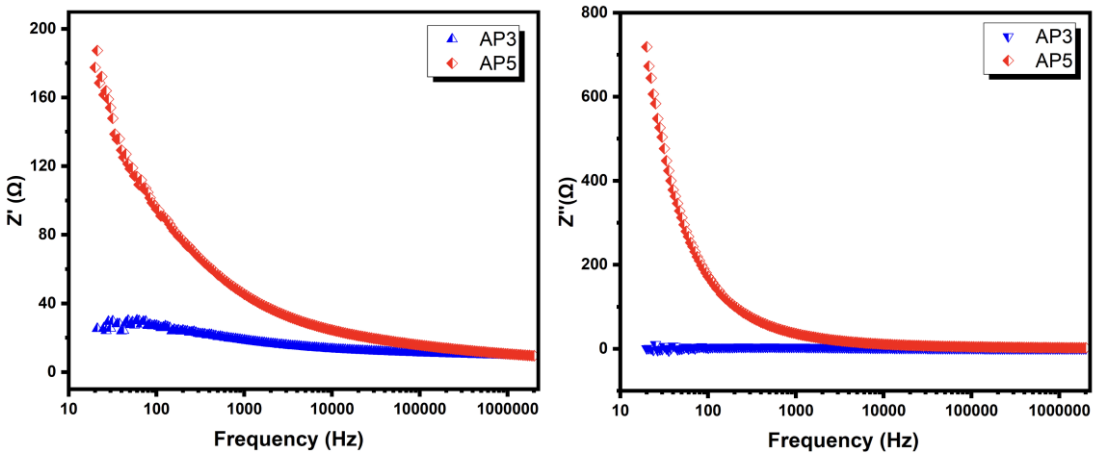

Figure 4.114: Dispersion in the (a) Dielectric Impedance Real (*Z′*), (b) Dielectric Impedance Imaginary (*Z″*) for Ferrite Sample $Ba_{0.2}Sr_{0.8}Co_xAl_xFe_{12-2x}O_{19}$ /PANI (*AP3, AP5)*

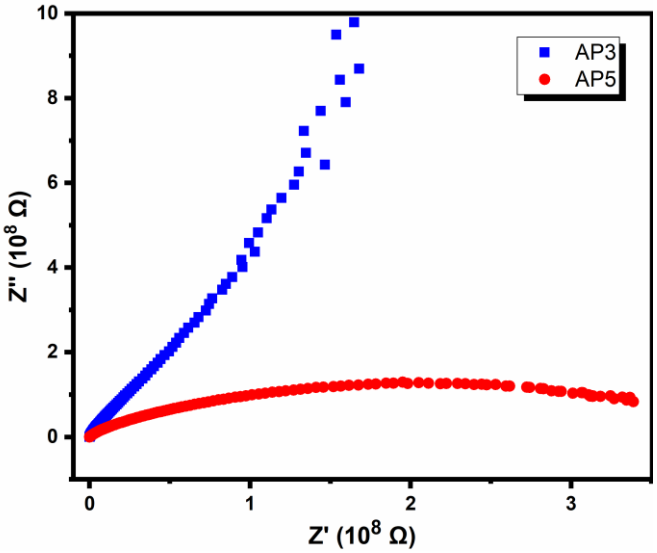

Figure 4.115: Dispersion in the (a) Dielectric Impedance Real (Z′) Part Versus Dielectric Impedance Imaginary (*Z″*) Part of $Ba_{0.2}Sr_{0.8}Co_xAl_xFe_{12-2x}O_{19}$ / PANI (*AP3, AP5)* as a Function of Frequency

The variation of the real portion of impedance (*Z′*) concerning frequency is depicted in Figure 4.114 (a). *Z′* for composite samples, *AP3*, and *AP5* is found to be continuously decreasing as frequency increases. In sample *AP3*, the value starts from 40, and in *AP5*, it starts at 170 eventually, this value (*Z′*) approaches constant after 100 kHz. The samples' space charge and dipole polarisation effect may be accountable for this decrease in (*Z′*) value.

As seen in Figure 4.114 (b), analysis has been done on the imaginary part of impedance change about frequency variation to better understand the space charge effect. Along with the low-frequency regime, there is a non-monotonic change in *Z″* values with increased Al and Co

content. No prominent change can be seen in *AP3*, but the value seems to suddenly decrease from 800, tending towards zero in the *AP5* sample with maximum doping content.

Figure 8 shows two curves that seem to be part of huge semicircles. For both samples, sample *AP3* as well as *AP5*, the center of the semicircle seems to be below the x-axis, depicting non-Debye-type relaxation. With doping content, the center of the semicircle seems to move more below the x-axis. For sample *AP5*, there is a depression of the curve in the high-frequency region, which is associated with dielectric polarization at grains. Here, grains contribute to the mechanism of electric transport. However, the doping of Co-Al/PANI shifts the arc toward a high-frequency regime.

4.6.2.4 AC Conductivity

The hopping of its valence electrons between Fe^{2+} and Fe^{3+} at octahedral sites is the main reason why conduction in ferrites is outlined. Conductivity rises as a result of the frequency increase, which also raises the charge carrier hopping frequency. The polaron hopping model described in [124] explains this frequency-dependent conduction mechanism. According to that model, AC conductivity exhibits a declining tendency for long-range polarisation hopping, whereas it increases with an increase in frequency for the limited range of polaron hopping. The conductivity phenomena are independent of frequency in the case of band conduction [125].

The curve of the ferrite samples *AP3* and *AP5*, as shown in Figure 4.116, depicts AC conductivity as a function of frequency. According to the current study, AC conductivity gradually rises after the applied AC field frequency of 20 kHz. It shows nearly frequency-independent behavior till this range of frequency, and this frequency marks the transition from DC conductivity to AC conductivity.

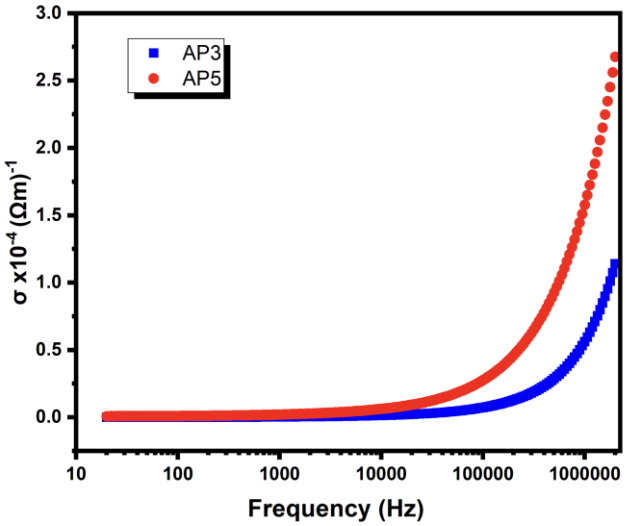

Figure 4.116: Variation of AC Conductivity Concerning Frequency for Ferrite Sample

of $Ba_{0.2}Sr_{0.8}Co_xAl_xFe_{12-2x}O_{19}$ /PANI (*AP3, AP5)*

The frequency-dependent AC conductivity expression of the Jonscher power law [126] is discussed in section 3.3.4. According to Funke [127], the value of n has a physical meaning: $n < 1$ means that the electron hopping involves a translational motion with sudden hopping, whereas $n > 1$ means that the motion involves localized hopping between neighboring sites. The value of n was calculated from fitting the plots: *AP3* - 0.8239, *AP5* - 0.5228. As consequently, the value of n is smaller than 1, suggesting the mechanism of ac conductivity along with charge carrier hopping. The large value of n in sample *AP3* sudden rise in charge careers at the high-frequency region. As previously mentioned, the high-frequency region's conductivity is influenced by grains [164-165].

4.6.3 Magnetic analysis

The saturation magnetization (M_s), coercivity (H_c), anisotropy field (H_a), and squareness ratio (M_r /M_s) values are depicted in the table 4.23 and are derived from the M-H loops and Linear fits of samples *AP3* and *AP5*.

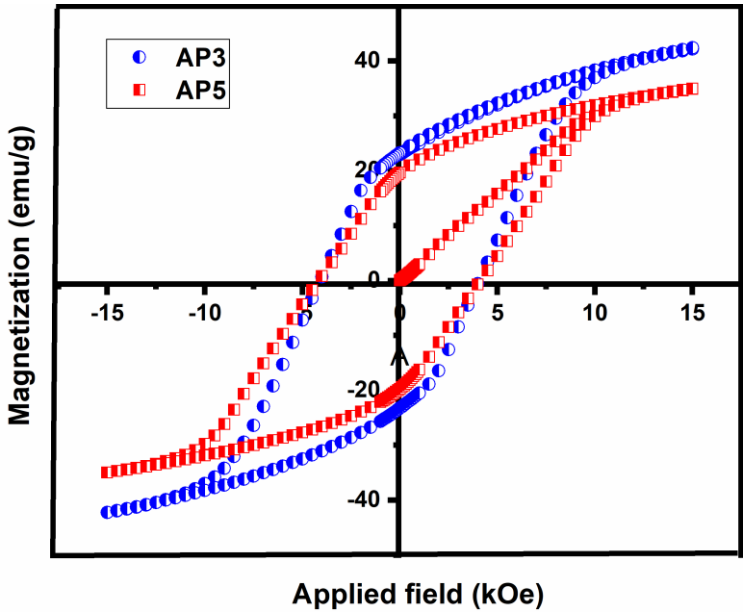

Figure 4.117: Hysteresis Loops of *AP3* and *AP5* Hexaferrite

It can be inferred that when the amount of substitution rises, the value of M_s first rises from the *AP1* (is undoped PANI sample which is *MP1*) to *AP3* samples before falling in the latter sample (*AP5*). From table 4.23, it can be seen that magnetization saturation first increases from *AP1* (44.54 emu/g) to *AP3* (46.60 emu/g) and is then decreased to *AP5* (40.57 emu/g). It is conceivable that the first 4% increase in M_s resulted from the Fe ions at spin-down sites substituting for both Co-Al ions. As was previously mentioned (section above), electronegativity parameters and ligand field theory can help account for this anticipated behavior.

Table 4.23: Magnetic Parameters M_s, H_c, H_a, M_r and M_r/M_s for Co-Al Doped Hexaferrite Samples

Sample	M_s (emu/g)	H_c (Oe)	H_a (kOe)	M_r (emu/g)	M_r/M_s
AP1	44.54	6112.67	17.49	22.78	0.50
AP3	46.61	4086.87	17.58	21.78	0.47
AP5	40.57	4320.34	20.45	19.16	0.47

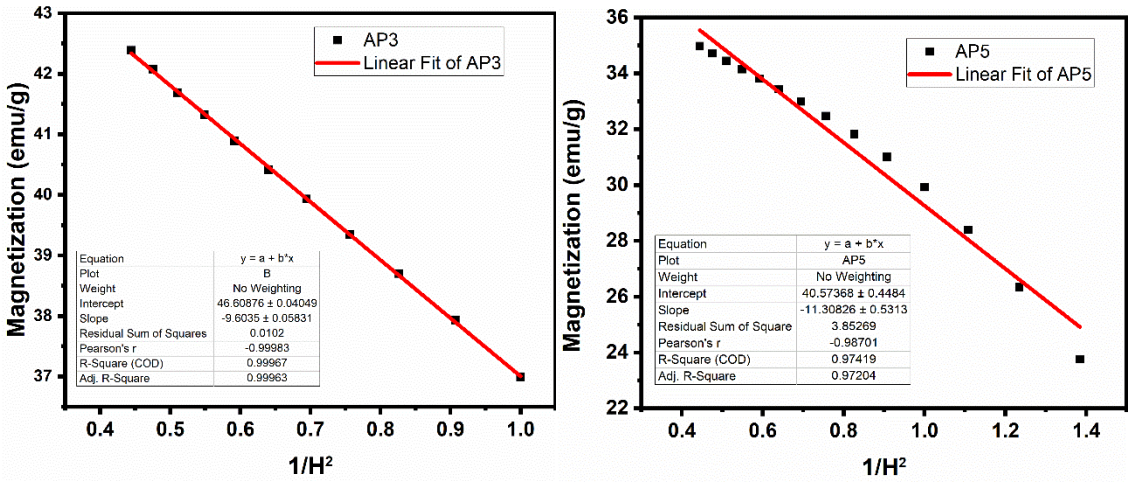

Figure 4.118: M_S Versus 1/ H^2 Plots for *AP3* and *AP5* Hexaferrite Samples

Figure 4.118 shows the M_s versus 1/ H^2 plots for *AP3* and *AP5* hexaferrite/PANI samples. The observed decrease in M_s value (*AP3* to *AP5*), which is almost a decrease of 9%, may be attributed to the substitution of non-magnetic (Al^{3+}) and weakly magnetic (Co^{2+}) cations at octahedral positions for Fe^{3+}. Because of this replacement, there are fewer Fe^{2+} ions in spin-up locations, which leads to ion conversion to preserve electrical neutrality. The magnetic moment decreases, and the strength of the superexchange interaction is diminished, which lowers M_s. Figure 4.117 makes it evident that the *AP1* sample's M-H curve is convex and smooth, whereas the other samples exhibit stepped loops that suggest the behavior of the hard and soft phases is uncoupled. The incomplete exchange coupling between the soft and hard ferrite phases may probably be the reason for this. As discussed earlier, the inter-grain group development and magnetic hardness of the material are evaluated using the M_r/M_s ratio, whose value should range from 0 to 1. Materials with a significant squareness ratio ($0.5<M_r/M_s<1$) implies single-domain while those with $0.05<M_r/M_s<0.5$ have randomly oriented multi-magnetic domains. From the table, it could be observed that the squareness ratio for *AP1*, i.e., for a pure composite sample, is between ($0.5<M_r/M_s<1$), implying single-domain, while for *AP3* and *AP5*, it is less than 0.5, implying randomly oriented multi-magnetic domains. The highest coercivity values (6112 Oe) are found in a pure composite sample of Ba-

Sr-hexaferrite PANI (*AP1*), which is associated with the absence of substituent cations in the crystal lattice. Extrinsic and intrinsic factors can both easily account for H_c's behavior. H_a, being an extrinsic factor, does not seem to have affected the coercivity prominently, here, H_a equals 17.58 kOe and 20.44 kOe for *AP3* and *AP5,* respectively. Remanence magnetization for these samples was seen reducing from pure composite to doped, 22.7 emu/g for pure and 21.78 emu/g, 19.16 emu/g for *AP3* and *AP5,* respectively.

4.6.4 Electromagnetic Characteristics

****no accepatable results were noted for Al/PANI samples**

4.7 Ba $^{2+}$-Sr^{2+} substituted $Ba_{1-x}Sr_xFe_{12}O_{19}$ hexaferrite

In this section, we have synthesized a hexaferrite with Ba and Sr substitutions via the sol-gel technique. This composition of hexaferrite will be given as $Ba_{1-x}Sr_xFe_{12}O_{19}$.The sample names with the codes for each level of substitution in $Ba_{1-x}Sr_xFe_{12}O_{19}$ are given in Table 4.24.

Table 4.24: The Assignment of Sample Names Corresponding to Various Substitution Levels in $Ba_{1-x}Sr_xFe_{12}O_{19}$ Hexaferrite

Sample Composition $Ba_{1-x}Sr_xFe_{12}O_{19}$	Sample Code Name	Sample Code (T-Series)
x = 0.0	$BaFe_{12}O_{19}$	T1
x = 0.2	$Ba_{0.8}Sr_{0.2}Fe_{12}O_{19}$	T2
x = 0.4	$Ba_{0.6}Sr_{0.4}Fe_{12}O_{19}$	T3
x = 0.6	$Ba_{0.4}Sr_{0.6}Fe_{12}O_{19}$	T4
x = 0.8	$Ba_{0.2}Sr_{0.8}Fe_{12}O_{19}$	T5
x = 1.0	$SrFe_{12}O_{19}$	T6

4.7.1 Structural Analysis

4.7.1.1 X-ray Analysis

Figure 4.119 depicts the X-ray diffraction pattern of prepared hexaferrite samples $Ba_{1-x}Sr_xFe_{12}O_{19}$ (*T1, T2, T3, T4, T5,* and *T6*) and the Bragg peaks of the prepared samples are well-defined. To determine Miller indices of the obtained peaks, Powder-X software has been used and peaks matched with a typical standard pattern of Barium strontium hexaferrite-$Ba_{0.5}$ $Sr_{0.5}$ $Fe_{12}O_{19}$ (JCPDS#51-1879). The lattice parameters (*a* = *b* and *c*), the volume of the unit cell and the crystallite size for the synthesized samples are calculated using equations 3.1, 3.2, and 3.3 from section 3.2.1 and specified in Table 4.25.

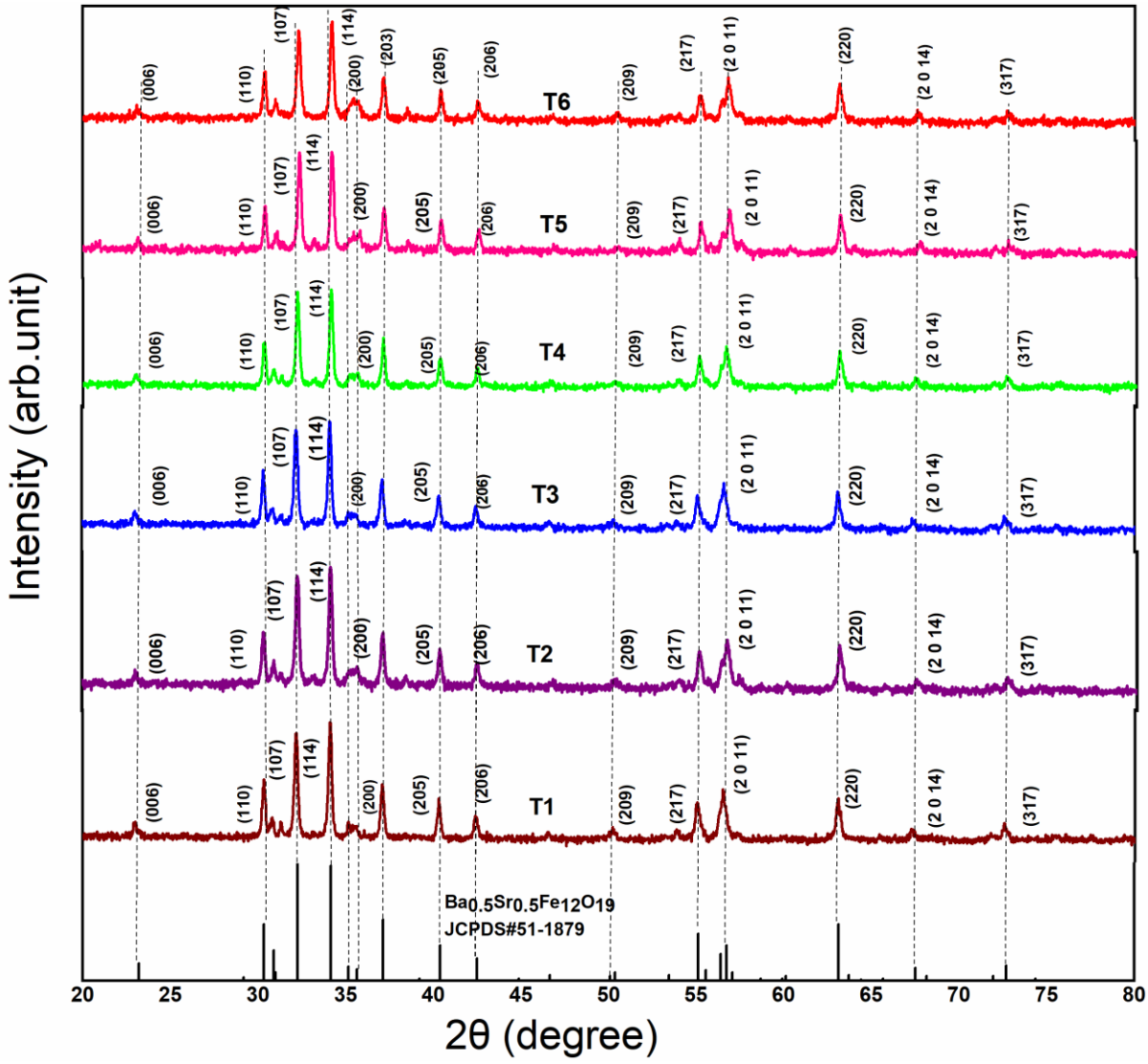

Figure 4.119: X-ray Diffractions of M -type $Ba_{1-x}Sr_xFe_{12}O_{19}$ (*T1, T2, T3, T4, T5,* and *T6*) Hexaferrites

The calculated lattice parameters of the prepared samples are listed in Table 4.25. It can be seen from the table that lattice constants (*a, c*) and cell volume do not owe much change with doping of Ba-Sr from samples *T1* and *T2*, whereas a significant change in lattice parameters is observed in samples *T3* and *T5*. The range of crystallite size stays between 36.95 to 75.75 nm.

Table 4.25: Ba-Sr Content, Lattice Constants, Ratio c/a and Unit Cell Volume Ferrite Sample $Ba_{1-x}Sr_xFe_{12}O_{19}$ (*T1, T2, T3, T4, T5,* and *T6*) Hexaferrites

Ba-Sr	Lattice parameters		Ratio	Unit cell vol.	Crystallite Size
Content (x)	a=b (Å)	c (Å)	c/a	V (Å) ^{3}	D_{xrd} (nm)
T1	5.8912	23.1822	3.9350	696.7750	42.0869

T2	5.8911	23.1823	3.9351	696.7544	36.9543
T3	5.8913	23.1821	3.9349	696.7957	65.8751
T4	5.8914	23.1831	3.9350	696.8494	58.2741
T5	5.8921	23.1834	3.9353	696.7874	75.7564
T6	5.8915	23.1841	3.9351	696.9031	60.6051

4.7.1.2 Field Emission Scanning Electron Microscopy

Figure 4.120 (a-f) displays the grain morphology of the samples $Ba_{1-x}Sr_xFe_{12}O_{19}$ (*T1, T2, T3, T4, T5,* and *T6*). The SEM graph of *T1* shows tiny but unfused grains coming together. As the doping is increased, the particles do not seem to change in size, but voids are seen now. Though the particles do not change much in shape and size after doping but can be seen fusing more and more with doping. Further, with increased doping, more fused grains can be seen in the graph. Due to the electrostatic and magnetic interactions between ferrite particles, doping results in grain clusters with an uneven size distribution. Figure 4.121 shows EDX spectra of $Ba_{1-x}Sr_xFe_{12}O_{19}$ hexaferrite for samples *T2* and *T3*. EDAX of *T2*, *T3* clarifies that there is Ba content found in the sample but in *T2* is less than that in *T3*.

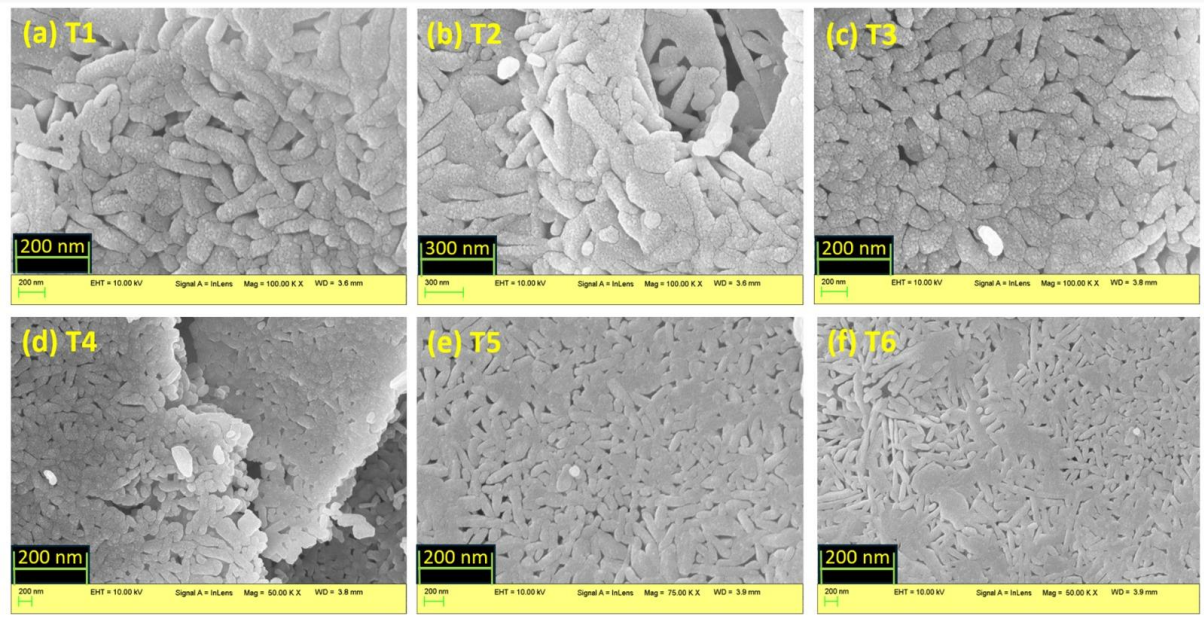

Figure 4.120: SEM Micrographs of Ferrite Samples: $Ba_{1-x}Sr_xFe_{12}O_{19}$ (*T1, T2, T3, T4, T5,* and *T6*)

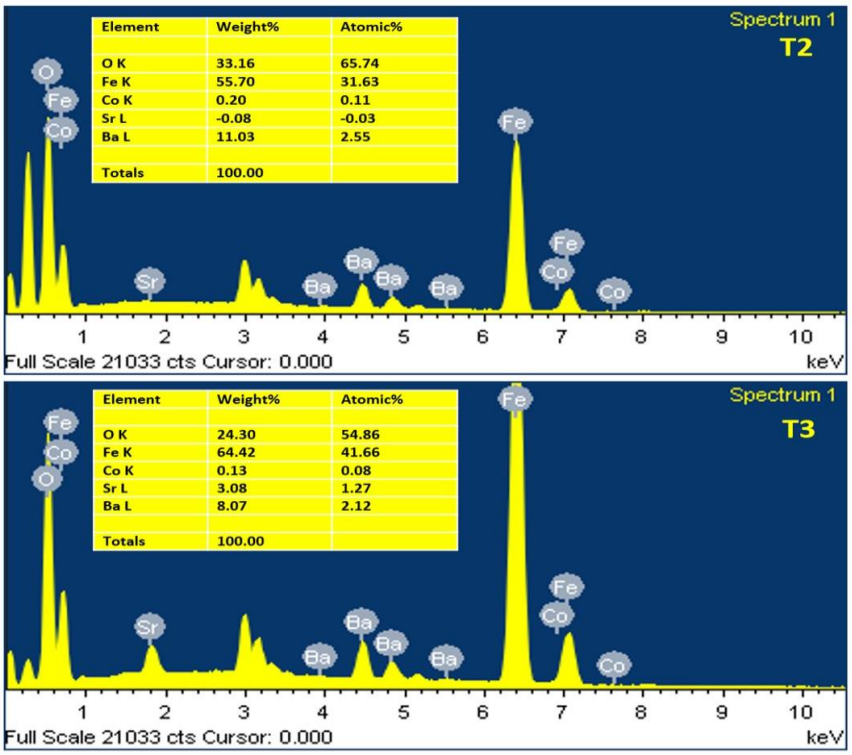

Figure 4.121: EDX Spectra $Ba_{1-x}Sr_xFe_{12}O_{19}$ Hexaferrite for Samples *T3* and *T6*

4.7.2 Electrical Analysis

4.7.2.1 Dielectric permittivity

Figure 4.122 demonstrates two types of plots with frequencies ranging from 10 Hz to 2 MHz, (a) the first real part accompanied by a dielectric permittivity and (b) the second, the imaginary part associated with dielectric loss. Due to measurement uncertainty in sample *T6*, it was not included in electrical characterization. It can be seen from Figure 4.122 (a) that the value of ε' shows dispersion with a fall in frequency in the low-frequency spectra. As can be seen in the figure *T3* and *T4* start with a high value of 450, *T5* starts with 250, and samples *T1*, and *T2* start with a value around 150 in the low-frequency regime. However, all the samples become independent of frequency after 2 kHz Frequency. From Figure 4.122 (b), ε'' spectra show T4 starting with the highest value of 12, but lowers down for *T3* at 5, *T1* at 4, and for *T2*, *T5* it is around 3.8. but just as ε' spectra, these values of ε'' become independent of frequency after 7 kHz.

As the applied frequency is increased, the dielectric permittivity falls. Additionally, the rate of dielectric dispersion varies depending on the sample. The Maxwell-Wagner interfacial polarisation model, which is frequently used to describe the dielectric characteristics of different hexaferrite systems, may be used for an explanation on the decreasing dielectric permittivity with frequency in these samples. Hexaferrites are composed of conducting grains that are separated by insulating grain borders, according to this concept. These grain boundaries

help polarisation by preventing electrical conduction. During the conduction process, the charged particles (electrons) hop in the direction of the grain boundaries. Due to the high resistance provided by grain boundaries, charge carriers gather there and generate polarisation, which results in a high Dielectric permittivity. The conduction mechanism is dominated by grain boundaries at low frequencies and by grains at high frequencies, according to Koops et al. [161]. Thus, when the frequency rises, the control of the grain boundaries is lost, and the dominant function of conducting grains leads to a low value of polarization. The dielectric permittivity drops as a result of this. The total core loss in hexaferrites includes dielectric loss or tan. Therefore, low dielectric losses are preferred for minimal core loss. The tan variation stands for the energy that is lost during dissipation in the dielectric system [199].

The existence of highly conductive grains with insulating grain boundaries outgrows confined aggregation of charge due to the impact of an electric field, resulting in space charge polarization. A definite time is required for space charge carriers in the sinusoidal electric field to arrange themselves parallel to the field. When there is an unceasing increment in the field reversal frequency, there comes a point wherein the space charges are not able to stay in synchronism with the sinusoidal field. And it lags behind the field henceforth reducing the dielectric permittivity of the material. In ferrite material, polarization can be related to the conduction process that takes place primarily as a result of the hopping conduction mechanism [161-162].

As discussed before in Figure 4.122 (a) (b), Dielectric permittivity/loss reaches a steady state value after certain frequency: the electron hopping accompanied by the electron exchange with +2 and +3 states is not able to follow it.

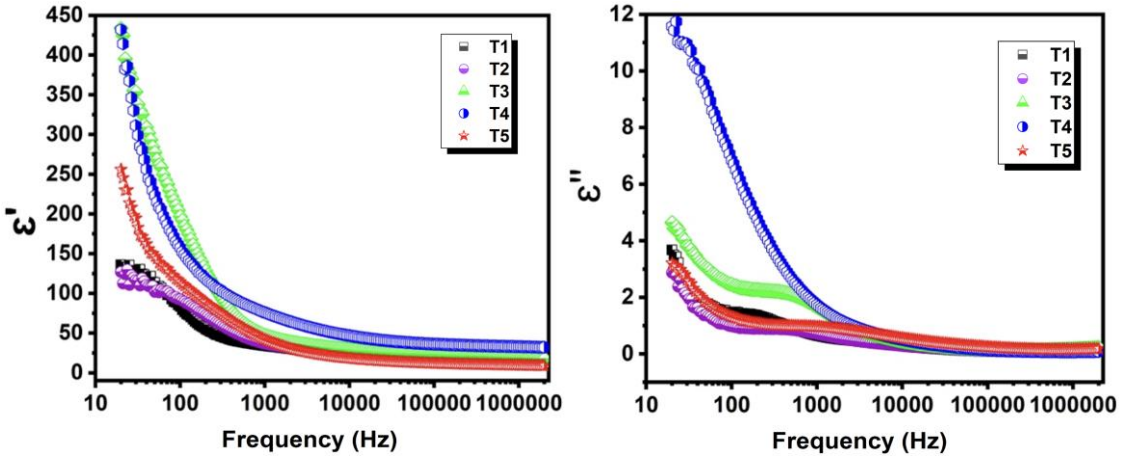

Figure 4.122: Variation of Dielectric Spectra of Ferrite $Ba_{1-x}Sr_xFe_{12}O_{19}$ (*T1, T2, T3, T4,* and *T5*) a) Real Component b) Imaginary Component as a Function of Frequency

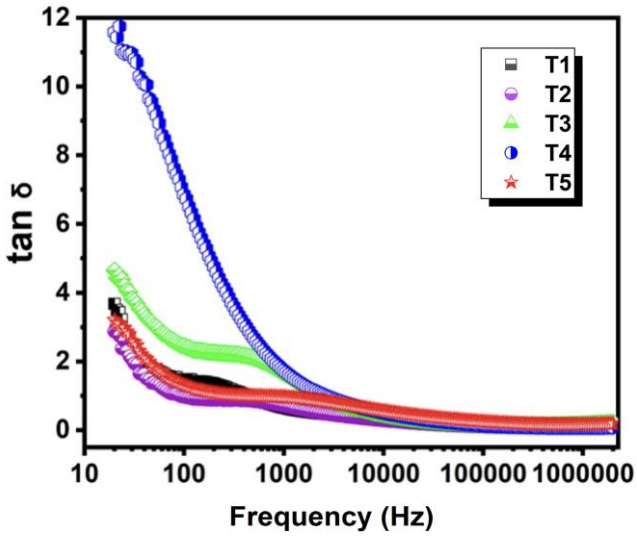

Figure 4.123: Variation of Dielectric loss Tangent of Ferrite Sample $Ba_{1-x}Sr_xFe_{12}O_{19}$ (*T1, T2, T3, T4,* and *T5*) as a Function of Frequency

Figure 4.123 attributes that the dielectric loss tangent decreases in its value with an increase in frequency in all samples. This decrease in the value of *tan* δ is explained by Koop's phenomenological theory of dielectrics [161]. The figure shows weak peaks of *tan* δ in the low-frequency region for all the samples except *T4.* With the doping variation, the decrease in Ba content, and the increase in Sr content, for *T1*, and *T2* there is not much change in the values of loss tangent. Then as the doping changes further, for *T3* the value increases from 3.8 to 4.9. With the further change in doping, with *T4* the values increase dramatically and touch 12 but further for *T5* there is a decrease to 3.8 again. There is an observation of a shift in the loss tangent peak from sample *T1* to *T3* towards a high-frequency regime attributed to the variation in dopant.

Interfacial polarisation and traps created between the interfaces are linked to peaking behavior in *tan* δ. The sintering process in ferrites creates the interfaces and traps, causing interfacial polarisation (an electric field) and bounded charge paths in the traps. The charge trajectories shift away from the trapped zone as a result of the applied AC signal creating a fluctuating electric field across the ferrite interfaces. The charge carriers experience a rapid field due to the rapidly changing electric field caused by the rise in frequency, which eventually causes them to move away from the traps. Grain boundaries provide obstacles to the expanded charge careers throughout this phase, which enhances the charge career's density.

As a result, the high value of ta*n* δ is caused by a larger energy loss due to the increased energy requirement for electron exchange. However, grains work effectively in the high-frequency range and help the charge carriers. As a result, at high frequencies, the energy needed for electron exchange between Fe^{2+} and Fe^{3+} ions is on the lower side, resulting in minimal energy

loss and a low loss tangent value. [193]. The nature of ε′, ε″ and *tan* δ is under the work reported earlier [194-195].

4.7.2.2 Electric modulus analysis

Calculating the dielectric modulus aids in clarifying the relaxation process and reducing the impact of electrode polarization. M' and M'' are the real and imaginary parts of the complex electric modulus and are calculated using equation 3.8 and equation 3.9 respectively (from section 3.3.2).

Figure 4.124 (a) illustrates the frequency-dependent variation in the real component of the dielectric modulus (*M'*). It gives information on conductivity and displays the change of the real component of the modulus (*M'*) vs. frequency. The value of *M'* remains at low levels (tending to zero) among doped samples and even for undoped samples for lower frequencies, it is around zero. All samples show a non-linear increase in *M'* with frequency. It is observed that as the doping in the sample is increased, the value of *M'* decreases from 0.08 (*T1*), 0.05 (*T2*), 0.049 (*T3*), and 0.025 (*T4*) and shows a drastic rise in value for sample *T5*. This value of *M'* for the *T5* sample is reported as 1.0. As discussed earlier, it is a well-known fact that the applied electric field affects the charge carriers. Nevertheless, the absence of the restoring force that governs the motion of these charge carriers affects these findings. This pattern suggests that electrical properties require conductive grains that dominate the high-frequency region.

As can be seen in Figure 4.124 (b), the divergence in the plots of the imaginary part of modulus in the frequency domain contributes to the information about charge transport mechanisms viz-a-viz electrical transport, conductivity, relaxation, and ion dynamics. It can be seen from the graph of M'' that as the doping content increases the peaks of each sample can be seen to reach their highest point; a peak of *T5* owes the highest value (0.023).

Ions can successfully hop from one location to another and move over greater distances in low-frequency zones. However, at higher frequencies, the peaks in M″ show that the ions are limited to their limiting potential wells rather than following the longer hopping. With a rise in frequency, the area covered by the peaks signifies the transition from long-range mobility to a shorter one. Therefore, the hopping mechanism for electrical conduction is shown by the modulus spectrum. Conduction relaxation time is represented by the peak frequency in this case, and a decrease in relaxation time is implied by the shifting of peak frequency variation in dopants towards the high-frequency region. The release of charge carriers (bounded in traps) under the impact of a rise in frequency is also ascribed to conductivity relaxation, as previously discussed. Moreover, large and asymmetric peaks with dopants show that the samples lack Debye-type relaxation.

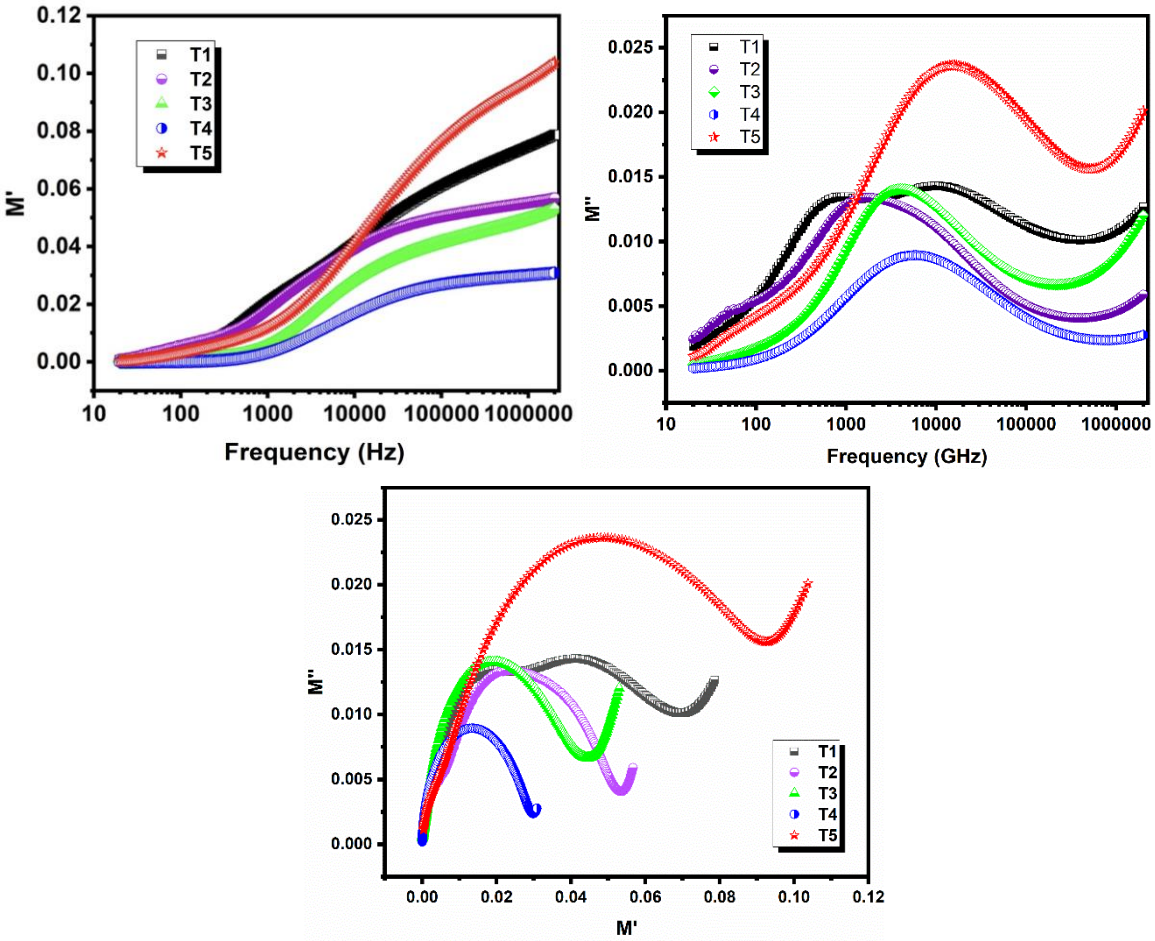

Figure 4.124: Electric Modulus Variation (a) Real Component, (b) imaginary Component of Ferrite Sample $Ba_{1-x}Sr_xFe_{12}O_{19}$ as a Function of Frequency (c) Cole-Cole (M' vs M'') Plot of Ferrite Sample

Figure 4.124 (c) depicts Cole-Cole plot (M' vs M'') of the sample $Ba_{1-x}Sr_xFe_{12}O_{19}$**.** The plots demonstrate asymmetric semi-circles in the samples. The doping shifts the arc towards a high-frequency regime; the intercept of the semicircular arc increases with doping. Hence grains contribute to the mechanism of electric transport and the center of the arc is found to lie below the x-axis (M') signifying non-Debye relaxation in the samples. The change in maxima of the semi-circle for the maximum frequency with doping illustrates the distribution of relaxation time. This distribution backs up the non-Debye type of relaxation [196].

4.7.2.3. Complex impedance spectra

Bulk grains and grain boundaries are the main causes of the impedance behavior of polycrystalline materials. Because they have distinct relaxation durations, the impedance of bulk grains and the impedance of grain boundaries can be handled differently.

Figure 4.125 (a) shows the variation of the real part of impedance (Z') concerning frequency. It has been observed that Z' constantly decreases with an increase in frequency and after a certain point, this value of Z' almost becomes constant.

Also with variation in doping the value seems to decrease from sample T1 to T5, the highest being for *T1* (3.8) and lowest for *T4* (0.5). However, only sample *T2* (5.0) is seen to increase. This reduction in the value of Z' can be due to the space charge and dipole polarization effect of the samples. It has been observed that there is a steep decrease in values after mid- frequency regime, and all the values saturate the same range after 10 kHz.

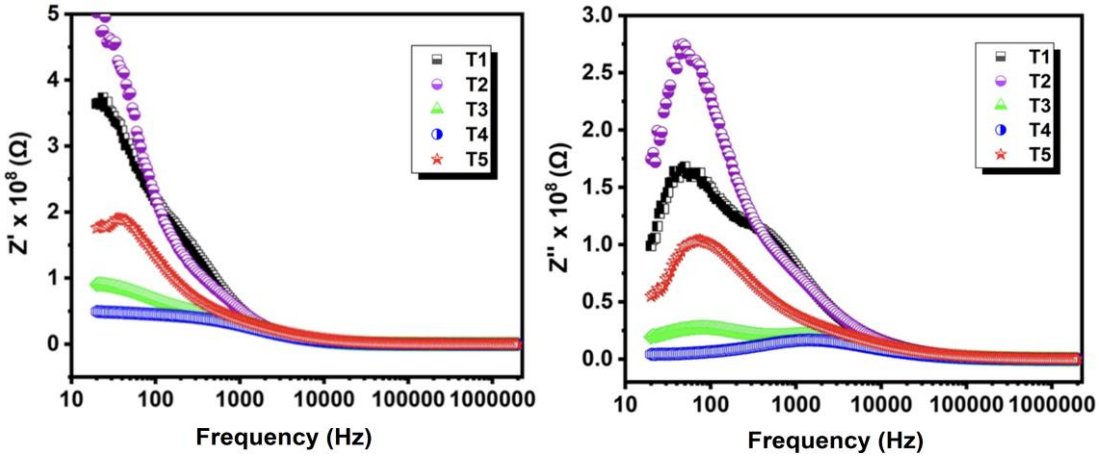

Figure 4.125: Dispersion in the (a) Dielectric Impedance Real (Z'), (b) Dielectric Impedance Imaginary (Z'') Of $Ba_{1-x}Sr_xFe_{12}O_{19}$ (*T1, T2, T3, T4,* and *T5*) as a Function of Frequency

To understand the space charge effect in a better way, the change in the imaginary part of impedance has been investigated with the variation in frequency as shown in Figure 4.125 (b). There is a non-monotonic shift in Z'' values along with the low-frequency regime with variation in Ba-Sr content. A similar trend in Z'' values is observed as observed in Z'. The values seem to decrease from sample *T1* to *T5*, the highest being for *T1* (1.0) and lowest for *T4* (0.1). However, for *T2* it is almost 1.7. There are peculiar relaxation peaks shown in samples *T1, T2, and T5* and weak peaks for *T3, and T4* in low-frequency regions. It has been noticed that after a certain point, even if the frequency rises, Z'' reaches a constant value and continues with the same.

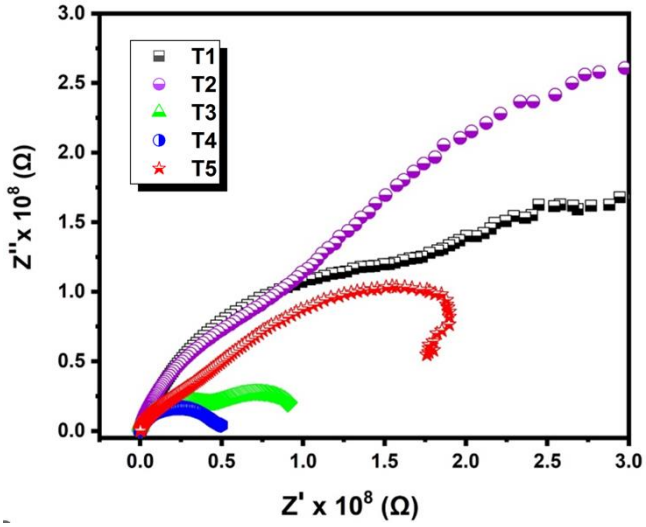

Figure 4.126: Dispersion in the (a) Dielectric Impedance Real (*Z′*) Part Versus Dielectric Impedance Imaginary (*Z″*) Part $Ba_{1-x}Sr_xFe_{12}O_{19}$ (*T1, T2, T3, T4,* and *T5*) as a Function of Frequency

In Figure 4.126, the plot of *Z″* versus *Z′* for each sample shows a semi-circular arc in the curves, the smallest semicircle being for sample *T4* and the largest for *T2*. For composition *T2* there seems an expansion of arc with doping variation of Ba-Sr content. However, for the samples (*T3, T4, T5*) there seems depression of arc. The Maxwell-Wagner phenomenon, related to interfacial polarization at grain boundaries, is linked to these low-frequency depressions. Now *T1* and *T2* samples display curves in the high-frequency region, depicting grains being more active. Sample *T5* plot occupies a position in the intermediate frequency regime indicating the role of both grain and grain boundaries for mechanisms, while the role of grain boundaries is prevalent explicitly for *T3* and *T4*.

4.7.2.4 AC Conductivity

As discussed earlier, it is well-known fact that the hopping of its valence electrons between Fe^{2+} and Fe^{3+} at octahedral sites is the main reason why conduction in ferrites. Conductivity rises as a result of the frequency increase, which also raises the charge carrier hopping frequency. The polaron hopping model described in [124] provides an explanation for this frequency-dependent conduction mechanism. According to that model, AC conductivity exhibits a declining tendency for long-range polarisation hopping, whereas it increases with an increase in frequency for the limited range of polaron hopping. The conductivity phenomena is independent of frequency in the case of band conduction [125].

Figure 4.127 depicts the plot of AC conductivity as a function of frequency in the ferrite samples. In the present investigation, it is seen that AC conductivity progressively increases after the 1 kHz frequency of the applied AC field. It shows nearly frequency-

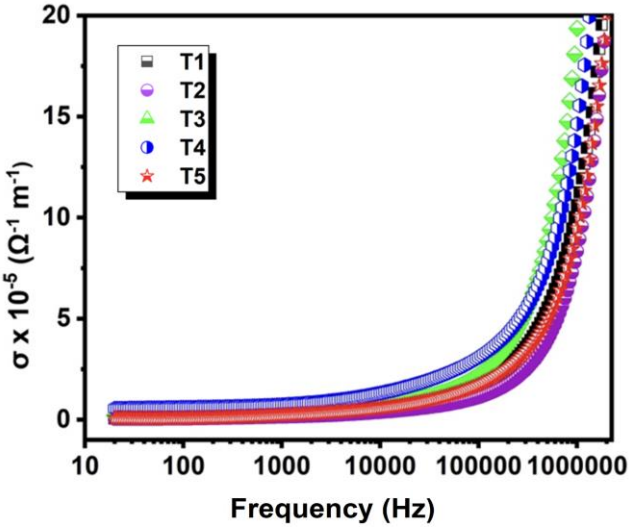

Figure 4.127: Variation of AC Conductivity Concerning Frequency for Ferrite Sample $Ba_{1-x}Sr_xFe_{12}O_{19}$ (*T1, T2, T3, T4,* and *T5*)

independent behavior below 1 kHz and this frequency marks the transition from DC conductivity to AC conductivity. The doping of variation of Ba-Sr- ions in place of Fe^{3+} bounds the scope of conduction hampering the Verwey hopping mechanism at octahedral sites. Here the n value was determined by fitting the plot, where n is taken from The Jonscher power law [126] expression: *T1* - 0.6866, *T2* - 0.3070, *T3* - 0.328, *T4* - 0.340, *T5* - 0.3828. Here the value of n turns out to be smaller than 1, hence charge carriers are hopping along with ac conductivity can be concluded.

4.7.3 Magnetic analysis

The law of saturation is used to determine the M_s and H_a values of the synthesized samples. The hysteresis loops (room temperature) for all synthesized composites are displayed in Figure 4.128. (M_r/M_s) ratio, saturation magnetization (M_s) anisotropy field (H_a), coercivity (H_c), and remanence magnetization (M_r) are enumerated in Table 4.26 which are calculated using Figure 4.27. that depicts M_s versus 1/ H^2 plots for all hexaferrite samples. All prepared specimens had a linear relationship, as demonstrated by the M-H loop in Figure 4.128, with a rapid increase in M_s at low-applied fields that slows down at high-applied fields. The variation in saturation magnetization (M_s) across the samples *T1* to *T6* reveals a relationship with cation distribution between spin-up and spin-down sites. Sample *T1* (105.29 emu/g) and *T6* (112.95 emu/g) show the highestM_s, likely due to a favorable cation occupancy at spin-down sites, which enhances magnetic alignment and increases magnetization. Conversely, samples *T2* (16.53 emu/g), *T3* (15.47 emu/g), and *T5* (17.36 emu/g) exhibit lower M_s values, possibly due to a higher concentration of cations occupying spin-up sites, resulting in less efficient spin alignment and

weaker magnetization. This highlights the crucial role of cation distribution in determining magnetic properties.

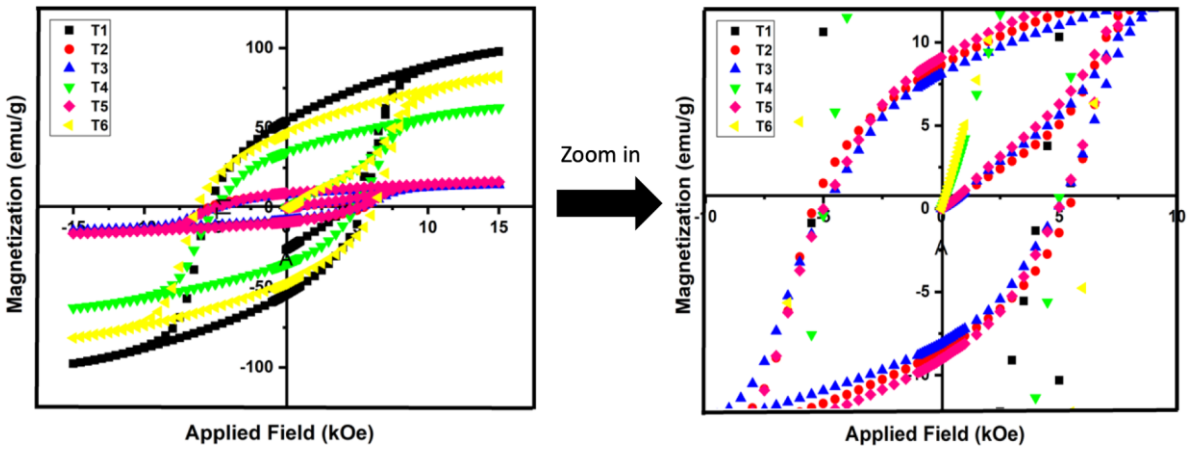

Figure 4.128: Hysteresis Loops of *T1, T2, T3, T4, T5* and T*6* Hexaferrite

In addition, the inter-grain group development and magnetic hardness of the material are evaluated using the M_r/M_sratio, whose value should range from 0 to 1. Materials with a significant squareness ratio ($0.5<M_r/M_s<1$) are more anisotropic, single-domain, and hard, while those with ($0.05<M_r/M_s<0.5$) have randomly oriented multi-magnetic domains [166]. In the present study M_r/M_s value for the *T1* to *T5* is larger than 0.5, indicating that the particles of the material are single-domain in nature. Conversely, *T6* shows that the material contains multiple domains with $M_r/M_s<0.5$.

Table 4.26: Magnetic Parameters M_s, H_c, H_a, M_r and M_r/M_s for Ba-Sr Hexaferrite Samples

Sample	M_s	H_c	H_a (kOe)	M_r	M_r/M_s
T1	105.29	5426.37	22.23	54.36	0.51
T2	16.53	4971.39	21.68	8.88	0.53
T3	15.47	4508.23	22.39	8.31	0.53
T4	67.28	4923.66	21.73	35.04	0.52
T5	17.36	4835.98	16.07	9.46	0.54
T6	112.95	6160.04	25.93	47.16	0.41

Sample *T6* exhibits the greatest values of coercivity (6160 Oe) whereas comparatively T5 has the value of coercivity (4835 Oe). H_a decreases prominently only for sample *T5* whereas for all the other samples it stays in the same range.

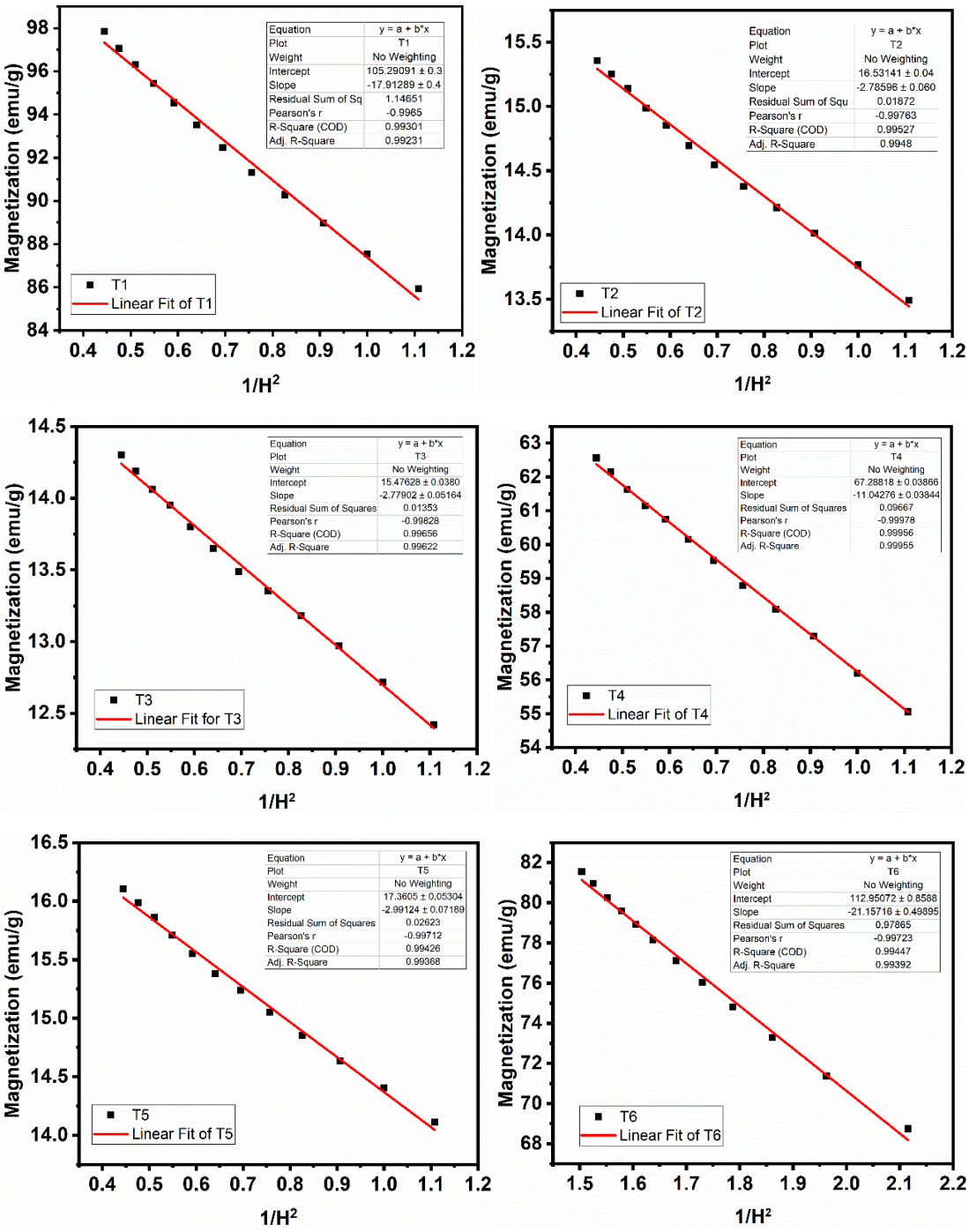

Figure 4.129: M_s Versus 1/ H^2 Plots for all Hexaferrite Samples

Figure 4.130: SEM Micrographs of ferrite samples: $Ba_{1-x}Sr_xFe_{12}O_{19}$ (*T1*, *T2*, *T3*, *T4*, *T5* and *T6*) and its correlation with magnetic data. As seen from the micrographs (Figure 4.130) the porosity is seen drastically decreasing from sample *T1* to *T2*, which can be one of the reasons that H_c is being lowered down from 5426 Oe to 4971 Oe. Rather not much impact of the micrographs can be stated here.

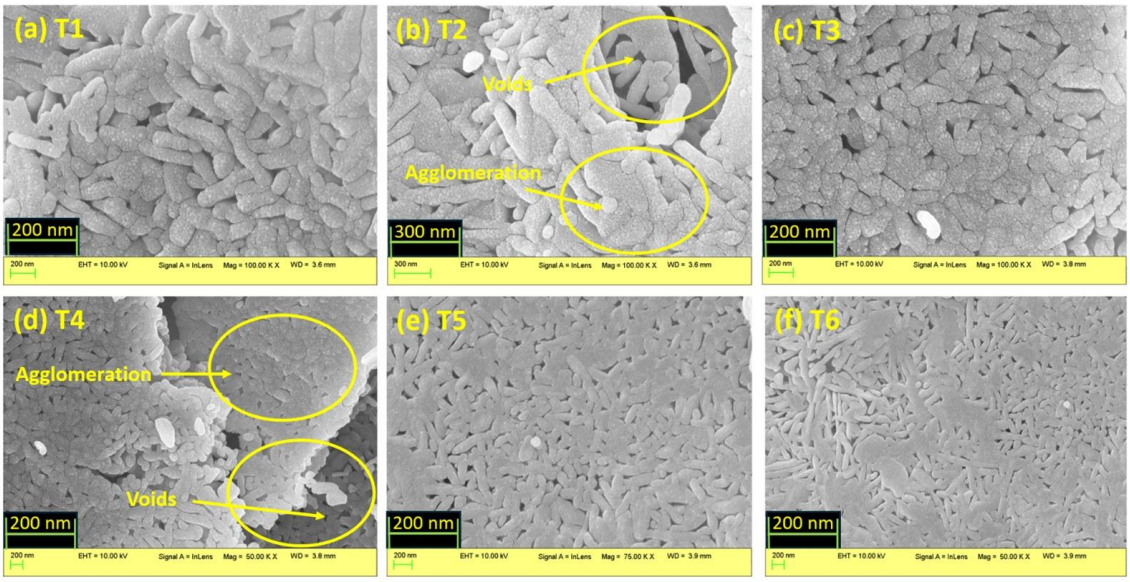

Figure 4.130: SEM Micrographs of Ferrite Samples: $Ba_{1-x}Sr_xFe_{12}O_{19}$ (*T1, T2, T3, T4, T5* and *T6*) and its Correlation with Magnetic Data

4.7.4 Electromagnetic Characteristics

4.7.4.1 Complex Permeability and Complex Permittivity

Figure 4.131 depicts the dependence of ε′, ε″, μ′, μ″ on frequency in ferrite compositions *T1, T3, T5 and T6.* Due to measurement uncertainty in samples *T1 and T4,* these samples were not included in the Complex Permeability and Complex Permittivity plots shown below. All the samples show good dispersion for the overall frequency region. In ε′ spectra, sample *T2*, the *T6* value lowers down till it reaches the frequency of 9.6 GHz, after which *T2* follows a dip, whereas the *T6* value is slightly increased. As soon as both the samples reach a value of 11.6 GHz, *T2* drastically increases, whereas *T6* slightly lowers in value. Sample *T3* shows a dielectric relaxation peak followed by a dip around 8.5 GHz but shows a large dip around 10 GHz. Sample *T5* does not vary much with frequency besides a weak peak around 8.8 GHz. In ε″ spectra, samples *T3, T5*, and *T6 stay* in the same range of values with multiple peaks and dips after certain frequency gaps. The range of values followed by these samples is around -1.2 to 1.5. Sample *T2* possesses a relaxation peak around 9.7 GHz, after which its value lowers down to -4. As can be seen in μ′ spectra, *T2* possesses a relaxation peak around 10 GHz, reaching the value of 3. Sample *T3* undergoes relaxation at around the same frequency, with a touching value of 6.5. However, samples *T4* and *T5* stay in a small range with weak peaks around. In μ″ spectra, sample *T2* undergoes a dip followed by a large relaxation peak of 10.2 GHz. Sample *T3* follows multiple weak dips and peaks but possesses a better peak in the high-frequency region, sample *T5* and *T6* possess a large peak in the low-frequency region followed by multiple peaks.

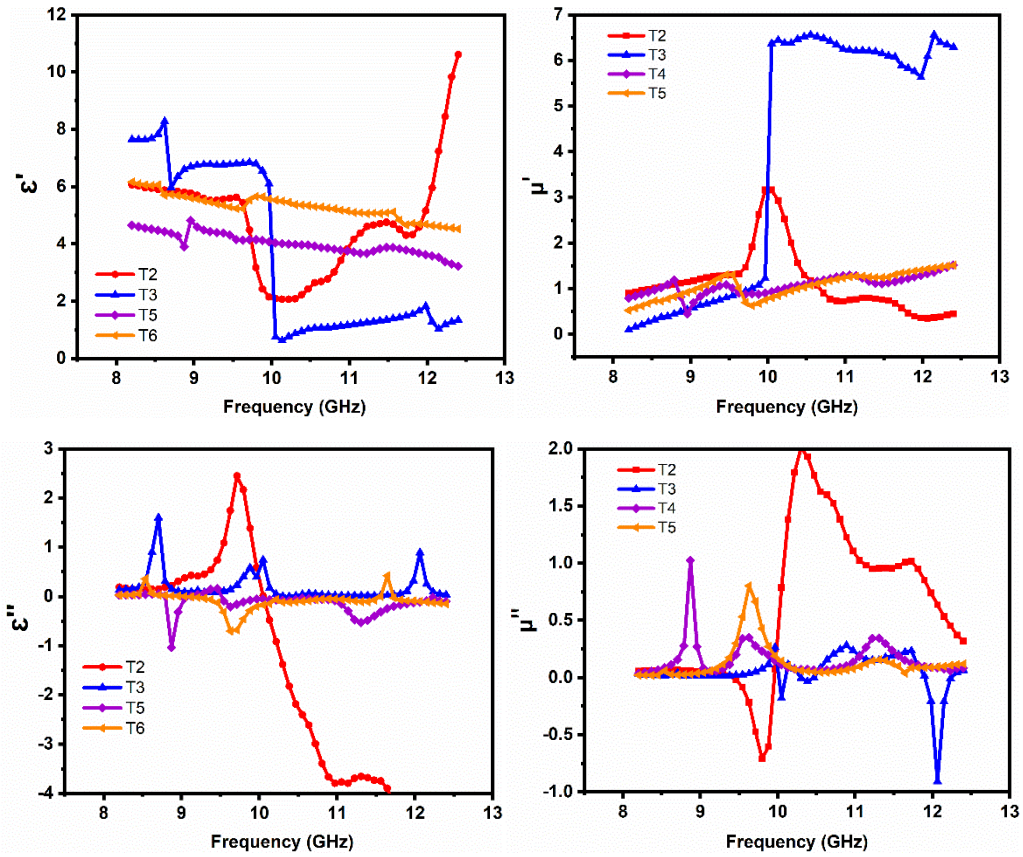

Figure 4.131: Dependence of ε′, ε′′, μ′, μ′′ on Frequency in Ferrite Compositions *T1, T3, T5 and T6*

Porosity, electron spin, grain size distribution, charge accumulation at grain borders, and dipole polarisation are some elements that affect the complex permittivity and permeability in the microwave range. Electron hopping in Fe^{2+}/Fe^{3+} is the cause of dielectric polarisation in ferrites. The porosity prevents polarisation and acts as a barrier to the field flow. The mechanism of complex permeability is controlled by ferromagnetic resonance and exchange resonance between Fe^{2+}/Fe^{3+} ions [170-171].

4.7.4.2 Microwave absorption in $Ba_{1-x}Sr_xFe_{12}O_{19}$

Examining a material's reflection loss is one method of determining its microwave absorption capability. Equations 3.16 and 3.17 are used to determine the RL of the compositions. This section will examine how different factors affect the material's microwave-absorbing capacity. These variables include the degree of reflection loss, impedance matching, and material thickness (λ/4).

4.7.4.3 Quarter Wavelength Mechanism

Plots showing reflection loss at different simulated thicknesses that depend on frequency are used to investigate the phenomenon of microwave absorption. Plots of RL against frequency at different thicknesses offer vital information about a material's microwave absorption

characteristics. These plots are crucial for optimizing material design for a variety of real-world applications and aid in understanding how materials interact with electromagnetic waves.

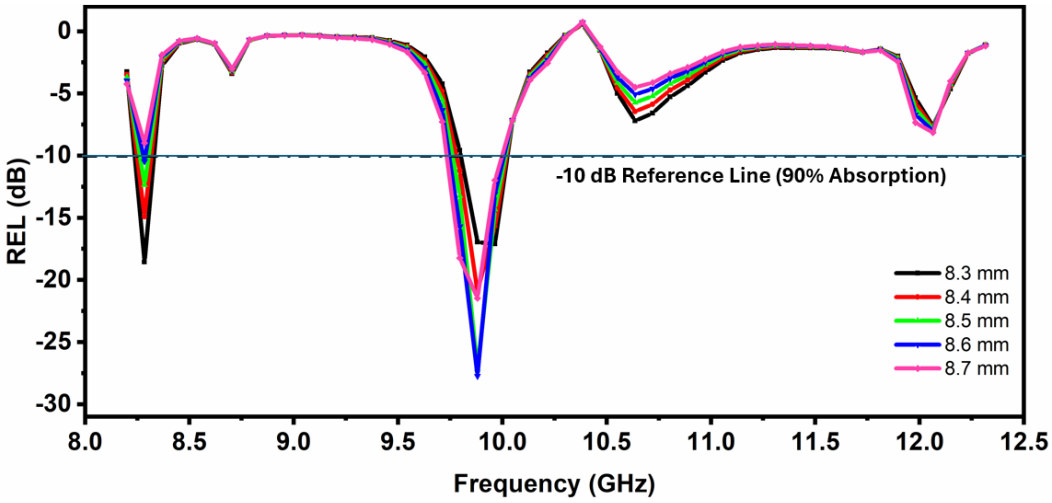

Figure 4.132: (a) Dependence of RL on Frequency in *T2* Composition

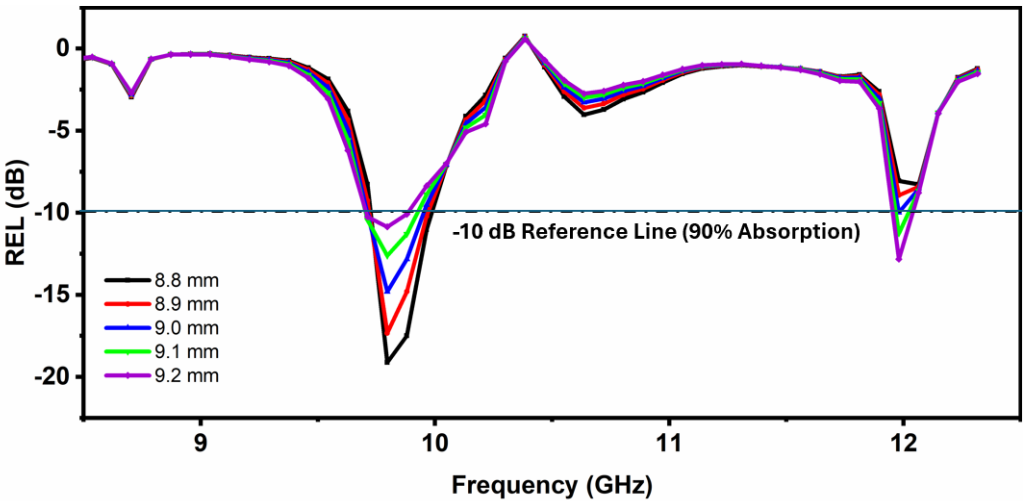

Figure 4.133: (a) Dependence of RL on Frequency in *T2* Composition

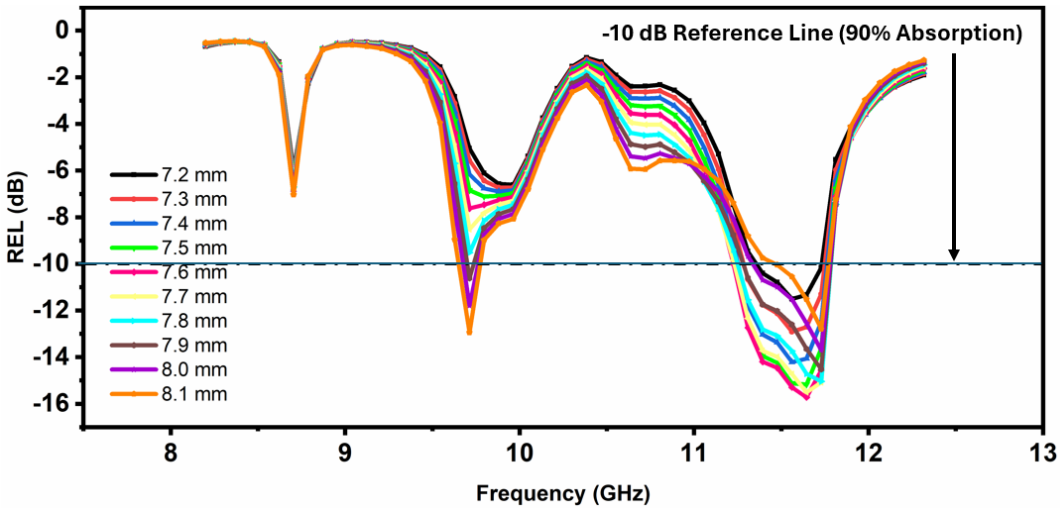

Figure 4.134: (a) Dependence of RL on Frequency in *T3* Composition

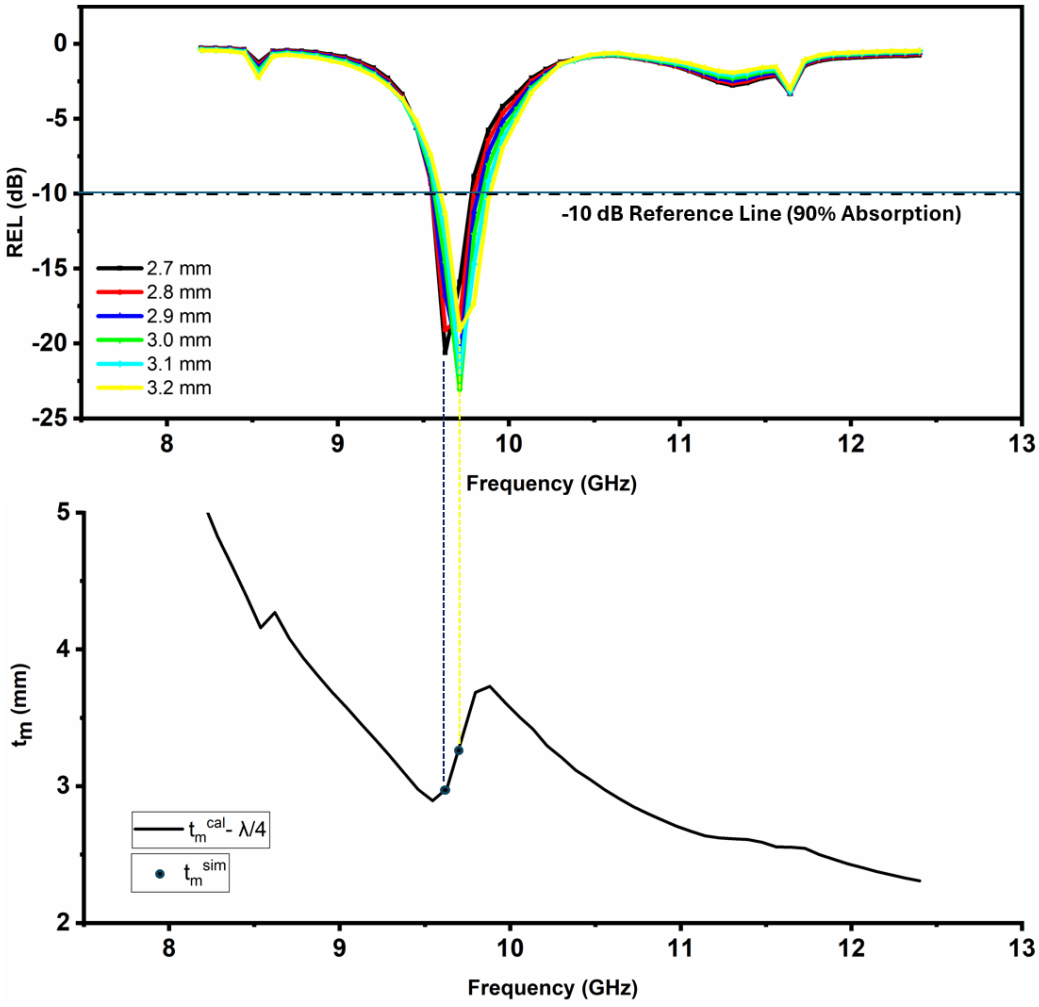

Figure 4.135: (a) Dependence of RL on Frequency in *T6* Composition and (b) t^{sim} and t^{cal} Versus Frequency for λ/4 in *T6* Composition

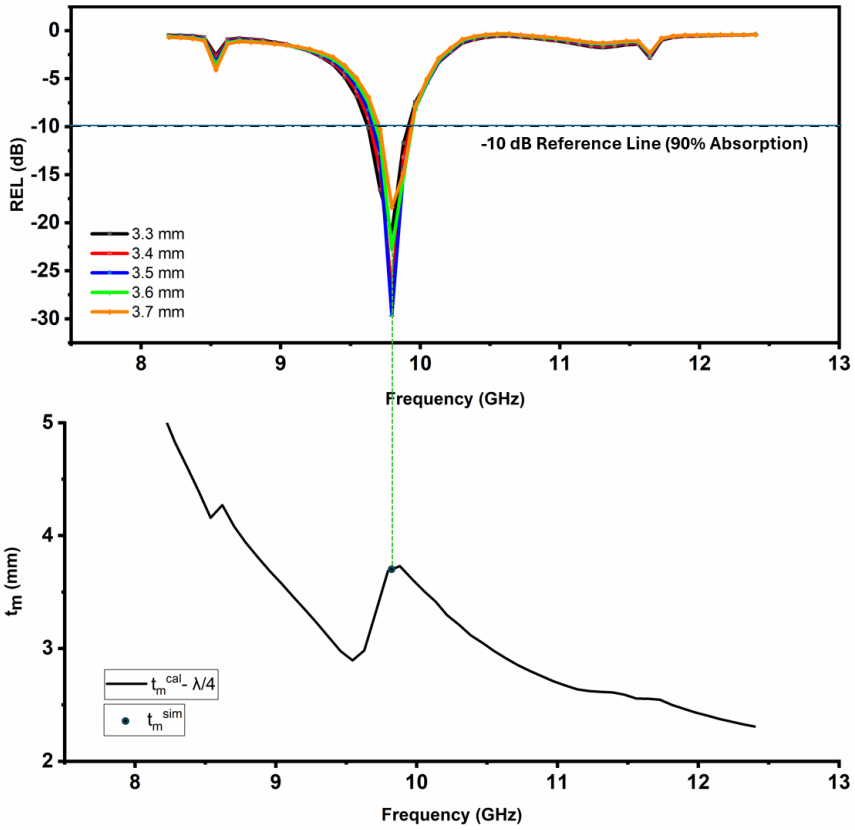

Figure 4.136: (a) Dependence of RL on Frequency in *T6* Composition and (b) t^{sim} and t^{cal} Versus Frequency for λ/4 in *T6* Composition

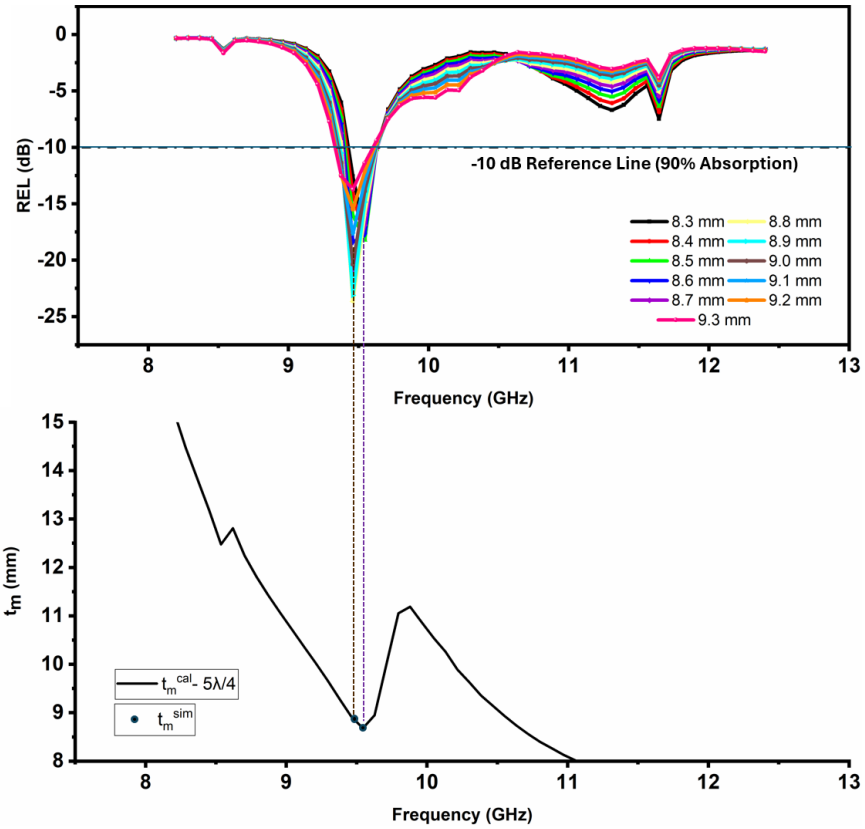

Figure 4.137: (a) Dependence of RL on Frequency in *T6* Composition and (b) t^{sim} and

t^{cal} Versus Frequency for 5λ/4 in *T6* Composition

The graphs of RL dependent on the frequency at different simulated thicknesses can be utilized to investigate the phenomenon of microwave absorption. Figure 4.132 to Figure 4.137 show RL plots of the ferrite compositions $Ba_{1-x}Sr_xFe_{12}O_{19}$ for RL ≥ -10 dB. The parameters, such as matching frequency/thickness, bandwidth, and frequency range, can be inferred from Figure 4.132 to Figure 4.137 which is summarised in Table 4.27. The highest RL dip of -29.60 dB is observed in *T6* composition at 9.80 GHz frequency and 3.5 mm thickness. According to Table II, the other two compositions have RL values between -14.81 to -27.15 dB, 8.4 to 8.9 mm thickness (*T2)*, and -11.50 to 15.71 dB, 7.2 to 8.1 mm thickness (*T3*). From the above graphs, it can be seen that samples *T2* and *T3* do not follow the quarter wavelength mechanism. However, sample *T6* follows the quarter wavelength mechanism for all the thicknesses.

The RL peaks are observed in *T2* [Figure 4.132 (a), Figure 4.133 (a)], in the frequency band ranging from 9.79 to 9.96 GHz and 9.79 to 9.88 GHz at thicknesses from 8.3 to 8.7 mm and 8.8 to 9.2 mm, respectively. The RL peaks are observed in *T3* [Figure 4.134 (a)], in the frequency band ranging from 11.03 to 11.86 GHz at thicknesses 7.2 to 8.1 mm. The RL peaks are observed in *T6* [Figure 4.135 (a), (b), Figure 4.136 (a), (b), Fig. 4.137 (a), (b)] in the frequency band ranging from 9.62 to 9.79 GHz, 9.79 to 9.79 GHz, 9.71 to 9.88 GHz at thicknesses 2.7 to 3.2 mm, 3.3 to 3.7, 8.3 to 9.3 mm, respectively.

Equation 3.18 states that the simulated thickness (t_m^{sim}) is employed to compute RL, and n = 1,3,5,..., etc. is used to obtain the calculated thickness (t_m^{cal}) from (6). To determine the link between RL peaks and the quarter wavelength mechanism, both parameters are investigated. Plots for sample *T6* of the calculated thickness (nλ/4) in the frequency regime are displayed in Figure 4.135 (a), (b) to 4.137 (a), (b). By stretching a vertical line from RL peaks towards thickness–frequency graphs, the computed thickness (nλ/4) and the simulated thickness (t_m^{sim}) are compared. Composition *T2* and *T3* seem to not follow the quarter wavelength mechanism, however, for *T6*, it seems to satisfy the mechanism. It follows from the plots that the λ/4 mechanism is satisfied in compositions with *T6* composition due to both λ/4 and 5λ/4 values. In Table 4.27, a -10 dB broad bandwidth of 0.78 GHz for composition *T3*, a bandwidth of 0.17 GHz for *T2*, and 0.18 GHz for *T6* is reported. Figure 4.138 depicts the 3D RL graphs of the samples *T2, T3* and *T6.* In sample *T2, the* Blue-violet region shows the highest peaks of RL around 9.79-9.96 GHz, which can be varied from Table 4.27. Similarly, for *T3* and *T6,* the blue-violet region in the graph shows RL peaks along with its thicknesses and BW covered [200].

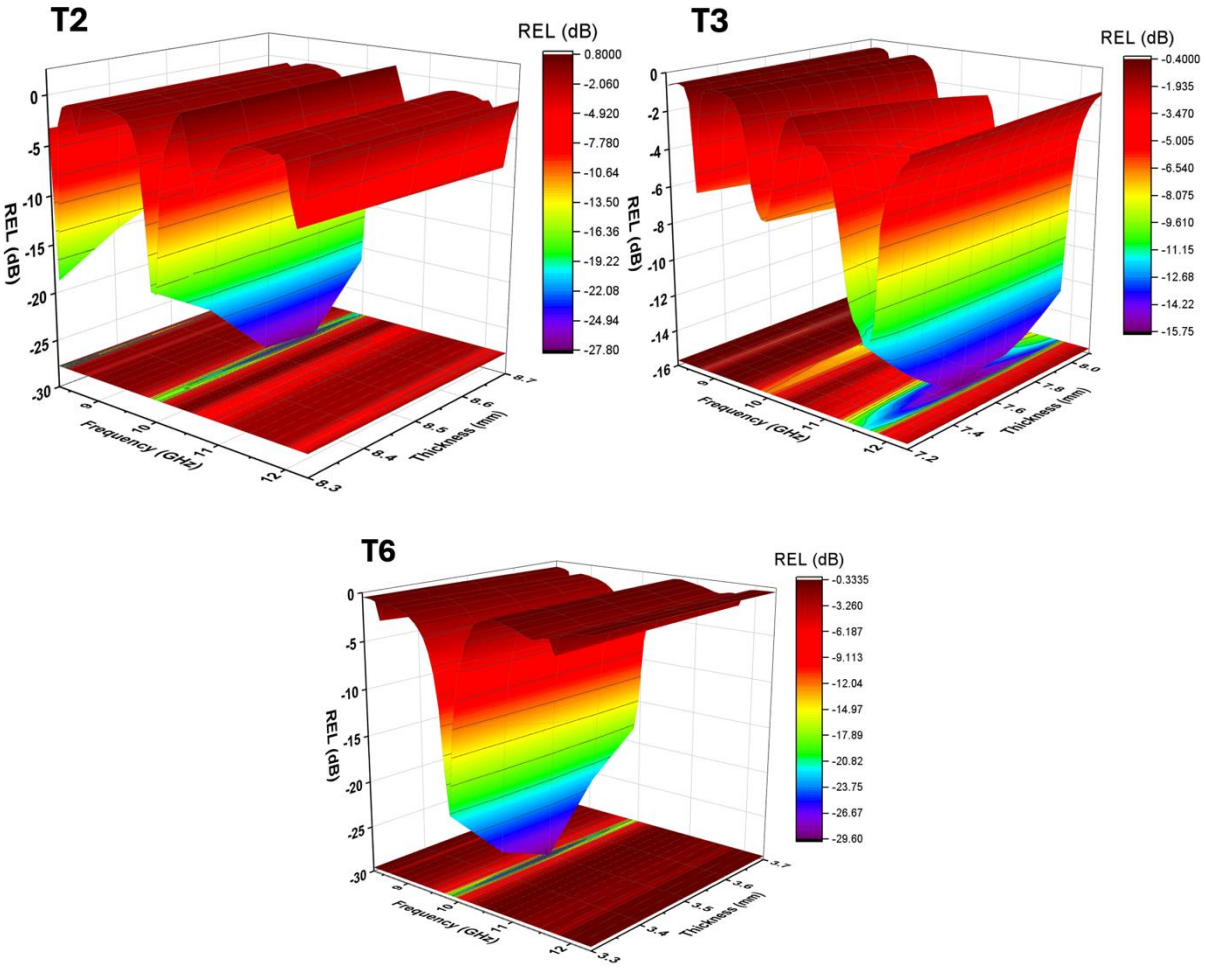

Figure 4.138: Three-Dimensional (3D) Plots of Reflection loss at Various Frequencies and Thicknesses for *T2, T3 and T6* Samples

Table 4.27: Computed Parameters for Microwave Absorption (RL > -10 dB)

Ba-Sr Content	Matching Thickness (mm)	Matching Frequency (GHz)	Maximum RL (dB)	Frequency Band for RL > -10 dB (GHz)	Bandwidth for RL > -10 dB (GHz)	BWT	PBW
T2	8.4	9.96	-15.70	9.79-9.96	0.17	0.02	1.69
	8.5	9.88	-27.15	9.79-9.96	0.17	0.02	1.70
	8.6	9.88	-27.73	9.79-9.96	0.17	0.02	1.70
	8.7	9.88	-21.46	9.79-9.96	0.17	0.02	1.70
	8.8	9.80	-19.12	9.79-9.96	0.17	0.02	1.71
	8.9	9.80	-17.33	9.79-9.96	0.17	0.02	1.71
	9.0	9.80	-14.81	9.71-9.88	0.17	0.02	1.74
T3	7.2	11.56	-11.50	11.47-11.72	0.25	0.03	2.16
	7.3	11.56	-12.91	11.03-11.81	0.78	0.11	6.75
	7.4	11.56	-14.22	11.30-11.72	0.42	0.06	3.63
	7.5	11.56	-15.11	11.30-11.72	0.42	0.06	3.63
	7.6	11.64	-15.71	11.22-11.72	0.50	0.07	4.29
	7.7	11.64	-15.50	11.30-11.72	0.42	0.05	3.61

	7.8	11.56	-13.73	11.39-11.86	0.47	0.06	4.07
	7.9	11.73	-14.51	11.30-11.72	0.42	0.05	3.58
T6	2.7	9.63	-20.61	9.62-9.71	0.08	0.03	0.87
	2.8	9.63	-19.09	9.62-9.71	0.08	0.03	0.87
	2.9	9.71	-21.18	9.62-9.71	0.16	0.06	1.67
	3.0	9.71	-23.12	9.62-9.71	0.08	0.03	0.86
	3.1	9.71	-21.90	9.62-9.71	0.08	0.03	0.86
	3.2	9.71	-19.11	9.62-9.71	0.33	0.10	3.42
	3.3	9.80	-21.05	9.62-9.71	0.33	0.10	3.39
	3.4	9.80	-27.08	9.71-9.98	0.18	0.05	1.84
	3.5	9.80	-29.60	9.71-9.98	0.18	0.05	1.84
	3.6	9.80	-22.75	9.71-9.98	0.18	0.05	1.84
	3.7	9.80	-18.41	9.71-9.98	0.18	0.05	1.84
	8.3	9.54	-17.59	9.71-9.98	0.18	0.02	1.89
	8.4	9.54	-18.17	9.46-9.62	0.16	0.02	1.68
	8.5	9.54	-18.22	9.46-9.62	0.16	0.02	1.68
	8.6	9.54	-17.74	9.46-9.62	0.16	0.02	1.68
	8.7	9.46	-21.25	9.46-9.62	0.16	0.02	1.69
	8.8	9.46	-23.67	9.46-9.62	0.16	0.02	1.69
	8.9	9.46	-23.11	9.37-9.54	0.17	0.02	1.80
	9.0	9.46	-20.36	9.37-9.54	0.17	0.02	1.80
	9.1	9.46	-17.67	9.37-9.54	0.17	0.02	1.80
	9.2	9.46	-15.49	9.37-9.54	0.17	0.02	1.80

4.7.4.4 Impedance matching mechanism

The characteristic impedance of free space is $Z_o = (\mu/\varepsilon)^{1/2} = 377\ \Omega$, where μ/ε are permeability/ permittivity of free space and the impedance of the absorber is Z_{in}. Because of the disparity in their permittivity/permeability values, the absorber impedance differs from free space. Depending on the impedance inequality between Z_{in} and Z_o, when a microwave signal traveling through free space interacts with an absorber, some of the signal will be reflected from the absorber; the greater the difference, the more the reflection. The bulk of the reflected signal is left behind, whereas just a small amount of the microwave signal enters the absorber due to the significant disparity between Z_{in} and Z_o. Because most of the signal is reflected, attenuation or absorption of the signal inside the absorber is minimal or meaningless, even if the absorber has maximal dielectric and magnetic loss. Thus, when designing the absorber, it is important to take the impedance matching of the absorber with free space into account.

The RL and impedance graphs (i.e., Z_{in}) with frequency regime for all compositions are displayed individually in Figures 4.139 and 4.140 In different compositions, impedance-matching conditions may arise in the form of RL peaks with $Z_{in} \sim Z_o$ (377) at specific

frequencies that correspond to different matching thicknesses. Z_{in} values for compositions are listed in Table 4.28 and are derived from Z_{in} plots in the aforementioned figures.

For sample *T2*, the value of Z_{in} varies from 287.78 to 353.26 Ω, which drifts away from 377Ω, for sample *T3*, the value of Z_{in} varies from 392.32 to 550.98 Ω, which is again away from 377 Ω. Hence, the RL values obtained for both these samples are less comparatively. There seems to be a problem with composition *T2*, even though good RL is obtained Z_{in} = 353.92 Ω, which drifts away from 377. Comparatively, sample T6 shows better RL values. However, in *T6*, for 3.5 mm thickness at 9.80 GHz frequency, RL = -29.60 dB, Z_{in} =357.78 Ω, in proximity to Z_o = 377 Ω and at the same frequency, 3.4 mm thickness, RL = -27.08 dB is recorded with Z_{in} = 351.42 Ω (Figure 4.139 and Table 4.28). So, in this case, it can be seen that as the Z_{in} value moves away from 377 Ω ,the RL values lower correspondingly.

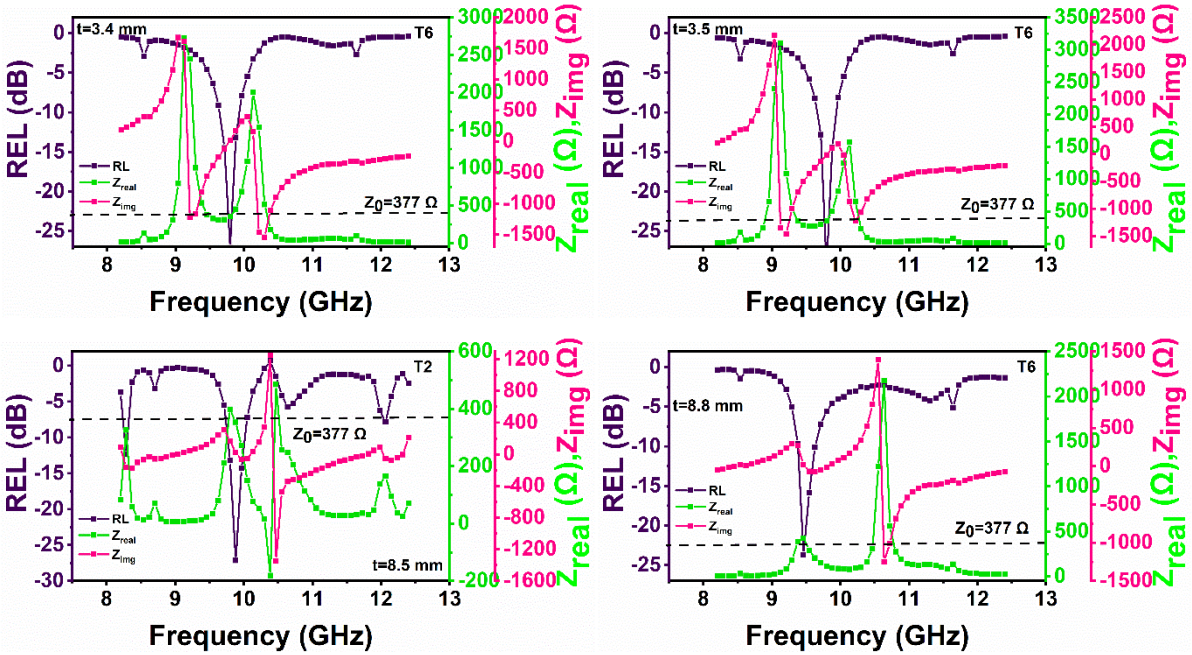

Figure 4.139: Dependence of RL, Z_{in}, Z_{real}, and Z_{img} on Frequency *T2* and *T6* Composition

It is explained by the fact that $|Z_{in}|$ in (3.18) is a complex expression that uses both real and imaginary terms, such as Z_{real} and Z_{img}. As a result, Z_{real} and Z_{img} are computed using (3.18), and the resulting graphs are displayed in the frequency and thickness domains for *T2* and *T6* composition (Figure 4.149). Likewise, Z_{real} and Z_{img} values for RL_{max} are calculated from plots, and displayed in Table 4.28.

Table 4.28: Impedance Parameters of RL Peaks at Different thickness

Ba-Sr Content	Matching Thickness (mm)	Matching Frequency	Maximum RL (dB)	Z_{real} (Ω)	Z_{img} (Ω)	Z_{in} (Ω)
T2	8.4	9.96	-15.70	282.78	-54.06	287.90
	8.5	9.88	-27.15	353.26	21.59	353.92
	8.6	9.88	-27.73	351.01	-14.77	351.32
	8.7	9.88	-21.46	340.19	-48.33	343.61
	8.8	9.80	-19.12	467.75	-22.49	468.29
	8.9	9.80	-17.33	444.58	-89.80	453.56
	9.0	9.80	-14.81	404.74	-141.73	428.84
T3	7.2	11.56	-11.50	518.90	198.59	555.60
	7.3	11.56	-12.91	550.98	120.63	564.03
	7.4	11.56	-14.22	554.69	36.94	555.91
	7.5	11.56	-15.11	531.84	-38.91	533.26
	7.6	11.64	-15.71	502.80	-71.24	507.82
	7.7	11.64	-15.50	459.52	-115.19	473.74
	7.8	11.56	-13.73	392.32	-161.10	424.10
	7.9	11.73	-14.51	425.96	-145.44	450.11
T6	2.7	9.63	-20.61	452.21	17.90	452.57
	2.8	9.63	-19.09	464.30	-33.60	465.51
	2.9	9.71	-21.18	318.72	17.20	319.19
	3.0	9.71	-23.12	328.49	-8.71	328.61
	3.1	9.71	-21.90	333.10	-36.53	335.10
	3.2	9.71	-19.11	332.06	-64.78	338.32
	3.3	9.80	-21.05	337.40	49.60	341.02
	3.4	9.80	-27.08	350.91	18.89	351.42
	3.5	9.80	-29.60	357.78	-14.94	358.09
	3.6	9.80	-22.75	357.08	-49.74	360.53
	3.7	9.80	-18.41	348.87	-83.11	358.64
	8.3	9.54	-17.59	289.25	5.59	289.31
	8.4	9.54	-18.17	294.50	-8.29	294.61
	8.5	9.54	-18.22	297.43	-22.92	298.31

8.6	9.54	-17.74	297.90	-37.79	300.29
8.7	9.46	-21.25	413.24	58.31	417.33
8.8	9.46	-23.67	425.82	19.68	426.27
8.9	9.46	-23.11	429.09	-21.48	429.63
9.0	9.46	-20.36	422.61	-62.00	427.14
9.1	9.46	-17.67	407.33	-98.84	419.15
9.2	9.46	-15.49	385.25	-129.75	406.51

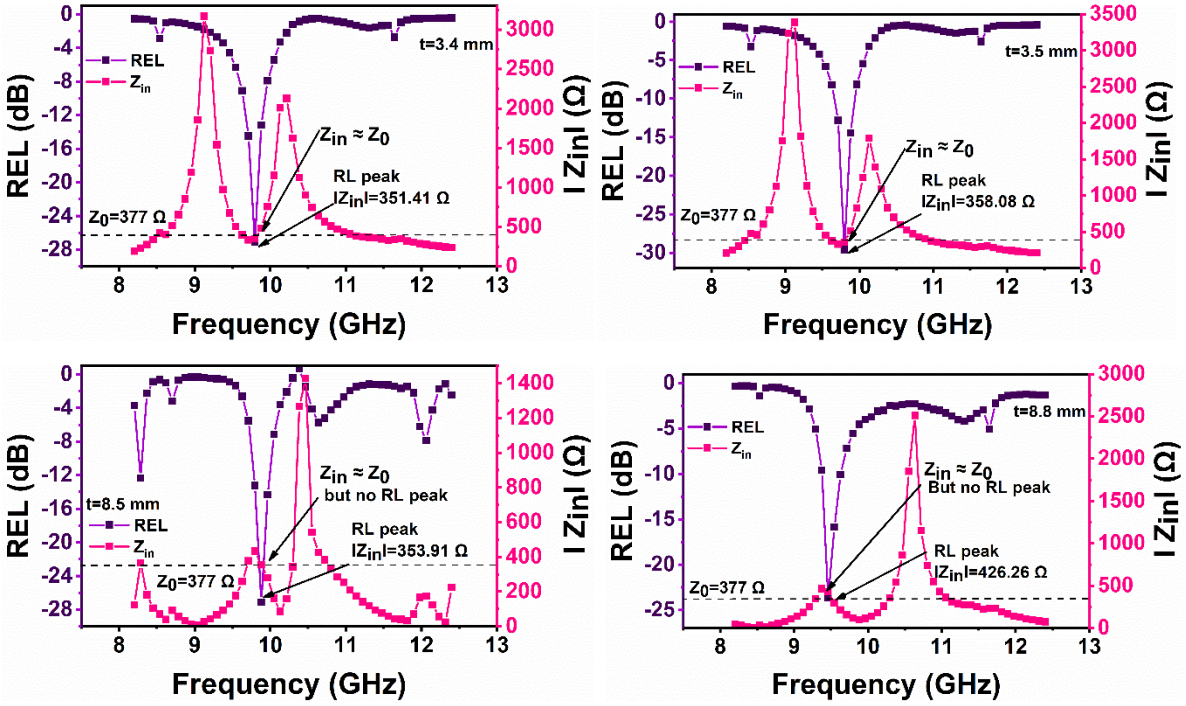

Figure 4.140: Dependence of RL and Z_{in} on Frequency in *T2 and T6* Composition

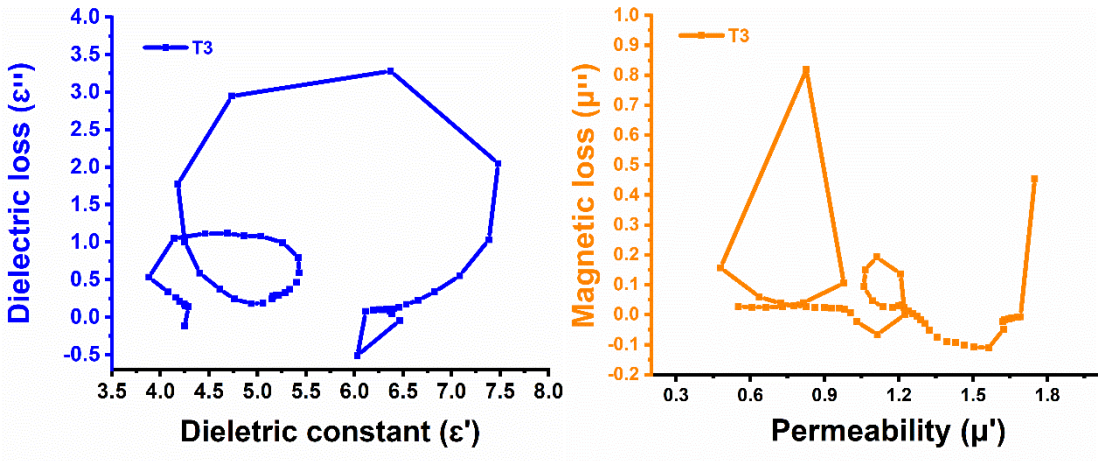

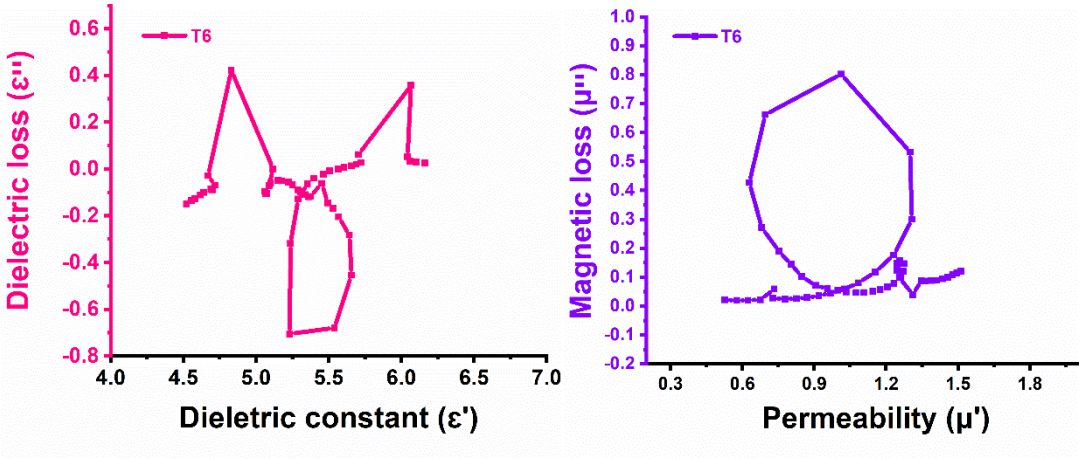

Figure 4.141: Cole–Cole plots in *T3* and T6 Compositions

Figure 4.141 shows Cole–Cole plots of *T3 and T6* samples to verify relaxation in the compositions. But no prominent effect of the Cole-Cole plot is seen concerning the RL peaks here. Multiple relaxations are shown in ε′ vs. ε″ plots of *T3* and inverted semicircles in μ′ vs. μ″ plots of *T6.* Large RL is not observed at corresponding relaxation peaks of Cole -Cole plots, so it can be said that the relaxation process may be dominated by impedance matching and quarter wavelength mechanism.

4.7.4.5. Eddy Current Loss

If Eddy current loss remains constant with frequency, it helps improve microwave absorption. Here, from graph 4.142, it can be seen that *T2* remains constant for 9 to 9.8 GHz and 10.5 to 11.8 GHz, *T3* remains constant for 9 to 9.8 GHz and 10.2 to 12.4 GHz, *T6* remains constant for 8.2 to 9.4 GHz and 10 to 12.4 GHz, so eddy current loss plays a vital role in microwave absorption only for these frequencies in the corresponding samples.

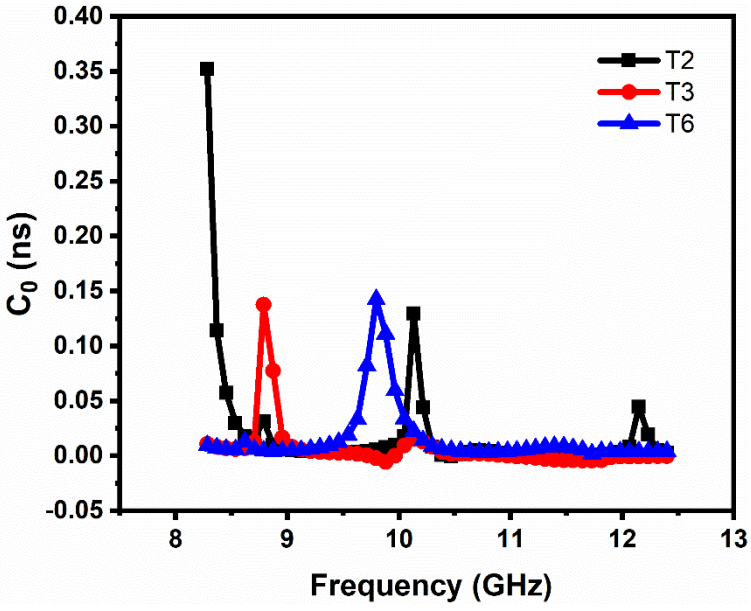

Figure 4.142: C_0 Versus Frequency Variation for Ferrite Compositions

4.7.4.6 BWT/Percentage Bandwidth Ratio

The high bandwidth at low thickness for a typical RL or absorption dip is a crucial metric to design and characterize absorber behavior, in addition to the criterion RL≥-10.

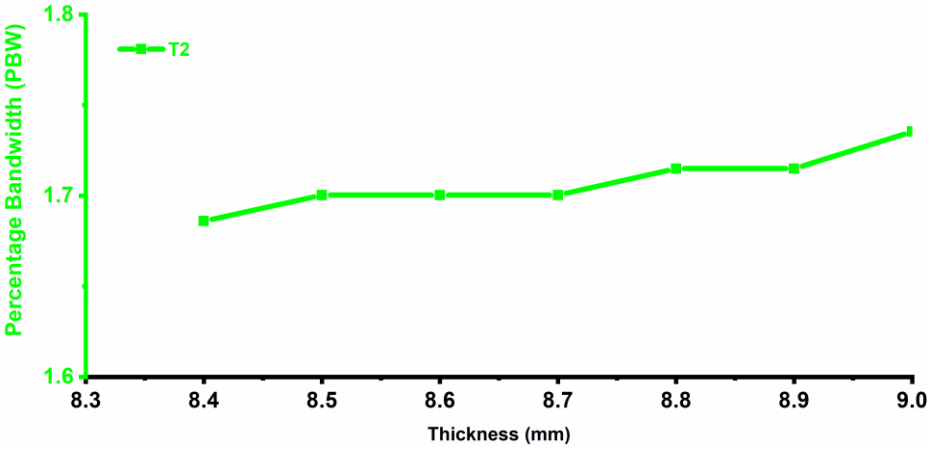

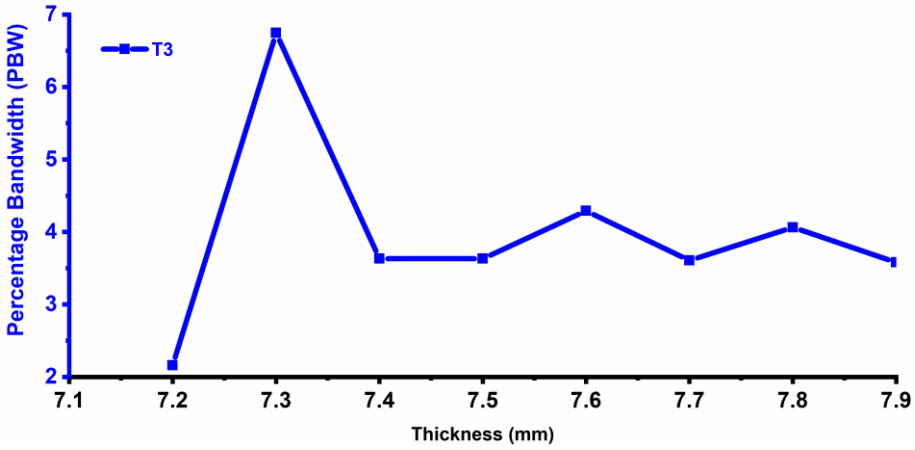

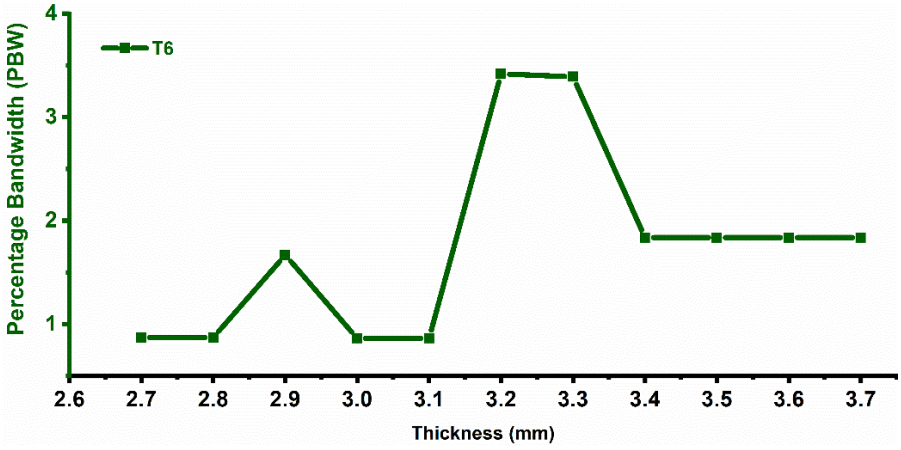

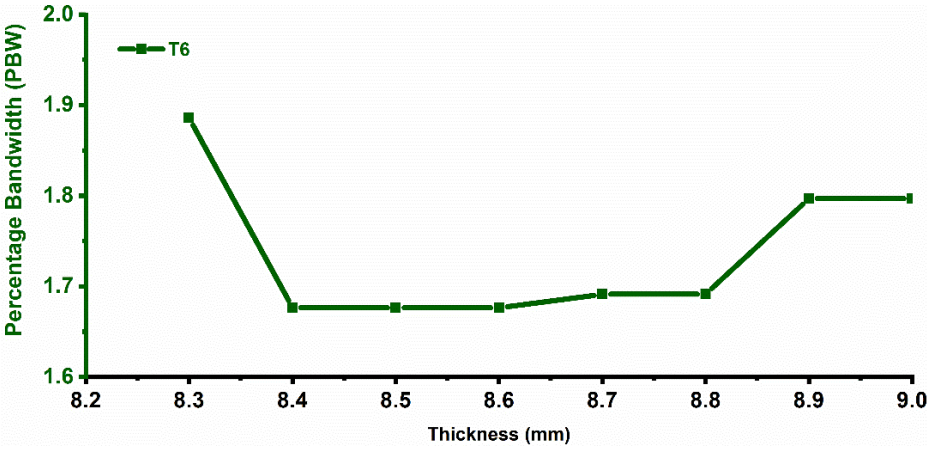

Figure 4.143: Bandwidth (%) Variation with thickness in Ferrite *T2, T3,* and *T6* Compositions

Table 4.27 provides BWT for maximum RL with frequency. The BWT is 0.17 for *T2*, 0.03 to 0.11 for *T3*, and 0.02 to 0.10 for *T6*. Hence, anything regarding doping cannot be concluded here. The BWT of 0.11 at 11.56 GHz and RL_{max} = -12.90 is the highest for *T3* at 7.3 mm thickness, AB of 0.78 GHz. From the graphs above, Figure 4.143, it can be seen that PBW values stand good for sample *T3*.

4.8 Ba $^{2+}$-Sr^{2+} substituted $Ba_{1-x}Sr_xFe_{12}O_{19}$/PANI hexaferrite

In this section, we have synthesized a hexaferrite with Ba and Sr substitutions via the sol-gel technique, using PANI as a matrix. This composition of hexaferrite will be given as $Ba_{1-x}Sr_xFe_{12}O_{19}$. The sample names with the codes for each level of substitution in $Ba_{1-x}Sr_xFe_{12}O_{19}$/PANI are given in Table 4.29.

Table 4.29: The Assignment of Sample Names Corresponding to Various Substitution Levels in $Ba_{1-x}Sr_xFe_{12}O_{19}$/PANI Hexaferrite

Sample Composition $Ba_{1-x}Sr_xFe_{12}O_{19}$/PANI	Sample Code Name	Sample Code (T-Series)
x = 0.2	$Ba_{0.8}Sr_{0.2}$ $Fe_{12}O_{19}$/PANI	TP2
x = 0.4	$Ba_{0.6}Sr_{0.4}$ $Fe_{12}O_{19}$/PANI	TP3
x = 1.0	Sr $Fe_{12}O_{19}$/PANI	TP6

4.8.1 Structural Analysis

4.8.1.2 Field Emission Scanning Electron Microscopy

Figure 4.144 (a-c) displays the grain morphology of the samples $Ba_{0.8}Sr_{0.2}$ $Fe_{12}O_{19}$/PANI *TP2, TP3, TP6*. SEM graphs of *TP2* display small, unfused grains assembling. The size of the particles does not appear to alter as the doping is increased, but voids are visible. Doping causes the particles to fuse more and more, even though their size and shape do not vary substantially.

Additionally, the graph shows more fused grains as doping increases. Doping causes grain clusters with an uneven size distribution because of the electrostatic and magnetic interactions between ferrite particles. Figure 4.145 shows EDX spectra of $Ba_{0.2}Sr_{0.8}Co_xMg_xFe_{12-2x}O_{19}$ hexaferrite for samples *TP3*. EDAX of *TP3* clarifies that Ba (4.56 % by weight) is present in the sample.

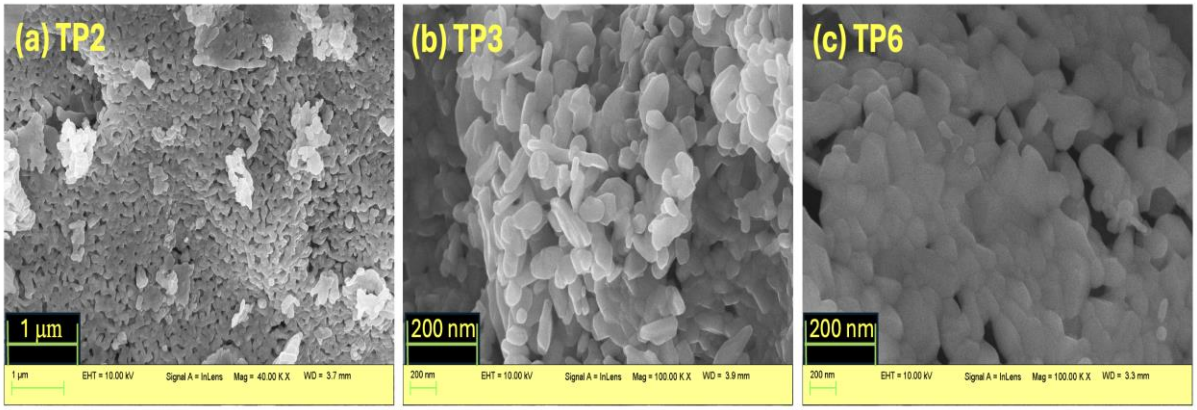

Figure 4.144: SEM Micrographs of Ferrite Samples $Ba_{0.8}Sr_{0.2}Fe_{12}O_{19}$/PANI (*TP2, TP3, TP6)*

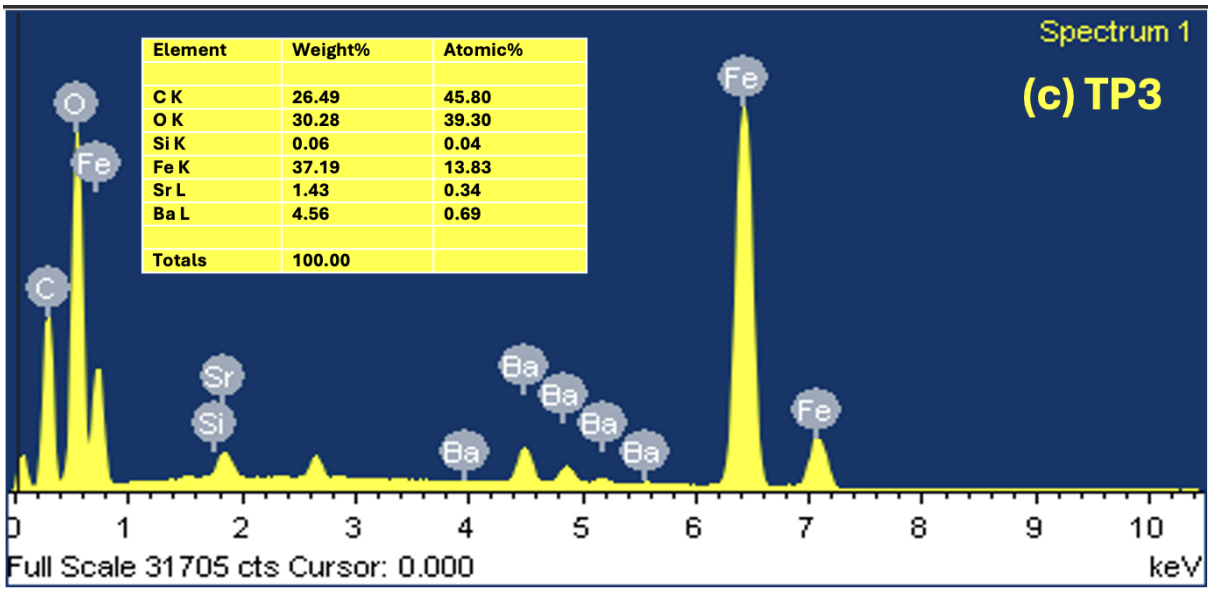

Figure 4.145: EDX Spectra of $Ba_{0.8}Sr_{0.2}Fe_{12}O_{19}$/PANI (*TP3)*

4.8.2 Electrical Analysis

4.8.2.1 Dielectric permittivity

The relevant mathematical equations for electrical parameters have already been mentioned in the earlier section 3.1.1. There were measurement uncertainties in the low-frequency region, thus the plots are drawn from 100 to 2 MHz. Figure 4.146 displays two distinct plot types with frequencies ranging from 100 Hz to 2 MHz: (a) the first real component of dielectric permittivity and (b) the second, which is the imaginary part associated with dielectric loss.

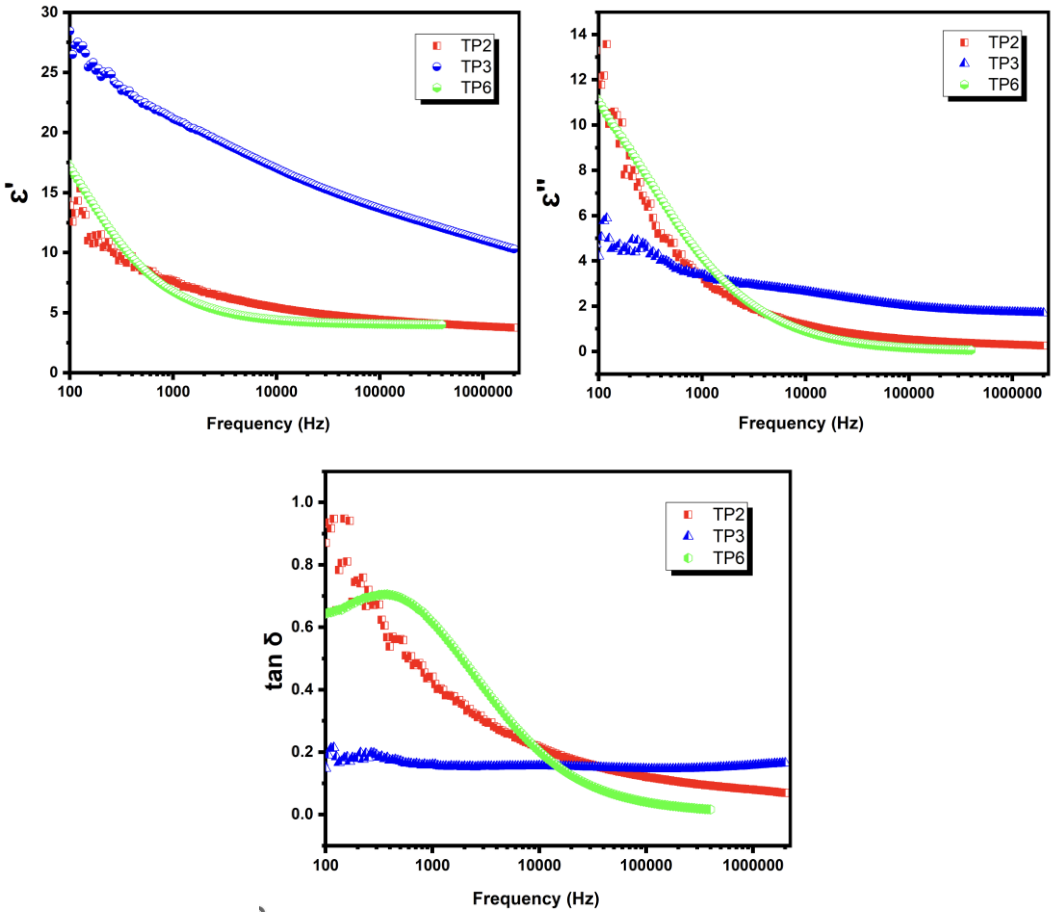

Figure 4.146: Variation of Dielectric Spectra of (a) Real Component (b) Imaginary Component (c) Variation of the Dielectric loss Tangent Ferrite Sample $Ba_{0.8}Sr_{0.2}Fe_{12}O_{19}$/PANI (*TP2, TP3, TP6)* Function of Frequency

As frequency drops, Figure 4.146 (a) shows how the value ε' depicts a dispersion in the low-frequency spectra, with *TP3* and *TP6* becoming frequency-independent after a certain frequency and TP3 decreasing nearly linearly with frequency. With a change in Ba and Sr content, initially, with Ba content decreasing and Sr increasing, the value ε' rises from 16 (*TP2*) to 27 (*TP3*) but then decreases to 17 (*TP6*). Samples *TP2* and *TP6* become constant after 20k Hz frequency however, sample *TP2* seems to follow a somewhat linear declining trend and does not follow a constant path even at high frequencies. Sample *TP2* and *TP6* reach the value 5 after becoming constant in ε'spectra while *TP3* declines to value 13.

When highly conductive grains with insulating grain boundaries surpass constrained charge aggregation brought on by an electric field, space charge polarisation occurs. Within a sinusoidal electric field, space charge carriers have a certain amount of time to align themselves parallel to the field. When the field reversal frequency rises, the space charges gradually become less capable of maintaining synchronism with the sinusoidal field. After that, it follows the field, lowering the dielectric permittivity of the material. The hopping conduction

mechanism is primarily responsible for the conduction process in ferrite materials, which can be linked to polarization. Here, in this case, there seems to be weak relaxation for samples for *TP2* and *TP6* ε'. Similarly, for ε'' the at frequency lower regime, the initial value for *TP2* is 14, *TP3* 6, and the increases *TP6* is 11, but then as the frequency increases, these values again reach a constant value or do not show much variation, or this can also be termed as weak relaxation as explained above. As was previously mentioned, the Dielectric permittivity/loss reaches a steady state value at a certain frequency, beyond which electron exchange and hopping with +2 and +3 states are not possible. Here, all the samples follow a constant trail after crossing 10 kHz frequency.

Figure 4.146 (c) demonstrates that the value of the dielectric loss tangent decreases as frequency increases for *TP2*. The decrease in the value of tan can be explained using Koop's phenomenological theory of dielectrics. For *TP2*, the value of *tan* δ starts with 1 and goes on decreasing till 0.1. For *TP3*, the value oscillates between 0.1 to 0.25, for *TP6*, value stars with 0.7 show weak relaxation at around 700 Hz frequency range, but then the value lowers down to 0.05. The criteria that eventually influence the loss tangent are the Fe^{2+}/Fe^{3+} content, interfacial polarisation, sample stoichiometry, interface traps, structural oneness, and, lastly, the sintering temperature.

4.8.2.2 Electric modulus analysis

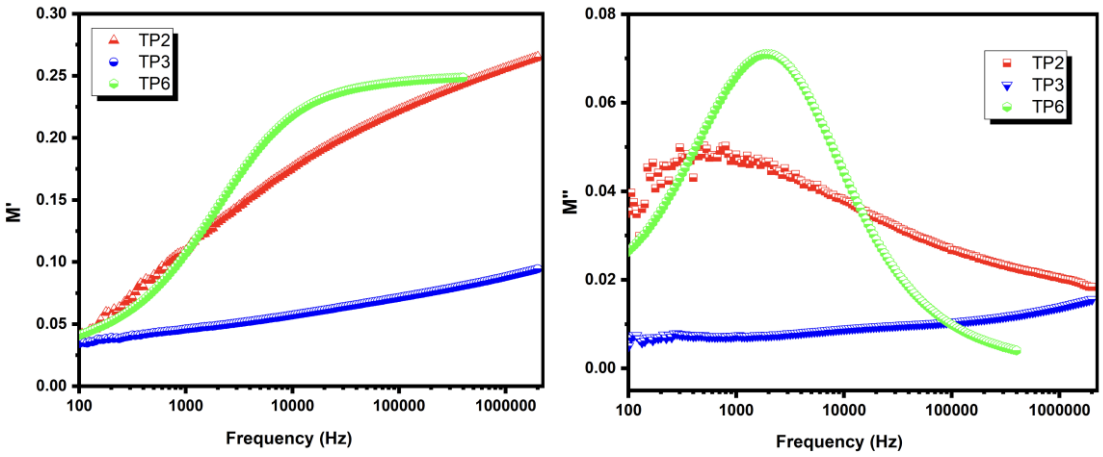

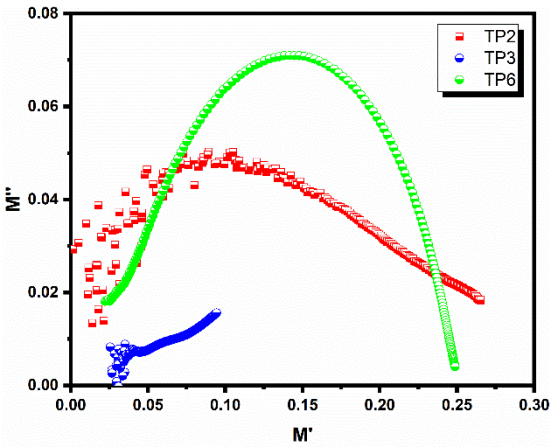

Figure 4.147: Electric Modulus Variation (a) Real Component, (b) Imaginary Component of Ferrite Sample $Ba_{1-x}Sr_xFe_{12}O_{19}$ /PANI (*TP2, TP3, TP6)* as a Function of Frequency (c) Cole-Cole (*M′* vs *M″*) Plot

The distinctive feature of Modulus along the frequency is depicted in Figure 4.147 as a large, asymmetric peak in the imaginary part of the electric modulus graph. Information on conductivity is provided by Figure 4.147 (a), which displays the fluctuation of the real component of the modulus (M′) vs. the log of frequency. It is limited to being set to lower values at lower frequencies, however, all samples also show a non-linear increase in M′ with frequency. Sample *TP2*, with higher Ba content, reaches a higher value at a higher frequency, but with doping, as the Ba content is reduced and Sr content is increased, the value of sample *TP3* is reduced. But with further changes in doping for *TP6*, the value is seen increasing. The highest value can be noted for sample *TP2*, being 0.27. The pattern depicts grains actively participating. In *M″* spectra, a larger relaxation peak can be seen for sample *TP6*, whereas a weak peak is visible for sample *TP2* but *TP3* shows two weak relaxation peaks. Sample *TP2* seems to have a higher value (0.023) compared to the samples. The relaxation peak of sample *TP6* justifies grain boundaries being more active.

Figure 4.147 (c) describes the Cole-Cole plot of $Ba_{1-x}Sr_xFe_{12}O_{19}$ /PANI for (*TP2, TP3, TP6*). The asymmetric nature of distorted semi-circles has been observed. The variation in Ba-Sr doping causes the semicircle to move towards a high-frequency domain, though the *TP3* arc is incomplete, however, it can be seen for *TP2* and *TP6*. The highest relaxation peak is found for sample *TP6*. Both the relaxation peaks (*TP2, TP6*) seem to be in the mid-frequency region depicting that grains as well as grain boundaries are actively participating.

4.8.2.3. Complex impedance spectra

The impedance performance of the polycrystalline materials, which is mostly caused by their bulk grains and grain boundaries, can be inferred from the details of resistance (*Z′*) and

reactance (*Z″*). Grain boundaries and bulk grains are treated differently in terms of impedance because of their varied relaxation durations.

Figure 4.148 (a) shows how *Z′* fluctuates along log frequency. It has been observed that Z′ steadily decreases as the frequency increases until it almost achieves a constant value at a particular point. It can be seen from the graph, that after 50 kHz all three samples follow a constant path, *TP2*, and *TP3* following nearly 0.01 value, and *TP6* approximately zero. The reduction in space charge polarization of the samples is accountable for this decrease in Z′ value.

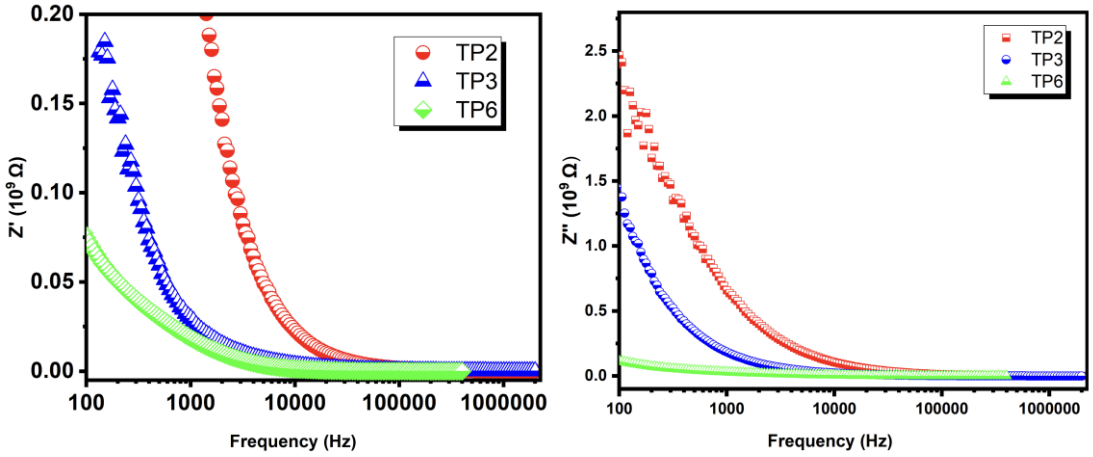

Figure 4.148: Variation in the (a) Dielectric Impedance Real (*Z′*) (b) Dielectric Impedance Imaginary (*Z″*) vs. Frequency $Ba_{1-x}Sr_xFe_{12}O_{19}$ /PANI for (*TP2, TP3, TP6*)

As seen in Figure 4.148 (b), the change in Z″ with the variation in frequency has been studied to better understand the impact of space charges. At a lower frequency regime, imaginary components have been found to fall sharply, and after 10 kHz, all values saturate in the same range. Figure 4.149 shows Z″ vs. Z′ graph, it can be seen that sample *TP2* shows a semicircular arc where as the other two samples do not.

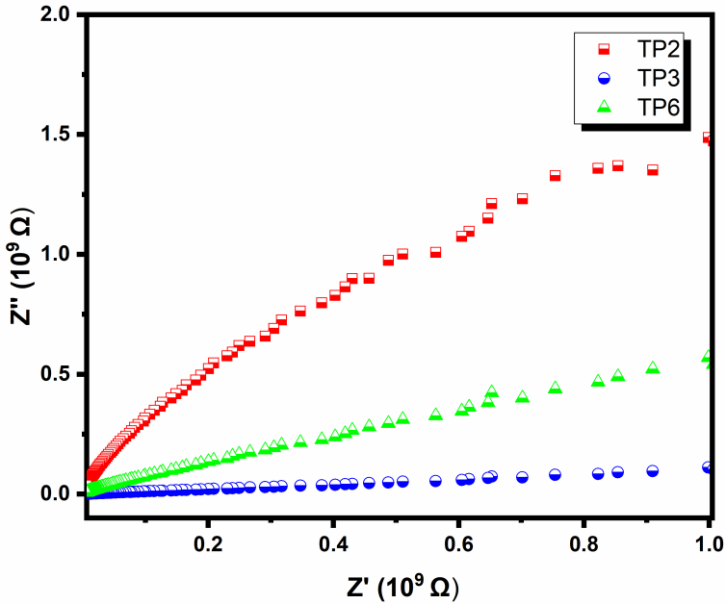

Figure 4.149: Variation in the Dielectric Impedance Real (Z′) Component Versus Dielectric Impedance Imaginary (*Z″*) Component $Ba_{1-x}Sr_xFe_{12}O_{19}$ /PANI (*TP2, TP3, TP6*)

4.8.2.4 AC Conductivity

Figure 4.150 displays the composite samples' AC conductivity curve as a function of frequency. In all three samples *TP2*, *TP3*, and *TP6* exhibit a progressive increase in AC conductivity. Samples *TP2* and *TP3* follow a constant path before reaching the frequency of 10 kHz.

Below 10 kHz, DC conductivity transforms to AC conductivity, and the behavior is almost frequency-independent. But for sample TP6, a constant path is followed only till 800 Hz, after which it is seen to rise exponentially.

Section 3.3.4 provides the frequency-dependent AC conductivity, also referred to as the Jonscher power law. When describing the behavior of dielectric materials throughout a broad frequency range, the Jonscher power law is helpful. *A* and *n* are constants in the Jonscher power law. Here, *A* and *n* are determined by the sample's composition. While *n* is dimensionless, *A* has conductivity units. In AC conductivity charts, the distribution is quantified by the second term, $A\omega^n$. According to Funke [127], the number n has a physical significance: $n < 1$ suggests a sudden translational motion with hopping, whereas $n > 1$ denotes localized hopping between nearby places.

The value of *n* was determined by fitting the plots: *TP2*, $n = 0.5759$, *TP3*, $n = 0.3563$ and *TP6*, $n = 0.8980$. Since n is smaller than 1 for all the samples, indicating that charge carriers are hopping along with ac conductivity.

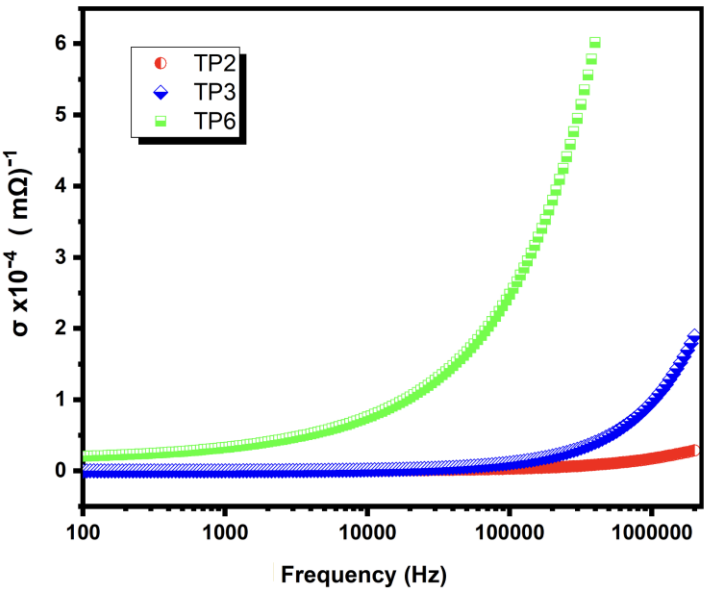

Figure 4.150: Variation of AC Conductivity for Ferrite Sample $Ba_{1-x}Sr_xFe_{12}O_{19}$ /PANI (*TP2, TP3, TP6*)

4.8.3 Magnetic analysis

The saturation magnetization (M_s), coercivity (H_c), anisotropy field (H_a), and squareness ratio (M_r /M_s) values are depicted in the table and are derived from the M-H loops and Linear fits of samples *TP2, TP3* and *TP6.*

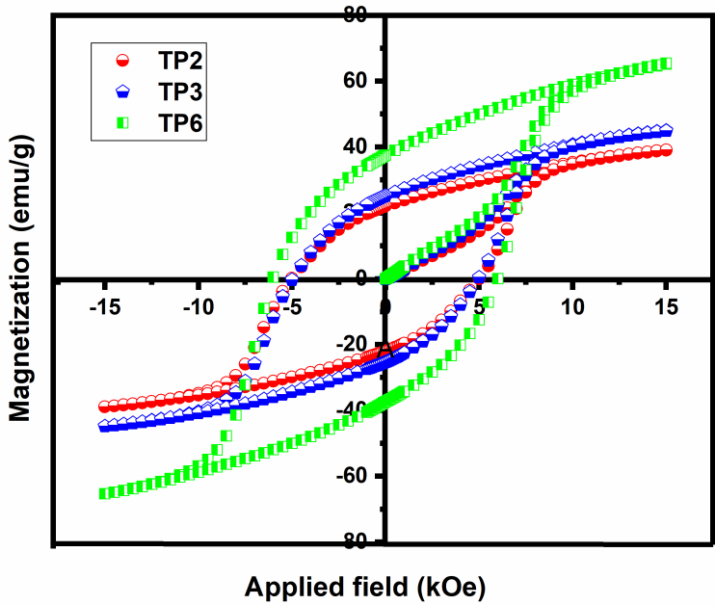

Figure 4.151: **Hysteresis loops of *TP2, TP3 and TP6* Hexaferrite**

It can be deduced that the value of M_s decreases from sample *TP3* to *TP6* as the variation in Ba-Sr doping changes. As from sample *TP3* to *TP6*, the Ba content reduces, and Sr content increases, the only M_s value is seen to have been affected. The values of H_c, H_a, M_r, M_r/M_s have not been affected much by the substitutions.

The observed decrease in M_s value (*TP3* to *TP6*), about 4.56%, might be explained by the replacement of Fe^{3+} at octahedral locations with non-magnetic (Ba^{2+}) and paramagnetic (Sr^{2+}) cations. Magnetization saturation is lowered as a result of a reduction in the magnetic moment and the strength of the superexchange interaction. The table displays an increase in saturation magnetization from *TP2* to *TP6*. This increase in magnetization can be attributed to site occupancy, more Ba-Sr ions towards spin-down sites. This decreases the magnetization at b-sites (M_b) more than a-sites (M_a), Hence M_s is seen to increase.

Table 4.30: Magnetic Parameters M_s, H_c H_a, M_r and M_r/M_s For Ba-Sr /PANI doped Hexaferrite Samples

Sample	M_s	H_c	H_a (kOe)	M_r	M_r/M_s
TP2	37.36	5051.67	16.75	19.01	0.50
TP3	50.72	4964.25	15.79	26.20	0.52
TP6	48.41	4916.78	15.79	25.65	0.53

It could be observed that the squareness ratio for *TP3* as well as for *TP6* is between ($0.5<M_r/M_s$) <1), implying single-domain. *TP3* sample has the higher coercivity values (4964.25 Oe) and is seen decreasing with doping, 4916.78 Oe for *TP6*, but this decrease is only 0.95 %. Since H_a is an extrinsic component, it does not appear to have a significant impact on coercivity and remains unchanged for both samples. The remanence magnetization for *TP3* and *TP6* is also nearly comparable.

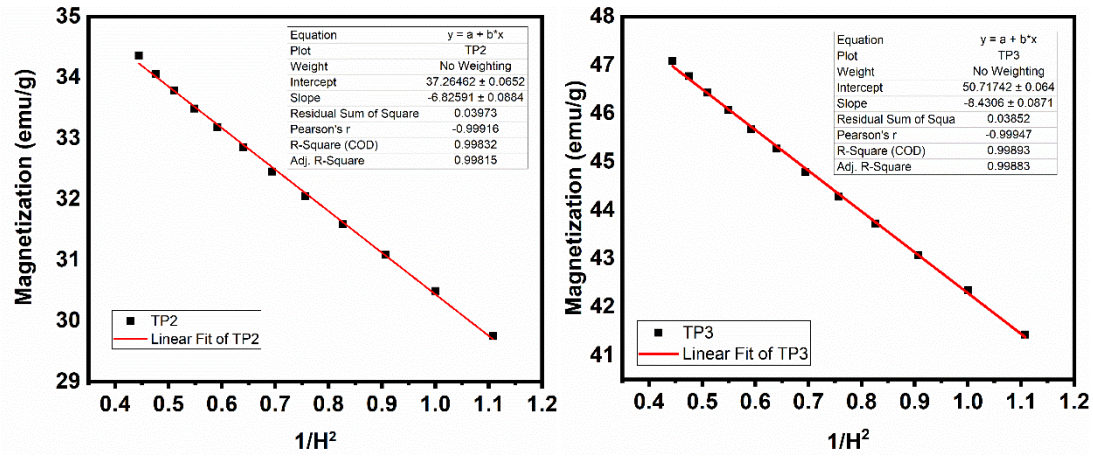

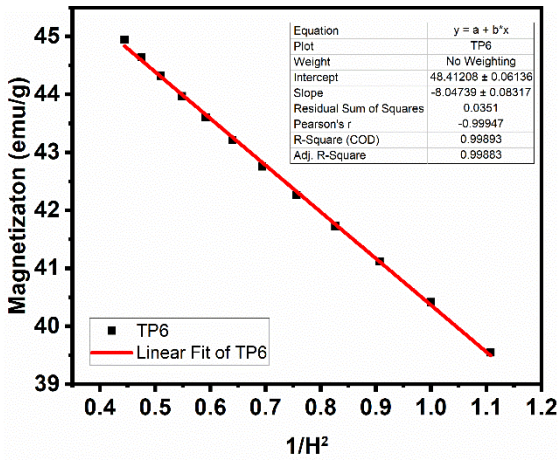

Figure 4.152: M_s Versus 1/ H^2 Plots for *TP2, TP3 and TP6* Hexaferrite Samples

Figure 4.153: SEM Micrographs of Ferrite Samples: Component $Ba_{1-x}Sr_xFe_{12}O_{19}$ /PANI for *TP2, TP3 and TP6* and its Correlation with Magnetic Data

4.8.4 Electromagnetic Characteristics

4.8.4.1 Complex Permeability and Complex Permittivity

RL below -10 dB was not detected in sample TP2, hence, for microwave calculations, sample *TP2* is not taken into consideration. Plots of the dielectric permittivity(ε′) and dielectric loss (ε″) along with plots of the permeability (μ') /magnetic loss (μ") versus frequency are shown in Figure 4.154.

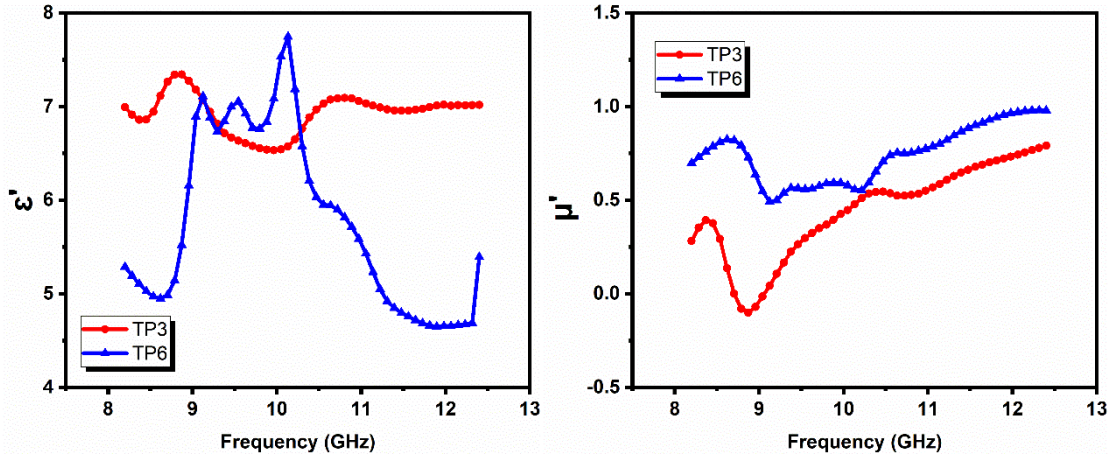

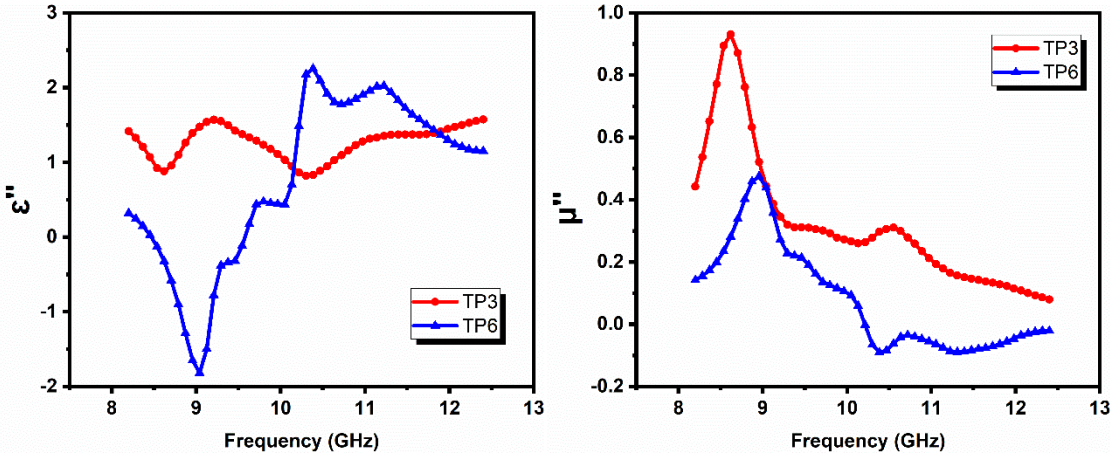

Figure 4.154: Dependence ε′, ε′′, μ′ and μ′′ on Frequency in Ferrite Compositions *TP3* and *TP6*

For *ε′,* much dispersion can be seen for both samples; two relaxation peaks can be seen for sample TP3. With doping changes, *TP6* shows three relaxation peaks reaching the value of around 7.8 but is reduced to 5.2 for higher frequency. In ε″ spectra, multiple relaxation peaks can be seen for both samples. *TP3* possesses a relaxation peak at around 9.2 GHz, followed by a dip at around 10.5 GHz. Sample *TP6* shows a dip at 9 GHz frequency followed by a relaxation peak around 10.5 GHz. The values for *TP3* and *TP6* in the high-frequency region are around 1.5 and 1.1, respectively.

In μ' spectra, samples *TP3* and *TP6* depicting good dispersion, with each having a relaxation peak at the very start, stay in the range of a lower set of values; *TP3* stays around -0.5 to 0.5, and *TP6* stays around 0.2 to 0.8. The μ" spectra also signify good dispersion; there are two relaxation peaks (one strong, the other weak) noted in *TP3* and a relaxation peak followed by two weak dips in *TP6*. The overall spectra above show better dispersion in its values.

In addition to charge accumulation at grain boundaries, the complex permittivity/permeability in the microwave range is dependent on dipole polarisation, electron spin, porosity, grain, and grain size distribution. Electron hopping in $Fe^{2+/}Fe^{3+}$ is the cause of dielectric polarisation in ferrites. The porosity prevents polarisation and acts as a barrier to the field flow. The mechanism of complex permeability is controlled by ferromagnetic resonance and exchange resonance between $Fe^{2+/}Fe^{3+}$ ions. Noticeable nonmagnetic voids in the compositions depicted in the micrographs (Figure 4.144) for samples *TP3* and *TP6* seem to produce demagnetizing fields, which change the magnetization and polarisation associated with complex permeability and permittivity. Thus, much variation in complex permeability and permittivity can be seen in both samples.

4.8.4.2 Microwave absorption in $Ba_{1-x}Sr_xFe_{12}O_{19}$ /PANI

One way to assess a material's capacity for microwave absorption is to look at its reflection loss. Equations 3.16 and 3.17 are employed to ascertain the compositions' RL. This section will look at how various elements impact the material's ability to absorb microwaves. These factors include material thickness (λ/4), impedance matching, and the extent of reflection loss.

4.8.4.3 Quarter Wavelength Mechanism

The graphs of RL dependent on the frequency at different simulated thicknesses can be utilized to investigate the phenomenon of microwave absorption. Figures 4.155 (a), (b) to 4.161 (a) shows RL plots of the ferrite compositions $Ba_{1-x}Sr_xFe_{12}O_{19}$ /PANI for (x = 0.4 *TP3* and x = 1 *TP6*) for RL ≥ -10 dB. The parameters, such as matching frequency/thickness, bandwidth, and frequency range, can be inferred from Figures 4.155 (a), (b) to 4.161 (a), which is summarised in Table 4.31.

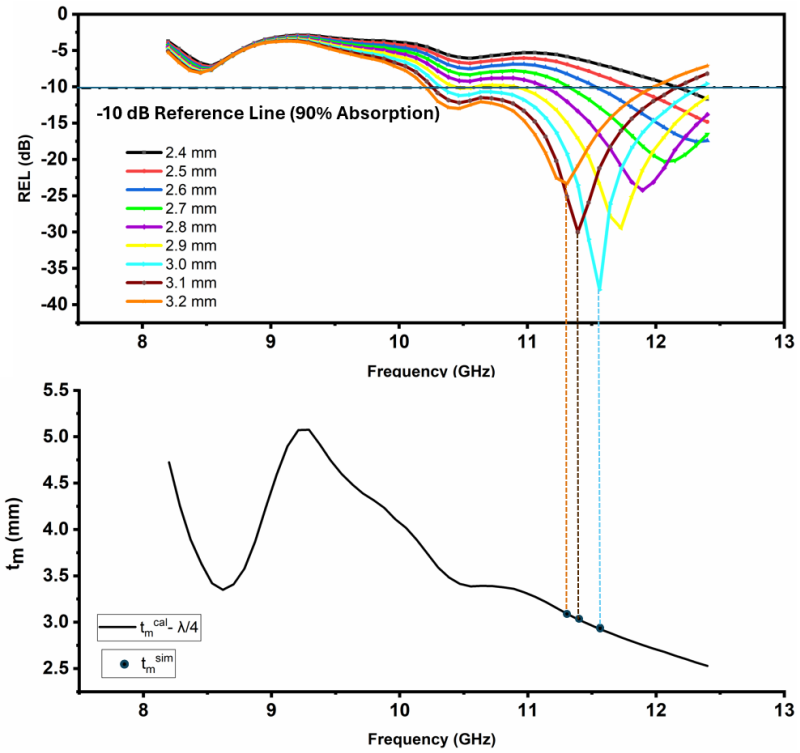

Figure 4.155: (a) Dependence of RL on Frequency in *TP3* Composition and (b) t^{sim} and t^{cal} Versus Frequency for λ/4 in *TP3* Composition

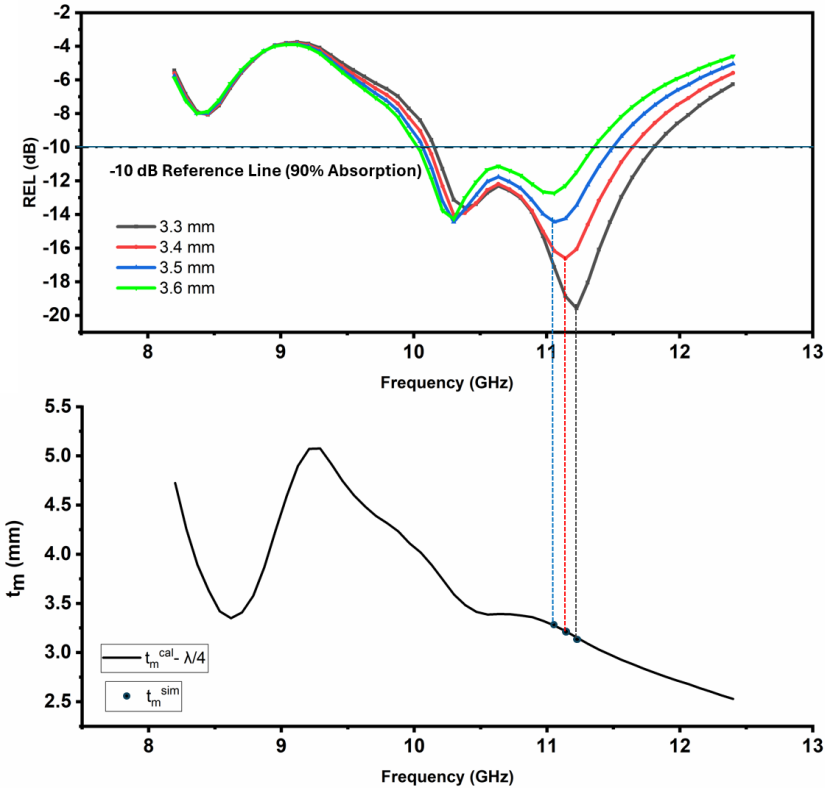

Figure 4.156: (a) Dependence of RL on Frequency in *TP3* Composition and (b) t^{sim} and t^{cal} Versus Frequency for λ/4 in *TP3* Composition

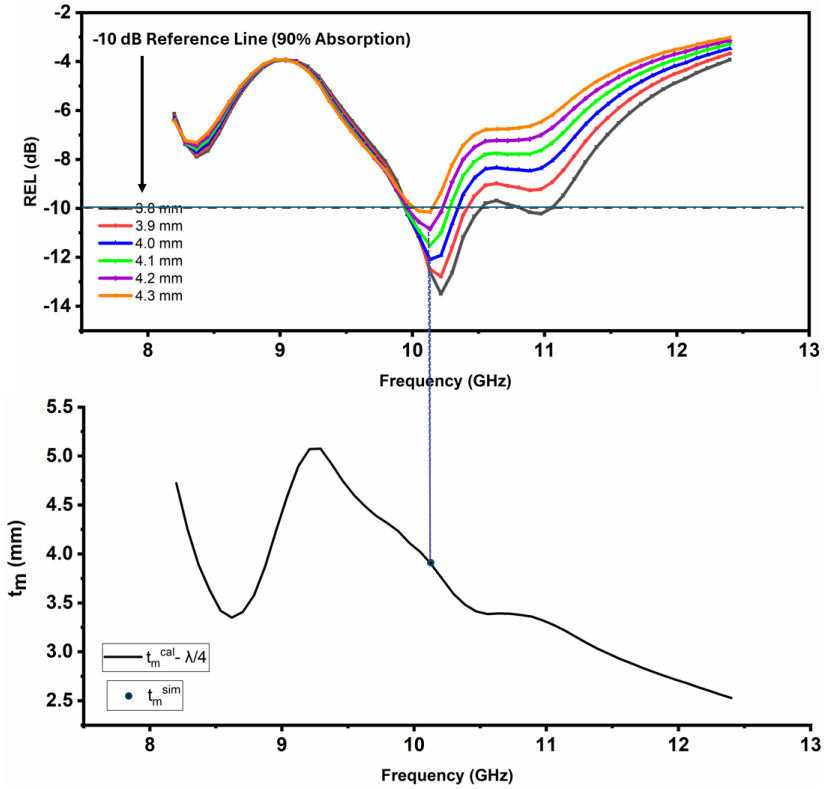

Figure 4.157: (a) Dependence of RL on Frequency in *TP3* Composition and (b) t^{sim} and t^{cal} Versus Frequency for λ/4 in *TP3* Composition

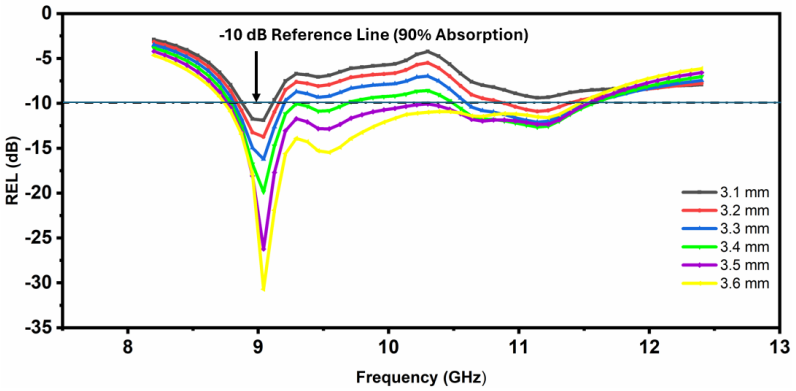

Figure 4.158: (a) Dependence of RL on Frequency in *TP6* Composition

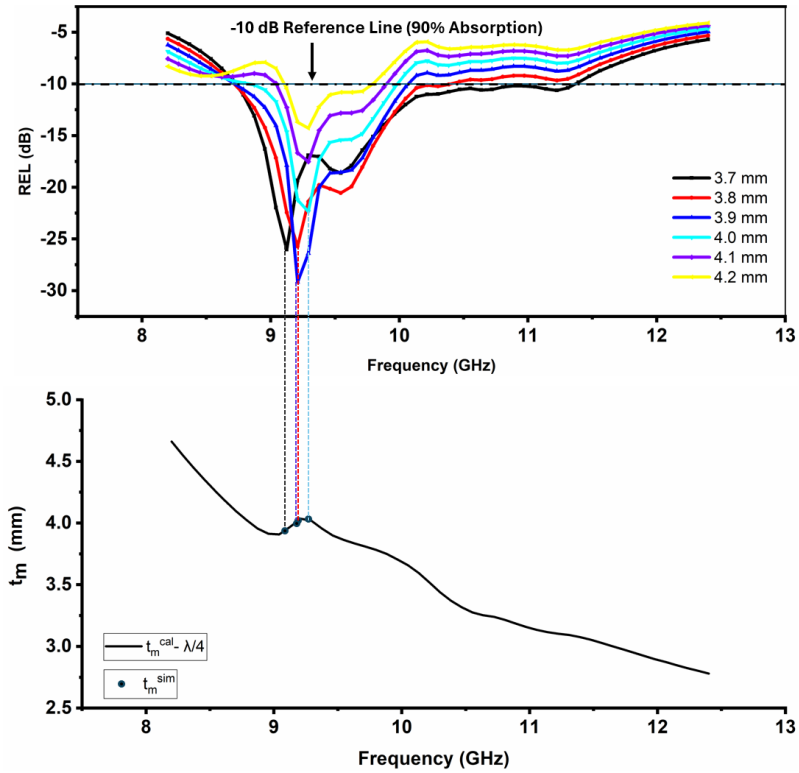

Figure 4.159: (a) Dependence of RL on Frequency in *TP6* Composition and (b) t^{sim} and t^{cal} Versus Frequency for λ/4 in *TP6* Composition

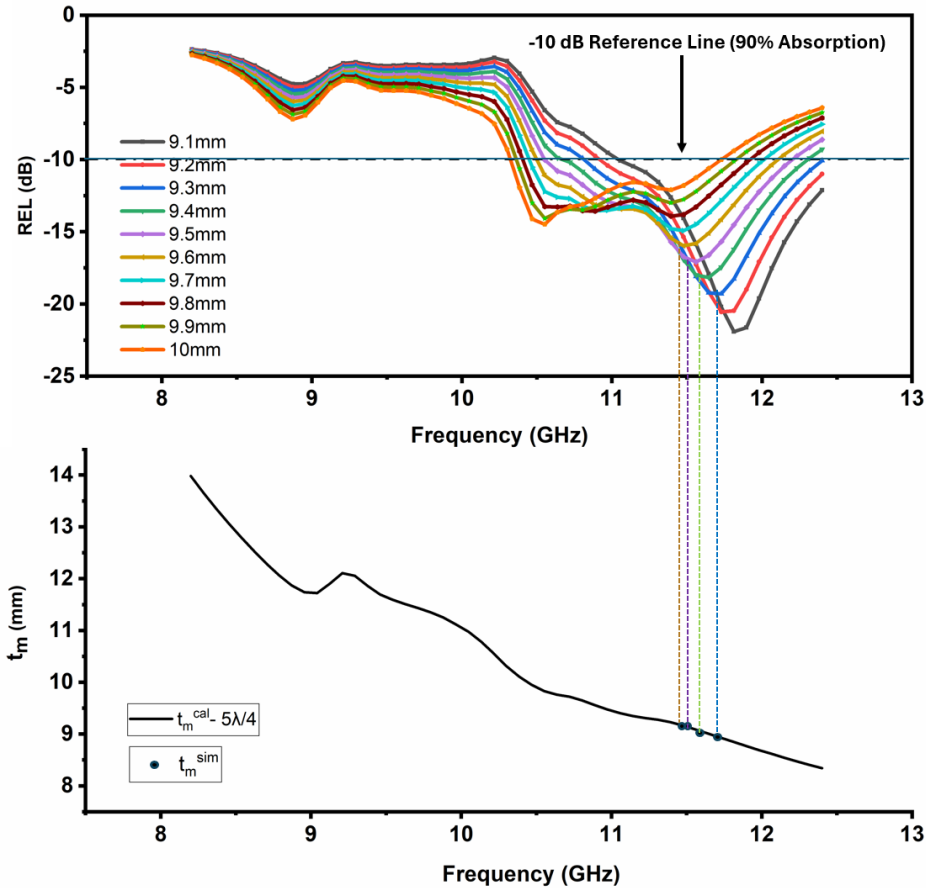

Figure 4.160: (a) Dependence of RL on Frequency in *TP6* Composition and (b) t^{sim} and t^{cal} Versus Frequency for 5λ/4 in *TP6* Composition

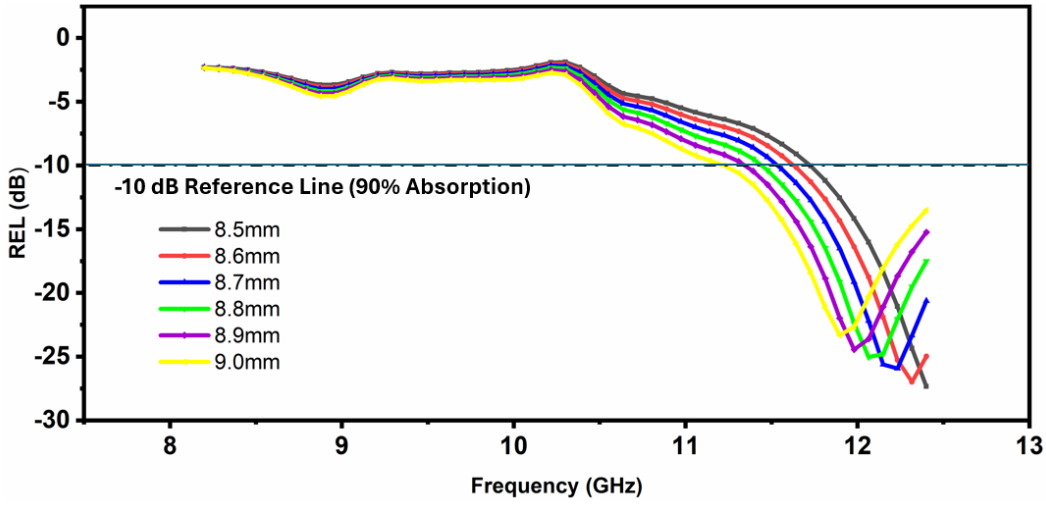

Figure 4.161: (a) Dependence of RL on Frequency in *TP6* Composition

The highest RL dip of -30.70 dB is observed in *TP6* composition at 9.04 GHz frequency and 3.6 mm thickness. According to Table 4.31, the remaining composition *TP3* has RL values between - 12.58 to -30.01 dB for 2.5 to 4.0 mm thickness. All the plots (except Figures 4.158 and 4.159) illustrate how RL peaks shift toward the low-frequency spectra as thickness

increases are depicted. This aligns with the quarter wavelength mechanism which states that the relationship between frequency and thickness is inversely proportional. The RL peaks are observed in *TP3* [Figure 4.155(a), (b), 4.156 (a), (b), Figure 4.157 (a), (b)], in the frequency band ranging from 11.31 to 12.40 GHz, 10.30 to 11.22 GHz and 10.13 to 10.30 GHz at thicknesses from 2.4 to 3.2 mm, 3.3 to 3.6 mm, and 3.8 to 4.3 mm, respectively. The RL peaks are observed in *TP6* [Figure 4.158(a), (b), Figure 4.159 (a) (b), Figure 4.160 (a), Figure 4.161 (a)], in the frequency band ranging from 8.96 to 9.04 GHz, 9.04 to 9.29 GHz, 11.90 to 12.40 GHz and 10.55 to 11.81 GHz at thicknesses from 3.1 to 3.6 mm, 3.7 to 4.2 mm, 8.5 to 9.0 mm and 9.1 to 10.0 mm, respectively.

Equation 3.18 states that the simulated thickness (t_m^{sim}) is employed to compute RL, and n = 1,3,5,..., etc. is used to obtain the calculated thickness (t_m^{cal}) from (6). To determine the link between RL peaks and the quarter wavelength mechanism, both parameters are investigated. Plots of the calculated thickness (nλ/4) in the frequency regime are displayed in Figures 4.155 (a)(b) to 31 (a)(b). By stretching a vertical line from RL peaks towards thickness–frequency graphs, the computed thickness (nλ/4) and the simulated thickness (t_m^{sim}) are compared. It follows from the plots that the λ/4 mechanism is satisfied in compositions with calculated thicknesses of λ/4 and n = 1 for *TP3*, whereas *TP6* composition is due to both λ/4 and 5λ/4 values. In Table 4.31, a -10 dB broad bandwidth of 2.10 GHz for composition *TP3* and 2.69 GHz for *TP6* is reported. This is the broadest AB detected within all the synthesized samples among all the series investigated. Also, it can be noted that with the PANI as a matrix, the RL values have considerably increased than that of the sample without PANI (*T2*, *T3*, and *T6*).

Figure 4.162 depicts Three-dimensional (3D) plots of reflection loss at various frequencies and thicknesses for *TP3* and *TP6* samples. The blue-violet portion in the graphs shows the RL peak area and its covered thickness and frequency range. These values can be cross-verified from the Table 4.31.

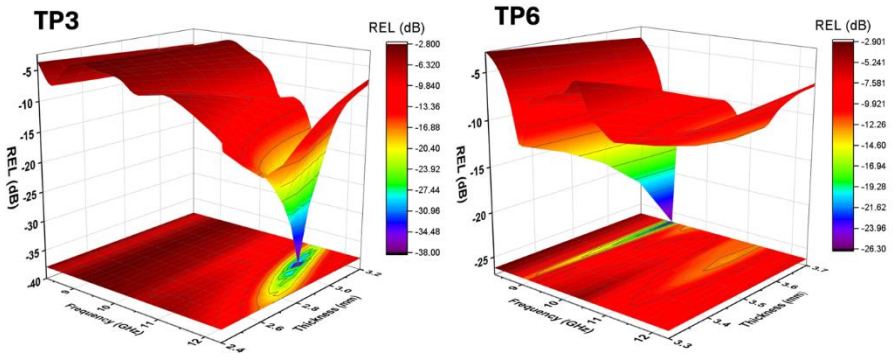

Figure 4.162: Three-Dimensional (3D) Plots of Reflection loss at Various Frequencies and thicknesses for *TP3* and *TP6* Samples

Table 4.31: Computed Parameters for Microwave Absorption (RL More Than -10)

Ba-Sr Content	Matching Thickness (mm)	Matching Frequency (GHz)	Maximum RL (dB)	Frequency Band for RL > -10 dB (GHz)	Bandwidth for RL > -10 dB (GHz)	BWT	PBW
TP3	2.5	12.40	-14.83	11.81-12.40	0.59	0.24	4.76
	2.6	12.32	-17.54	11.56-12.40	0.84	0.32	6.82
	2.7	12.06	-20.26	11.39-12.40	1.01	0.37	8.37
	2.8	11.90	-24.23	11.14012.40	1.26	0.45	10.59
	2.9	11.73	-29.47	10.46-10.55, 10.92-12.40	0.09, 1.48	0.03, 0.51	0.26, 4.34
	3.0	11.56	-37.96	10.38-12.40	2.02	0.67	17.47
	3.1	11.39	-30.01	10.30-12.40	2.10	0.68	18.43
	3.2	11.31	-23.33	10.21-11.98	1.77	0.55	15.65
	3.3	11.22	-19.58	10.21-11.72	1.51	0.46	13.45
	3.4	11.06	-16.16	10.13-11.56	1.43	0.42	12.93
	3.5	11.06	-14.45	10.13-11.47	1.34	0.38	12.12
	3.6	10.30	-13.73	10.04-11.30	1.26	0.35	12.23
	3.7	10.30	-13.58	10.04-11.14	1.10	0.30	10.68
	3.8	10.22	-13.49	10.04-10.46	0.42	0.11	4.11
	3.9	10.22	-12.79	9.96-10.38	0.42	0.11	4.11
	4.0	10.13	-12.09	9.96-10.38	0.42	0.11	4.15
TP6	3.1	9.04	-11.89	8.95-9.04	0.09	0.03	1.00
	3.2	8.96	-13.23	8.87-9.12	0.25	0.08	2.79
	3.3	9.04	-16.21	8.87-9.12, 10.63-11.56	0.25,0.93	0.07, 0.28	2.76, 10.28
	3.4	9.04	-19.86	8.87-9.62, 10.55-11.56,	0.25, 1.01	0.08, 0.29	2.76, 11.17
	3.5	9.04	-26.23	8.78-11.47	2.69	0.77	29.76
	3.6	9.04	-30.70	8.78-11.39	2.61	0.73	28.87
	3.7	9.04	-21.97	8.78-11.30	2.52	0.68	27.88
	3.8	9.21	-25.72	8.78-10.38	1.60	0.42	17.38
	3.9	9.21	-29.17	8.78-10.04	1.26	0.32	13.68
	4.0	9.21	-21.24	9.12-9.88	0.76	0.19	8.25
	4.1	9.29	-17.53	9.12-9.71	0.59	0.14	6.35
	4.2	9.29	-8.70	12.14-12.40	0.26	0.06	2.80
	8.0	12.40	-11.85	12.23-12-40	0.17	0.02	1.37
	8.1	12.40	-13.63	12.14-12.40	0.26	0.03	2.10
	8.2	12.40	-15.88	12.06-12.40	0.34	0.04	2.74
	8.3	12.40	-7.45	12.06-12.40	0.34	0.04	2.74
	8.4	12.40	-22.98	11.89-12.40	0.51	0.06	4.11
	8.5	12.40	-27.35	11.72-12.40	0.68	0.08	5.48
	8.6	12.32	-26.98	11.64-12.40	0.76	0.09	6.17
	8.7	12.23	-25.92	11.56-12.40	0.84	0.10	6.87
	8.8	12.06	-25.03	11.56-12.40	0.84	0.10	6.96

8.9	11.98	-8.39	11.47-12.40	0.93	0.10	7.76
9.0	11.90	-23.32	11.39-12.40	1.01	0.11	8.49
9.1	11.81	-21.91	10.55-12.06	1.51	0.17	12.78
9.2	11.81	-8.94	11.22-12.40	1.18	0.13	9.99
9.3	11.73	-19.30	10.88-12.40	1.52	0.16	12.96
9.4	11.64	-18.16	10.72-12.23	1.51	0.16	12.97
9.5	11.56	-17.08	10.55-12.14	1.59	0.17	13.75
9.6	11.48	-15.97	10.55-12.06	1.51	0.16	13.16
9.7	11.48	-14.92	10.46-11.98	1.52	0.16	13.25
9.8	11.39	-13.91	10.46-11.89	1.43	0.15	12.55
9.9	10.55	-14.07	10.38-11.81	1.43	0.14	13.55
10.0	10.55	-14.48	10.38-11.72	1.34	0.13	12.70

4.8.4.4 Impedance matching mechanism

The characteristic impedance of free space $Z_o = (\mu/\varepsilon)^{1/2} = 377\ \Omega$, where μ/ε is the space's permeability/permittivity and Z_{in} is the absorber's impedance. Absorbers have various impedances from free space due to differences in their permittivity/permeability characteristics. Depending on the impedance inequality between Z_{in} and Z_o, a portion of a microwave signal traveling through free space will be reflected from an absorber; the larger the difference, the higher the reflection. Only a small portion of the microwave signal passes through the absorber because of the significant difference between Z_{in} and Z_o, leaving the majority of the reflected signal behind. Because most of the signal is reflected, attenuation or absorption of the signal inside the absorber is minimal or meaningless, even if the absorber has maximal dielectric and magnetic loss. Thus, when designing the absorber, it is important to take the impedance matching of the absorber with free space into account.

The RL and impedance graphs (i.e., Z_{in}) with frequency regime for all compositions are displayed individually in Figures 4.162 and 4.163. In different compositions, impedance-matching conditions may arise in the form of RL peaks with $Z_{in} \sim Z_o$ (377 Ω) at specific frequencies that correspond to different matching thicknesses. Z_{in} values for compositions are listed in Table 4.32 and are derived from Z_{in} plots in the aforementioned figures.

For *TP3* composition, for thicknesses 2.5 to 2.9 mm, the Z_{in} lies in the range 402.75 to 497.67 Ω, and from thicknesses 3.3 to 4.0, it lies between 228.51 to 313.25 Ω, which seems to drift away from the value 377 Ω. But in the same composition for a thickness of 3.0 mm, the highest RL peak is detected where the Z_{in} = 379.24 Ω, which is nearly equal to 377 Ω.There seems to be a problem with a thickness of 3.1 mm, where a higher RL of -30.70 dB is noted, but Z_{in} = 354.74 Ω that again drifts away from the value of 377 Ω.In composition *TP6,* RL peak is noted at *the* thickness of 3.6 mm, where Z_{in} = 399.17 Ω, which is in the proximity of 377 Ω. However, there is a problem with the thickness of 3.5 mm where RL is -26.23 dB, though the Z_{in} =

380.01 Ω, which is nearer to 377 Ω than 399.17 Ω for 3.6 mm thickness, for which RL is -30.70 dB.

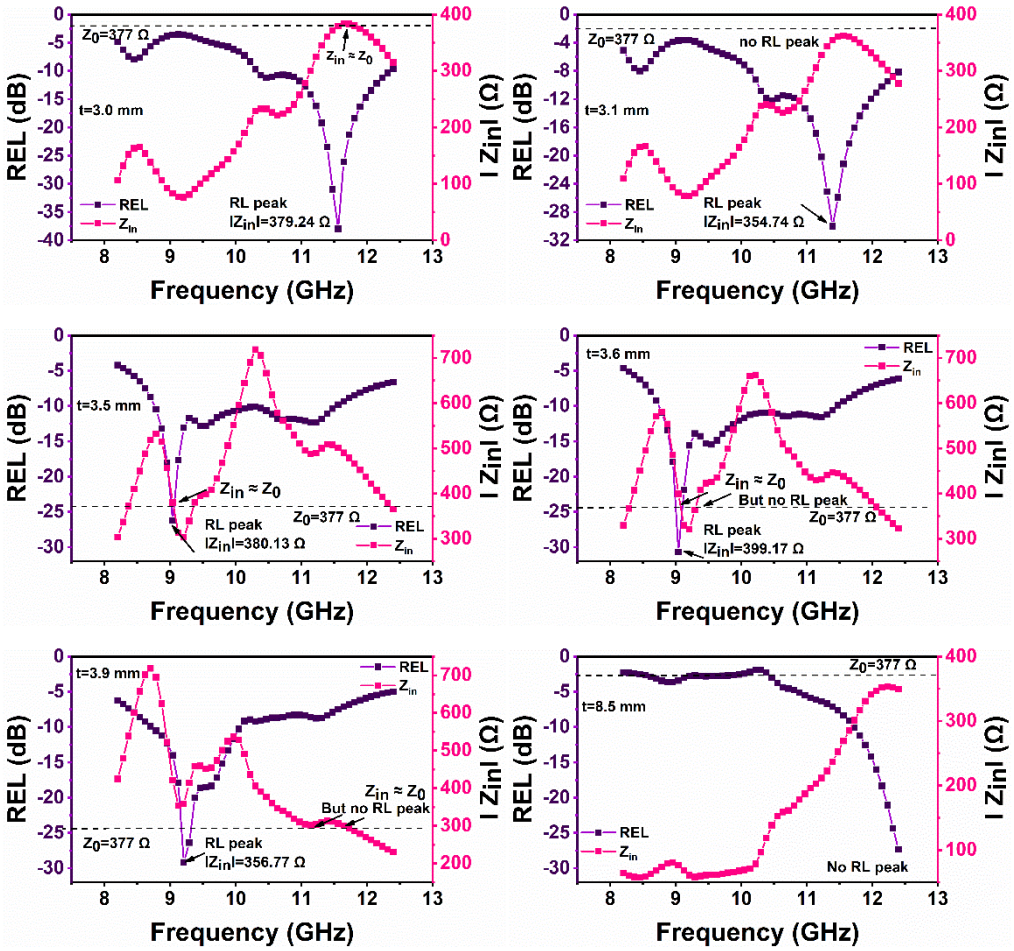

Figure 4.163: Dependence of RL and Z_{in} on Frequency in *TP3, TP6* Composition

It is explained by the fact that $|Z_{in}|$ (in equation 3.17) is a complex expression that uses both real and imaginary terms, such as Z_{real} and Z_{img}. As a result, Z_{real} and Z_{img} are computed using equation 3.17 and the resulting graphs are displayed in the frequency and thickness domains for *TP3* and *TP6* composition (Figure 4.163). Likewise, Z_{real} and Z_{img} values for RL_{max} are calculated from plots and displayed in Table 4.32. It is evident from Table III that the maximum RL value in accordance with Z_{real} = 377 Ω and/or Z_{img} = 0 is observed in both the compositions *TP3* and *TP6. TP3* has a maximum RL of -37.96 dB and a thickness of 3.0 mm, where Z_{real} = 379.24 Ω and Z_{img} = -9.33 in accordance with Z_{real} = 377 Ω and/or Z_{img} = 0. Similarly, *TP6* has a maximum RL of -30.70 dB and a thickness of 3.5 mm, where Z_{real} = 399.24 Ω and Z_{img} = -4.74 in accordance with Z_{real} = 377 and/or Z_{img} = 0. Since the value drifts more in sample TP6, the RL is also less compared to TP3 composition. Hence, it can be concluded that the quarter wavelength mechanism is satisfied in both compositions along with the impedance matching mechanism.

Table 4.32: Impedance Parameters of RL Peaks at Different thickness

Ba-Sr Content	Matching Thickness (mm)	Matching Frequency	Maximum RL (dB)	Z_{real} (Ω)	Z_{img} (Ω)	Z_{in} (Ω)
TP3	2.5	12.40	-14.83	497.67	104.65	508.56
	2.6	12.32	-17.54	488.61	27.32	489.38
	2.7	12.06	-20.26	449.38	34.63	450.71
	2.8	11.90	-24.23	425.63	8.23	425.71
	2.9	11.73	-29.47	402.75	-4.91	402.78
	3.0	11.56	-37.96	379.13	-9.33	379.24
	3.1	11.39	-30.01	354.69	-6.09	354.74
	3.2	11.31	-23.33	334.46	-23.32	335.27
	3.3	11.22	-19.58	313.25	-34.56	315.15
	3.4	11.06	-16.16	277.91	-23.96	278.94
	3.5	11.06	-14.45	265.13	-48.72	269.56
	3.6	10.30	-13.73	208.38	94.92	228.98
	3.7	10.30	-13.58	249.92	-33.88	252.21
	3.8	10.22	-13.49	246.77	-21.57	247.71
	3.9	10.22	-12.79	240.45	-38.80	243.56
	4.0	10.13	-12.09	228.51	-26.00	229.99
TP6	3.1	9.04	-11.89	262.51	119.56	288.46
	3.2	8.96	-13.23	330.90	150.92	363.69
	3.3	9.04	-16.21	321.14	93.57	334.49
	3.4	9.04	-19.86	351.04	69.67	357.89
	3.5	9.04	-26.23	378.22	36.91	380.01
	3.6	9.04	-30.70	399.14	-4.74	399.17
	3.7	9.04	-21.97	409.99	-53.48	413.46
	3.8	9.21	-25.72	349.23	25.38	350.15
	3.9	9.21	-29.17	357.40	-16.40	357.78
	4.0	9.21	-21.24	354.52	-59.57	359.49
	4.1	9.29	-17.53	396.06	-101.89	408.96
	4.2	9.29	-8.70	228.85	178.66	290.33
	8.0	12.40	-11.85	294.90	156.07	333.65
	8.1	12.40	-13.63	317.84	135.07	345.35
	8.2	12.40	-15.88	336.13	108.53	353.22
	8.3	12.40	-7.45	346.12	-336.99	483.08
	8.4	12.40	-22.98	352.33	45.64	355.28
	8.5	12.40	-27.35	349.15	14.02	349.43
	8.6	12.32	-26.98	345.04	4.95	345.07
	8.7	12.23	-25.92	340.77	-2.09	340.78
	8.8	12.06	-25.03	340.30	16.47	340.70
	8.9	11.98	-8.39	480.06	-334.90	585.33
	9.0	11.90	-23.32	330.31	12.35	330.54
	9.1	11.81	-21.91	322.27	12.40	322.51

9.2	11.81	-8.94	546.31	-303.16	624.78
9.3	11.73	-19.30	303.68	-8.39	303.79
9.4	11.64	-18.16	294.28	-6.90	294.36
9.5	11.56	-17.08	284.58	-5.17	284.62
9.6	11.48	-15.97	273.53	-2.88	273.55
9.7	11.48	-14.92	263.22	-16.53	263.74
9.8	11.39	-13.91	251.09	-13.30	251.45
9.9	10.55	-14.07	261.06	50.91	265.98
10.0	10.55	-14.48	260.62	31.17	262.48

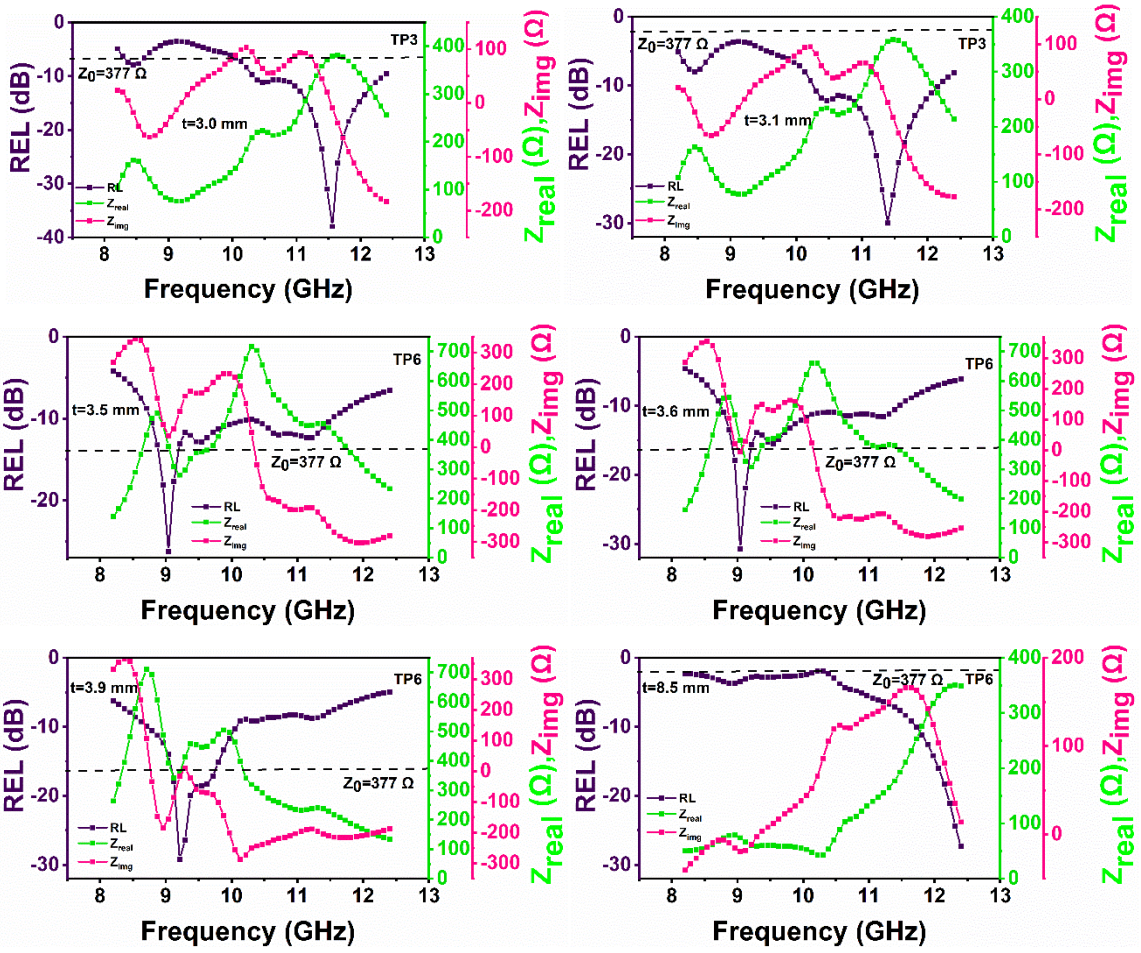

Figure 4.164: Dependence of RL, Z_{in}, Z_{real}, and Z_{img} on Frequency in *TP3, TP6* Composition

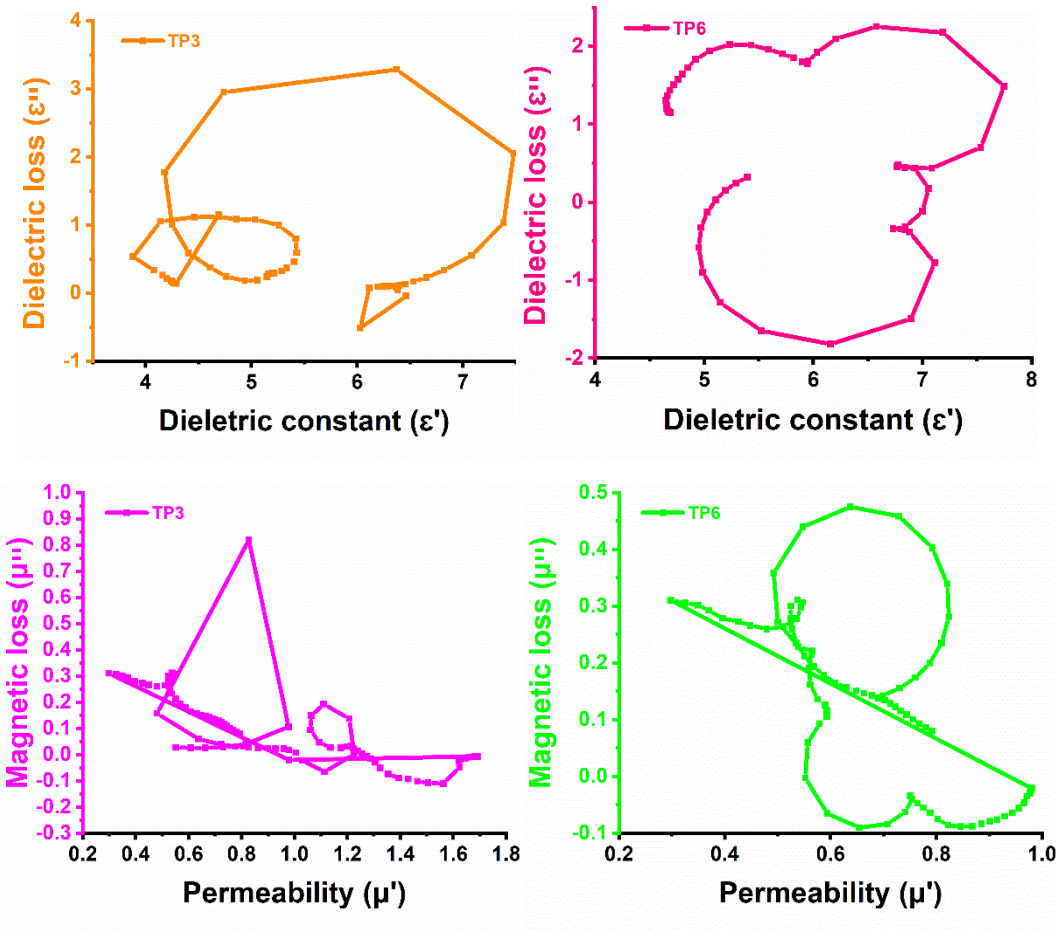

Figure 4.165: Cole–Cole Plots in *TP3* and *TP6* Compositions

Figure 4.164 shows Cole–Cole plots to verify relaxation for compositions *TP3* and *TP6*. But no prominent effect of the Cole-Cole plot is seen concerning the RL peaks here. Though multiple relaxations and inverted semicircles are shown in ε′ vs. ε″ plots and in μ′ vs. μ″ plots, the relaxation process may be dominated by impedance matching and quarter wavelength mechanism.

4.8.4.5. Eddy Current Loss

The role of the eddy current loss in the magnetic loss contribution is also discussed in section 4.1.4.5. For the given test frequency, the value of C_0 remains constant for *TP6* composition but not for the frequency range 8 to 9.7 GHz in *TP3*. So, it can be concluded here that the eddy current loss contributes to the microwave absorption in *TP6* composition but does not contribute much to the microwave absorption in *TP3* (for 8 to 9.7 GHz but contributes from 9.7 to 12.4 GHz)

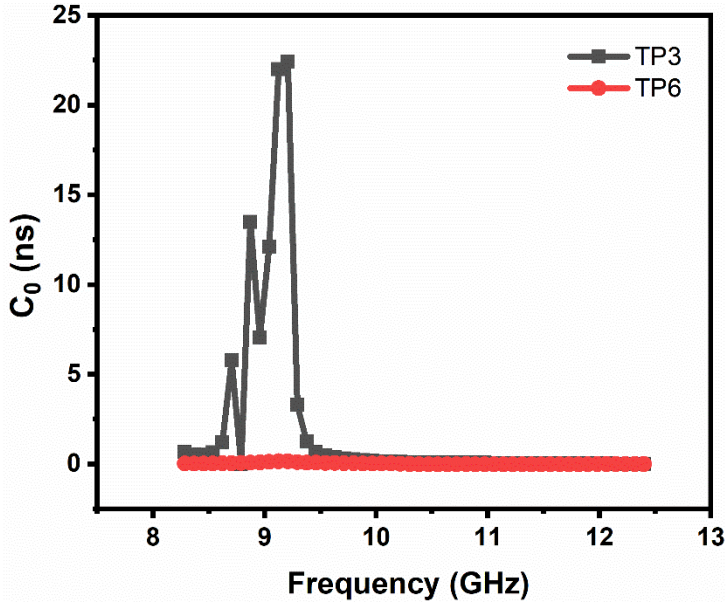

Figure 4.166: C_0 Versus Frequency Variation for Compositions TP3 and TP6

4.8.4.6 BWT/Percentage Bandwidth Ratio

The relations used to estimate the bandwidth-to-thickness ratio (BWT) and percentage bandwidth (PBW) in ferrite samples are already discussed in section 3.8. Figure 4.166 shows Bandwidth (%) variation with thickness in ferrite *TP3* and *TP6* compositions. Table 4.31 depicts BWT for maximum RL with frequency, *TP6* shows greater BWT values than *TP3*. This shows that by reducing Ba content to zero and using only Sr content, the BWT has increased. It has the highest value of 0.77 at 3.5 mm thickness, matching frequency of 9.04 GHz, RL = -26.23 dB with the broader AB of 2.69 GHz.

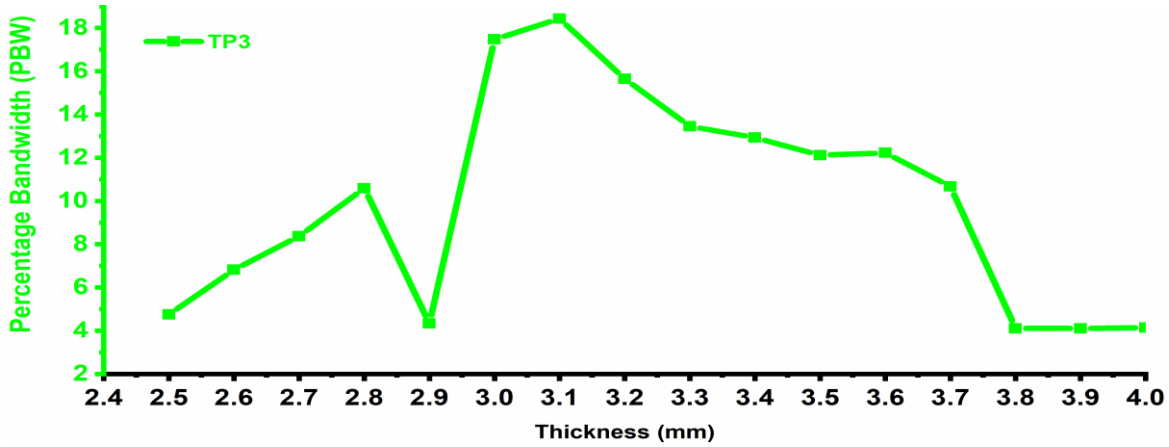

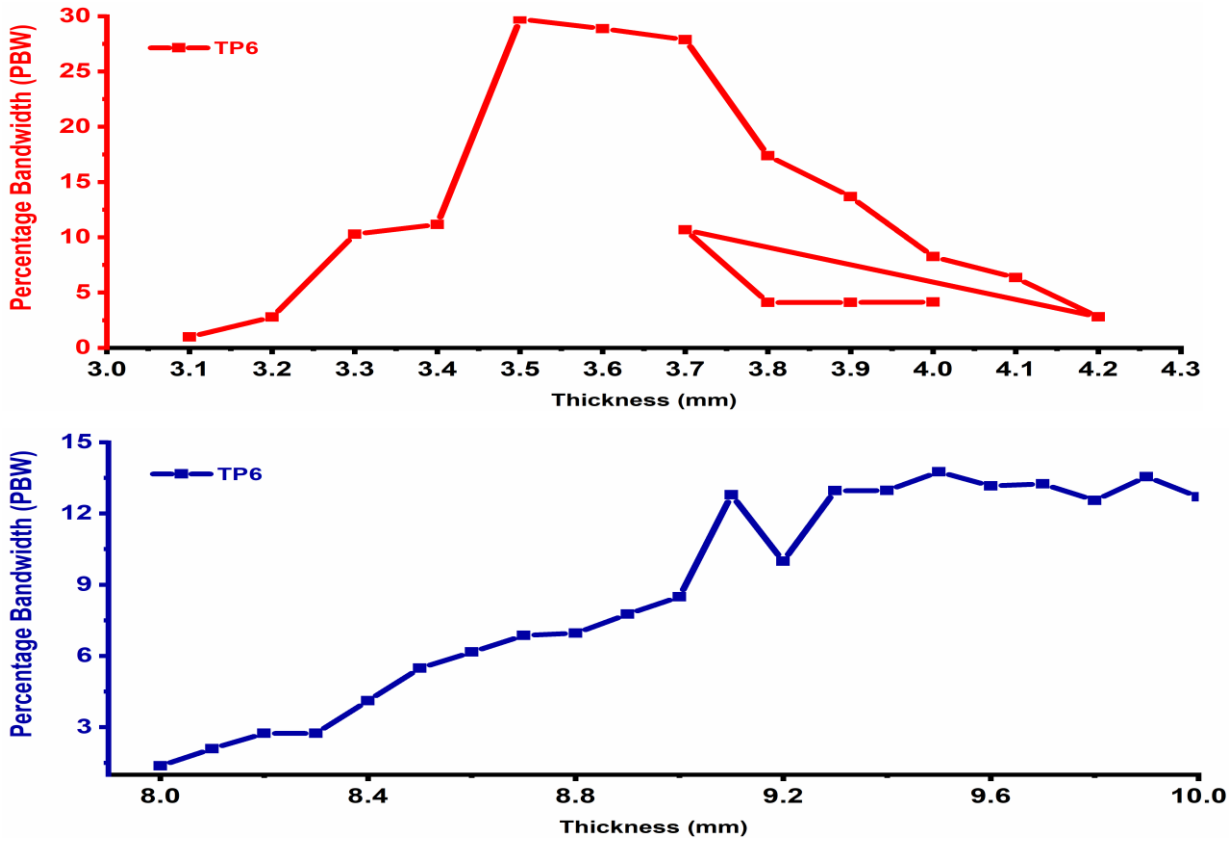

Figure 4.167: Bandwidth (%) Variation with thickness in Ferrite *TP3* and *TP6* Composite

Summary:

(i) $Ba_{0.2}Sr_{0.8}Co_xMg_xFe_{12-2x}O_{19}$ (x = 0.0, 0.2, 0.4, 0.6, 0.8,1.0)

(ii) $Ba_{0.2}Sr_{0.8}Co_xCu_xFe_{12-2x}O_{19}$ (x = 0.0, 0.2, 0.4, 0.6, 0.8,1.0)

(iii) $Ba_{0.2}Sr_{0.8}Co_xAl_xFe_{12-2x}O_{19}$ (x = 0.0, 0.4, 0.8, 1.2, 1.6, 2.0)

(iv) $Ba_{1-x}Sr_xFe_{12}O_{19}$ (x = 0.0, 0.2, 0.4, 0.6, 0.8,1.0)

The research investigates the properties of above-mentioned hexaferrites and their composites with polyaniline (PANI) for microwave absorption applications. Structural analysis, including X-ray diffraction and Field Emission Scanning Electron Microscopy (FESEM), was conducted to determine the crystalline phases and morphology. Electrical properties such as dielectric permittivity, electric modulus, complex impedance, and AC conductivity were analyzed. Magnetic properties were evaluated using hysteresis loops and permeability measurements. The study also explored the electromagnetic characteristics, including complex permeability and permittivity, to understand the microwave absorption mechanisms. Two key absorption mechanisms, quarter wavelength, and impedance matching, were investigated. Additionally, the effect of doping on eddy current loss and the bandwidth-to-thickness ratio (BWT) was analyzed. The study also focused on the enhancement of microwave absorption in the composite ferrites, with results indicating improved absorption properties due to the

incorporation of PANI, suggesting potential for lightweight and efficient microwave absorption in various applications.

CHAPTER 5

CONCLUSION AND FUTURE SCOPE

In the M-series, the Crystallite Size does not change much with the substitutions, in fact, the size almost remains the same. Sem analysis depicts oval-shaped grains turning rice-like with doping. Due to the electrostatic and magnetic interactions between ferrite particles, doping results in grain clusters with an uneven size distribution. The undoped sample here shows reaches 400 values in low-frequency spectra but as doping is intruded this value drops to 80-20 for the dielectric permittivity. Similarly, the dielectric loss value also seems to reduce. It is also observed from the graph that the plots tend to saturate at a certain point for all the samples, with the lowest for the pure/undoped *M1* sample at around 0.015 and the maximum for *M4* and *M5* at around 0.19. For *M″*, as the doping content increases, the peaks of each sample reach their highest point; a peak of *M5* owes the highest value. Also, a shift of peaks towards the high-frequency region can be observed as the doping percentage is changed. The AC conductivity starts to slowly rise as the applied AC field frequency surpasses 1 kHz. It behaves in a nearly frequency-independent manner below 1 kHz, and at this frequency, DC conductivity transforms into AC conductivity. The magnetic analysis shows that M5 samples possess the highest M_s whereas the coercivity is reduced with doping, as the substitution rises, H_c is reduced. The highest RL Noted for this is for sample *M6* which is around -43.75 dB at 8.9 mm thickness. For M-series with PANI, sample *MP5* shows the highest RL.

In C-series, the samples' c/a ratio matches the standard value of 3.93, and the crystallite size stays within 73.13-52.24 nm. FESEM depicts that though the observation of grain aggregation is there, it is easy to detect individual grains too in doped samples, unlike pure samples. The value of loss tangent for all doping samples at higher frequencies comes together to stay around 0.0-0.08. Magnetic analysis shows that the sample possesses the highest M_s value but as the Cu content is increased the coercivity is reduced. For C-series/PANI samples, there is no peculiar change in the magnetic behavior of the samples. There was no absorption found for *CP1,* i.e. $Ba_{0.2}Sr_{0.8}CoCuFe_{12}O_{19}$/PANI composite sample. The highest RL dip of -20.12 dB is observed in *CP3* composition at 10.88 GHz frequency and 10 mm thickness. For *CP3* composition RL peaks shift towards the low-frequency spectra from the high-frequency spectra as thickness is increased. This is in line with the quarter wavelength mechanism, which states that the relationship between frequency and thickness is inversely proportional.

In A-series, the XRD investigation of the samples depicts the existence of the primary phase as M-type (hexagonal) along with minor traces of the secondary spinel phase ($BaFe_2O_4$) and magnetite. The crystallite size remains in the narrow range of 15.3604-17.7419 nm. FESEM

investigation depicts as the doping increases from *A1* to *A6*, needle-shaped along with hexagonal-shaped platelets are noticed. The small size of individual grains is seen in the gain clusters; thus, grain size is inhibited with the doping at high doping levels. It is observed that the value ε' decreases non-monotonically with an increase in doping of Co^{2+} and Al^{3+}, the lowest being for *A6* and the highest being for *A1*. Similar behavior is observed for ε'' and *tan* δ. The Cole-Cole plot (M' vs M'') shows that doping of Co-Al shifts the arc towards a low-frequency regime; the intercept of the semicircular arc increases with doping. In the magnetic investigation, it is seen that sample *A6* with high Al content shows the highest M_s as 95.35 but coercivity is decreased with doping highest being for *A1* and lowest for *A6*. In microwave analysis, it is seen that *A4* composition exhibits the largest RL peak of -30.99 dB at 1.48 GHz frequency and 3 mm thickness.

In the T-series, XRD analysis shows that there is a significant change in lattice parameters observed in samples *T3* and *T5*. FESEM investigation reveals, that as the doping is increased, the particles do not seem to change in size, but more voids are seen. Though the particles do not change much in shape and size after doping but can be seen fusing more and more with doping. The value ε' shows dispersion with a fall in frequency in the low-frequency spectra. The Dielectric permittivity/loss reaches a steady state value after a certain frequency: the electron hopping accompanied by the electron exchange with +2 and +3 states is not able to follow it. The change in maxima of the semi-circle for the maximum frequency with doping illustrates the distribution of relaxation time. This distribution backs up the non-Debye type of relaxation in electric modulus spectra. The highest RL dip of -29.60 dB is observed in *T6* composition at 9.80 GHz frequency and 3.5 mm thickness. The other two compositions have RL values between -14.81 to -27.15 dB, 8.4 to 8.9 mm thickness (*T2)*, and -11.50 to 15.71 dB, 7.2 to 8.1 mm thickness (*T3*). In the T-series/PANI composition. The highest RL dip of -30.70 dB is observed in *TP6* composition at 9.04 GHz frequency and 3.6 mm thickness, the remaining composition *TP3* has RL values between - 10.73 to -30.01 dB for 2.5 to 4.0 mm thickness.

Table 5.1: Performance Parameters comparison

Series	Sample	Maximum RL (dB)	Thickness (mm)
Mg	M6	-43.75	8.9
Cu	NA	NA	NA
Al	A4	-30.99	3.0
Ba-Sr	T6	-29.60	3.5
Mg/PANI	MP5	-40.06	9.2

Cu/PANI	CP3	-20.12	10
Al/PANI	NA	NA	NA
Ba-Sr/PANI	TP6	-37.96	3.0

Future scope

- Multilayered Structures: Investigating the design of multilayered or hybrid composite structures to enhance the absorption bandwidth and reduce the reflection losses at various frequencies.
- Nanostructured M-type Hexaferrites: Research into nanostructuring M-type hexaferrites to achieve higher surface-to-volume ratios, leading to better electromagnetic wave interaction and absorption performance. Nanostructured materials are often more efficient at higher frequencies.
- Hexaferrite-Based Hybrid Nanocomposites: Investigate hybrid materials that combine hexaferrites with nanoparticles of metals, semiconductors, or ceramics (e.g., metal oxide nanoparticles, ferrite-based nanocomposites) for enhanced microwave absorption properties.
- Tunable Microwave Absorbers: Explore techniques to tune the microwave absorption properties of M-type hexaferrites across different frequency bands (X-band, Ku-band, etc.). This could include doping with elements that change the ferrimagnetic resonance frequency.
- Eco-Friendly Microwave Absorbers: Investigate the use of non-toxic, abundant, and environmentally friendly materials in combination with M-type hexaferrites. The development of "green" microwave-absorbing materials with minimal environmental impact could be a key area of future research.

Real-time application and social impact of this research: The results of this study have significant practical applications in the development of advanced materials for electromagnetic interference (EMI) shielding and microwave absorption. The high-performance hexaferrite composites, especially those with optimal doping, can be used in electronic devices to reduce signal interference, ensuring better performance and protection for sensitive equipment. These materials are crucial for military, aerospace, and telecommunication industries, where efficient microwave absorption is necessary for stealth technology and secure communications.

REFERENCES:

[1] A. Raveendran, M. T. Sebastian, and S. Raman, "Applications of Microwave Materials: A Review," *J. Electron. Mater.* (February 2019), DOI: 10.1007/s11664-019-07049-1.

[2] Z. S. A. Rahman, "Microwave Radiations and Its Effects on Human Health: A Review," *Int. J. Eng. Sci.* 7, 16–20 (2018), DOI: 10.9790/1813-0705021621.

[3] "Polymers for Aerospace Structures," *Introd. to Aerosp. Mater.*, 268–302 (2012), DOI: 10.1533/9780857095152.268.

[4] W. L. Song, L. Z. Fan, Z. L. Hou, K. L. Zhang, Y. Ma, and M. S. Cao, "A Wearable Microwave Absorption Cloth," *J. Mater. Chem. C* 5, 2432–2441 (2017), DOI: 10.1039/c6tc05577j.

[5] P. P. Parikh, M. G. Kanabar, and T. S. Sidhu, "Opportunities and Challenges of Wireless Communication Technologies for Smart Grid Applications," *IEEE PES Gen. Meet. PES 2010*, no. Cc (2010), DOI: 10.1109/PES.2010.5589988.

[6] A. G. Francis and A. Professor, "Design of Optimized High Frequency Antennas," no. March 2020, *Int. J. Pure Appl. Math.*, [Online] Available: http://www.ijpam.eu.

[7] K. P. Dahal, "Mobile Communication and Its Adverse Effects," *Himal. Phys.* 4, 51–59 (2013), DOI: 10.3126/hj.v4i0.9429.

[8] Zothansiama, M. Zosangzuali, M. Lalramdinpuii, and G. C. Jagetia, "Impact of Radiofrequency Radiation on DNA Damage and Antioxidants in Peripheral Blood Lymphocytes of Humans Residing in the Vicinity of Mobile Phone Base Stations," *Electromagn. Biol. Med.* 36, 295–305 (2017), DOI: 10.1080/15368378.2017.1350584.

[9] L. Pachuau and Z. Pachuau, "Study of Cell Tower Radiation and Its Health Hazards on the Human Body," *IOSR J. Appl. Phys.* 6, 1–6 (2014), DOI: 10.9790/4861-06110106.

[10] D. S. Aherrao, C. Singh, and A. K. Srivastava, "Review of Ferrite-Based Microwave-Absorbing Materials: Origin, Synthesis, Morphological Effects, Dielectric/Magnetic Properties, Composites, Absorption Mechanisms, and Optimization," *J. Appl. Phys.* 132, 240701 (2022), DOI: 10.1063/5.0123263.

[11] H. Ahmad et al., "Stealth Technology: Methods and Composite Materials—A Review," *Polym. Compos.* 40, 4457–4472 (2019), DOI: 10.1002/pc.25311.

[12] S. S. S. Afghahi, M. Jafarian, and Y. Atassi, "Microstructural and Magnetic Studies on $BaMg_xZn_xX_{2x}Fe_{12-4x}O_{19}$ (X = Zr, Ce, Sn) Prepared via Mechanical Activation Method to Act as a Microwave Absorber in X-band," *J. Magn. Magn. Mater.* 406, 184–191 (2016), DOI: 10.1016/j.jmmm.2015.12.052.

[13] H. R. Luthfianti, W. Widanarto, S. K. Ghoshal, M. Effendi, and W. T. Cahyanto, "Magnetic and Microwave Absorption Properties of Mn^{4+} Doped Barium-Natural Ferrites Prepared by the Modified Solid-State Reaction Method," *J. Phys. Conf. Ser.* 1494, 1 (2020), DOI: 10.1088/1742-6596/1494/1/012043.

[14] A. Okamoto, "The Invention of Ferrites and Their Contribution to the Miniaturization of Radios," *2009 IEEE Globecom Workshop 1*, 1–6 (2009), DOI: 10.1109/GLOCOMW.2009.5360693.

[15] J. Y. Shin and J. H. Oh, "The Microwave Absorbing Phenomena of Ferrite Microwave Absorbers," *IEEE Trans. Magn.* 29, 3437–3439 (1993), DOI: 10.1109/20.281188.

[16] M. F. Shakir et al., "EMI Shielding Characteristics of Electrically Conductive Polymer Blends of PS/PANI in Microwave and IR Region," *J. Electron. Mater.* 49, 1660–1665 (2020), DOI: 10.1007/s11664-019-07631-7.

[17] M. Jasna, N. K. Pushkaran, M. Manoj, C. K. Aanandan, and M. K. Jayaraj, "Facile Preparation of Lightweight and Flexible PVA/PEDOT/MWCNT Ternary Composite for High-Performance EMI Shielding in the X-band Through Absorption Mechanism," *J. Electron. Mater.* 49, 1689–1701 (2020), DOI: 10.1007/s11664-019-07676-8.

[18] S. V. Dravid, S. D. Bhosale, S. Datar, and R. K. Goyal, "Nickel Nanoparticle-Filled High-Performance Polymeric Nanocomposites for EMI Shielding Applications," *J. Electron. Mater.* 49, 1630–1637 (2020), DOI: 10.1007/s11664-019-07535-6.

[19] M. Sugimoto, "The Past, Present, and Future of Ferrites," *J. Am. Ceram. Soc.* 82, 269–280 (1999), DOI: 10.1111/j.1551-2916.1999.tb20058.x.

[20] M. Ebrahimi, R. Raeisi Shahraki, S. A. Seyyed Ebrahimi, and S. M. Masoudpanah, "Magnetic Properties of Zinc Ferrite Nanoparticles Synthesized by Coprecipitation Method," *J. Supercond. Nov. Magn.* 27, 1587–1592 (2014), DOI: 10.1007/s10948-014-2485-4.

[21] Y. Liang et al., "Effect of Ball Milling on the Absorption Properties of Fe_3O_4," *Materials (Basel)* 13, 883 (2020), DOI: 10.3390/ma13040883.

[22] D. Chen, Y. Zhang, and Z. Kang, "A Low Temperature Synthesis of $MnFe_2O_4$ Nanocrystals by Microwave-Assisted Ball-Milling," *Chem. Eng. J.* 215–216, 235–239 (2013), DOI: 10.1016/j.cej.2012.10.061.

[23] J. Zhao, C. Lei, and Y. Du, "Influence of Precursor and Salt-Assisted Calcination on Magnetic Properties of Sr-Ferrites," *J. Mater. Sci. Mater. Electron.* 30, 12597–12602 (2019), DOI: 10.1007/s10854-019-01620-6.

[24] P. Liu et al., "Delamination Strategy to Achieve $Ti_3C_2T_x$/CNZF Composites with Tunable Electromagnetic Absorption," *Mater. Sci. Semicond. Process.* 112, 105008 (2020), DOI: 10.1016/j.mssp.2020.105008.

[25] D. Jiang et al., "Electromagnetic Interference Shielding Polymers and Nanocomposites - A Review," *Polym. Rev.* 59, 280–337 (2019), DOI: 10.1080/15583724.2018.1546737.

[26] S. B. Narang, C. Singh, Y. Bai, and I. S. Hudiara, "Microstructure, Hysteresis, and Microwave Absorption Analysis of $Ba_{(1-x)}Sr_xFe_{12}O_{19}$ Ferrite," *Mater. Chem. Phys.* 111, 225–231 (2008), DOI: 10.1016/j.matchemphys.2008.03.025.

[27] S. R. Saeedi Afshar, S. M. Masoudpanah, and M. Hasheminiasari, "Effects of Calcination Temperature on Magnetic and Microwave Absorption Properties of $SrFe_{12}O_{19}/Ni_{0.6}Zn_{0.4}Fe_2O_4$ Composites," *J. Electron. Mater.* 49, 1742–1748 (2020), DOI: 10.1007/s11664-020-07943-z.

[28] J. Singh, C. Singh, D. Kaur, S. B. Narang, A. Kagdi, R. Joshi, A. S. Bezerra, D. Zhou, S. Trukhanov, and A. Trukhanov, "Optimization of Performance Parameters of Doped Ferrite-Based Microwave Absorbers: Their Structural, Tunable Reflection Loss, Bandwidth, and Input Impedance Characteristics," *IEEE Trans. Magn.* 57(7), 1–7 (2021), DOI: 10.1109/TMAG.2021.3065590.

[29] J. Ding et al., "Boosted Interfacial Polarization from Multishell TiO_2@Fe_3O_4@PPy Heterojunction for Enhanced Microwave Absorption," *Small* 15, 1–10 (2019), DOI: 10.1002/smll.201902885.

[30] N. He, X. F. Yang, R. Ji, S. H. Fu, G. Tong, and W. Wu, "Polarization and Matching Modulation of Peapod-Like Cu/C Nanowires to Improve Microwave Absorption," *J. Alloys Compd.* 822, (2020), DOI: 10.1016/j.jallcom.2019.153633.

[31] B. Zohuri, *Radar Energy Warfare and the Challenges of Stealth Technology* (2020).

[32] P. Saville, "Review of Radar Absorbing Materials," *Def. Res. Dev. Canada*, no. January, 62 (2005).

[33] A. D. M. Charles, A. N. Rider, S. A. Brown, and C. H. Wang, "Multifunctional Magneto-Polymer Matrix Composites for Electromagnetic Interference Suppression, Sensors, and Actuators," *Prog. Mater. Sci.* 115, 100705 (2021), DOI: 10.1016/j.pmatsci.2020.100705.

[34] M. S. Dahiya, V. K. Tomer, and S. Duhan, *Metal-Ferrite Nanocomposites for Targeted Drug Delivery* (Elsevier Inc., 2018).

[35] I. Sharifi, H. Shokrollahi, and S. Amiri, "Ferrite-Based Magnetic Nanofluids Used in Hyperthermia Applications," *J. Magn. Magn. Mater.* 324, 903–915 (2012), DOI: 10.1016/j.jmmm.2011.10.017.

[36] A. Hanini, K. Kacem, J. Gavard, H. Abdelmelek, and S. Ammar, *Ferrite Nanoparticles for Cancer Hyperthermia Therapy* (Elsevier Inc., 2018).

[37] S. V. Trukhanov et al., "Preparation and Investigation of Structure, Magnetic, and Dielectric Properties of $(BaFe_{11.9}Al_{0.1}O_{19})_{1-x}$-$(BaTiO_3)_x$ Bicomponent Ceramics," *Ceram. Int.* 44, 21295–21302 (2018), DOI: 10.1016/j.ceramint.2018.08.180.

[38] J. Singh et al., "Tunable Microwave Absorption in Co-Al Substituted M-Type Ba[–]Sr Hexagonal Ferrite," *Mater. Des.* 110, 1646–761 (2016), DOI: 10.1016/j.matdes.2016.08.049.

[39] C. Singh, S. Bindra Narang, I. S. Hudiara, Y. Bai, and F. Tabatabaei, "Static Magnetic Properties of Co and Ru Substituted Ba-Sr Ferrite," *Mater. Res. Bull.* 43, 176–184 (2008), DOI: 10.1016/j.materresbull.2007.06.050.

[40] M. Chen, R. H. Fan, Z. D. Zhang, Y. S. Yin, and L. H. Dong, "Synthesis of Uniform Barium Ferrite Powders by Co-Precipitation Method," *Mater. Sci. Forum* 898 MSF, 1649–1654 (2017), DOI: 10.4028/www.scientific.net/MSF.898.1649.

[41] D. H. Chen and Y. Y. Chen, "Synthesis of Barium Ferrite Ultrafine Particles by Coprecipitation in the Presence of Polyacrylic Acid," *J. Colloid Interface Sci.* 235, 9–14 (2001), DOI: 10.1006/jcis.2000.7340.

[42] J. Y. Kwak, C. S. Lee, D. Kim, and Y. Il Kim, "Characteristics of Barium Hexaferrite Nanoparticles Prepared by Temperature-Controlled Chemical Coprecipitation," *J. Korean Chem. Soc.* 56, 609–616 (2012), DOI: 10.5012/jkcs.2012.56.5.609.

[43] M. Ebrahimi, R. Raeisi Shahraki, S. A. Seyyed Ebrahimi, and S. M. Masoudpanah, "Magnetic Properties of Zinc Ferrite Nanoparticles Synthesized by Coprecipitation Method," *J. Supercond. Nov. Magn.* 27, 1587–1592 (2014), DOI: 10.1007/s10948-014-2485-4.

[44] L. S. Zaremba and W. H. Smoleński, "Optimal Portfolio Choice Under a Liability Constraint," *Ann. Oper. Res.* 97, 131–141 (2000), DOI: 10.1023/A.

[45] F. Majid, J. Rauf, S. Ata, I. Bibi, M. Yameen, and M. Iqbal, "Hydrothermal Synthesis of Zinc-Doped Nickel Ferrites: Evaluation of Structural, Magnetic and Dielectric Properties," *Zeitschrift für Phys. Chemie* (2018), DOI: 10.1515/zpch-2018-1305.

[46] G. Packiaraj, N. R. Panchal, and R. B. Jotania, "Structural and Dielectric Studies of Cu Substituted Barium Hexaferrite Prepared by Sol-Gel Auto Combustion Technique," *Solid State Phenom.* 209, 102–106 (2014), DOI: 10.4028/www.scientific.net/SSP.209.102.

[47] A. Dehghanghadikolaei, J. Ansary, and R. Ghoreishi, "Sol-Gel Process Applications: A Mini-Review," *Proc. Nat. Res. Soc.* 2, (June 2018), DOI: 10.11605/j.pnrs.201802008.

[48] R. S. Yadav et al., "$NiFe_2O_4$ Nanoparticles Synthesized by Dextrin from Corn-Mediated Sol-Gel Combustion Method and Its Polypropylene Nanocomposites Engineered with Reduced

Graphene Oxide for the Reduction of Electromagnetic Pollution," *ACS Omega* 4, 22069–22081 (2019), DOI: 10.1021/acsomega.9b03191.

[49] K. Qian et al., "The Influence of Nd Substitution in Ni-Zn Ferrites for the Improved Microwave Absorption Properties," *Ceram. Int.* 46, 227–235 (2020), DOI: 10.1016/j.ceramint.2019.08.255.

[50] Y. A. Alshataif, S. Sivasankaran, F. A. Al-Mufadi, A. S. Alaboodi, and H. R. Ammar, *Manufacturing Methods, Microstructural and Mechanical Properties Evolutions of High-Entropy Alloys: A Review* 26, 8 (The Korean Institute of Metals and Materials, 2020).

[51] M. Beygisangchin, S. A. Rashid, S. Shafie, A. R. Sadrolhosseini, and H. N. Lim, "Preparations, properties, and applications of polyaniline and polyaniline thin films—A review," *Polymers* 13, 2003 (2021), https://doi.org/10.3390/polym13122003.

[52] M. Ljaz et al., "Influence of ferromagnetic cobalt on microstructural and magnetic trends of sol-gel routed rare earth and aluminium based BaSr-Hexaferrites ($Ba_{0.6}Sr_{0.3}Er_{0.1}Fe_{11.5-x}Al_{0.5}Co_xO_{19}$)," *Mater. Sci. Eng. B* 299, (Jan. 2024), https://doi.org/10.1016/j.mseb.2023.116933.

[53] Y. Jin et al., "Effect of Ce doping on electromagnetic characteristics and absorbing properties of M-type barium ferrite," *Mater. Today Chem.* 39, 108596 (2024), https://doi.org/10.1016/j.mtcomm.2024.108596.

[54] X. Jing et al., "Praseodymium dysprosium co-doped M-type strontium ferrite: Intentionally manufacturing heterophase growth to improve microwave absorption performance," *Mater. Today Chem.* 39, 102151 (2024), https://doi.org/10.1016/j.mtcomm.2024.102151.

[55] M.A. Siddique et al., "Role of Zn cations substitution on structural, vibrational, elastic, dielectric, bandwidth, and microwave absorbance of Co–Cd ferrites at high frequencies," *Mater. Chem. Phys.* 315, 128972 (2024), https://doi.org/10.1016/j.matchemphys.2024.128972.

[56] Kumari, S., Dalal, J., Kumar, A., Pal, R., Chahal, R., and Ohlan, A., "Enhanced microwave absorption properties of conducting polymer@graphene composite to counteract electromagnetic radiation pollution: green EMI shielding," *RSC Adv.* 14, 662–676 (2024), https://doi.org/10.1039/d3ra07245b. PMID: 38173587; PMCID: PMC10760626.

[57] El-Gawad, W. M. A., Eldesouki, E. M., and El-Ghany, W. A. A., "Development of high performance microwave absorption modified epoxy coatings based on nano-ferrites," *Sci. Rep.* 14, 55571 (2024), https://doi.org/10.1038/s41598-024-55571-y.

[58] M. Kaur and S. Bahel, "Characterization of sol-gel synthesized $Zn_{0.25}Co_{0.75}(NiZr)_xFe_{2-2x}O_4$ ($0.05 \leq x \leq 0.25$) spinel ferrites based microwave absorbers in Ka frequency band," *J. Phys. Chem. Solids* 184, 111671 (2024), https://doi.org/10.1016/j.jpcs.2023.111671.

[59] S. Caliskan et al., "Impact of vanadium substitution on structural, magnetic, microwave absorption features and hyperfine interactions of SrCo hexaferrites," *J. Alloys Compd.* 960, 170578 (Oct. 2023), https://doi.org/10.1016/j.jallcom.2023.170578.

[60] D. Thanh, N. Tran, N. Thi Viet Chinh, N. Thi Ngoc Anh, D. H. Manh, and N. Q. Tuan, "Excellent microwave absorption performances of cobalt-doped $SrFe_{12}O_{19}$ hexaferrite with varying incident angles," *J. Alloys Compd.* 952, 170060 (2023), https://doi.org/10.1016/j.jallcom.2023.170060.

[61] K. Khan, H. Abbas, and K. Nadeem, "Magnetic exchange coupling and effect of grain and grain boundaries on conduction mechanism of $(MgFe_2O_4)_{100-x}$ /$(BaFe_{12}O_{19})_x$ nanocomposites," *Ceram. Int.* 49, 13982–13993 (2023), https://doi.org/10.1016/j.ceramint.2022.12.280.

[62] K. Rana, S. Thakur, M. Tomar, V. Gupta, and A. Thakur, “Effect of low sintering temperature on the structural and magnetic properties of M-type strontium hexaferrite,” *J. Magn Magn Mater*, vol. 587, p. 171289, Dec. 2023, https://doi.org/10.1016/j.jmmm.2023.171289.

[63] A. Yu. Mironovich, V. G. Kostishin, H. I. Al-Khafaji, A. V. Timofeev, A. I. Ril, and R. I. Shakirzyanov, "Study of structure, cation distribution and magnetic properties of Ni substituted M-type barium hexaferrite," *Materialia* (Oxf.) 101898, (2023), https://doi.org/10.1016/j.mtla.2023.101898.

[64] V. Bilovol, M. Sikora, and K. Berent, "Exchange coupling in $SrFe_{12}O_{19}/CoFe_2O_4$ composites: Effect of component proportions," *J. Magn. Magn. Mater.* 568, 170384 (2023), https://doi.org/10.1016/j.jmmm.2023.170384.

[65] K. R. Nishkala, R. R. Rao, S. Mutalik, M. S. Murari, and M. D. Daivajna, "Investigations on structural, Mossbauer, dielectric, and ferroelectric properties of La-doped barium hexaferrite," *Physica B Condens. Matter* 664, 414954 (2023), https://doi.org/10.1016/j.physb.2023.414954.

[66] K. Rana, S. Thakur, M. Tomar, V. Gupta, and A. Thakur, "Effect of low sintering temperature on the structural and magnetic properties of M-type strontium hexaferrite," *J. Magn. Magn. Mater.* 587, 171289 (2023), https://doi.org/10.1016/j.jmmm.2023.171289.

[67] A. Gupta and P. K. Roy, "Effect of Zn^{2+} ion substitution in Al^{3+}-substituted rare-earth free Sr-hexaferrite for different permanent magnet applications," *Inorg. Chem. Commun.* 111114, (2023), https://doi.org/10.1016/j.inoche.2023.111114.

[68] M. Zarrar Khan, I. Hussain Gul, and F. A. Tahir, "Encapsulation of Ba–Sr hexaferrite nanoparticles and MWCNTs in conductive polymer matrix for improved dielectric spectroscopy, electromagnetic shielding, and microwave absorption applications," *Ceram. Int.* 49(17), 27796–27814 (2023), https://doi.org/10.1016/j.ceramint.2023.05.266.

[69] X. Liu, R. Ji, M. Yang, W. Chen, H. Chen, X. Song, J. Liu, M. Zhang, and L. Zhang, "Facilitating enhanced microwave absorption properties of barium hexaferrite/polyaniline composites based on tunable interfacial polarization by rare earth doping," *J. Alloys Compd.* 937, 168391 (2023), https://doi.org/10.1016/j.jallcom.2022.168391.

[70] M. Dilshad, H. M. Khan, M. Zahid, et al., "Structural, optical and dielectric properties of aluminum-substituted $SrAl_{2x}Fe_{12-2x}O_{19}$ x = (0.0, 0.2, 0.4, 0.6, 0.8, 1.0) M-type hexagonal ferrites," *J. Mater. Sci. Mater. Electron.* 33, 21519–21530 (2022), https://doi.org/10.1007/s10854-022-08943-x.

[71] T. Fricke et al., "Anisotropic properties of $Ba_{1-x}Sr_xFe_{12}O_{19}$ single crystals," *Cry. Engg. Comm.* 24, 5052–5059 (2022), https://doi.org/10.1039/d2ce00165a.

[72] D. Baba Basha, N. Suresh Kumar, K. Chandra Babu Naidu, and G. Ranjith Kumar, "Structural, electrical, and magnetic properties of nano $Sr_{1-x}La_xFe_{12}O_{19}$ (X=0.2–0.8)," *Sci. Rep.* 12, 12723 (2022), https://doi.org/10.1038/s41598-022-15250-2.

[73] A. Garg, S. Goel, A. K. Dixit, M. K. Pandey, N. Kumari, and S. Tyagi, "Investigation on the effect of neodymium doping on the magnetic, dielectric and microwave absorption properties of strontium hexaferrite particles in X-band," *Mater. Chem. Phys.* 257, 123771 (2021), https://doi.org/10.1016/j.matchemphys.2021.123771.

[74] M. Rostami, M. Jafarpour, M. H. Majles Ara, "An investigation on the microwave absorption properties of Co–Al–Ti substituted barium hexaferrite-MWCNT nanocomposites," *J. Alloys Compd.* 872, 159656 (2021), https://doi.org/10.1016/j.jallcom.2021.159656.

[75] A. Garg, S. Goel, A. K. Dixit, M. K. Pandey, N. Kumari, and S. Tyagi, "Investigation on the effect of neodymium doping on the magnetic, dielectric and microwave absorption properties of strontium hexaferrite particles in X-band," *Mater. Chem. Phys.* 257, 123771 (2021), https://doi.org/10.1016/j.matchemphys.2020.123771.

[76] H. Li, L. Zheng, D. Deng, X. Yi, X. Zhang, X. Luo, Y. Wu, W. Luo, and M. Zhang, "Multiple natural resonances broaden microwave absorption bandwidth of substituted M-type hexaferrites," *J. Alloys Compd.* 862, 158638 (2021), https://doi.org/10.1016/j.jallcom.2021.158638.

[77] S. Goel, A. Garg, H. B. Baskey, M. K. Pandey, and S. Tyagi, "Studies on dielectric and magnetic properties of barium hexaferrite and bio-waste derived activated carbon composites

for X-band microwave absorption," *J. Alloys Compd.* 875, 160028 (2021), https://doi.org/10.1016/j.jallcom.2021.160028.

[78] G. Gultom, M. Rianna, P. Sebayang, and M. Ginting, "The effect of Mg–Al binary doped barium hexaferrite for enhanced microwave absorption performance," *Case Studies in Thermal Engineering* 18, 100580 (2020), https://doi.org/10.1016/j.csite.2019.100580.

[79] Z. Zhang, "The influence of Ce-Cu doping M-type strontium hexaferrites on structure and magnetic properties," *J. Supercond. Nov. Magn.* 33, 3607–3613 (2020), https://doi.org/10.1007/s10948-020-05631-x.

[80] D. S. Winatapura, D. Deswita, A. A. Wisnu, S. Purwanto, and Y. F. Buys, "Influence of La, Mn and Zn substitution on the structure, magnetic and absorption properties of M-type barium ferrites," *Key Eng. Mater.* 855, 145–153 (2020), https://doi.org/10.4028/www.scientific.net/kem.855.145.

[81] A. Haq and M. Anis-ur-Rehman, "Structural, morphological and electrical analysis of dual doped Sr-hexaferrite nanoparticles," *Physica B: Condens. Matter* 601, 412445 (2021), https://doi.org/10.1016/j.physb.2020.412445.

[82] A. Kumar, M. K. Verma, S. Singh, et al., "Electrical, magnetic and dielectric properties of cobalt-doped barium hexaferrite $BaFe_{12-x}Co_xO_{19}$ (x = 0.0, 0.05, 0.1 and 0.2) ceramic prepared via a chemical route," *J. Electron. Mater.* 49, 6436–6447 (2020), https://doi.org/10.1007/s11664-020-08364-8.

[83] Y. K. R. Shariff, H. K. Choudhary, V. Khopkar, A. Yadav, R. Madhusudhana, and B. Sahoo, "Sol-gel auto-combustion synthesis of Ba–Sr hexaferrite ceramic powders," *Ceram. Int.* 47, 14907–14912 (2021), https://doi.org/10.1016/j.ceramint.2020.07.034.

[84] A. Garg, S. Goel, N. Kumari, et al., "Yttrium-doped strontium hexaferrite particles for microwave absorption application in X-band," *J. Mater. Sci.: Mater. Electron.* 31, 13746–13755 (2020), https://doi.org/10.1007/s10854-020-03934-2.

[85] W. Widanarto, M. Effendi, S. K. Ghoshal, C. Kurniawan, E. Handoko, and M. Alaydrus, "Bio-silica incorporated barium ferrite composites: Evaluation of structure, morphology, magnetic and microwave absorption traits," *Curr. Appl. Phys.* 20, 638–642 (2020), https://doi.org/10.1016/j.cap.2020.02.019.

[86] H. Nikmanesh, S. Hoghoghifard, B. Hadi-Sichani, and M. Moradi, "Erbium-chromium substituted strontium hexaferrite particles: Characterization of the physical and Ku-band microwave absorption properties," *Mater. Sci. Eng. B* 262, 114796 (2020), https://doi.org/10.1016/j.mseb.2020.114796.

[87] P. Li, Y. Sun, and Y. Akinay, "The influence of MWCNTs on microwave absorption properties of Co/C and Ba-hexaferrite hybrid nanocomposites," *Synth. Met.* 263, 116369 (2020), https://doi.org/10.1016/j.synthmet.2020.116369.

[88] G. A. Ashraf, L. Zhang, W. Abbas, et al., "Structural, optical, dielectric, and magnetic characteristics of Nd ions substituted $BaFe_{11}(Sn_{0.5}Mg_{0.5})_xO_{19}$ M-type hexaferrite via co-precipitation," *J. Supercond. Nov. Magn.* 32, 3273–3284 (2019), https://doi.org/10.1007/s10948-019-5047-y.

[89] M. A. Almessiere, Y. Slimani, A. Demir Korkmaz, S. Güner, A. A. Maarouf, and A. Baykal, "Comparative study of sonochemically synthesized Co-Zr and Ni-Zr substituted Sr-hexaferrites: Magnetic and structural investigations," *J. Magn. Magn. Mater.* 497, 165996 (2020), https://doi.org/10.1016/j.jmmm.2019.165996.

[90] K. Zhang, J. Luo, N. Yu, M. Gu, X. Sun, "Synthesis and excellent electromagnetic absorption properties of reduced graphene oxide/PANI/$BaNd_{0.2}Sm_{0.2}Fe_{11.6}O_{19}$ nanocomposites," *J. Alloys Compd.* 779, 270-279 (2019), https://doi.org/10.1016/j.jallcom.2018.11.284.

[91] M. Shezad, X. Liu, S. Feng, X. Kan, W. Wang, C. Liu, T. J. Shehzad, K. M. Ur Rehman, "Characterizations analysis of magneto-structural transitions in Ce-Co doped SrM based nano $Sr_{1-x}Ce_xFe_{12-x}Co_xO_{19}$ hexaferrite crystallites prepared by ceramic route," *J. Magn. Magn. Mater.* 497, 166013 (2020), https://doi.org/10.1016/j.jmmm.2019.166013.

[92] İ. Araz, "The effect of Ce–Co substitution on the structural and the electromagnetic properties of barium hexaferrite," *J. Mater. Sci.: Mater. Electron.* 30, 5130–5136 (2019), https://doi.org/10.1007/s10854-019-00811-5

[93] G. Venkatesh, R. Subramanian, T. Satish Kumar, J. Abuthakir, L. John Berchmans, and K. Sethupathi, "Investigation on structural and magnetic properties of Al^{3+} and Ce^{3+} doped hexaferrites," *Mater. Today: Proc.* 28, Part 2, 440–449 (2020), https://doi.org/10.1016/j.matpr.2019.10.029.

[94] H. Sözeri, F. Genç, M. A. Almessiere, İ. S. Ünver, A. D. Korkmaz, and A. Baykal, "Cr^{3+}substituted Ba nanohexaferrites as high-quality microwave absorber in X band," *J. Alloys Compd.* 779, 420–426 (2019), https://doi.org/10.1016/j.jallcom.2018.11.309.

[95] N. Tran, D. H. Kim, and B. W. Lee, "Influence of fabrication conditions on the structural and magnetic properties of Co-doped $BaFe_{12}O_{19}$ hexaferrites," *J. Korean Phys. Soc.* 72, 731–736 (2018).

[96] M. Ayub, I. H. Gul, K. Nawaz, and K. Yaqoob, "Effect of rare earth and transition metal La-Mn substitution on electrical properties of co-precipitated M-type Ba-ferrites nanoparticles," *J. Rare Earths* 37, 193–197 (2019), https://doi.org/10.1016/j.jre.2018.08.005.

[97] S. Mortazavinik and M. Yousefi, "Preparation, magnetic properties, and microwave absorption of Zr–Zn–Co substituted strontium hexaferrite and its nanocomposite with polyaniline," *Russ. J. Appl. Chem.* 90, 298–303 (2017).

[98] G. Ramezanzaeh, A. Ghasemi, R. Mozaffarinia, and A. Alizadeh, "Electromagnetic wave reflection loss and magnetic properties of M-type $SrFe_{12-x}(Mn_{0.5}Sn_{0.5})_xO_{19}$ hexagonal ferrite nanoparticles in the Ku microwave band," *Ceram. Int.* 43, 10231–10238 (2017), https://doi.org/10.1016/j.ceramint.2017.05.050.

[99] M. Ramzan, M. I. Arshad, K. Mahmood, et al., "Investigation of structural and optical properties of Pr3+-substituted M-type Ba–Ni nano-ferrites," *J. Supercond. Nov. Magn.* 34, 1759–1764 (2021), https://doi.org/10.1007/s10948-020-05751-4.

[100] S. K. Godara, H. Singh, P. S. Malhic, V. Kaur, S. B. Narang, A. K. Sood, G. R. Bhadu, and J. C. Chaudhari, "Synthesis and characterization of Zn^{2+}-Zr^{4+} substituted barium hexaferrite by sol gel auto combustion method," *Mater. Today: Proc.* 17, 371-379 (2019).

[101] C. Lei, S. Tang, and Y. Du, "Synthesis of aligned La^{3+}-substituted Sr-ferrites via molten salt assisted sintering and their magnetic properties," *Ceram. Int.* 42, 15511-15516 (2016), https://doi.org/10.1016/j.ceramint.2016.06.204.

[102] Z. Mosleh, P. Kameli, A. Poorbaferani, M. Ranjbar, and H. Salamati, "Structural, magnetic and microwave absorption properties of Ce-doped barium hexaferrite," *J. Magn. Magn. Mater.* 397, 101-107 (2016), https://doi.org/10.1016/j.jmmm.2015.08.078.

[103] M. A. Rafiq, M. Waqar, T. A. Mirza, A. Farooq, and A. Zulfiqar, "Effect of Ni^{2+} substitution on the structural, magnetic, and dielectric properties of barium hexagonal ferrites ($BaFe_{12}O_{19}$)," *J. Electron. Mater.* (2016).

[104] İ. Araz, "Microwave characterization of Co-doped barium hexaferrite absorber material," *J. Supercond. Nov. Magn.* 29, 1545–1550 (2016), https://doi.org/10.1007/s10948-016-3447-9.

[105] Z. Vakil, A. Kumar, A. Jain, K. M. Gupta, M. Najim, and D. Singh, "Effect of Cerium (Ce3+) doping on structural, magnetic and dielectric properties of Barium Ferrite ($BaFe_{12}O_{19}$)," *IEEE Int. Conf. Electr. Comput. Commun. Technol. (ICECCT)*, Coimbatore, India, 2015, pp. 1-4, https://doi.org/10.1109/ICECCT.2015.7225982.

[106] H. M. Khan, M. U. Islam, Y. Xu, M. N. Ashiq, I. Ali, M. A. Iqbal, and M. Ishaque, "Structural and magnetic properties of Pr-Ni substituted $Ca_{0.5}Ba_{0.5}Fe_{12}O_{19}$ hexa-ferrite

nanoparticles," *Ceram. Int.* 40, 6487–6493 (2014), https://doi.org/10.1016/j.ceramint.2013.11.101.

[107] A. Sharbati and J. M. V. Khani, "Effect of Ho3+ substitution on magnetic and microwave absorption properties of $Sr(ZnZr)_{0.5}Fe_{12}O_{19}$ hexagonal ferrite nanoparticles," *J. Mater. Sci.: Mater. Electron.* 24, 3629–3633 (2013), https://doi.org/10.1007/s10854-013-1295-y.

[108] A. Ghasemi, A. Saatchi, M. Salehi, A. Hossienpour, A. Morisako, and X. Liu, "Magnetic characteristics of Mn–Co–Ti substituted barium ferrite synthesized by sol–gel processing," *Phys. Status Solidi A* 203, 2513–2521 (2006), https://doi.org/10.1002/pssa.200622002.

[109] R. Tang, C. Jiang, W. Qian, et al., "Dielectric relaxation, resonance and scaling behaviours in $Sr_3Co_2Fe_{24}O_{41}$ hexaferrite," *Sci. Rep.* 5, 13645 (2015), https://doi.org/10.1038/srep13645.

[110] Md. K. Shamim, S. Sharma, S. Sinha, and E. Nasreen, "Dielectric relaxation and modulus spectroscopy analysis of $(Na_{0.47}\ K_{0.47}\ Li_{0.06})\ NbO_3$ ceramics," *J. Adv. Dielectrics* 7, 1750020 (2017), https://doi.org/10.1142/S2010135X17500205.

[111] M. Belal Hossen, A. K. M. Akther Hossain, and A.K.M., "Complex impedance and electric modulus studies of magnetic ceramic $Ni_{0.27}Cu_{0.10}Zn_{0.63}Fe_2O_4$," *J. Adv. Ceram.* 4, 217-225 (2015), https://doi.org/10.1007/s40145-015-0152-2.

[112] A. K. Pradhan, T. K. Nath, and S. Sah, "Impedance spectroscopy and electric modulus behavior of Molybdenum doped Cobalt–Zinc ferrite," *Mater. Res. Express* 4, 076107 (2017), https://doi.org/10.1088/2053-1591/aa7c8c.

[113] A. Bagum, M. Belal Hossen, and F.-U.-Z. Chowdhury, "Complex impedance and electric modulus studies of Al substituted $Co_{0.4}Cu_{0.2}Zn_{0.4}Al_xFe_{2-x}O_4$ ferrites prepared by auto combustion technique," *Ferroelectrics* 494, 19-32 (2016).

[114] M. J. Iqbal, M. Nadeem, and M. M. Hassan, "Low temperature ac electrical study of $Pr_{0.52-x}La_xCa_{0.5}MnO_3$ (x = 0.0–0.4) ceramics by employing impedance spectroscopy," *J. Appl. Phys.* 114, 113708 (2013).

[115] M. M. Costa, G. F. M. Pires, A. J. Terezo, M. P. F. Graça, and A. S. B. Sombra, "Impedance and modulus studies of magnetic ceramic oxide $Ba_2Co_2Fe_{12}O_{22}$ (Co_2Y) doped with Bi2O3," *J. Appl. Phys.* 110, 034107 (2011), https://doi.org/10.1063/1.3615935.

[116] Md. T. Rahman and C. V. Ramana, "Impedance spectroscopic characterization of gadolinium substituted cobalt ferrite ceramics," *J. Appl. Phys.* 116, 164108 (2014), https://doi.org/10.1063/1.4896945.

[117] A. Selmi, S. Hcini, H. Rahmouni, A. Omri, M. L. Bouazizi, and A. Dhahri, "Synthesis, structural and complex impedance spectroscopy studies of $Ni_{0.4}Co_{0.4}Mg_{0.2}Fe_2O_4$ spinel ferrite," *Phase Transitions* 90, 942-954 (2017), https://doi.org/10.1080/01411594.2017.1309403.

[118] S. Kumar, K. M. Batoo, R. Prakash, and H. K. Choi, "Impedance spectroscopy study on $Mn_{1+x}Fe_{2-2x}Ti_xO_4$ ($0 \leq x \leq 0.5$) ferrites," *J. Cent. South Univ. Technol.* 17, 1133-1138 (2010), https://doi.org/10.1007/s11771−010−0608−z.

[119] W. Chen, W. Zhu, O. K. Tan, and X. F. Chen, "Frequency and temperature-dependent impedance spectroscopy of cobalt ferrite composite thick films," *J. Appl. Phys.* 108, 034101 (2010), https://doi.org/10.1063/1.3457217.

[120] L. Shu, Y. Shao, F. Huang, Y. Yang, Z. Wu, L. Lei, X. Lu, and J. Zhu, "Magnetoelectric coupling induced by Jahn–Teller Cu^{2+} in $SrFe_{12}O_{19}$ ceramics," *J. Mater. Chem. C* 11, 241-2250 (2023), https://doi.org/10.1039/D2TC03863C.

[121] M. Dilshad, H. M. Khan, M. Zahid, et al., "Structural, optical and dielectric properties of aluminum-substituted $SrAl_{2x}Fe_{12-2x}O_{19}$ (x = 0.0, 0.2, 0.4, 0.6, 0.8, 1.0) M-type hexagonal ferrites," *J. Mater. Sci.: Mater. Electron.* 33, 21519-21530 (2022), https://doi.org/10.1007/s10854-022-08943-x.

[122] A. Hashhash, A. Hassen, W. S. Baleidy, and H. S. Refai, "Impact of rare-earth ions on the physical properties of hexaferrites $Ba_{0.5}Sr_{0.5}RE_{0.6}Fe_{11.4}O_{19}$ (RE = La, Yb, Sm, Gd, Er, Eu, and Dy)," *J. Alloys Compd.* 873, 159812 (2021), https://doi.org/10.1016/j.jallcom.2021.159812.

[123] F. S. H. Abu-Samaha and M. I. M. Ismail, "AC conductivity of nanoparticles $Co_xFe_{(1-x)}Fe_2O_4$ (x = 0, 0.25 and 1) ferrites," *Mater. Sci. Semicond. Process.* 19, 50–56 (2014), https://doi.org/10.1016/j.mssp.2013.11.027.

[124] B. Louati, M. Gargouri, K. Guidara, and T. Mhiri, "AC electrical properties of the mixed crystal $(NH_4)_3H(SO_4)_{1.42}(SeO_4)_{0.58}$," *J. Phys. Chem. Solids* 66, 762–765 (2005).

[125] A. Verma, O. P. Thakur, C. Prakash, T. C. Goel, and R. G. Mendiratta, "Temperature dependence of electrical properties of nickel-zinc ferrites processed by the citrate precursor technique," *Mater. Sci. Eng. B* 116, 1-6 (2005).

[126] A. K. Jonscher, *Dielectric Relaxation in Solids* (Chelsea Dielectrics Press Ltd., London, 1983).

[127] K. Funke, "Jump relaxation in solid electrolytes," *Prog. Solid State Chem.* 22, 111–137 (1993).

[128] R. Nongjai, S. Khan, K. Asokan, H. Ahmed, and I. Khan, "Magnetic and electrical properties of In-doped cobalt ferrite nanoparticles," *J. Appl. Phys.* 112, 084321 (2012), https://doi.org/10.1063/1.4759436.

[129] D. K. Mahato, "AC conductivity analysis of nanocrystallite $MgFe_2O_4$ ferrite," *Mater. Today: Proc.* 5, 9191–9195 (2018).

[130] S. I. Ahmad, A. Rauf, T. Mohammed, A. Bahafi, D. R. Kumar, and M. B. Suresh, "Dielectric, impedance, AC conductivity, and low-temperature magnetic studies of Ce and Sm co-substituted nanocrystalline cobalt ferrite," *J. Magn. Magn. Mater.* 492, 165666 (2019), https://doi.org/10.1016/j.jmmm.2019.165666.

[131] C. Singh, S. B. Narang, I. S. Hudiara, Y. Bai, and F. Tabatabaei, "Static magnetic properties of Co and Ru substituted Ba-Sr ferrite," *Mater. Res. Bull.* 43, 176-184 (2008), https://doi.org/10.1016/j.materresbull.2007.06.050.

[132] H. Wei, Z. Zhang, G. Hussain, L. Zhou, Q. Li, and K. Ostrikov, "Techniques to enhance magnetic permeability in microwave absorbing materials," *Appl. Mater. Today* 19, 100596 (2020), https://doi.org/10.1016/j.apmt.2020.100596.

[133] S. V. Trukhanov et al., "Preparation and investigation of structure, magnetic and dielectric properties of $(BaFe_{11.9}Al_{0.1}O_{19})1\text{-}x\text{-}(BaTiO_3)_x$ bicomponent ceramics," *Ceram. Int.* 44, 21295–21302 (2018), https://doi.org/10.1016/j.ceramint.2018.08.180.

[134] J. Singh et al., "Tunable microwave absorption in Co–Al substituted M-type Ba–Sr hexagonal ferrite," *Mater. Des.* 110, 749–761 (2016), https://doi.org/10.1016/j.matdes.2016.08.049.

[135] S. K. Godara, V. Kaur, K. Chuchra, S.B. Narang, G. Singh, M. Singh, A. Chawla, S. Verma, G.R. Bhadu, J.C. Chaudhari, P.D. Babu, A.K. Sood, "Impact of Zn^{2+}-Zr^{4+} substitution on M-type Barium Strontium Hexaferrite's structural, surface morphology, dielectric and magnetic properties," *Results Phys.* 22, 103892 (2021), https://doi.org/10.1016/j.rinp.2021.103892..

[136] V. A. Turchenko, S. V. Trukhanov, V. G. Kostishin, et al., "Features of structure, magnetic state and electrodynamic performance of $SrFe_{12-x}In_xO_{19}$," *Sci. Rep.* 11, 18342 (2021), https://doi.org/10.1038/s41598-021-97684-8.

[137] Shalom Ann Mathews, D. Rajan Babu, "Analysis of the role of M-type hexaferrite-based materials in electromagnetic interference shielding," *Curr. Appl. Phys.* 29, 39–53 (2021), https://doi.org/10.1016/j.cap.2021.06.001.

[138] Yana Taryana, Yuyu Wahyu, Azwar Manaf, M. Manawan, Wisnu Ari Adi, "Structural and microwave absorption properties of $BaFe_{(12-2x)}Sn_xZnxO_{19}$ (x = 0.05-1.0) ceramic magnets," *Materialia* 23, 101455 (2022), https://doi.org/10.1016/j.mtla.2022.101455.

[139] Shifan Lu, Yingli Liu, Qisheng Yin, Jianfeng Chen, Jie Li, Jian Wu, "Effects of Ce-Zn co-substitution on the structural and magnetic properties of M-type barium hexaferrites," *J. Magn. Magn. Mater.* 564, 170068 (2022), https://doi.org/10.1016/j.jmmm.2022.170068.

[140] Zihan Wang, Min Yang, Biyu Zheng, Panpan Wang, Yue Wang, Huiwen Chen, Xiaoli Song, Junliang Liu, Ming Zhang, "Tunable magnetization of single domain M-type barium hexagonal ferrite nano powders by Co–Ti substitution via chemical co-precipitation plus molten salts method," *Ceram. Int.* 48, 27779-27784 (2022), https://doi.org/10.1016/j.ceramint.2022.06.079.

[141] S. Verma, A. Singh, S. Sharma, P. Kaur, S.K. Godara, P.S. Malhi, J. Ahmed, P.D. Babu, M. Singh, "Magnetic and structural analysis of $BaZn_xZr_xFe_{12-2x}O_{19}$ (x = 0.1–0.7) hexaferrite samples for magnetic applications," *J. Alloys Compd.* 930, 167410 (2023), https://doi.org/10.1016/j.jallcom.2022.167410.

[142] L. Shu, Y. Shao, F. Huang, Y. Yang, Z. Wu, L. Lei, X. Lu, J. Zhu, "Magnetoelectric coupling induced by Jahn–Teller Cu^{2+} in $SrFe_{12}O_{19}$ ceramics," *J. Mater. Chem. C* 11, 2241–2250 (2023), https://doi.org/10.1039/D2TC03863C.

[143] T. Tekou Carol T., J. Sharma, J. Mohammed, S. Kumar, A.K. Srivastava, "Effect of temperature on the magnetic properties of nano-sized M-type barium hexagonal ferrites," *AIP Conf. Proc.* 1860, 020008 (2017), https://doi.org/10.1063/1.4990307.

[144] S. K. Chawla, R. K. Mudsainiyan, S. S. Meena, S. M. Yusuf, "Structural and magnetic properties of $BaCo_xZr_xFe_{(12-2x)}O_{19}$ prepared by citrate precursor sol-gel route," *AIP Conf. Proc.* 1536, 569 (2013), https://doi.org/10.1063/1.4810354.

[145] A. M. Nicolson and G. F. Ross, "Measurement of the intrinsic properties of materials by time-domain techniques," *IEEE Trans. Instrum. Meas.* 19, 377–382 (1970).

[146] G. Shen, Z. Xu, and Y. Li, "Absorbing properties and structural design of microwave absorbers based on W-type La-doped ferrite and carbon fiber composites," *J. Magn. Magn. Mater.* 301, 325–330 (2006).

[147] X. J. Zhang, S. W. Wang, G. S. Wang, Z. Li, A. P. Guo, J. Q. Zhu, D. P. Liu, and P. G. Yin, "Magnetic properties and microwave absorption of La-doped ferrite composites," *RSC Adv.* 7, 22454 (2017).

[148] H. Kaur et al., "Investigation of structural, hysteresis and electromagnetic parameters 749, *Alloys Compd.* 806, 1220-1229 (2019), https://doi.org/10.1016/j.jallcom.2019.07.032.

[149] S. M. Abbas, A. K. Dixit, R. Chatterjee, and T. C. Goel, "Complex permittivity, complex permeability and microwave absorption properties of ferrite-polymer composites," *J. Magn. Magn. Mater.* 309, 20–24 (2007), https://doi.org/10.1016/j.jmmm.2006.06.006.

[150] Y. Chang et al., "Microwave absorption in 0.1–18 GHz, magnetic and structural properties of $SrFe_{12-x}Ru_xO_{19}$ and $BaFe_{12-x}Ru_xO_{19}$," *J. Alloys Compd.* 818, 152930 (2020), https://doi.org/10.1016/j.jallcom.2019.152930.

[151] C. Stergiou, "Magnetic, dielectric and microwave absorption properties of rare earth doped Ni-Co and Ni-Co-Zn spinel ferrites," *J. Magn. Magn. Mater.* 426, 629–635 (2017), https://doi.org/10.1016/j.jmmm.2016.11.001.

[152] H. Sözeri, F. Genç, B. Ünal, A. Baykal, and B. Akta, "Magnetic, electrical and microwave properties of Mn-Co substituted Nix $Zn_{0.8-x}Fe_2O_4$ nanoparticles," *J. Alloys Compd.*, 660, 324–335 (2016).

[153] Y. Zhang, F. Xu, G. Tan, J. Zhang, T. Wang, and F. Li, "Improvement of microwave-absorbing properties of Co_2Z barium ferrite composite by coating Ag nanoparticles," *J. Alloys Compd.*, 615, 749–753 (2014).

[154] M. Wu et al., "Microwave magnetic properties of $Co_{50}/(SiO_2)_{50}$ nanoparticles," *Appl. Phys. Lett.*, 80, 4404-4406 (2002).

[155] G. Shen, Z. Xu, and Y. Li, "Absorbing properties and structural design of microwave absorbers based on W-type La-doped ferrite and carbon fiber composites," *J. Magn. Magn. Mater.*, 301, 325-330 (2006).

[156] G. Wei et al., "Enhanced microwave absorption of barium cobalt hexaferrite composite with improved bandwidth via c-plane alignment," *J. Magn. Magn. Mater.*, 471, 267-273 (2019).

[157] C. A. Stergiou, M. Y. Koledintseva, and K. N. Rozanov, *Hybrid Polymer Composites for Electromagnetic Absorption in Electronic Industry* (Elsevier, Amsterdam, The Netherlands, 2017).

[158] Z. W. Li and Z. H. Yang, "Microwave absorption properties and mechanism for hollow Fe3O4 nanosphere composites," *J. Magn. Magn. Mater.*, 387, 131–138 (2015).

[159] A. Jaiswal, R. Das, V. K. Vivekanand, T. Maity, P. M. Abraham, S. Adyanthaya, and P. Poddar, "Magnetic and dielectric properties and Raman spectroscopy of $GdCrO_3$ nanoparticles," *J. Appl. Phys.*, 107, 013912 (2010).

[160] C. D. P. Charmi, N. D. Preksha, S. S. Meena, C. S. Charanjeet, K. Srikanti, M. Ellouze, and R. B. J. Rajshree, "Influence of Co^{4+} Ca^{2+} substitution on structural, microstructure,

magnetic, electrical and impedance characteristics of M-type barium–strontium hexagonal ferrites," *Ceram. Int.*, 46, 24816-24830 (2020).

[161] C. G. Koops, "Resistivity and Dielectric constant: On the dispersion of resistivity and Dielectric constant of some semiconductors at audio frequencies," *Phys. Rev.*, 83, 121 (1951).

[162] G. Aravind, B. Nehru, R. V. Kumar, and D. Ravinder, "Dielectric properties of nano crystalline cobalt substituted lithium ferrites by citrate-gel auto combustion method," *Mater. Today: Proc.*, 3, 1423-1428 (2016).

[163] B. Louati, M. Gargouri, K. Guidara, and T. Mhiri, "AC electrical properties of the mixed crystal $(NH_4)_3H(SO_4)_{1.42}(SeO_4)_{0.58}$," *J. Phys. Chem. Solids*, 66, 762-765 (2005).

[164] B. Arslan, S. O. Tan, H. Tecimer, and S. Altındal, "Comparison of dielectric characteristics for metal-semiconductor structures fabricated with different interlayer thicknesses," *J. Mater. Sci.: Mater. Electron.*, 32, 26700–26708 (2021), https://doi.org/10.1007/s10854-021-06575-2.

[165] S. Demirezen, H. G. Cetinkaya, and S. Altındal, "Doping rate, interface states and polarization effects on dielectric properties, electric modulus, and AC conductivity in PCBM/NiO/p-Si structures in wide frequency range," *Silicon*, 14, 8517–8527 (2022), https://doi.org/10.1007/s11041-022-01737-7.

[166] M. F. Din et al., "Influence of Cd substitution on structural, electrical and magnetic properties of M-type barium hexaferrites co-precipitated nanomaterials," *J. Alloys Compd.*, 584, 646–651 (2014), https://doi.org/10.1016/j.jallcom.2013.09.043.

[167] J. Singh et al., "Elucidation of phase evolution, microstructural, Mössbauer and magnetic properties of Co^{2+}-Al^{3+} doped M-type Ba–Sr hexaferrites synthesized by a ceramic method," *J. Alloys Compd.*, 695, 1112–1121 (2017), https://doi.org/10.1016/j.jallcom.2016.10.237.

[168] H. Lv et al., "Co_xFe_yC composites with tunable atomic ratios for excellent electromagnetic absorption properties," *Sci. Rep.*, 5, 18249 (2015), https://doi.org/10.1038/srep18249.

[169] M. A. Abdeen, "Dielectric behaviour in Co–Zn ferrites," *J. Magn. Magn. Mater.*, 192, 121–129 (1999), https://doi.org/10.1016/S0304-8853(98)00628-2.

[170] X. D. Liu, Yunchen, et al., "Shell thickness-dependent microwave absorption of core-shell Fe_3O_4@C composites," *ACS Appl. Mater. Interfaces*, 6(12), 12997-13006 (2014), https://doi.org/10.1021/am5056579.

[171] M. Wu et al., "Microwave magnetic properties of $Co_{50}/(SiO_2)_{50}$ nanoparticles," *Appl. Phys. Lett.*, 80(23), 4404-4406 (2002), https://doi.org/10.1063/1.1487192.

[172] H. Sözeri, F. Genç, B. Ünal, A. Baykal, and B. Akta, "Magnetic, electrical and microwave properties of Mn-Co substituted $Ni_xZn_{0.8-x}Fe_2O_4$ nanoparticles," *J. Alloys Compd.*, 660, 324-335 (2016), https://doi.org/10.1016/j.jallcom.2015.10.144.

[173] Y. Zhang, F. Xu, G. Tan, J. Zhang, T. Wang, and F. Li, "Improvement of microwave-absorbing properties of Co_2Z barium ferrite composite by coating Ag nanoparticles," *J. Alloys Compd.*, **615**, 749–753 (2014), https://doi.org/10.1016/j.jallcom.2014.06.157.

[174] K. Watanabe, Y. Taka, and O. Fujiwara, "Cole-Cole measurement of dispersion properties for quality evaluation of red wine," *Measurement Sci. Rev.*, 9(5), 113–116 (2009), https://doi.org/10.2478/v10048-009-0016-1.

[175] W. Kuang and S. O. Nelson, "Dielectric relaxation characteristics of fresh fruits and vegetables from 3 to 20 GHz," *J. Microwave Power Electromagn. Energy*, 32(2), 114–122 (1997), https://doi.org/10.1080/08327823.1997.11688323.

[176] L. Wang, H. Xing, Z. Liu, Z. Shen, X. Sun, and G. Xu, "Facile synthesis of net-like Fe_3O_4/MWCNTs decorated by SnO_2 nanoparticles as a highly efficient microwave absorber," *RSC Adv.*, 6(99), 97142–97151 (2016), https://doi.org/10.1039/C6RA20823A.

[177] C. Singh et al., "Controllable morphology, dielectric, magnetic and reflection loss characteristics of ferrite/wax composites for low-loss applications," *J. Alloys Compd.*, 888, 161611 (2021), https://doi.org/10.1016/j.jallcom.2021.161611.

[178] Z. W. Li and Z. H. Yang, "Microwave absorption properties and mechanism for hollow Fe_3O_4 nanosphere composites," *J. Magn. Magn. Mater.*, 387, 131-138 (2015), https://doi.org/10.1016/j.jmmm.2015.02.033.

[179] Z. Jing, R. Qinghong, and Y. Atassi, "Design of ternary-component X-band microwave absorber based on FeCo/Sr hexaferrite/PANI nanocomposite in silicon resin matrix," *J. Magn. Magn. Mater.*, 512, 167037 (2020), https://doi.org/10.1016/j.jmmm.2020.167037.

[180] S. Goel, A. Garg, R. K. Gupta, A. Dubey, N. E. Prasad, and S. Tyagi, "Effect of neodymium doping on microwave absorption property of barium hexaferrite in X-band," *Mater. Res. Express*, 7(1), 16109 (2020), https://doi.org/10.1088/2053-1591/ab74fb.

[181] H. Sözeri, F. Genç, M. A. Almessiere, Ä. S. Ünver, A. D. Korkmaz, and A. Baykal, "Cr^{3+}-substituted Ba nanohexaferrites as high-quality microwave absorber in X-band," *J. Alloys Compd.*, 779, 420–426 (2019), https://doi.org/10.1016/j.jallcom.2018.11.131.

[182] E. Handoko et al., "Magnetic and microwave absorbing properties of $BaFe_{12-2x}Co_xZn_xO_{19}$ (x = 0.0; 0.2; 0.4; 0.6) nanocrystalline," *Mater. Res. Express*, 5(5), 056103 (2018), https://doi.org/10.1088/2053-1591/aab0c1.

[183] S. Sharma et al., "Tailoring the structural and magnetic traits of copper-modified $BaFe_{12}O_{19}$ nanostructured hexaferrites for recording media applications," *J. Magn. Magn. Mater.*, 564, 170124 (2022), https://doi.org/10.1016/j.jmmm.2022.170124.

[184] W. Zhang, A. Sun, X. Zhao, N. Suo, L. Yu, and Z. Zuo, "Structural and magnetic properties of La^{3+} ion doped Ni–Cu–Co nano ferrites prepared by sol-gel auto-combustion method," *J. Sol-Gel Sci. Technol.*, 90(3), 599–610 (2019), https://doi.org/10.1007/s10971-019-04941-4.

[185] S. H. Mahmood, A. A. Ghanem, I. Bsoul, A. Awadallah, and Y. Maswadeh, "Structural and magnetic properties of $BaFe_{12-x}Cu_xMn_xO_{19}$ hexaferrites," *Mater. Res. Express*, 4(3), 036103 (2017), https://doi.org/10.1088/2053-1591/aa646c.

[186] C. Singh, S. B. Narang, I. S. Hudiara, Y. Bai, and F. Tabatabaei, "Static magnetic properties of Co and Ru substituted Ba–Sr ferrite," *Mater. Res. Bull.*, 43(1), 176–184 (2008), https://doi.org/10.1016/j.materresbull.2007.02.021.

[187] D. R. Mane, U. N. Devatwal, and K. M. Jadhav, "Structural and magnetic properties of aluminium and chromium co-substituted cobalt ferrite," *Mater. Lett.*, 44(2), 91–95 (2000), https://doi.org/10.1016/S0167-577X(00)00207-4.

[188] T. R. Wagner, "Preparation and crystal structure analysis of magneto plumbite type $BaGa_{12}O_{19}$," *J. Solid State Chem.*, 136(2), 120–124 (1998), https://doi.org/10.1006/jssc.1997.7702.

[189] V. Dhage, M. Mane, S. B. Rathod, S. M. Rathod, and K. M. Jadhav, "Electric, dielectric, and AC electrical conductivity study of Al^{3+} substituted barium hexaferrite nanoparticles synthesized by Sol-gel auto-combustion technique," *Mater. Today: Proc.*, 47, 1982–1987 (2021), https://doi.org/10.1016/j.matpr.2020.08.305.

[190] A. Jaiswal et al., "Magnetic and dielectric properties and Raman spectroscopy of $GdCrO_3$ nanoparticles," *J. Appl. Phys.*, 107(1), 013912 (2010), https://doi.org/10.1063/1.3298774.

[191] R. S. Devan and B. K. Chougule, "Effect of composition on coupled electric, magnetic, and dielectric properties of two-phase particulate magnetoelectric composites," *J. Appl. Phys.*, 101(1), 014109 (2007), https://doi.org/10.1063/1.2436171.

[192] C. B. Kolekar, P. N. Kamble, S. G. Kulkarni, and A. S. Vaingankar, "Effect of Gd^{3+} substitution on dielectric behavior of copper-cadmium ferrites," *J. Mater. Sci.*, 30(22), 5784-5788 (1995), https://doi.org/10.1007/BF00354499.

[193] M. Hashim et al., "Structural, magnetic, and electrical properties of Al^{3+} substituted Ni-Zn ferrite nanoparticles," *J. Alloys Compd.*, 511(1), 107-114 (2012), https://doi.org/10.1016/j.jallcom.2011.08.101.

[194] T. Gupta et al., "Investigation on structural, hysteresis, Mössbauer properties, and electrical parameters of lightly Erbium substituted x-type $Ba_2Co_2Er_xFe_{28-x}O_{46}$ hexaferrites," *Ceram. Int.*, 46(7), 8209-8216 (2020), https://doi.org/10.1016/j.ceramint.2019.11.274.

[195] A. R. Kagdi et al., "Influence of Mg substitution on structural, magnetic, and dielectric properties of x-type barium–zinc hexaferrites $Ba_2Zn_{2-x}Mg_xFe_{28}O_{46}$," *J. Alloys Compd.*, 741, 377-391 (2018), https://doi.org/10.1016/j.jallcom.2018.01.138.

[196] R. Ranjan, R. Kumar, N. Kumar, B. Behera, and R. N. P. Choudhary, "Impedance and electric modulus analysis of Sm-modified $Pb(Zr_{0.55}Ti_{0.45})_{1-x}/_4O_3$ ceramics," *J. Alloys Compd.*, 509(19), 6388–6394 (2011), https://doi.org/10.1016/j.jallcom.2011.03.106.

[197] Aherrao, D. S., Singh, C., Mathe, V. L., Maji, P. K., & Srivastava, A. K. (2023) Investigation of structural, morphological, electric modulus, AC conductivity characteristics, and validation of software-based simulated impedance/material parameters of bicomponent Co-Al doped Ba-Sr ferrites. *Phys. Scr.*, 98, 015813. https://doi.org/10.1088/1402-4896/aca6b0

[198] J. Singh, C. Singh, D. Kaur, S. Bindra Narang, R. Jotania, and R. Joshi, "Microwave absorbing characteristics in Co^{2+} and Al^{3+} substituted $Ba_{0.5}Sr_{0.5}Co_xAl_xFe_{12-2x}O_{19}$ hexagonal ferrite," *J. Mater. Sci. Mater. Electron.*, 28(3), pp. 2377–2384, 2017, doi: 10.1007/s10854-016-5807-4.

[199] M. Thakur, C. Singh, and A. K. Srivastava, "Tunable structural, morphological, and hysteresis characteristics of $SrFe_{12}O_{19}/Fe_3O_4$ composites," *J. Mater. Sci. Mater. Electron.*, 35(9), 12395 (2024), https://doi.org/10.1007/s10854-024-12395-w.

[200] Shin, J. Y. and Oh, J. H., "The microwave absorbing phenomena of ferrite microwave absorbers," *IEEE Trans. Magn.*, 29(6), 3437–3439 (1993). https://doi.org/10.1109/20.281188.